Renormalization-Group Calculations for the Critical Properties of Perovskite Manganites, Uranium Superconductors, and Hexagonal Manganites

A thesis submitted in
partial fulfillment of the requirements
for the degree of

DOCTOR OF PHILOSOPHY

by

Rohit Singh

to the

Department of Physics
Indian Institute of Technology Guwahati
Guwahati - 781039, India

Declaration

The research work contained in this thesis entitled "**Renormalization-Group Calculations for the Critical Properties of Perovskite Manganites, Uranium Superconductors, and Hexagonal Manganites**" has been carried out by me with the supervision of **Dr. Malay K. Nandy**, and that this work has not been submitted elsewhere for a degree.

(Rohit Singh)

Department of Physics

Indian Institute of Technology Guwahati

Guwahati - 781039

January 30, 2017

Certificate

This is to certify that the research work contained in this thesis, entitled "**Renormalization-Group Calculations for the Critical Properties of Perovskite Manganites, Uranium Superconductors, and Hexagonal Manganites**" has been carried out by **Mr. Rohit Singh** with my supervision, and that this work has not been submitted elsewhere for a degree.

(Dr. Malay K. Nandy)
Associate Professor
Department of Physics
Indian Institute of Technology Guwahati
Guwahati - 781039

January 30, 2017

To My Mother

Acknowledgements

I would like to thank my supervisor, Dr. Malay K. Nandy, Associate Professor, IIT Guwahati, for his guidance in the area of statistical field theory. In particular, course on the statistical field theory taught by him helped me to learn various field theoretic concepts in renormalization-group and critical phenomena. I would also like to thank my doctoral committee members, Dr. G. S. Setlur, Dr. T. N. Dey, and Dr. Manabendra Sarma for their valuable suggestions throughout this thesis work. Many discussions with my doctoral committee chairman Dr. G. S. Setlur helped me a lot. I would like to acknowledge Department of Physics, Indian Institute of Technology, Guwahati, for providing me financial assistance and all the necessary requirements which were needed to carry out this research.

I owe a greater debt towards my mentor and collaborator Dr. Kishore Dutta. His help, motivations, discussions, kept my spirit towards research in tough times. Working with him was a quite nice experience for me, and I feel fortunate for his support in my research work.

I would take this opportunity to thank Dr. Uma Dutta Setlur for her encouragements. At IIT Guwahati, time with a few seniors, Swarnadeep Acharyya and Dr. Enamullah was also good and they also helped me in various ways.

For the prayers and encouragements during all these years in IIT Guwahati, I would like to thank the Christian fellowship members, Dr. Agile Mathew, Mrs. Blessy Agile, Simon Peter and Ravi Bolleddu.

I thank my childhood friend Abhishek Singh for his constant support throughout all years. Encouragements from Varsha Singh are also acknowledged.

I am grateful to my family members, my father Sri. Ajay Singh, my mother Smt. Kamlesh Singh, my brother Sri. Manish Singh his wife Smt. Sony Singh and nephews Harshit Singh and Raj Singh. My mother's love I really acknowledge which is beyond words.

Finally, I thank my spiritual source of inspiration Jesus Christ for his unconditional love.

Synopsis

This dissertation considers magnetic systems where spin-lattice coupling plays a major role in determining their critical properties near the critical point of second-order phase transition. To be more specific, we consider the critical properties in perovskite manganites, Mn-site doped perovskite manganites, uranium ferromagnetic superconductors, and hexagonal antiferromagnetic manganites. Perovskite manganites, represented by the formula $R_{1-x}A_xMnO_3$ [where R stands for trivalent rare-earth elements (e.g., La, Nd, Pr) and A stands for divalent alkaline earth elements (e.g., Ca, Ba, Sr)], exhibit a range of critical exponents varying with the parameters R, A, and x. To our knowledge, attempts to explain such a *varying range* of critical exponents do not exist in the literature. Early theoretical attempts [56,236,237,4] for spin-lattice coupled systems suggested the emergence of nonlocal quartic interaction on elimination of the lattice degrees of freedom. Such nonlocal interaction was also demonstrated to explain tricritical behavior [4]. However, although a few perovskite manganite samples exhibit near tricriticlal behavior, a vast majority of them are away from tricriticality. Thus there exist a great majority of perovskite manganite samples whose critical properties require a suitable theoretical explanation.

One aim of this dissertation is to construct a suitable nonlocal model capable of explaining such a varying range of critical exponents. Other aims are to consider critical properties of systems such as uranium superconductors and hexagonal an-

tiferromagnetic manganites that are also spin-lattice coupled systems. In addition, we also consider doped uniaxial ferromagnets and isomorphous salts that exhibit anomalous critical behavior.

The origin of nonlocality may be traced from the early works of Fisher, Wagner, and Aharony[56,237,4] that eventually led to a model involving nonlocal four-spin (quartic) coupling term that generated tricritical behavior. Thus it is interesting to consider a model Hamiltonian with nonlocal interaction in the quartic term and see whether such a model can generate critical properties both near and away from tricriticality as exhibited by perovskite manganite samples. We thus write a modified Ginzburg-Landau (GL) Hamiltonian involving nonlocal quartic interaction as

$$H[\Phi] = \int d^d x \left[\frac{c_0}{2} |\nabla \Phi(\mathbf{x})|^2 + \frac{r_0}{2} \Phi^2(\mathbf{x}) + \int d^d x' \Phi^2(\mathbf{x}) u(\mathbf{x}-\mathbf{x}') \Phi^2(\mathbf{x}') \right], \qquad (1)$$

where $u(\mathbf{x}-\mathbf{x}')$ is a nonlocal coupling function, $\Phi(\mathbf{x})$ is an n-component order parameter, and d is the space dimension.

Existence of a Tricritical Point. In Ch. 2, we take the simplest form for the coupling function, namely $u(\mathbf{k}) = \lambda_0 |\mathbf{k}|^{2\rho}$ in the Fourier space, where λ_0 is the coupling constant and ρ is refereed to as the nonlocal exponent. Employing Wilson's momentum shell decimation scheme at one-loop order, we carry out a renormalization-group (RG) analysis and calculate the static critical exponents, namely, the Fisher exponent η, correlation length exponent ν, specific heat exponent α, magnetization exponent β, susceptibility exponent γ, and the critical isotherm exponent δ, in the leading order of $\epsilon = 4 - d - 2\rho$. It is interesting to note that we obtain a non-zero value for the exponent η at one-loop order and the model generates exponents near tricritical mean-field (namely, $\alpha = 1/2$, $\beta = 1/4$, $\gamma = 1$, and $\delta = 5$) at $\epsilon = 0$ for $d = 3$. Thus, our RG scheme, being an expansion about $\epsilon = 0$, is an expansion about the tricritical mean-field[208].

On analysing the predictability of this theory, we find that although this model works well near tricriticality, it is unable to capture the critical exponents that are away from tricriticality in perovskite manganites. In particular, samples exhibiting values for β higher than 0.375 are not captured by this model. This requires a modification of the model to capture the critical exponents both near and away from tricriticality for perovskite manganites.

Static Critical Exponents of Perovskite Manganites. Capability of the above-mentioned model in explaining the nearly tricritical exponents in some perovskite manganites motivates us to consider a modified model and see whether it is capable of explaining the universality classes of perovskite manganites where a widely varying critical exponents (including tricritical mean-field exponents) have been observed in a number of experiments on samples with different compositions and doping levels[68,117,118,167,52]. For this purpose, in Ch. 3, we investigate a modified Ginzburg-Landau model with a screened nonlocal interaction in the quartic term, given by $u(\mathbf{k}) = \frac{\lambda_0}{[\mathbf{k}^2+m^2]^\sigma}$, where σ is the nonlocal exponent and m is the screening parameter which is assumed to be very small such that $m << \Lambda$. Since Λ is the ultraviolet cut-off, it is related to the lattice constant a as $\Lambda \sim a^{-1}$. Our assumption of low screening thus implies $m^{-1} >> a$ so that the range of interaction m^{-1} extends over a large number of lattice points unlike the conventional models with nearest neighbour interactions. We carry out an RG analysis at one-loop order in the leading order of $\epsilon = d_c - d$, where the upper critical dimension is found to be $d_c = 4 + 2\sigma$. We see that[205] the resulting critical exponents calculated for $n = 3$ in three dimensions for suitable values of σ are in satisfactory agreement with the available experimental estimates for various perovskite manganite samples including those exhibiting β values higher than 0.375 as displayed in Table 3.2. We find that the critical exponents vary slowly with respect to low values of m/Λ. For the

purpose of experimental verification, we chose $w = m^2/\Lambda^2 = 0.001$. It may be noted that if we had not taken screening explicitly into account in the model, agreements for the critical exponents would be greatly reduced, particularly for samples away from tricriticality with β values higher than 0.375. Thus screening, although small, it appears to play a fundamental role in determining the critical exponents for perovskite manganite samples.

Static Critical Exponents of Mn-site Doped Perovskite Manganites. A number of recent experiments on direct Mn-site doped perovskite manganites near the critical point of paramagnetic-to-ferromagnetic (PM-FM) phase transition [248,191,165] also exhibit widely varying critical exponents. In Ch. 4, we attempt to explain these critical exponents and find that the above nonlocal model with screened interaction captures satisfactorily the critical exponents for perovskite manganites where the Mn-site is doped by magnetic cations (such as Cr, Fe, Co, Ni) as well as nonmagnetic cations (such as Ti, Zn, and Ga) as displayed in Table 4.1. Thus the above nonlocal model Hamiltonian with screened interaction contains the universality classes of both parent undoped and doped Mn-site perovskite manganite samples. Since the predicted critical exponents vary with the model parameters σ and m/Λ, this situation is analogous to that in the case of Ashkin-Teller Potts model where the critical exponents vary continuously with the strength of energy-energy coupling giving a line of critical points [106]. This situation does not require a modification of the concept of universality or renormalization-group [106,47].

Dynamic Critical Exponents of Perovskite Manganites. Despite varying static critical exponents, experiments on the dynamic critical behavior of perovskite manganites near the critical point predicted an almost constant value for the linewidth exponent ϖ (≈ 0.5) irrespective of their chemical compositions [123,13,253]. The existing theoretical attempts to explain this behavior (namely, an almost constant

value of the linewidth exponent ϖ despite widely varying static critical exponents) have not rewarded satisfactory results. As our nonlocal model with screening captures satisfactorily the widely varying static critical exponents of perovskite manganites, we investigate the nonconserved critical dynamics of such a model Hamiltonian in the spirit of Model A (TDGL) of Halperin and Hohenberg [89] in Ch. 5. Carrying out a dynamic RG analysis at one-loop order, we calculate the dynamic critical exponent z and the linewidth exponent ϖ in the leading order of ϵ. Quite interestingly, we find that the model yields an almost constant value for ϖ (≈ 0.5) for a range of σ wherein we find varying static critical exponents in agreement with different experimental samples [207]. This suggests that the quartic nonlocal screened interaction plays an important role in determining the static as well as dynamic critical behavior of perovskite manganites.

Critical Behavior of Uranium Ferromagnetic Superconductors. Uranium ferromagnetic superconductors exhibit a strong uniaxial anisotropy and the coexistence of superconductivity and ferromagnetism has been explored in such systems extensively [143,198,12,252]. In addition, the critical behavior near the PM-FM phase transition in such systems have been investigated in a number of experiments [120,195,221]. Although, a three dimensional (3D) Ising universality class was expected due to their strong uniaxial anisotropy, the observed static critical exponents do not belong to any known universality classes including those for conventional (short-range) GL model Hamiltonian and its long-range (LR) version proposed by Fisher *et. al* [57]. This is due to the fact that experiments on UGe_2 samples [222,221] indicate the existence of a tricritical point similar to several other itinerant ferromagnets such as $ZrZn_2$, $Co(S_{1-x}Se_x)_2$, and MnSi. In addition, recent theoretical works [39,38] pointed out that the order parameter is a conserved quantity in such itinerant systems. As pointed out earlier, our model Hamiltonian

with nonlocal interaction has a tricritical fixed point. This motivates us to explore the conserved critical dynamics governed by the nonlocal Hamiltonian in Ch. 6. Taking a LR interaction with the coupling given by $u(\mathbf{k}) = \lambda_0|\mathbf{k}|^{2\rho}$, we carry out a dynamic RG analysis at one-loop order. The critical exponents determined from the non-trivial fixed point are comparable with the experimental estimates for uranium ferromagnetic superconductors. A comparison of the predicted critical exponents with the available experimental estimates are given in Table 6.2 [206].

Critical Exponents for Anomalous Uniaxial Ferromagnets. Pure samples of uniaxial ferromagnets (such as TbF_3 [28] and $LiTbF_4$ [62]) exhibit logarithmic corrections to mean field exponents that is well-explained by the marginal dimensionality of an anisotropic model Hamiltonian [126,60]. However, there exists doped samples (such as $LiTb_{0.3}Y_{0.7}F_4$ [18]) that exhibit departure from the logarithmic critical behavior and show anomalous critical exponents. In addition, uniaxial isomorphous salts (such as $Cu(NH_4)_2Br_4.2H_2O$ [232]) also exhibit anomalous critical behavior not explainable by the existing theories. In Ch. 7, we investigate the conserved critical dynamics governed by the above screened nonlocal model Hamiltonian. We carry out a dynamic RG analysis at one-loop order and calculate the dynamic critical exponent z and the linewidth exponent ϖ in the leading order of ϵ. Although there seems to be no experimental measurements for the dynamic exponents, their exist several experimental measurements for the static critical exponents for these anomalous uniaxial systems. We show that the present model predicts these anomalous static exponents in reasonably good agreements with the experiments.

Critical Exponents of Hexagonal Antiferromagnetic Manganites. Finally, we address the consequence of spin-lattice coupling in multiferroic hexagonal rare earth manganites. These compounds have attracted a great deal of attention in re-

cent years due to the coexistence of ferroelectricity and antiferromagnetism. In Ch. 8, we investigate the critical properties of a nonlocal quartic model Hamiltonian involving a coupling between the order parameter $\Phi(\mathbf{x})$ and the energy density $\varepsilon(\mathbf{x})$. Employing Wilson's momentum shell decimation scheme at one loop order, we perform an RG analysis and obtain the critical exponents corresponding to the non-trivial fixed point by invoking a double-expansion. We find that the specific heat exponent α lies in the range $-0.20 < \alpha < 0$ for the allowed range of nonlocal parameter ρ in three dimensions. The nonlocal model Hamiltonian is thus capable of capturing the experimentally observed specific heat exponent for antiferromagnetic hexagonal manganites[164] as displayed in Table 8.1.

Contents

List of Figures

List of Tables

Chapter 1

Introduction

"So nat'ralists observe, a flea
Has smaller fleas that on him prey;
And these have smaller fleas to bite 'em.
And so proceeds Ad infinitum." *. . . Jonathan Swift*

Summary

In this Chapter, we begin with the Landau theory of phase transition and discuss the consequences of the scaling hypothesis. We introduce Kadanoff's block spin ideas and discuss the underlying concepts behind Wilson's momentum shell decimation scheme and the renormalization-group transformation. Subsequently we consider critical dynamics as described by the relaxational models. Experimental scenario on the magnetic phase transitions in perovskite manganites, uranium superconductors, hexagonal manganites, and anomalous uniaxial ferromagnets are also presented. Finally, we discuss the theoretical developments for spin-lattice coupled systems elucidating the nonlocal nature of the effective model Hamiltonian.

1.1 Landau Theory of Phase Transition

Phase transition of the second kind involving a continuous change of order parameter of a system from one phase to another has received a great deal of attention for the past four or five decades [139,125,71,10,215,107]. A common example is the ferromagnet where the ordered (ferromagnetic) phase turns into a disordered (paramagnetic) phase when the temperature is increased across a critical (Curie) temperature (T_c). The ordered state is less symmetrical than the disordered state. Static critical properties near such order-disorder phase transition are related with equilibrium properties such as magnetization, susceptibility, specific heat, etc., while the dynamic critical behavior is associated with time dependent properties such as relaxation, diffusion, and propagation of spin-waves [139].

Within the Landau's phenomenological picture [125], such a second-order phase transition can be dealt with a quantity ϕ, known as *order parameter* that is directly related with physical measurable quantities such as magnetization in the case of paramagnetic-to-ferromagnetic (PM-FM) phase transition, staggered magnetization in the case of paramagnetic-to-antiferromagnetic (PM-AFM) phase transition. The free energy F is expected to be a function of the order parameter ϕ (assumed here to be one-component, for simplicity) and the temperature T. For critical properties one needs to consider temperature close to T_c so that the order parameter ϕ is expected to be small (below T_c). This allows one to expand the free energy as

$$F(\phi, T) = F_0 + a_1\phi + r_0\phi^2 + a_3\phi^3 + u_0\phi^4 + \ldots, \tag{1.1}$$

where the coefficients carry the temperature dependence. Since the numerical value of the free energy is expected to be the same when the magnetization is reversed, the above expansion should not contain odd powers of the order parameter

so that $a_1 = a_3 = 0$. This leads to

$$F(\phi, T) = F_0 + r_0\phi^2 + u_0\phi^4 + \ldots. \tag{1.2}$$

The essential features of the phase transition, are captured by taking the above expansion up to ϕ^4 with $u_0 > 0$ and by taking $r_0 = a(T - T_c)$. This ensures that $\phi = 0$ is the minimum free energy state for $T > T_c$ (symmetrical phase) and a state with $\phi \neq 0$ becomes the minimum free energy state for $T < T_c$ (less symmetrical phase) as shown in Fig. 1.1. As there are two degenerate minimum free energy states for $T < T_c$, the system can choose any one of these states leading to what is called symmetry breaking.

Since equilibrium properties of the system are determined by the minimum free energy state, minimizing Eq. (1.2) yields

$$\left[\frac{\delta F}{\delta \phi}\right]_{\phi_m} = 2a(T - T_c)\phi_m + 4u_0\phi_m^3 = 0, \tag{1.3}$$

which gives

$$\phi_m^2 = \begin{cases} \frac{a(T_c - T)}{2u_0} & \text{when } T < T_c, \\ 0 & \text{when } T > T_c. \end{cases} \tag{1.4}$$

The entropy S is related to the thermodynamic potential F as $S = -\partial F/\partial T$, yielding

$$S = \begin{cases} S_0 + \frac{a^2(T - T_c)}{2u_0} & \text{when } T < T_c, \\ S_0 & \text{when } T > T_c. \end{cases} \tag{1.5}$$

It shows that the entropy changes continuously at the transition point. Further, the specific heat C is calculated as $C = T(\partial S/\partial T)$, yielding

$$C = \begin{cases} C_0 + \frac{a^2 T}{2u_0} & \text{when } T < T_c, \\ C_0 & \text{when } T > T_c. \end{cases} \tag{1.6}$$

which shows that the specific heat is discontinuous, instead of being divergent at

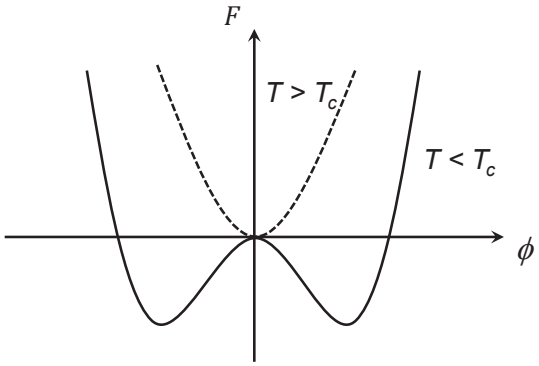

Figure 1.1: Ginzburg-Landau free energy functional F for an one component order parameter ϕ.

the transition point.

In order to obtain susceptibility χ, the thermodynamic potential F in the presence of magnetic field h can be expressed as

$$F(\phi,t) = F_0 + at\phi^2 + u_0\phi^4 - \phi hV, \tag{1.7}$$

where $t = T - T_c$. At thermodynamic equilibrium, minimization of F gives

$$2at\phi_m + 4u_0\phi_m^3 = hV. \tag{1.8}$$

This together with Eq. (1.4) yields

$$\chi = (\partial\phi_m/\partial h)_{h\to 0} = \begin{cases} \frac{V}{2at} & \text{when } t > 0, \\ -\frac{V}{4at} & \text{when } t < 0. \end{cases}$$

This indicates that the susceptibility diverges as one approaches the transition point. In order to estimate the role of fluctuations near the transition point, one can expand the free energy functional F about the equilibrium value ϕ_m in a Taylor's series as

$$\delta F = \frac{1}{2}(\phi - \phi_m)^2 \left(\frac{\partial^2 F(\phi,t)}{\partial\phi^2}\right)_{\phi=\phi_m}, \tag{1.9}$$

where the quantity $(\phi - \phi_m) \equiv (\delta\phi)$ can be regarded as fluctuation of the order parameter. In order to calculate $\langle(\delta\phi)^2\rangle$, one can use the canonical probability distribution for the above free energy configuration which is proportional to

$$P \propto \exp\left(-\frac{\delta F}{T}\right). \tag{1.10}$$

This together with Eq. (1.9) finally yields

$$\langle(\delta\phi)^2\rangle = \frac{\chi T}{V}. \tag{1.11}$$

The same result can also be obtained from the fluctuation-dissipation theorem. This indicates that the mean square fluctuations, being proportional to χ, diverges at the critical point. Thus the effect of fluctuations cannot be neglected and it is necessary to go beyond the mean-field description.

In writing the expression for thermodynamic potential given by Eq. (1.2), any inhomogeneity present in the system was neglected. By incorporating inhomogeneities, we can write Eq. (1.2) as

$$F(\Phi, t) = \int d^d x [F_0 + at\phi^2(\mathbf{x}) + c|\nabla\phi(\mathbf{x})|^2 + u_0\phi^4(\mathbf{x})], \tag{1.12}$$

where d is the space dimension. Using this free energy function and limiting ourselves to the Gaussian level, the fluctuating free energy can be written in the Fourier space as

$$\delta F = V \sum_k (at + ck^2)|\delta\phi_{\mathbf{k}}|^2, \tag{1.13}$$

for the symmetric phase ($\phi = 0$) where $\delta\phi_{\mathbf{k}}$ is the Fourier transform of $\delta\phi(\mathbf{r})$. We thus calculate

$$\langle|\delta\phi_{\mathbf{k}}|^2\rangle = \frac{T}{2V(at + ck^2)}, \tag{1.14}$$

indicating that it is the long-wavelength ($k \to 0$) fluctuations that increases as one

reaches the critical point. The correlation function of the fluctuations is expressed as

$$G(\mathbf{r}) = \langle \delta\phi(\mathbf{x}_1)\delta\phi(\mathbf{x}_2)\rangle. \tag{1.15}$$

where $\mathbf{r} = \mathbf{x}_1 - \mathbf{x}_2$. Invoking the Fourier transformed correlation together with statistical homogeneity, the above equation can be expressed as

$$G(\mathbf{r}) = \sum_k \langle |\delta\phi_{\mathbf{k}}|^2\rangle \exp(i\mathbf{k}\cdot\mathbf{r}), \tag{1.16}$$

using Eq. (1.14) in the above equation, one can arrive at

$$G(\mathbf{r}) = \frac{T}{8\pi c r}\exp(-r/\xi), \tag{1.17}$$

in three dimensions, where $\xi = \sqrt{\frac{c}{at}}$ is the correlation radius of the fluctuations. This indicates that at the critical point correlation fluctuations varies as $1/r$ in three dimensions. The above preliminary discussions clearly indicate that in critical phenomena, it is the long-wavelength ($k \to 0$) fluctuations that contribute to the singular behavior of the thermodynamic function.

1.2 Critical Exponents and the Scaling Hypothesis

In critical phenomena, observable quantities such as magnetization, susceptibility, specific heat, etc. exhibit power law behavior in the vicinity of the critical point. The associated power law exponents, commonly known as critical exponents, are independent of the specific systems under consideration. Thus the notion of *universality* comes into the picture which implies that systems sharing the same set of critical exponents belong to the same universality class. In fact, the critical exponents are universal in the sense that they do not depend on the microscopic details of the system and generally found to depend on the space dimension d, the number

of components n of order parameter, and the range of interaction [71].

In the case of a ferromagnet, the spontaneous magnetization M is a decreasing function of T below the Curie temperature T_c showing a power law behavior

$$M \propto (T_c - T)^{\beta}, \tag{1.18}$$

where β is identified as the spontaneous magnetization exponent. In the presence of an external magnetic field h, it is found that at $T = T_c$

$$M \propto |h|^{1/\delta}, \tag{1.19}$$

for small h, where δ is called as the critical isotherm exponent.

As pointed out by Widom [240], the above behavior of magnetization can be deduced from a single relation as

$$\begin{aligned} M(t,h) &= t^{\beta} F_{+}\left(\frac{h}{t^{\Delta}}\right) \qquad t > 0, \\ &= (-t)^{\beta} F_{-}\left(\frac{h}{(-t)^{\Delta}}\right) \qquad t < 0, \end{aligned} \tag{1.20}$$

where $t = (T - T_c)/T_c$ is the reduced temperature, F_+ and F_- are the scaling functions, and Δ is called as the gap exponent. Experimentally, to test the scaling hypothesis one needs to plot $M/|t|^{\beta}$ against $|h|/|t|^{\Delta}$ whence all the data fall on two curves: one above T_c and the other below T_c. This *data collapse* is a consequence of the scaling hypothesis.

From the above scaling hypothesis, the power law behavior of magnetic susceptibility $\chi = (\partial M/\partial h)_{h\to 0}$ as $T \to T_c$ can be obtained as

$$\chi \propto |T - T_c|^{-\gamma}, \tag{1.21}$$

where γ is identified as the susceptibility exponent. Singularity of the specific heat

C in the close vicinity of T_c is captured by the exponent α as

$$C \propto |T - T_c|^{-\alpha}. \tag{1.22}$$

where α is the specific heat exponent. According to the scaling hypothesis, there is an important length-scale ξ known as the correlation length which measures the average distance over which the order-parameter fluctuations are correlated. The hypothesis also says that the correlation length ξ diverges near T_c as

$$\xi \propto |T - T_c|^{-\nu}, \tag{1.23}$$

where ν is identified as the correlation length exponent, as $T \to T_c$, ξ becomes infinite. This implies that as $T \to T_c$, the system approaches self-similarity that is it would look the same under a change in length scale. For instance, if the unit of length scale is increased by a factor l, the system appears to shrink by a factor l in the new unit. In this case the free energy per unit volume becomes

$$f(\xi) = l^{-d} f(\xi/l). \tag{1.24}$$

Since the correlation length is the only relevant length scale of the problem, we can choose $l = \xi$ and write

$$f(\xi) = l^{-d} f(\xi/l) = \xi^{-d} f(\xi/\xi) = \xi^{-d} f(1) \propto |T - T_c|^{\nu d}. \tag{1.25}$$

From this relation, the specific heat can be obtained as

$$C = -T \frac{\partial^2 f}{\partial t^2} \propto |T - T_c|^{\nu d - 2}, \tag{1.26}$$

leading to the well known Josephson's scaling law

$$\alpha = 2 - \nu d, \tag{1.27}$$

where we have used Eq. (1.22). In order to obtain the other scaling laws, it is important to use the behavior of two-point correlation function $G(\mathbf{r})$ at T_c which goes like

$$G(\mathbf{r}) \propto r^{-d+2-\eta} \tag{1.28}$$

where η is identified as the correlation function exponent. Using the relation between the susceptibility and two-point correlation function, namely

$$\chi \sim \int d^d x [\langle \phi(\mathbf{x})\phi(\mathbf{x}')\rangle - \langle \phi(\mathbf{x})\rangle^2], \tag{1.29}$$

giving

$$\chi \sim |T - T_c|^{-\nu(2-\eta)}, \tag{1.30}$$

which yields the Fisher's scaling relation

$$\gamma = \nu(2 - \eta). \tag{1.31}$$

This relation and Eq. (1.27) followed from the assumption that the correlation length is a dominating length scale and the correlation function has a power law behavior at the critical point. The other scaling laws can also be derived by using the homogeneity assumption for the singular free energy as

$$f_s(t, h) = t^{2-\alpha} f(h/t^{\Delta}). \tag{1.32}$$

The magnetization is calculated as

$$M(t, h) \sim -\frac{\partial f_s}{\partial h} \sim t^{2-\alpha-\Delta} f'(h/t^{\Delta}), \tag{1.33}$$

we see that in limit $h \to 0$, $f'(0)$ is a constant so that

$$\beta = 2 - \alpha - \Delta. \tag{1.34}$$

Differentiating Eq. (1.33) we find the susceptibility as

$$\chi \sim t^{2-\alpha-2\Delta} f''(h/t^{\Delta}), \tag{1.35}$$

which gives

$$\gamma = \alpha + 2\Delta - 2. \tag{1.36}$$

Eliminating Δ from Eqs. (1.34) and (1.36) we get the relation

$$\alpha + 2\beta + \gamma = 2. \tag{1.37}$$

The limit $t \to 0$ in Eq. (1.33) gives

$$M(0,h) \sim t^{2-\alpha-\Delta}(h/t^{\Delta})^{x}. \tag{1.38}$$

for this limit to be independent of temperature

$$x\Delta = 2 - \alpha - \Delta, \tag{1.39}$$

so that

$$M(0,h) \sim h^{(2-\alpha-\Delta)/\Delta}, \tag{1.40}$$

This gives

$$\delta = \Delta/(2 - \alpha - \Delta). \tag{1.41}$$

We thus have

$$\delta - 1 = \frac{\Delta}{2-\alpha-\Delta} - 1 = \frac{2\Delta - 2 + \alpha}{2-\alpha-\Delta} = \frac{\gamma}{\beta}. \tag{1.42}$$

Thus, we have four scaling relations, namely

Widom's relation: $\gamma = \beta(\delta - 1)$

Fisher's relation: $\gamma = \nu(2 - \eta)$

Rushbrooke's relation: $\alpha + 2\beta + \gamma = 2$

Josephson's relation: $\nu d = 2 - \alpha$.

Since there are four independent relations among the six critical exponents, any two of the critical exponents are required to find all of them.

Having defined the critical exponents, we are in a stage to summarize the exponents of Landau's theory, namely

$$\alpha = 0, \quad \beta = 1/2, \quad \gamma = 1, \quad \delta = 3, \quad \nu = \frac{1}{2}, \quad \eta = 0 \tag{1.43}$$

which are also known as the *mean-field exponents*. It may however be noted that Josephson's (hyperscaling) relation, given by Eq. (1.27), is satisfied by the mean field values only for $d = 4$.

It is important to note that the argument of scaling hypothesis, namely, *"the only relevant length scale near the critical point is the correlation-length*" is not exactly true as can be seen from a simple dimensional argument given in Ref.[71]. This argument is as follows. The two-point correlation function of the Landau theory defined in previous section can be written in the Fourier space as

$$G_0(\mathbf{k}) = \frac{1}{2}(c_0\mathbf{k}^2 + r_0)^{-1}, \tag{1.44}$$

which after a change of scale $\mathbf{k}' = b\mathbf{k}$, rescales as

$$G'(\mathbf{k}') = b^{-2}G(\mathbf{k}). \tag{1.45}$$

Now using the same scale transformation in the form of two-point correlation func-

tion at criticality, namely $G(\mathbf{k}) \sim k^{-2+\eta}$, one can obtain

$$G'(\mathbf{k}') \sim b^{-2+\eta} G(\mathbf{k}). \tag{1.46}$$

Obviously, these two equations do not match unless $\eta = 0$. This implies that the critical exponents other than that of Landau theory violates the dimensional analysis. To resolve this discrepancy, a length scale other than the correlation length should be incorporated in the dimensional analysis, as described in Ref.[71]. The only possible length scale is the lattice spacing a or, in other words, the ultraviolet cut-off Λ which when incorporated in the dimensional analysis, the two-point correlation function becomes

$$G(\mathbf{k}, T_c) \propto a^{\eta} k^{-2+\eta}, \tag{1.47}$$

giving

$$G'(\mathbf{k}', T_c) = b^{-2} G(\mathbf{k}, T_c). \tag{1.48}$$

Thus, dimensional consideration indicates that the anomalous dimension can only be accounted by invoking the microscopic length scale a (or lattice spacing) where $a \ll \xi$. As we shall explore below the Wilson's RG procedure, the microscopic length scale introduces a physical ultraviolet cut-off Λ in the momentum integrations.

1.3 The Renormalization-Group

The basic ingredient of renormalization-group (RG) stems from the imposed physical cut-off $\Lambda \sim a^{-1}$. In the block spin picture of Kadanoff, spin blocks of size Λ^{-1} are assumed where all the spins within each block behave like one unit. One can define the block spin as the mean of cell spin $s_x = b^{-d} \sum_c^x s_c$, where s_x is the sum over all cell spin in the block. The procedure to obtain the block Hamiltonian H'

from the cell Hamiltonian H is the Kadanoff transformation, namely $H' = K_b H$. The spatial resolution of the block Hamiltonian H' is b. If one is interested in the variation of the block spin s_k (the Fourier transform of s_x) with k smaller than the cut-off Λ, one can integrate out all those s_k with $k > \Lambda$ from $e^{-H/T}$ so that the new probability distribution becomes

$$P' \propto \int \exp(-H[s]/T) \prod_{i,k>\Lambda} ds_{ik}. \tag{1.49}$$

By repeating this transformation, one can construct one block Hamiltonian from the other as $H'' = K_{b'} H'$ with the probability distribution

$$P'' \propto \int \exp(-H'[s]/T) \prod_{i,\Lambda/b<k<\Lambda} ds_{ik}. \tag{1.50}$$

These successive block transformation will lower the cut-off. Further, one can easily see that

$$K_{b'} H' = K_{b'} K_b H = K_{b'b} H. \tag{1.51}$$

Within this picture, the scaling comes out from the ingenious argument of block transformation. To show the dependence of free energy on block parameters t_b and h_b, it is reasonable to assume the power law behavior $t_b = t b^{y_t}$, $h_b = h b^{y_h}$ where $y_t > 0$ and $y_h > 0$. Thus, free energy per unit volume can be expressed as

$$f(t, h) = b^{-d} f(t b^{y_t}, h b^{y_h}). \tag{1.52}$$

Since b is arbitrary, one can choose $b = |t|^{-1/y_t}$ and arrive at

$$f(t, h) = |t|^{d/y_t} f(1, h|t|^{-y_h/y_t}), \tag{1.53}$$

which is quite similar to the singular form of free energy [Eq. (1.32)] with

$$2-\alpha=\frac{d}{y_t}, \tag{1.54}$$

and

$$\Delta=\frac{y_h}{y_t}. \tag{1.55}$$

One can see that the exponents y_t or y_h are related to the usual known exponents. For instance, the correlation length of the system changes $\xi'=\xi/b$ so that

$$\xi(t,h)=b\xi(b^{y_t}t,b^{y_h}h)=t^{-1/y_t}\xi(1,h/t^{y_h/y_t}) \tag{1.56}$$

this yields

$$\nu=1/y_t. \tag{1.57}$$

This constitutes the first step of RG transformation where the cut-off is reduced from Λ to Λ/b and so on in successive transformations. The next step of RG is to rescale the momentum and fields such that the original cut-off is restored. These facts imply that the new probability distribution is equivalent to old one. If the parameter space of H is represented by $X=(r_0,c,u_0)$, then the above set of transformations will lead a probability distribution P to another probability distribution P' as

$$X'=R_bX, \tag{1.58}$$

where R_b represents the RG transformation with $b>1$. In the parameter space the points which are invariant under R_b, i.e., $X^*=R_bX^*$, are called fixed points. The fixed point X^* which is invariant under RG, lies on a critical surface where the RG transformation R_b drives any point towards X^*. A point which is not on the critical surface but very close to it, the RG transformation R_b drives it away from X^*. Thus

all points X lying on the critical surface have the property

$$\lim_{b\to\infty} R_b X = X^*. \tag{1.59}$$

Thus the critical phenomena are related to the properties of R_b near the fixed point and the critical exponents are related to the eigenvalues of the linearised R_b.

In order to carry out the analysis around a fixed point X^*, one can write

$$X = X^* + \delta X, \tag{1.60}$$

where δX is a small deviation from X^*. Thus, Eq. (1.58), can be written by using this definition of X as

$$\delta X' = R_b^l \delta X + O(\delta X^2), \tag{1.61}$$

where the linear operator R_b^l is a matrix with components

$$R_{ij} = \left.\frac{\partial X_i'}{\partial X_j}\right|_{X=X*}. \tag{1.62}$$

From the eigenvalue equation for the matrix, $R_{ij}e_j = \lambda_j e_j$, we can calculate its eigenvalues $\lambda_j = b^{y_j}$ where y_j are constants and independent of b. Expanding δX in terms of the eigenvector e_j of R as $\delta X = \sum_j a_j e_j$, one can obtain

$$\delta X' = R_b^l \delta X = R_{ij} \sum_j a_j e_j = \sum_j \lambda_j a_j e_j = \sum_j a_j' e_j, \tag{1.63}$$

where

$$a_j' = a_j b^{y_j}. \tag{1.64}$$

is the projection of $\delta X'$ along e_j. For $y_j > 0$, a_j' becomes a relevant variable because it grows as b increases. The variable a_j' becomes marginal and irrelevant for $y_j = 0$ and $y_j < 0$ respectively.

With this background, we shall now discuss the application of RG on the GL

model Hamiltonian and see how it improves upon the mean field exponents.

1.4 Renormalization-Group Treatment of the Ginzburg-Landau Model

We recall that the GL model Hamiltonian is given by

$$H(\Phi) = \int d^d x \left[\frac{r_0}{2} \Phi^2(\mathbf{x}) + \frac{c}{2} |\nabla \Phi(\mathbf{x})|^2 + u_0 \Phi^4(\mathbf{x}) + \cdots \right], \tag{1.65}$$

where Φ is an n-component order parameter. As discussed in the previous section, the formal RG procedure consists of coarse graining the field and rescaling which together produce a transformed Hamiltonian

$$H'(\Phi') = \int d^d x' \left[\frac{r'}{2} \Phi'^2(\mathbf{x}') + \frac{c'}{2} |\nabla \Phi'(\mathbf{x}')|^2 + u' \Phi'^4(\mathbf{x}') + \cdots \right]. \tag{1.66}$$

where the transformed parameters are functions of the original ones defining a mapping $X'(r', c', u') = R_b X(r_0, c_0, u_0)$ in the parameter space of RG. Indeed, the RG analysis on such a model Hamiltonian can most conveniently be performed in terms of the Fourier modes. Thus in Fourier space, the field $\phi_i(\mathbf{k})$ can be decomposed as $\phi_i(\mathbf{k}) = \phi_i^<(\mathbf{k}) + \phi_i^>(\mathbf{k})$ where the fast modes $\phi_i^>(\mathbf{k})$ lies in the range $\Lambda/b < k < \Lambda$ and the slow modes $\phi_i^<(\mathbf{k})$ lies in the range $0 < k < \Lambda/b$. The coarse-grained partition function can be expressed as

$$Z = \int D(\phi_i^<(\mathbf{k})) \exp\left[\int_0^{\Lambda/b} \frac{d^d q}{2\pi^d} \frac{c_0 \mathbf{k}^2 + r_0}{2} |\phi_i^<(\mathbf{k})|^2 \right]$$

$$\times \int D(\phi_i^>(\mathbf{q})) \exp\left[\int_{\Lambda/b}^{\Lambda} \frac{d^d \mathbf{q}}{(2\pi)^d} \frac{c_0 \mathbf{q}^2 + r_0}{2} |\phi_i^>(\mathbf{q})|^2 \right] \times \exp\left[-U[\phi_i^<(\mathbf{k}), \phi_i^>(\mathbf{q})] \right], \tag{1.67}$$

where $U = u_0\Phi^4$. From the above equation one can write

$$H[\phi_i^<(\mathbf{k})] = C + \int_{k=0}^{\Lambda/b} \frac{d^dk}{(2\pi)^d} \frac{c_0\mathbf{k}^2 + r_0}{2} |\phi_i^<(\mathbf{k})|^2 - \ln\langle \exp\{-U[\phi_i^>, \phi_i^<]\}\rangle_{\phi_i^>}, \quad (1.68)$$

where the average occurring in the last term is defined as

$$\langle \mathcal{O} \rangle = \int \frac{d\phi_i^>}{Z(\phi_i^>)} \mathcal{O} \exp\left[-\int_{\Lambda/b}^{\Lambda} \frac{d^dq}{(2\pi)^d} \frac{c_0\mathbf{q}^2 + r_0}{2} |\phi_i^>(\mathbf{q})|^2 \right], \quad (1.69)$$

with

$$C = -nV/2 \int_{\Lambda/b}^{\Lambda} \frac{d^dq}{(2\pi)^d} \ln(c_0\mathbf{q}^2 + r_0). \quad (1.70)$$

Thus the final expression appearing in Eq. (1.68) can be calculated perturbatively in a cumulant expansion as

$$\ln\langle \exp\{-U\}\rangle_{\phi^>} = -\langle U\rangle_{\phi^>} + \frac{1}{2}\left(\langle U^2\rangle - \langle U\rangle^2\right)_{\phi^>} + \ldots\ldots \quad (1.71)$$

The perturbation calculation gives the RG flow for scale dependant parameters as

$$r' = b^2 \left[r_0 + 4u_0(n+2) \int_{\frac{\Lambda}{b}}^{\Lambda} \frac{d^dq}{(2\pi)^d} \frac{1}{c_0\mathbf{q}^2 + r_0} \right], \quad (1.72)$$

$$u' = b^{4-d} \left[u_0 - 4u_0^2(n+8) \int_{\frac{\Lambda}{b}}^{\Lambda} \frac{d^dq}{(2\pi)^d} \frac{1}{(c_0\mathbf{q}^2 + r_0)^2} \right]. \quad (1.73)$$

The Wilson-Fisher fixed point is obtained from the above RG flow equations as

$$\frac{r^*}{c} = -\frac{(n+2)\epsilon\Lambda^2}{2(n+8)} + O(\epsilon^2), \quad (1.74)$$

$$\frac{u^*}{c^2} = \frac{\epsilon\Lambda^{d-4}}{4(n+8)K_4} + O(\epsilon^2), \quad (1.75)$$

where $\epsilon = 4 - d$ and K_4 is the surface area of an unit sphere in 4-dimensions. Corresponding to this fixed point, the critical exponents in the leading order of ϵ

are obtained as

$$\eta = 0 + O(\epsilon^2), \tag{1.76}$$

$$\nu = \frac{1}{2} + \frac{\epsilon(n+2)}{4(n+8)} + O(\epsilon^2), \tag{1.77}$$

$$\alpha = \frac{\epsilon(4-n)}{2(n+8)} + O(\epsilon^2), \tag{1.78}$$

$$\beta = \frac{1}{2} - \frac{3\epsilon}{2(n+8)} + O(\epsilon^2), \tag{1.79}$$

$$\gamma = 1 + \frac{(n+2)\epsilon}{2(n+8)} + O(\epsilon^2), \tag{1.80}$$

$$\delta = 3 + \epsilon + O(\epsilon^2). \tag{1.81}$$

The above analytical expressions indicate corrections to the mean field exponents up to $O(\epsilon)$. Thus the critical exponents for 3D Ising and 3D Heisenberg can be approximately calculated from the above expressions for $n = 1$ and $n = 3$ respectively. It is important to note that the critical exponents can be calculated up to $O(\epsilon^2)$ and beyond by considering higher order terms in the perturbative (cumulant) expansion. Such calculations have been performed by Wilson and Kogut in Ref. [244].

1.5 Critical Dynamics

The dynamic critical behavior is related to the time variations of the large scale fluctuations of the order parameter near the critical point. It involves the time dependant processes such as diffusion, spin wave propagation, damping, and inelastic scattering etc. [139]. The long wavelength modes usually have very long relaxation times often refereed to as "critical slowing down". In equilibrium, $\partial H/\partial \phi_i(\mathbf{r}) = 0$, however, when the system is out of equilibrium, it is customary to assume a Langevin-type dynamics for the relaxation of the order parameter fluctuations,

given by[71]

$$\frac{\partial \phi_i(\mathbf{x},t)}{\partial t} = -\Gamma_0 \frac{\delta H}{\delta \phi_i(\mathbf{x},t)} + \eta_i(\mathbf{x},t), \tag{1.82}$$

where the phenomenological parameter Γ_0 sets the time scale. The noise $\eta_i(\mathbf{x},t)$ is assumed to have Gaussian statistics with ensemble averages

$$\langle \eta_i(\mathbf{x},t)\rangle = 0, \quad \langle \eta_i(\mathbf{x},t)\eta_j(\mathbf{x}',t')\rangle = D\delta^d(\mathbf{x}-\mathbf{x}')\delta(t-t')\delta_{ij}, \tag{1.83}$$

where D and Γ_0 are related by the fluctuation-dissipation theorem, namely, $D = 2\Gamma_0 k_B T$.

The above Langevin equation involving the standard GL model Hamiltonian H [Eq. 1.65] is known as *time-dependent Ginzburg-Landau (TDGL) model*. It can be portrayed in the Fourier space within the Gaussian approximation ($u_0 = 0$) as

$$\frac{\partial \phi_i(\mathbf{k},t)}{\partial t} = -\Gamma_0(c_0 k^2 + r_0)\phi_i(\mathbf{k},t) + \eta_i(\mathbf{k},t). \tag{1.84}$$

Its solution, representing the evolution of each mode, can be readily obtained as

$$\phi_i(\mathbf{k},t) = \phi_i(\mathbf{k},0)e^{-\gamma(\mathbf{k})t} + \int_0^t dt' e^{-\gamma(\mathbf{k})(t-t')}\eta_i(\mathbf{k},t), \tag{1.85}$$

where $\gamma(\mathbf{k}) = \Gamma_0(c_0 k^2 + r_0)$. Thus the fluctuations in each mode decay with relaxation time

$$\tau(\mathbf{k}) \equiv \frac{1}{\gamma(\mathbf{k})} = \left[\Gamma_0(c_0 k^2 + r_0)\right]^{-1}. \tag{1.86}$$

Recalling the correlation length as $\xi = (c_0/r_0)^{1/2}$, the above relaxation time can be written as

$$\tau(\mathbf{k}) = \xi^2(1+\xi^2 k^2)^{-1}(c\Gamma_0)^{-1}. \tag{1.87}$$

This can be compared with the general dynamic scaling for relaxation time

$$\tau(\mathbf{k}) = \xi^z f(\mathbf{k}\xi), \tag{1.88}$$

where z is known as the *dynamic critical exponent*, giving $z = 2$.

The dynamic critical behavior is much diverse as compared to the static one. For the same static universality class, different dynamic universality classes can be obtained depending on the associated conservation laws for the order parameter. Although in the above analysis, the dissipation rate Γ_0 is treated as a constant, there are systems in which the order parameter may be conserved and the dynamics should be constraint by this conservation law. In such as situation, Γ_0 and D need to be replaced by $-\Gamma_0\nabla^2$ and $-D\nabla^2$ respectively. A systematic classification of various dynamic universality classes has been offered by Halperin, Hohenberg, and Ma [80,79] an elaborated discussion of which is given in the review article by Hohenberg and Halperin [89].

In the terminology of Ref. [89], model with $\Gamma_0(\mathbf{k}) = \Gamma_0$ is known as "model A" critical dynamics where the order parameter is not conserved. Thus it is applicable for the investigation of PM-FM phase transition in systems where magnetization is not a conserved quantity. Systems with conserved order parameter such as in strongly uniaxial ferromagnets, the dissipation rate $\Gamma_0(\mathbf{k}) = \Gamma_0 k^2$ and its dynamics is known as "model B" critical dynamics. In the theoretical picture of the Gaussian approximation, the dynamic critical exponent z turns out to be $z = 2$ for the case of model A and $z = 4$ for model B critical dynamics. It can be shown that if the above analysis is performed with the full correlation function, then

$$\tau(\mathbf{k}) = \xi^{2-\eta} f(\mathbf{k}\xi), \tag{1.89}$$

for nonconserved (model A) case and

$$\tau(\mathbf{k}) = \xi^{4-\eta} f(\mathbf{k}\xi), \tag{1.90}$$

for the conserved (model B) case.

In addition to the dynamic critical exponent z, there is another experimentally measurable critical exponent ϖ for the linewidth Δ scale like

$$\Delta \sim |T - T_c|^{-\varpi}, \tag{1.91}$$

in the close vicinity of T_c. The linewidth is related to the two-point dynamic correlation function $C(\mathbf{k},\omega)$ as[78,90]

$$\Delta = \int \frac{d^d k}{(2\pi)^d} C(\mathbf{k}, \omega = 0), \tag{1.92}$$

where

$$\langle \phi_i(\mathbf{k},\omega)\phi_j(\mathbf{k}',\omega')\rangle = C(\mathbf{k},\omega)[2\pi]^{d+1}\delta^d(\mathbf{k}+\mathbf{k}')\delta(\omega+\omega')\delta_{ij}. \tag{1.93}$$

The linewidth exponent ϖ follows the scaling relation

$$\varpi = \nu(z + 2 - d - \eta). \tag{1.94}$$

The value of ϖ can be obtained from linewidth measurement experiments such as electron paramagnetic resonance (EPR), muon spin relaxation (μSR), nuclear magnetic resonance (NMR), etc. Since the dynamic critical behavior near the second-order phase transition is determined by z and ϖ, in this thesis, we make an attempt to calculate these exponents from different models corresponding to different magnetic systems. In the following section, we provide an overview of recently explored critical behavior for various strongly correlated magnetic systems.

1.6 Experiments on Various Strongly Correlated Magnetic Systems

In this section, we present a brief discussion regarding the experimental situations on various strongly correlated magnetic systems, namely, perovskite manganites, uranium ferromagnetic superconductors, and hexagonal manganites. We provide evidences from various experiments suggesting that these systems are dominated by strong spin-lattice coupling. In addition, we also report a few uniaxial systems, namely, doped uniaxial ferromagnets and isomorphous salts that exhibit anomalous critical behavior.

1.6.1 Perovskite Manganites

Perovskite manganites represented by the generic formula $R_{1-x}A_xMnO_3$ where R stands for trivalent rare-earth (e.g., La, Nd, or Pr) and A stands for divalent alkaline earth (e.g., Ca, Ba, or Sr) elements respectively. Its chemical structure is schematically shown in Fig. 1.2. In the last two decades, there have been a considerable number of experimental investigations on their magnetic and electrical properties. These experiments showed that a variety of phases appear in these samples while tuning the temperature as well as the doping level x. For instance, $La_{1-x}Ca_xMnO_3$ shows a PM-FM phase transition for $0.2 < x < 0.5$ with the transition temperature $T_c(x) \approx 200 - 250$K[148]. It behaves as ferromagnetic insulator for $x < 0.2$ and as an antiferromagnet for $x > 0.5$.

Critical behavior of perovskite manganites near their PM-FM phase transition points have been investigated [142,68,155,92,117,162,220,176,185,233,52] in a number of experimental works . These studies indicate that their critical exponents near the PM-FM phase transition varies measurably with chemical compositions (R and/or A) as well as the level of doping (x). For some of the samples the critical exponents

belong to the universality class of tricritical mean field [117,233,52] whereas most of them exhibit critical exponents that are away from tricriticality [142,68,155,92]. It is in fact evident that the standard GL model predicts critical exponents that are not in agreement with the majority of observed exponents in perovskite mangnaites.

Regarding interactive processes in perovskite manganites, two microscopic mechanisms namely, the spin-spin *double exchange (DE)* interaction [255] and electron-phonon *Jahn-Teller (JT) lattice distortions* [102] play significant role in elucidating their physical behavior particularly, the emergence of colossal magnetoresistance (CMR) and doping dependence of T_c [150,188]. The DE mechanism takes into account of the transfer of an electron between the neighbouring Mn^{3+} and Mn^{4+} ions through the Mn–O–Mn path [255,44]. DE mechanism provides explanation for the change in resistivity as the system passes through the low temperature to high temperature phases [148,197]. However, the localization of electrons in the high temperature phase could not be explained only from the DE mechanism. In addition, the DE mechanism overestimates T_c and underestimates the magnetoresistance. To overcome these discrepancies, an additional mechanism, viz. electron-phonon coupling has been proposed [151,148].

Associated with electron-lattice coupling, there are mainly two types of distortion, namely, the buckling of MnO_6 octahedra and JT coupling. The buckling related to the ionic radii r_A of A atoms is measured in terms of tolerance factor (f) which is given by

$$f = \frac{\langle r_A \rangle + r_O}{\sqrt{2}(r_{Mn} + r_O)}, \tag{1.95}$$

where r_O and r_{Mn} are the radii of oxygen and manganese atoms respectively. By fixing the Mn^{+3}/Mn^{+4} ratio and varying tolerance factor, Hwang *et al.* [99] showed that with decreasing r_A the critical temperature T_c decreases and magnetoresistance increases drastically near T_c. Further, they also obtained a sharp magnetic

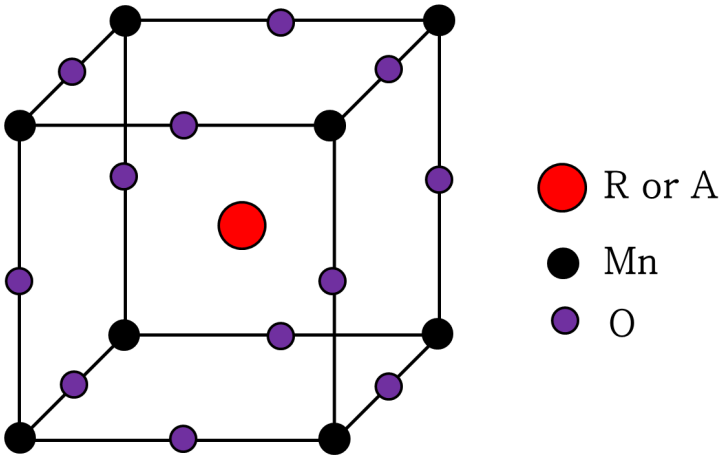

Figure 1.2: Schematic chemical structure of perovskite manganites $R_{1-x}A_xMnO_3$.

transition with decreasing r_A, indicating a sign of first order phase transition. The JT lattice distortion, on the other hand, is shown to be responsible for localizing electrons by forming a self trapped state known as polaron.

The variation of the cation concentration or the alternation of Mn^{3+}/Mn^{4+} ratio changes the strength of DE interaction. Further, with increasing hole doping, the JT distortion decreases[27]. The ratio of Mn^{3+}/Mn^{4+} can be altered in perovskite manganites by doping the direct Mn-site with 3D transition metals (e.g., Ni, Fe, Co, Ti, Ga, Zn, Cr, V). In such systems, represented by $R_{1-x}A_xMn_{1-y}M_yO_3$ where M stands for transition metal elements, Mn couples directly to neighbouring atoms by both antiferromagnetic super-exchange (SE) and ferromagnetic DE mechanisms. Recently, critical behavior of such direct Mn-site perovskite manganites have been explored experimentally[248,86,250,165,67,20,45,46,191,178,153,177]. These experiments indicated that just like the parent compounds, their critical exponents vary with varying doping level y and varying transition metal M, leading to a wide diversity of universality classes.

In addition to the above, there have been a few experiments on dynamic crit-

ical properties of perovskite manganites [123,13,253]. These experiments are mainly based on the measurement of linewidth via EPR, ESR, μ-SR, and NMR which suggest that the linewidth in these compounds have a constant value ($\varpi \approx 0.5$) irrespective of the sample composition R, and A and varying doping level x.

In Chs. 3 and 4, the static critical behavior of perovskite manganites are discussed elaborately in the light of existing experimental findings. Their dynamic critical behavior is addressed in Ch. 5.

1.6.2 Uranium Ferromagnetic Superconductors

Recently, uranium ferromagnetic superconductors, such as UGe_2, URhGe, and UIr, have attracted a great deal of attention due to the coexistence of superconductivity and ferromagnetism [143,198,12]. The chemical structure of UGe_2 is shown in Fig. 1.3. Ferromagnetism in these uniaxial systems occur due to the mobile $5f$ electrons which have a dual nature between itinerant and localized character [252,195]. This duality is also found to be a key mechanism for the conservation of total magnetization in such itinerant systems [38]. The PM-FM phase transition in these materials have been recently explored via a number of experiments [221,120,195]. Experiments aiming at determining the critical behavior also suggested that the transition temperature T_c strongly depends on pressure [84,210,96,222]. A tricritical point with a first-order phase transition was observed in UGe_2 [66,152] under the application of sufficient pressure.

Experimental estimates for their static critical exponents suggested that the critical behavior of uranium ferromagnetic superconductors could not be described by conventional models, a detail discussion of which is given in Ref. [221]. Neutron scattering experiment, on the other hand, provide evidences for strong influence of magnetoelastic coupling near such phase transitions [212].

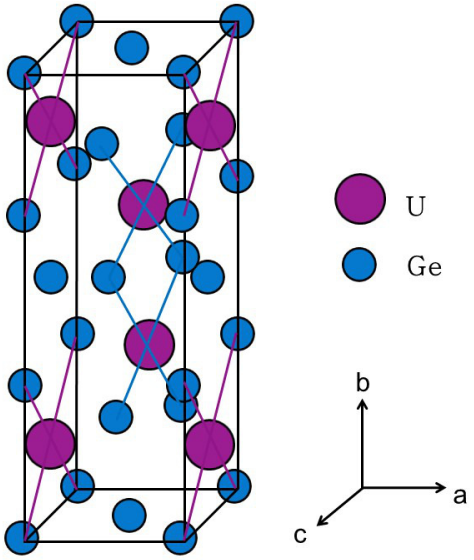

Figure 1.3: Schematic chemical structure of UGe_2.

1.6.3 Anomalous Uniaxial Ferromagnets

Critical phenomena have been explored over the decades via a number of experiments in widely different uniaxial systems[217,231,232,28,62]. Examples of this kind are isomorphous salts[217,231,232] $Cu(NH_4)_2Br_4.2H_2O$, $CuRb_2Br_4.2H_2O$, and $CuK_2Cl_4.2H_2O$. Other uniaxial magnetic systems include the pure (undoped) uniaxial ferromagnets such as TbF_3, and $LiTbF_4$[28,62] and impure (doped) uniaxial ferromagnetic compounds such as $LiTb_{1-x}Y_xF_4$ and $LiY_{1-x}R_xF_4$[18,141]. The measured critical exponents in these samples show deviations from that of conventional SR models (Ising, mean-field, Heisenberg).

Theoretical understanding of critical dynamics in uniaxial ferromagnets has been mainly based on the realization that dipole-dipole interaction can lead to a new critical behavior[59]. RG analyses performed on the GL type model Hamiltonian for an n-component uniaxial spin system with isotropic exchange coupling and dipolar interaction[126,3,58,60] predicted logarithmic behavior coupled with mean

field exponents. This result was found to match well with the pure uniaxial ferromgantes such as TbF_3 and $LiTbF_4$ while it could not capture the critical behavior for isomorphous salts and doped uniaxial samples.

1.6.4 Hexagonal Antiferromagnets

An interesting class of magnetic systems which is one of the main focus areas in condensed matter due to their *multiferroic* behavior is the class of hexagonal manganites $R\mathrm{MnO_3}$ (where R= Ho, Er, Tm, Yb, Lu, or Y, Sc, In) [213]. These materials exhibit ferroelectric ordering at high temperatures ($T_c \sim$1000 K) and antiferromagnetic ordering at low temperatures ($T_N \sim$100 K). Some experimental works provide evidence for coupling of the order parameters of these two distinct phases [55]. As a consequence, the electrical properties are shown to be altered by the application of magnetic field and vice versa [95,50,37]. Further, the coupling between the magnetic and ferroelectric order parameters was shown to generate a strong-spin lattice coupling [171,199,51].

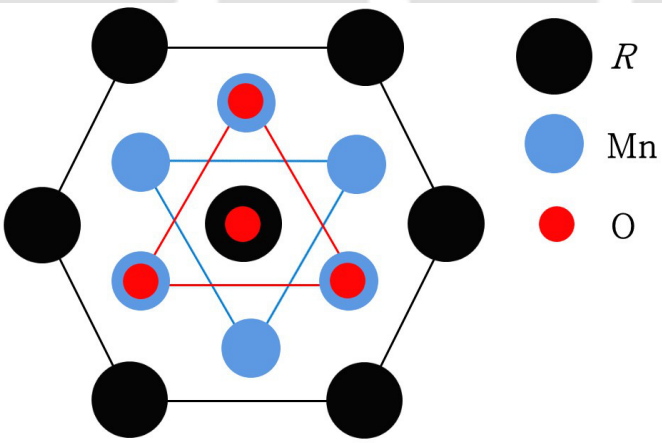

Figure 1.4: Plan view for hexagonal $R\mathrm{MnO_3}$.

Experiments aiming at determining the critical exponents related to PM-AFM

phase transition in various RMnO$_3$ compounds suggested that the observed exponents do not belongs to the known universality classes of critical phenomena. It may be noted that, hexagonal manganites consist of stacked Mn-O and R layers where the Mn ions form nearly a two-dimensional triangular lattice, a schematic (planer) view of which is shown in Fig. 1.4. The spins of Mn atom orders antiferromagnetically below Néel temperatures and the magnetic frustration arises from the triangular geometry of the lattice [130]. Although a chiral Heisenberg and a chiral XY universality classes [111,109] were proposed for triangular antiferromagnets, recent thermal measurements for the specific heat exponents in various RMnO$_3$ samples excluded these possibilities [164]. This may be attributed to the fact that the spin-lattice coupling has a dominating role in such systems and it affects their critical properties.

1.7 Theoretical Investigations

Experiments on the above mentioned strongly correlated magnetic systems revealed about the coupling between electronic, magnetic, and lattice degrees of freedom. The spin-lattice couplings in perovskite manganites, uranium superconductors, and hexagonal manganites, play a significant role in determining their critical behavior related to PM-FM and PM-AFM phase transitions. The role of elastic degrees of freedom on the critical phenomena have been studied analytically for a long time [236,235,237,4,5,21,228]. Theoretical considerations in Refs. [236,235,237,4,228] indicated that an effective nonlocal interaction in the quartic term of the Hamiltonian arises as a result of eliminating the lattice degrees of freedom. Systematic strain variations in perovskite crystals SrTiO$_3$ and LaAlO$_3$ were first carried out by Aharony and Bruce [5]. They pointed out that strain variations give rise to floplike displacive transition in these perovskite samples. The flop line ends at $T = T_C$ (at

zero stress) and a bicritical point predicts a crossover from Heisenberg to Ising or XY like behavior. Incorporating strain degrees of freedom into an Ising-like system, Bergman [21] showed a first-order transition for free boundary conditions (constant pressure) while no critical behavior was obtained for the constraint constant volume condition. Their model gives pseudotricritical behavior at constant pressure while at constant volume, Fisher-renormalized behavior was obtained. Recently, a theoretical work [6] aiming at elucidating the role of electron-lattice interactions in perovskite manganites, suggested that the imposed strain could be long-range in nature. These studies provide us a basis for a quantitative description of the PM-FM phase transition recently observed in a considerable number of experiments on perovskite manganites.

The role of spin-lattice (magnetoelastic) interaction is also found to be important in the case of itinerant ferromagnetic systems such as uranium superconductors. Theoretical investigations, mainly based on GL phenomenological approach, indicated that such magnetoelastic mechanism leads to a first-order transition when the transition temperature (T_c) strongly depends on pressure [152]. Interestingly, this itinerant fermionic system possess a quantum critical point (QCP) under the application of pressure, magnetic field, or disorder. Within the GL approach, it was shown that the transition temperature T_c is a very strong function of strain near the quantum critical point (QCP) and $\partial T_c/\partial p$ diverges, indicating a first-order transition [66]. The observed dependence of T_c on pressure implies a coupling between magnetic energy and lattice, as suggested in Ref. [16].

In addition to the above mentioned strongly correlated systems, there are strong experimental evidences [184,183,180] for spin-lattice coupling in multiferroic hexagonal $RMnO_3$ where both ferroelectric and antiferromagentic phase transition occurs at different transition temperatures. A theoretical work [111] within the RG

framework suggested that the universality class for triangular antiferromagnets should belong to that of either chiral XY or chiral Heisenberg. However, recent experiments [164,184] on the critical behavior of $RMnO_3$ ruled out these possibilities and suggested a new universality class. Early theoretical work within the GL phenomenology [183,181,182,180,186], however, indicate that the quartic coupling term becomes nonlocal due to the presence of magnetoelastic coupling in such systems. This provides us a strong hint to analyse the problem with a suitable nonlocal model Hamiltonian so that it would be able to capture the experimental results related to PM-AFM phase transition of such spin-lattice coupled systems.

While exploring the theoretical developments mentioned above, we find that no further attempts along this line has been made to explain the experimentally observed widely varying critical exponents in strongly correlated magnetic systems such as perovskite manganites, uranium superconductors, and hexagonal manganites. It was the seminal work of Fisher, Ma, and Nickel [57] who proposed a long-range model where the exchange interactions $J(\mathbf{r})$ depend on distance as $J(\mathbf{r}) = J/r^{d+\sigma}$ with d the space dimension and σ parametrises the the range of interaction. Their detailed RG calculations yield varying critical exponents for $d/2 < \sigma < 2$ corresponding to the non-trivial fixed point. This analytical work has motivated researchers for a long time and consequently, there have been a number of studies on this model which we shall discuss in Ch. 2. However, the formulation of this LR model was entirely different from the above mentioned theoretical developments [237,2] where, in the later, the importance was given to the effect of spin-lattice interaction on compressible systems. As discussed in Ch. 2, the model of Fisher, Ma, and Nickel [57] is unable to capture the tricritical behavior observed in the above mentioned magnetic systems. Since the tricritical behavior is observed in many samples of such diverse systems, we incline our motivation in the line of the

theoretical developments due to Fisher, Wagner, Aharony, and Bergman [56,237,4,21] because their studies provide a signature for a tricritical point.

1.8 Outline of the Thesis

With the above mentioned motivation, we investigate a GL model Hamiltonian with a nonlocal quartic coupling term. The most interesting feature observed in experiments is nearly tricritical mean-field behavior for some perovskite manganite samples. A detailed RG calculation with a simple algebraic model for the quartic interaction is presented in Ch. 2. The critical exponents of this model are found to agree well with the above mentioned near tricritical behavior. However, this model predictions do not agree with a majority of perovskite mangnaite samples that show departure away from tricriticality. In order to capture the widely varying critical exponents in various samples of perovskite manganites, we consider a screened nonlocal coupling function for the quartic interaction and find that the model contains the universality classes of such systems both near and away from tricriticality, the detail calculations involved in the analysis are presented in Ch. 3. We also find that the varying critical exponents for direct Mn-site doped perovskite manganite samples are close to those predicted by this theory as shown in Ch. 4. These agreements motivate us to perform the analysis of non-conserved critical dynamics for such a nonlocal model Hamiltonian. A detailed dynamic RG analysis is presented in Ch. 5, wherein we find that the predicted dynamic critical exponents are also in satisfactory agreement with those of the available experiments on dynamic critical behavior for perovskite manganites. It has been suggested that the order parameter in uranium ferromagnetic superconductors follow a conserved dynamics [38]. As indicated earlier, they also posses a strong spin-lattice coupling. We thus propose a conserved critical dynamics govern by a Hamiltonian with nonlocal

quartic interaction. A dynamic RG analysis is carried out on this model in Ch. 6 and a comparison is made with the available experimental critical exponents. We also investigate the critical behavior for other uniaxial magnetic systems within the same theoretical framework and presented them in Ch. 7. Finally, since magnetoelastic coupling was shown to play a dominant role in hexagonal $R\mathrm{MnO}_3$, we extend our work with a new formulation of the model Hamiltonian along the line of model C of Halperin, Hohenberg, and Ma. The detailed calculations and a comparison with experimental results are presented in Ch. 8. The thesis is concluded with Ch. 9 that includes a discussion elaborating upon the impact of the thesis on future prospectives.

Chapter 2

A Nonlocal Model and Phase Transition Near Tricriticality

Summary

We consider a modified Ginzburg-Landau model with a nonlocal mode-coupling interaction in the quartic term. Employing Wilson's renormalization-group scheme, we carry out the calculations at one-loop order and obtain the critical exponents in the leading order of $\epsilon = 4 - d - 2\rho$, where ρ is an exponent occurring in the nonlocal interaction term and d is the space dimension. Interestingly, the correlation exponent η is found to be non-zero at one-loop order and the ϵ expansion corresponds to an expansion about the tricritical mean field theory in three dimensions, unlike the conventional Φ^4 theory. Our analysis indicates that tricriticality is a feature only in three dimensions. The model captures well the critical exponents obtained for some perovskite manganite samples exhibiting near tricritical behavior.

2.1 Introduction

Critical phenomena near a phase transition point have been an subject of extensive studies and many new ideas have been developed in order to understand the

critical behavior of increasingly complex systems. The role of short-range (SR) interactions [243,241,138,244,139,75,242,260] on the critical behaviour of a d-dimensional system with an n-component order parameter, governed by the Ginzburg-Landau free energy functional, has been a topic of much interest among the researchers to a considerable extent. Analytical investigations based on the renormalization-group (RG) approach yield various critical exponents. In addition, the effect of long-range (LR) interactions on critical phenomena has been extensively investigated analytically [57,218,194,2,223,76,93,23] as well as numerically [137,136,134,225,226,227] for quite some time. Fisher, Ma, and Nickel [57] made an attempt based on the RG approach to investigate the critical behaviour of such systems by incorporating long-range interactions in the quadratic term appearing in the dimensionless Ginzburg-Landau functional, given by

$$H = \int d^d x \left\{ \frac{r_0}{2}\Phi^2(\mathbf{x}) + \frac{j_\sigma}{2}\int d^d x' \frac{\Phi(\mathbf{x})\Phi(\mathbf{x}')}{(\mathbf{x}-\mathbf{x}')^{d+\sigma'}} + \frac{c}{2}|\nabla\Phi(\mathbf{x})|^2 + u\Phi^4(\mathbf{x}) \right\}, \qquad (2.1)$$

where the exponent σ' associated with the algebraically decaying interaction is referred to as the long-range exponent. This investigation led to a novel nontrivial fixed point. The critical exponents, particularly, the exponents γ and η for susceptibility and two-point correlation function, were calculated via the RG scheme as an expansion in the parameter $\epsilon' = 2\sigma' - d$ for $\epsilon' > 0$. Their analysis identified different regimes characterized by the long-range exponent σ'. It was found that for $\sigma' > 2$ the exponents had their short-range values while for $\sigma' < 2$ they became σ' dependent. The exponent η calculated via the ϵ' expansion was found to be $\eta = 2 - \sigma'$ with no corrections up to $O(\epsilon'^3)$. As a result, for σ' sufficiently close to 2, the critical exponents turned out to be discontinuous at $\sigma' = 2$. Further, the upper critical dimension of the system was found to be $d_c = 2\sigma'$ and ϵ'-expansion was an expansion about the mean-field. Similar results were also reported independently

by Suzuki *et al.* [218].

Motivated by their model, the corresponding critical behaviors were further investigated in a number of theoretical [194,2,223,76,93,23] as well as numerical studies [226,227,136,137,135,134]. Most of these studies were devoted to the investigation of a crossover between the LR and SR regions mainly concentrating on the resolution of a jump discontinuity of the critical exponent η at the crossover value $\sigma' = 2$ [194,223,76,93,23,136,137,134]. Sak [194] showed via RG calculations that the jump discontinuity is smoothened out and the crossover takes place at $\sigma' = 2 - \eta_{SR}$, where η_{SR} is the short-range value of the exponent η. Numerical simulations based on the same LR model [134,179,25] were also focused on the crossover particularly in $d = 2$ and obtained a smooth interpolation between the SR and LR regimes. Recently, using Fourier Monte Carlo algorithm, Tröster [226,227] observed Wilson-Fisher type critical fixed point. The critical exponents obtained via these simulations were compared with those obtained from perturbation theory, ϵ'-expansion, and earlier Monte Carlo simulations [136,134].

In the theoretical and numerical approaches mentioned above, the interactions were considered to be long-range in the sense that $|\nabla\Phi(\mathbf{x})|^2$ term was effectively modified to $|\nabla\Phi(\mathbf{x})|^2 + |\nabla^{\sigma/2}\Phi(\mathbf{x})|^2$, which affects the Green's function of the problem without affecting the interaction term (Φ^4 term) in the Ginzburg-Landau functional.

It is important to note that recent experiments on some perovskite manganite samples ($R_{1-x}A_xMnO_3$) [117,249,233,52,163,175,131], exhibit near tricritical behavior (cf. Sec. 1.6). In an attempt to find a theory for the phase transition near tricriticality in perovskite manganites, we verified whether the above mentioned LR theory can capture the critical behavior predicted by experiments on perovskite manganites. Table 2.1 shows the upper and lower bounds of various critical exponents obtained

Table 2.1: Allowed ranges for the critical exponents for different values of d and n between lower and upper bounds, $[\sigma'_{\min}, \sigma'_{\max}]$, of the long-range exponent σ', as predicted by the RG calculations of Ref.[57] incorporating the correction due to Sak[194]. The rows with single entries correspond to the best possible values nearest to the tricritical values as predicted by the same RG theory. The tricritical exponents, taken from Ref.[94], are given in last row for comparison.

d	n	σ'	α	β	γ	δ
3	1	$[1.5, 1.981]$	$[0.0, 0.082]$	$[0.5, 0.338]$	$[1.0, 1.240]$	$[3.0, 4.076]$
	2	$[1.5, 1.980]$	$[0.018, -0.013]$	$[0.5, 0.359]$	$[1.0, 1.296]$	$[3.0, 4.083]$
	3	$[1.5, 1.979]$	$[0.003, -0.092]$	$[0.5, 0.375]$	$[1.0, 1.341]$	$[3.0, 4.084]$
2	1	$[1.0, 1.926]$	$[0.058, -0.003]$	$[0.5, 0.183]$	$[1.0, 1.636]$	$[3.0, 5.320]$
	2	$[1.0, 1.920]$	$[0.013, -0.254]$	$[0.5, 0.232]$	$[1.0, 1.790]$	$[3.0, 5.358]$
	3	$[1.0, 1.917]$	$[0.0, -0.462]$	$[0.5, 0.272]$	$[1.0, 1.917]$	$[3.0, 5.367]$
2	1	1.646	0.012	0.251	1.485	4.812
	2	1.830	-0.237	0.250	1.737	5.209
	3	1.917	-0.462	0.272	1.917	5.367
Tricritical Exponents		—	0.50	0.25	1.00	5.00

via RG calculations of Fisher, Ma, and Nickel incorporating Sak's correction for the continuity between the LR and SR regimes[57,194]. For $d = 3$, the tricritical values $\beta = \frac{1}{4}$ and $\delta = 5$ lie outside the ranges as shown in the Table 2.1. Further, for $d = 2$, these values cannot be generated for any value of σ'; the exponent γ turns out to be quite higher (compared to the tricritical value $\gamma = 1$) for a matching value of $\beta = 0.25$. This necessitates an alternative theoretical model capable of capturing the wide range of critical behavior of perovskite manganites, including their nearly tricritical behavior.

A tricritical point was shown to emerge in systems where the exchange interaction involves coupling between the spin and lattice degrees of freedom. Theoretical developments[56,236,235,237,4,21] have a long history in elucidating the critical behavior of such spin-lattice coupled systems. In particular, Fisher[56] considered a compressible Ising system with spin-lattice coupling resulting from the fact that the exchange interaction varies with the separation between the spins. Wagner[236,237]

reconsidered the problem and obtained an effective Hamiltonian involving a long-range four spin interaction term as a result of the spin-lattice coupling. Aharony considered a continuum generalization of this model[4] with wavevector dependent four-spin (quartic) coupling and showed the existence of tricriticality in the system.

Spin-lattice interactions are known to play an important role in perovskite manganites[24,200,43,99,148,26] (cf. Sec. 1.6). Any model describing the critical properties of these systems should include the effect of spin-lattice coupling and it should be able to capture the observed tricritical behavior. Thus the quartic term of the model Hamiltonian describing the spin-lattice coupled system could not be treated as a contact interaction. In a recent numerical simulation on the spin-lattice coupled system[21], quartic nonlocality was shown to originate in the case of an elastic isotropic system as a consequence of long-range strain interactions[228]. Using the Fourier Monte-Carlo method, Tröster performed a numerical simulation on this compressible Φ^4 model with the nonlocal character and obtained convincing evidence for Fisher-renormalized critical behaviour as well as the existence of a tricritical point. We may thus expect that a nonlocal model Hamiltonian, containing the quartic nonlocality, may reveal some insight regarding tricritical mean-field behavior observed in perovskite manganite samples.

The original Φ^4 term in the Ginzburg-Landau functional is equivalent to a contact (or short-range) self-interaction of the $\Phi(\mathbf{x})$ field in physical space. However, as a consequence of spin-lattice interaction present in the magnetic systems an effective interaction with a nonlocal term $\int d^dx \int d^dx' \, \Phi^2(\mathbf{x})\, u(\mathbf{x}-\mathbf{x}')\, \Phi^2(\mathbf{x}')$ is expected to be generated as discussed earlier. This effective nonlocal term represents the interaction between spins separated by points in the physical space as depicted by the Feynman diagram in Fig. 2.1.

In this Chapter, we shall investigate, by means of Wilson's momentum shell decimation scheme, the critical behaviour of a modified n-component Ginzburg-Landau model with such a nonlocal interaction. The coupling is assumed to have an algebraic form $u(\mathbf{k}) = \lambda_0 |\mathbf{k}|^{2\rho}$ in the Fourier space, where λ_0 is a coupling constant and the exponent ρ will be referred to as the nonlocal exponent. As we shall see, the RG calculations yields a nontrivial fixed point and its stability restricts the values of ρ in the range $0 < \rho < \frac{1}{2}$ in three dimensions. The upper critical dimension is found to be $d_c = 4 - 2\rho$ and we obtain the critical exponents in the leading order in $\epsilon = d_c - d$. A marked feature of the RG scheme is that it yields a nonzero value of

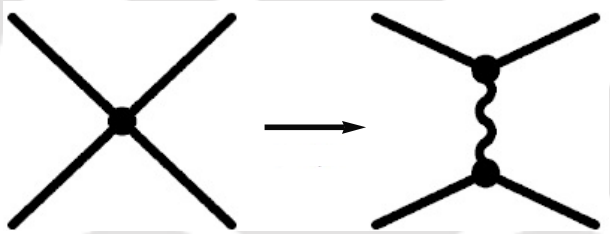

Figure 2.1: Feynman diagrams representing the quartic term. The first (second) diagram represents a local (nonlocal) interaction. A wavy line connecting two points $\mathbf{x}$ and $\mathbf{x}'$ represents the coupling $u(\mathbf{x} - \mathbf{x}')$.

the exponent η at one-loop order in the leading order of ϵ. We find another interesting feature that for the marginal case $\epsilon = 0$ the values of the critical exponents for $d = 3$ are exactly those of tricritical mean field exponents [94], namely, $\alpha = \frac{1}{2}$, $\beta = \frac{1}{4}$, $\gamma = 1$, and $\delta = 5$. However, as observed in Ref. [94,172], a Φ^6 term is necessary for obtaining the tricritical mean field exponents. Thus, an interesting feature of the nonlocal model is that it captures the tricritical behaviour without the necessity of a Φ^6 term in the model Hamiltonian. We further see from our calculations that the tricritical exponents are not reproduced in two dimensions for any value of ρ. Remarkably, experiments on perovskite manganite samples exhibiting tricritical exponents agree well with the present analytical estimates.

2.2 Nonlocal Model Hamiltonian

We consider a nonlocal model Hamiltonian for an n-component order parameter $\Phi(\mathbf{x})$ as

$$H[\Phi] = \int d^d x \left[\frac{c_0}{2} |\nabla \Phi(\mathbf{x})|^2 + \frac{r_0}{2} \Phi^2(\mathbf{x}) + \int d^d x' \, \Phi^2(\mathbf{x}) \, u(\mathbf{x} - \mathbf{x}') \, \Phi^2(\mathbf{x}') \right], \tag{2.2}$$

where $u(\mathbf{x} - \mathbf{x}')$ represents an effective nonlocal interaction, and the quadratic operators are expressed in terms of the components of the field $\Phi(\mathbf{x})$ as

$$\Phi^2 = \sum_{i=1}^{n} \phi_i^2 \quad \text{and} \quad |\nabla \Phi|^2 = \sum_{i=1}^{n} \nabla \phi_i \cdot \nabla \phi_i. \tag{2.3}$$

Defining the Fourier transform of the field $\Phi(\mathbf{x})$ as

$$\phi_i(\mathbf{x}) = \int \frac{d^d k}{(2\pi)^d} \, \phi_i(\mathbf{k}) \, e^{i\mathbf{k}\cdot\mathbf{x}}, \tag{2.4}$$

we express the model Hamiltonian given by Eq. (2.2) in the Fourier space,

$$H[\Phi] = \int \frac{d^d k}{(2\pi)^d} \left[\sum_{i=1}^{n} \frac{1}{2} \left(c_0 \mathbf{k}^2 + r_0 \right) |\phi_i(\mathbf{k})|^2 + \right.$$
$$\left. \sum_{i=1}^{n} \sum_{j=1}^{n} \int \frac{d^d k_1}{(2\pi)^d} \int \frac{d^d k_2}{(2\pi)^d} \, u(-\mathbf{k} - \mathbf{k}_1) \, \phi_i(\mathbf{k}) \phi_i(\mathbf{k}_1) \phi_j(\mathbf{k}_2) \phi_j(-\mathbf{k} - \mathbf{k}_1 - \mathbf{k}_2) \right]. \tag{2.5}$$

As stated earlier, we model the nonlocal coupling $u(\mathbf{k})$ to be of the form

$$u(\mathbf{k}) = \lambda_0 |\mathbf{k}|^{2\rho}. \tag{2.6}$$

where the exponent ρ, referred to as the nonlocal exponent, is restricted to positive values due to the finiteness of the free energy. We shall see that the allowed values of ρ are further determined by the stability of the RG scheme.

The nonlocality in interaction changes the upper critical dimension of this model in comparison to the standard Φ^4 model. From the dimensional argument, one can

see that the momentum dimension of the field is $[\phi_i(\mathbf{k})] = [\Lambda^{-1-d/2}]$, so that the dimension of λ_0 is $[\lambda_0] = [\Lambda^{4-d-2\rho}]$. This naive dimension of the quartic coupling constant gives the upper critical dimension $d_c = 4 - 2\rho$. The same upper critical dimension is obtained from the marginal stability of the stable eigenvalue as we shall show in Sec. 2.4. It may be mention that the essential ingredient for developing the momentum shell decimation is based upon treating the quartic term as a perturbation about the Gaussian random field. This suggests that the average of even number of fields with respect to Gaussian distribution can be expressed as the sum of bare correlation functions [33]. We thus write the bare correlation of the order parameter with respect to Gaussian weight as [139,71,33]

$$\langle \phi_i(\mathbf{q})\, \phi_j(\mathbf{q}') \rangle_0 = G_0(\mathbf{q})\, (2\pi)^d \delta^d(\mathbf{q}+\mathbf{q}')\, \delta_{ij}, \tag{2.7}$$

where

$$G_0(\mathbf{q}) = \frac{1}{c_0 \mathbf{q}^2 + r_0} \tag{2.8}$$

is the bare propagator.

2.3 Renormalization-Group Scheme

We perform an RG analysis of the Fourier transformed nonlocal model Hamiltonian given by Eq. (2.5), by means of Wilson's momentum shell decimation [244,138,107] scheme. Calculating the self-energy and vertex corrections at one-loop order, we subsequently construct the recursion relations for the model parameters r_0, c_0, and λ_0. The details of the scheme are presented below.

2.3.1 Self-energy Corrections

To implement the RG scheme, we begin with the elimination of the fast modes $[\phi^{>}(\mathbf{q})]$ in Fourier space from the ultraviolet (small scale) end lying in the shell $\frac{\Lambda}{b} < q < \Lambda$, where $\Lambda \sim \frac{1}{a}$ is an ultraviolet cut-off determined by the lattice spacing a. This scale elimination procedure yields self-energy corrections and vertex corrections. The self-energy corrections at one-loop order, namely, Σ_a and Σ_b, represented by the Feynman diagrams in Fig. 2.2 (a) and Fig. 2.2 (b), are given by the integrals

$$\Sigma_a(\mathbf{0}) = 2n \int \frac{d^d q}{(2\pi)^d}\, u(\mathbf{0}) G_0^{>}(\mathbf{q}), \tag{2.9}$$

and

$$\Sigma_b(\mathbf{k}) = 4 \int \frac{d^d q}{(2\pi)^d}\, u(-\mathbf{k}-\mathbf{q}) G_0^{>}(\mathbf{q}). \tag{2.10}$$

Using the form of the nonlocal coupling given by Eq. (2.6), we find that the self-energy correction Σ_a given by Eq. (2.9) does not contribute as $u(\mathbf{0})$ vanishes because $\rho > 0$. Further, employing the expansion for the nonlocal coupling function $u(-\mathbf{k}-\mathbf{q})$ appearing in the self-energy expression $\Sigma_b(\mathbf{k})$ as

$$u(-\mathbf{k}-\mathbf{q}) = \lambda_0 |\mathbf{k}+\mathbf{q}|^{2\rho} = \lambda_0 q^{2\rho}\left[1 + 2\rho\frac{\mathbf{k}\cdot\mathbf{q}}{q^2} + \rho\frac{k^2}{q^2} + 2\rho(\rho-1)\frac{(\mathbf{k}\cdot\mathbf{q})^2}{q^4} + \ldots\right], \tag{2.11}$$

in the limit $q \gg k$, we obtain the corrections Δr and Δc to the bare parameters r_0 and c_0 as

$$\Sigma_a(\mathbf{0}) + \Sigma_b(\mathbf{k}) = \frac{1}{2}\Delta r + \frac{1}{2}\Delta c\, k^2 + \ldots, \tag{2.12}$$

where

$$\Delta r = 8\lambda_0 \frac{S_d}{(2\pi)^d} \int_{\Lambda/b}^{\Lambda} \frac{q^{d-1+2\rho}}{c_0 q^2 + r_0}\, dq, \tag{2.13}$$

and

$$\Delta c = -8\lambda_0 \frac{\rho(2-2\rho-d)}{d} \frac{S_d}{(2\pi)^d} \int_{\Lambda/b}^{\Lambda} \frac{q^{d-3+2\rho}}{c_0 q^2 + r_0}\, dq, \tag{2.14}$$

with $S_d = \frac{2\pi^{d/2}}{\Gamma(d/2)}$. Expanding the denominators of the above integrands in the same limit ($q \gg k$) and performing the momentum integrations, we obtain

$$\Delta r = \frac{8\lambda_0}{c_0}\frac{S_d}{(2\pi)^d}\left[\frac{(b^{2-2\rho-d}-1)\Lambda^{d+2\rho-2}}{2-2\rho-d} - \frac{r_0}{c_0}\frac{(b^{4-2\rho-d}-1)\Lambda^{d+2\rho-4}}{4-2\rho-d}\right], \tag{2.15}$$

and

$$\Delta c = -\frac{8\lambda_0}{c_0}\frac{\rho(2-2\rho-d)}{d}\frac{S_d}{(2\pi)^d}\left[\frac{(b^{4-2\rho-d}-1)\Lambda^{d+2\rho-4}}{4-2\rho-d} - \frac{r_0}{c_0}\frac{(b^{6-2\rho-d}-1)\Lambda^{d+2\rho-6}}{6-2\rho-d}\right]. \tag{2.16}$$

Figure 2.2: Feynman diagrams for self-energy correction at one loop order. Σ_a and Σ_b in Eqs. (2.9) and (2.10) are obtained from the amputated parts of diagram (a) and (b). A wavy line represents the coupling $u(\mathbf{0})$ in **(a)** and $u(-\mathbf{k}-\mathbf{q})$ in **(b)**; the internal solid lines in the loop comes from the contraction of $\phi^>$ fields.

We note that the above diagrammatic self-energy corrections are obtained at the lowest order of perturbation expansion for interaction term $\langle H_I \rangle$ of the GL Hamiltonian which do not renormalize the interaction vertex λ_0. In order to account for the vertex renormalization, we perform the same procedure to order $-\frac{\langle H_I^2\rangle - \langle H_I\rangle^2}{2}$.

2.3.2 Vertex Corrections

The corrections to the coupling constant λ_0 at one-loop order can be obtained from the Feynman diagrams shown in Fig. 2.3. The amputated parts of these diagrams

are represented by the integrals

$$\Pi_a(\mathbf{k},\mathbf{k_1}) = -4nu^2(-\mathbf{k}-\mathbf{k_1})\int \frac{d^dq}{(2\pi)^d} G_0^>(\mathbf{q})G_0^>(-\mathbf{k}-\mathbf{k_1}-\mathbf{q}), \tag{2.17}$$

$$\Pi_b(\mathbf{k},\mathbf{k_1},\mathbf{k_2}) = -16u(-\mathbf{k}-\mathbf{k_1})\int \frac{d^dq}{(2\pi)^d} u(\mathbf{q}-\mathbf{k_2})G_0^>(\mathbf{q})G_0^>(-\mathbf{k}-\mathbf{k_1}-\mathbf{q}), \tag{2.18}$$

and

$$\Pi_c(\mathbf{k},\mathbf{k_1},\mathbf{k_2}) = -16\int \frac{d^dq}{(2\pi)^d} u(-\mathbf{k}-\mathbf{q})u(\mathbf{q}-\mathbf{k_1})G_0^>(\mathbf{q})G_0^>(-\mathbf{k}-\mathbf{k_2}-\mathbf{q}), \tag{2.19}$$

respectively, where $\mathbf{k}$, $\mathbf{k}_1$, $\mathbf{k}_2$, and $\mathbf{k}_3 = -\mathbf{k}-\mathbf{k}_1-\mathbf{k}_2$ are the external momenta carried by the four external legs.

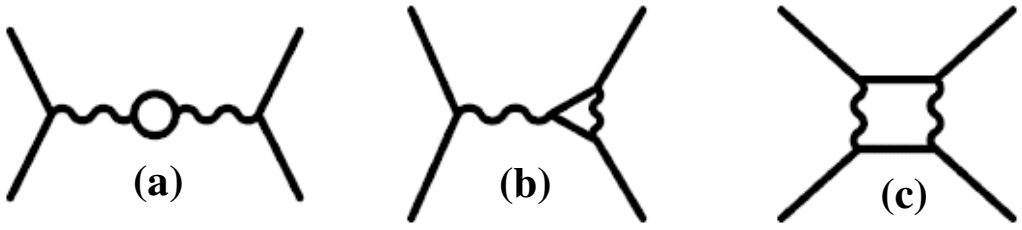

Figure 2.3: Feynman diagrams for vertex correction $\Delta\lambda$ at one-loop order.

Noting that the above expressions for Π_a and Π_b are in the form of the bare vertex $u(-\mathbf{k}-\mathbf{k}_1)$ [Eq. (2.6)] appearing in the original Hamiltonian [Eq. (2.5)], they yield correction $\Delta\lambda$ to the bare parameter λ_0. The expression for Π_c [Eq. (2.19)] cannot be accommodated as a term similar to the bare vertex $u(-\mathbf{k}-\mathbf{k}_1)$ [Eq. (2.6)] in the original Hamiltonian [Eq. (2.5)] and therefore this correction is irrelevant. Further, in the limit of vanishing external momenta, the expression for Π_a does not contribute as it gives a factor $u(\mathbf{0})$. It may be noticed that the expression for Π_b, given by Eq. (2.18), is proportional to $u(-\mathbf{k}-\mathbf{k}_1)$. Thus, the expression for Π_b [Eq. (2.18)], has the same momentum dependence of the original

vertex $u(-\mathbf{k}-\mathbf{k}_1)$ [Eq. 2.6] in the original Hamiltonian. As a result the relevant correction to the bare vertex comes only from Π_b, giving

$$\Delta\lambda = -\frac{16\lambda_0^2}{c_0^2}\frac{S_d}{(2\pi)^d}\left[\frac{(b^{4-2\rho-d}-1)\Lambda^{d+2\rho-4}}{4-2\rho-d} - \frac{2r_0}{c_0}\frac{(b^{6-2\rho-d}-1)\Lambda^{d+2\rho-6}}{6-2\rho-d}\right]. \quad (2.20)$$

2.3.3 Rescaling and Recursion Relations

The expressions given in Eqs. (2.15), (2.16), and (2.20) are obtained by elimination of modes from the ultraviolet end lying in the shell $\frac{\Lambda}{b} < k < \Lambda$, and this process modifies the original Hamiltonian as

$$H[\Phi^<] = \sum_{i=1}^{n}\int_0^{\Lambda/b}\frac{d^dk}{(2\pi)^d}\frac{1}{2}[(c_0+\Delta c)\mathbf{k}^2+(r_0+\Delta r)]|\phi_i^<(\mathbf{k})|^2$$

$$+\sum_{i=1}^{n}\sum_{j=1}^{n}\int_0^{\Lambda/b}\frac{d^dk}{(2\pi)^d}\int_0^{\Lambda/b}\frac{d^dk_1}{(2\pi)^d}\int_0^{\Lambda/b}\frac{d^dk_2}{(2\pi)^d}|-\mathbf{k}-\mathbf{k}_1|^{2\rho}(\lambda_0+\Delta\lambda)\phi_i^<(\mathbf{k})\phi_i^<(\mathbf{k}_1)$$

$$\phi_j^<(\mathbf{k}_2)\phi_j^<(-\mathbf{k}-\mathbf{k}_1-\mathbf{k}_2). \quad (2.21)$$

To recover the full Hamiltonian in its original form we rescale the momenta and fields as $\mathbf{k}' = b\mathbf{k}$ and $\Phi'(\mathbf{k}') = \zeta^{-1}\Phi^<(\mathbf{k})$. The spin rescaling factor can be obtained by writing the two-point correlation function for rescaled field variables as

$$\langle\phi_i'(\mathbf{k}_1')\phi_j'(\mathbf{k}_2')\rangle = G_0'(\mathbf{k}_1')(2\pi)^d\delta(\mathbf{k}_1'+\mathbf{k}_2')\delta_{ij}. \quad (2.22)$$

Comparing this with the original form given by Eq. (2.7) and using the scale invariance property of the correlation function at the critical point[139,71,10], namely, $G(\mathbf{k}) \sim k^{-2+\eta}$, we find

$$\zeta = b^{(d+2-\eta)/2}. \quad (2.23)$$

With this choice of field rescaling factor, Eq. (2.21) can be written in terms of rescale momenta and fields as

$$H'[\Phi'] = \sum_{i=1}^{n} \int_0^{\Lambda} \frac{d^d k'}{(2\pi)^d} \frac{1}{2} (c' \mathbf{k}'^2 + r') \, |\phi_i'(\mathbf{k}')|^2 + \sum_{i=1}^{n} \sum_{j=1}^{n} \int_0^{\Lambda} \frac{d^d k'}{(2\pi)^d}$$

$$\int_0^{\Lambda} \frac{d^d k_1'}{(2\pi)^d} \int_0^{\Lambda} \frac{d^d k_2'}{(2\pi)^d} \lambda' |-\mathbf{k}' - \mathbf{k}_1'|^{2\rho} \phi_i'(\mathbf{k}') \phi_i'(\mathbf{k}_1') \phi_j'(\mathbf{k}_2') \phi_j'(-\mathbf{k}' - \mathbf{k}_1' - \mathbf{k}_2'). \tag{2.24}$$

This leads to the recursion relations for the parameters r_0, c_0, and λ_0 as

$$r' = b^{2-\eta}(r_0 + \Delta r), \tag{2.25}$$

$$c' = b^{-\eta}(c_0 + \Delta c), \tag{2.26}$$

$$\lambda' = b^{4-d-2\eta-2\rho}(\lambda_0 + \Delta\lambda). \tag{2.27}$$

2.4 Flow Equations and Fixed Point

From the recursion relations given by Eqs. (2.25)–(2.27), and using Eqs. (2.15), (2.16), and (2.20) with $b = e^{\delta l}$, we derive the RG flow equations for the running parameters $r(l)$, $c(l)$, $\lambda(l)$ and obtain

$$\frac{dr}{dl} = (2-\eta)r + \frac{8\lambda}{c} \frac{S_d}{(2\pi)^d} \left(\Lambda^{d+2\rho-2} - \frac{r}{c} \Lambda^{d+2\rho-4} \right), \tag{2.28}$$

$$\frac{dc}{dl} = -\eta c - \frac{8\lambda}{c} \frac{\rho(2-2\rho-d)}{d} \frac{S_d}{(2\pi)^d} \left(\Lambda^{d+2\rho-4} - \frac{r}{c} \Lambda^{d+2\rho-6} \right), \tag{2.29}$$

and

$$\frac{d\lambda}{dl} = (4-d-2\eta-2\rho)\lambda - \frac{16\lambda^2}{c^2} \frac{S_d}{(2\pi)^d} \left(\Lambda^{d+2\rho-4} - \frac{2r}{c} \Lambda^{d+2\rho-6} \right). \tag{2.30}$$

As we are interested in the nontrivial fixed point corresponding to $r \to r^*$, $\lambda \to \lambda^*$, $c \to c^* = c$, we solve the above flow equations and arrive at the following fixed

point values

$$\frac{r^*}{c} = -\frac{(4-d-2\eta-2\rho)\Lambda^2}{2(2-\eta)}, \tag{2.31}$$

and

$$\frac{\lambda^*}{c^2} = \frac{1}{16}\frac{(2\pi)^d}{S_d}(4-d-2\eta-2\rho)\,\Lambda^{4-d-2\rho}. \tag{2.32}$$

Linearizing the flow equations [Eqs. (2.28) and (2.30)] for r and λ around this fixed point by introducing small deviations to r^* and λ^* as $r = r^* + \delta r$ and $\lambda = \lambda^* + \delta\lambda$, we obtain the matrix equation

$$\begin{bmatrix} d\delta r/dl \\ d\delta\lambda/dl \end{bmatrix} = \begin{bmatrix} \frac{d+2\rho}{2} & \frac{8S_d}{(2\pi)^d}\frac{\Lambda^{d+2\rho-2}}{c}\left(1-\frac{r^*}{c\Lambda^2}\right) \\ 0 & -(4-d-2\eta-2\rho) \end{bmatrix} \begin{bmatrix} \delta r \\ \delta\lambda \end{bmatrix}. \tag{2.33}$$

The stability matrix has the eigenvalues

$$y_1 = \frac{d+2\rho}{2}, \tag{2.34}$$

and

$$y_2 = d+2\eta-4+2\rho. \tag{2.35}$$

In addition to the previous condition $\rho > 0$, this stability analysis induces further constraints on the values of ρ, namely, $0 < \rho < \frac{1}{2}$ in three dimensions and $0 < \rho < 1$ in two dimensions. The exponent ν (occurring in the correlation length $\xi \sim |T - T_c|^{-\nu}$) can be directly obtained from the unstable eigenvalue y_1 as [139,71]

$$\nu = \frac{1}{y_1}. \tag{2.36}$$

The upper critical dimension d_c of the system is obtained from the condition of marginality of the stable eigenvalue y_2, giving

$$d_c = 4-2\rho. \tag{2.37}$$

which is consistent with the dimensional argument presented in Sec. 2.2

2.5 ϵ-expansion and Critical Exponents

Identifying the small RG parameter ϵ as $\epsilon = d_c - d = 4 - 2\rho - d$, we employ the ϵ-expansion and obtain the expression for the critical exponents. The correlation length exponent is obtained as

$$\nu = \frac{1}{2} + \frac{\epsilon}{8} + O(\epsilon^2). \tag{2.38}$$

The other independent static exponent, namely, Fisher exponent η [occurring in the correlation function $G(r) \sim \frac{e^{-r/\xi}}{r^{d-2+\eta}}$] is calculated from Eq. (2.29) as

$$\eta = \frac{\rho\epsilon}{4} + O(\epsilon^2). \tag{2.39}$$

Remarkably, we obtain a nonzero value of the exponent η in the leading order of ϵ at one-loop order. This is in contrast with the calculation of Fisher, Ma, and Nickel[57] where η does not get any correction even up to $O(\epsilon'^3)$ where $\epsilon' = 2\sigma' - d$.

By using the above expressions for ν and η in the scaling relations [given in Sec. 1.2], we calculate the other critical exponents, namely, the specific heat exponent α, the spontaneous magnetization exponent β, the susceptibility exponent γ, and the critical isotherm exponent δ and obtain

$$\alpha = \rho\left[1 + \frac{\epsilon}{4}\right] + O(\epsilon^2), \tag{2.40}$$

$$\beta = \frac{1-\rho}{2} - \frac{\epsilon(2+\rho)}{16} + O(\epsilon^2), \tag{2.41}$$

$$\gamma = 1 + \frac{\epsilon}{4}\left[1 - \frac{\rho}{2}\right] + O(\epsilon^2), \tag{2.42}$$

$$\delta = \frac{3-\rho}{1-\rho} + \frac{\epsilon}{(1-\rho)^2}\left[1 + \frac{\rho(\rho-2)}{4}\right] + O(\epsilon^2). \tag{2.43}$$

The above expressions for the critical exponents depend on the space dimension d and the model parameter ρ coming from the nonlocal interaction term. Plots for these exponents in the allowed range of ρ for $d = 3$ are displayed in Fig. 2.4.

From the above expressions for the critical exponents, we observe that for the marginal case $\epsilon = 0$, that is, at the maximum value of ρ ($\rho_{\max} = 0.5$) for $d = 3$, the values of the critical exponents exactly coincide with those of the tricritical mean field exponents[94], namely, $\alpha = \frac{1}{2}$, $\beta = \frac{1}{4}$, $\gamma = 1$, and $\delta = 5$. This comes as a pleasant surprise because our model Hamiltonian incorporates a nonlocal Φ^4 term whereas, as shown in Ref.[94], a Φ^6 term is necessary in the model Hamiltonian to obtain the tricritical mean field behaviour. This suggests that our RG results are basically an expansion about the tricritical mean field. The tricritical mean-field exponents cannot be obtained for any value of ρ in two dimensions, suggesting that tricriticality is a feature only in three dimensions.

2.6 Tricriticality in some Perovskite Manganites

A great deal of attention has been paid recently to determine the critical behavior of perovskite manganites near their PM-FM phase transition. It was found that some experimental samples[117,249,233,52,175,163,131,178] exhibit critical exponents close to those of the tricritical mean-field theory. In Ref.[117], the ferromagnetic phase transition of single crystal $La_{1-x}Ca_xMnO_3$ sample was investigated where, for $x = 0.33$, the magnetization and specific heat data show a first order transition while, for $x = 0.4$, they obtained the tricritical mean-field exponents, as displayed in Table. 2.2. Their results were further confirmed in an another experimental study[163]. In Ref.[233], using modified Arrot plots for $Nd_{1-x}Sr_xMnO_3$, a tricritical point was observed for $x = 0.33$. In order to explain this transition together with its magnetocaloric effect, the authors discussed upon the importance of magnetoelastic cou-

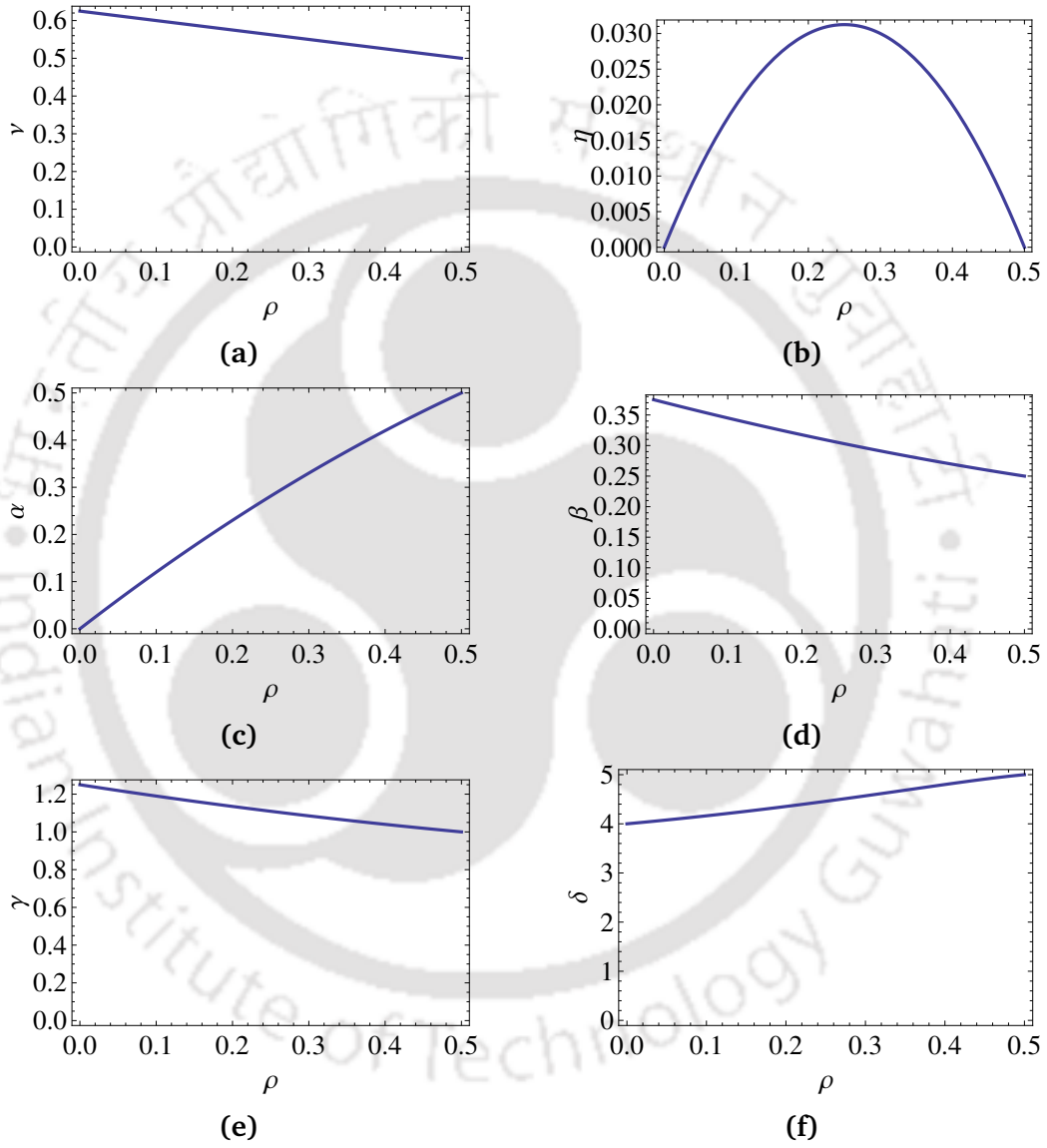

Figure 2.4: Plots of critical exponents with respect to the nonlocal parameter ρ in three dimensions.

pling. In Ref. [52], the magnetic data for polycrystalline sample $La_{0.1}Nd_{0.6}Sr_{0.3}MnO_3$ was analysed in the critical region using modified Arrot plot, Kouvel-Fisher method and critical isotherm analysis and obtained the trictical mean-field exponents. In Ref. [175], for the single crystal $La_{0.7}Ca_{0.2}Sr_{0.1}MnO_3$ sample, the analysis of the magnetic data via Kouvel-Fisher method gives an indication for a first-order transition. The authors also emphasized the effect of lattice-distortions on such phase transition arising from the doping of Sr ions. Recently, Li *et al.* [131] used the same methods and analysed the critical properties of hole-doped $La_{0.5}Ca_{0.4}Li_{0.1}MnO_3$ sample, suggesting the existence of a tricritical point. Similar results were also obtained for samples $La_{0.7}Ca_{0.2}Sr_{0.1}MnO_3$ [178], and $La_{0.9}Te_{0.1}MnO_3$ [249]. Thus the experiments on perovskite manganites, on the one hand, demands that spin-lattice interaction has a dominant role and, on the other hand, they exhibit tricritical behavior. Since our present model Hamiltonian involves a nonlocal quartic interaction term the origin of which is traced back to the spin-lattice interaction as discussed in Sec. 2.1, it is capable of capturing the near tricritical exponents obtained for the above mentioned perovskite manganite samples.

The predictions of the critical exponents coming from the present model and their comparison with the experimental ones are displayed in Table. 2.2. While comparing, we first match the value of β obtained from Eq. (2.41) for a particular value of ρ. Using this value of ρ, we calculate the values of γ and δ (for the same sample) from Eqs. (2.42) and (2.43), respectively. As displayed in Table. 2.2, the critical exponents [following from Eqs. (2.41), (2.42), and (2.43)] for varying ρ values are in good agreement with the experimental values. Although, the present theoretical estimates for the critical exponents near tricritcality are in a good agreement with those of different perovskite manganite samples displayed in Table 2.2, there exist a considerable number of other samples with $\beta \geqslant 0.375$.

Obviously, the critical behavior of such samples could not be able to capture by the present model because the β values are restricted in the range $0.250 < \beta < 0.375$. This may be attributed to the fact that due a simple choice of the nonlocal coupling, the stability restricts ρ values strictly in $0 < \rho < 0.5$. To overcome this restriction, an alternative form for the coupling function is chosen, which is addressed in the next chapter.

Table 2.2: Analytical predictions of critical exponents and their comparison with the experimentally measured critical exponents for some perovskite mangnaite samples.

ρ	Sample	Reference	β	γ	δ
0.499			0.250	1.000	4.998
	$La_{0.6}Ca_{0.4}MnO_3$	[117]	0.25 ± 0.03	1.03 ± 0.05	5.0 ± 0.8
	$Nd_{0.67}Sr_{0.33}MnO_3$	[233]	0.23 ± 0.02	1.05 ± 0.03	5.13 ± 0.04
	$La_{0.1}Nd_{0.6}Sr_{0.3}MnO_3$	[52]	0.248 ± 0.006	1.066 ± 0.002	–
	$La_{0.6}Ca_{0.4}MnO_3$	[163]	0.248	0.995	4.896
	$La_{0.9}Te_{0.1}MnO_3$ (PC)	[249]	0.201 ± 0.003	1.27 ± 0.04	7.14 ± 0.04
0.465			0.257	1.013	4.939
	$La_{0.1}Nd_{0.6}Sr_{0.3}MnO_3$ (PC)	[52]	0.257 ± 0.005	1.12 ± 0.03	5.17 ± 0.02
0.470			0.260	1.011	4.949
	$La_{0.7}Ca_{0.2}Sr_{0.1}MnO_3$ (SC)	[178]	0.26 ± 0.01	1.06 ± 0.02	–
0.475			0.255	1.010	4.958
	$La_{0.5}Ca_{0.4}Li_{0.1}MnO_3$ (PC)	[131]	0.255 ± 0.001	0.987 ± 0.006	4.90 ± 0.07

2.7 Discussion and Conclusion.

In this Chapter, we carried out a Wilson type RG calculation at one-loop order starting with the modified Ginzburg-Landau model Hamiltonian [given by Eq. (2.5)], where a nonlocal coupling [given by Eq. (2.6)] was assumed in the quartic interaction term. We observed that some of the loop diagrams for the self-energy and vertex become vanishingly small. The relevant corrections to the parameters r_0, c_0, and λ_0 were obtained in Eqs. (2.15), (2.16), and (2.20) and the RG scheme leads to a set of RG flow equations given by Eqs. (2.28), (2.29), and (2.30). The flow equations exhibit a nontrivial fixed point. The stability of the nontrivial fixed point and the finiteness of the self-energy restrict the values of the nonlocal parameter ρ to the positive values and the allowed range for ρ depends on the space dimension d. We find $0 < \rho < \frac{1}{2}$ for $d = 3$ and $0 < \rho < 1$ for $d = 2$. The upper critical dimension of the system is found to be $d_c = 4 - 2\rho$, as obtained from the marginal stability of the nontrivial fixed point with respect to the stable eigenvalue y_2.

We obtained the analytical expressions for the critical exponents ν and η in the leading order of $\epsilon = d_c - d$. The critical exponent ν was calculated from the unstable eigenvalue y_1 of the stability matrix while η was derived from the flow equation for $c(l)$. Interestingly, our nonlocal model yields a nonzero value for the exponent η at one-loop order in the leading order of ϵ. This is quite unlike the original Φ^4 model where a nonzero value for η is obtained only at two-loop order. This is also unlike the long-range calculation of Fisher *et al.* [57] where η received no contributions up to $O(\epsilon'^3)$.

Using the known scaling relations for the critical exponents, we derived the expressions for the critical exponents α, β, γ, δ in the leading order of ϵ, as given by Eqs. (2.40), (2.41), (2.42), and (2.43). We see that the critical exponents are independent of the number of components n of the order parameter and they de-

pend only on the space dimension d and the nonlocal parameter ρ. This is due to the nature of the nonlocal coupling for which, as stated earlier, the n dependent corrections to the self energy and vertex become vanishingly small in the RG scheme.

We have also seen that our results compare well with the experimental estimates [117,249,233,52,175,163,131,178] for PM-FM phase transition of perovskite manganite samples showing near tricritical beahvior. The experimenters had attributed the transitions to a first-order phase transition with tricritical exponents. Our analytical estimates for the critical exponents for varying ρ in three dimensions are comparable with the experimental values as shown in Table 2.2.

Remarkably, our analytical expressions for the critical exponents yield the tricritical mean-field exponents for the marginal case $\epsilon = 0$ only for $d = 3$. In contrast, the tricritical behaviour is usually shown to occur by incorporating a Φ^6 term in the Ginzburg-Landau functional [94,172]. Thus, one of the distinguishing features of our nonlocal model is that it reproduces the tricritical mean-field behaviour without a Φ^6 term. It has been suggested that to reach the tricritical point the parameters must be tuned in such a way that the renormalized counterpart of the Φ^4 term in the Hamiltonian vanishes [172]. We observe exactly the same feature as the renormalized coupling given by Eq. (2.32) vanishes for $\epsilon = 0$. Further, the upper critical dimension of our nonlocal model is $d_c = 3$ for $\epsilon = 0$ which is again consistent with the criterion of three dimensionality for the existence of tricritical behaviour, as pointed out in Ref. [172]. Our RG scheme, being an expansion about $\epsilon = 0$, is thus an expansion about the tricritical mean-field theory. We have further noted that the tricritical mean-field exponents are obtained only for $d = 3$ and they cannot be reproduced for $d = 2$ for any value of ρ. This suggests that tricriticality is a feature only in three dimensions.

Chapter 3

A Screened Nonlocal Model and Critical Behavior of Perovskite Manganites

Summary

In this Chapter, we consider a modified Ginzburg-Landau model Hamiltonian with a screened nonlocal interaction in the quartic term. By treating this model Hamiltonian via Wilson's renormalization-group scheme at one-loop order, we explore the critical behavior of paramagnetic-to-ferromagnetic phase transition in perovskite manganites. We find the Fisher exponent η to be of $O(\epsilon)$ and the correlation exponent $\nu = \frac{1}{2} + O(\epsilon)$ in an epsilon expansion in the parameter $\epsilon = d_c - d$, where d is the space dimension, $d_c = 4 + 2\sigma$ is the upper critical dimension, and σ is a parameter coming from the nonlocal interaction in the model Hamiltonian. The ensuing critical exponents in three dimensions for different values of σ compare well with various existing experimental estimates for perovskite manganites with various doping levels. This suggests that the nonlocal model Hamiltonian contains a wide variety of such universality classes.

3.1 Introduction

The well known short-range Ginzburg-Landau (GL) model Hamiltonian treated via Wilson's RG scheme leads to universality classes that depend on the number of components n of the order parameter and the space dimension d. Recent experiments on colossal magnetoresistive materials, however, indicate that their critical behavior near the paramagnetic-to-ferromagnetic (PM-FM) phase transition does not belong to these well known universality classes. By taking into account the experimental fact that spin-lattice interactions are important in such materials, here we consider a suitable modification in the nature of interaction in the GL model Hamiltonian and show that the modified model possesses the capability of capturing the widely varying experimental critical exponents. To begin with, we make an extensive overview on the experimentally observed critical behavior of such systems as well as the numerical simulation results from the microscopic models involving double-exchange (DE) mechanism and lattice distortions.

3.1.1 Experiments on the Critical Behavior of Perovskite Manganites

Perovskite manganites ($R_{1-x}A_xMnO_3$) (cf. Sec. 1.6.1) have been investigated extensively for decades due to their exotic structural, electronic, and magnetic behavior and due to the existence of colossal magnetoresistance (CMR)—the dramatic reduction of resistivity in a magnetic field [234,104,148,14,197]. In these compounds, different choice of R and A have different atomic sizes and therefore produce varying stresses on the Mn-O-Mn bond. It was shown that the average R/A size in terms of ionic radii, expressed by the tolerance factor f [148,197], affects their critical behavior. To investigate the PM-FM phase transition, various experiments have been performed based on the DC magnetization [68], AC suceptibility [162], and

specific heat [117] measurements followed by scaling analysis with Arrot plot, modified Arrot plot (MAP) [117,92], Kouvel-Fisher (KF) formalism, and critical isotherm (CI) [155,185,52,162] analysis. These experiments clearly show that a change either in the doping level (x) or in the tolerance factor (f) lead to different critical exponents.

In fact, although initial experimental investigations [142,68] suggested inconclusive results as regards the universality classes, a number of subsequent experimental studies on some samples [117,233,52,163] showed that the critical exponents were close to those of the tricritical mean-field theory ($\beta = \frac{1}{4}$, $\gamma = 1$, and $\delta = 5$) [94]. For instance, in a polycrystalline $La_{0.6}Ca_{0.4}MnO_3$, the specific heat and magnetization measurements with MAP and CI analysis [117] yield $\alpha = 0.48 \pm 0.06$, $\beta = 0.25 \pm 0.03$, $\gamma = 1.03 \pm 0.05$, and $\delta = 5.0 \pm 0.8$. The magnetization data for polycrystalline $La_{0.1}Nd_{0.6}Sr_{0.3}MnO_3$ yields two sets of results, namely, $\beta = 0.248 \pm 0.006$, $\gamma = 1.066 \pm 0.002$ with MAP and $\beta = 0.257 \pm 0.005$, $\gamma = 1.12 \pm 0.03$, and $\delta = 5.17 \pm 0.02$ with KF method and CI analysis. In polycrystalline $Nd_{0.67}Sr_{0.33}MnO_3$, the magnetization data analysed with MAP yields $\beta = 0.23 \pm 0.02$, $\gamma = 1.05 \pm 0.03$, and $\delta = 5.13 \pm 0.04$.

Although the above mentioned samples exhibit tricritical mean-field exponents, there are other compounds [68,92,118,162,220,176,167,185,53,69,154] whose critical exponents deviate from those of the tricritical mean-field values. For instance, in single crystal $La_{0.7}Sr_{0.3}MnO_3$, the critical exponents obtained via Arrot plot and CI analysis are $\beta = 0.37 \pm 0.04$, $\gamma = 1.22 \pm 0.03$, and $\delta = 4.25 \pm 0.2$ [68]. In polycrystalline $Pr_{0.5}Sr_{0.5}MnO_3$, the MAP analysis yields $\beta = 0.443 \pm 0.002$, $\gamma = 1.339 \pm 0.006$, while the KF method as well as CI analysis give $\beta = 0.448 \pm 0.009$, $\gamma = 1.334 \pm 0.010$, and $\delta = 3.955 \pm 0.001$ [185].

In a number of studies, a change in the doping level x in the same compound

led to different critical exponents[68,92,117,162,233]. For instance, different sets of critical exponents were obtained for $La_{1-x}Ca_xMnO_3$ when $x = 0.2$[92] and $x = 0.4$[117]. Similar behavior was noted for $La_{1-x}Sr_xMnO_3$ when $x = 0.3$[68] and $x = 0.125$[162]. This was also observed in Ref.[233] for a different compound, namely, $Nd_{1-x}Sr_xMnO_3$ with $x = 0.33$ and $x = 0.4$.

The above mentioned experimental findings clearly indicate that different critical exponents are obtained with different choices for R and/or A as well as with different levels of doping, x. Although in some of these experimental works[68,162,52], the critical exponents were compared with those of the existing theoretical models, namely, mean-field, tricritical mean-field, 3D Ising, and 3D Heisenberg, these existing models were unable to reproduce their widely varying critical exponents.

3.1.2 Studies on Microscopic Models

An essential microscopic mechanism in perovskite manganites is the coupling of spin and lattice degrees of freedom (cf. Sec. 1.6.1). The electron-phonon JT coupling leading to lattice distortions are known to be important as indicated by a number of theoretical[151,188,148,149,6] and experimental studies[99,200,43,24,26]. A pronounced variation of electrical resistivity and a large shift of T_c after isotope exchange (^{18}O for ^{16}O) indicate a strong spin-lattice coupling[257,14]. The lattice distortions are shown to be directly related to the imposed strain due to perturbations induced via changes in R, A, and x[148,149,26,200,105]. A quantitative analysis[149] predicted a dramatic sensitivity of material properties to strain, particularly the shifting of T_c with strain. Different strain modes are shown to evolve depending on whether the perturbation is due to the size distribution of R/A atoms or to the change in the doping concentration x. Elastic interactions are shown to play an essential role in the formation of superstructures[115,116] and texturing[6] ob-

served in perovskite manganites. In addition to JT distortions, another essential microscopic mechanism is the spin-spin DE interaction [255,148,197]. The microscopic models for the magnetic (and electrical) properties of perovskite manganites are based on the framework of these two mechanisms which provide a satisfactory explanation for the origin of CMR and the change in resistivity as the system passes through the PM-FM transition. They also explain satisfactorily the systematic variation of T_c with doping [99,148,188]. A number of Monte Carlo (MC) simulations have been performed [32,158,157,156] on a DE model Hamiltonian [32]

$$H = -J \sum_{i,j} \sqrt{1 + \mathbf{S}_i . \mathbf{S}_j} \tag{3.1}$$

for the investigation of the static critical behavior. These simulations yield $\nu = 0.6949 \pm 0.0038$, $\beta = 0.3535 \pm 0.0030$, $\gamma = 1.3909 \pm 0.0030$ in Ref. [32], $\beta \approx 0.365$ in Refs. [158,156], $\beta = 0.36 \pm 0.01$ in Ref. [157], and $\nu = 0.686 \pm 0.010$, that are close to those of the 3D Heisenberg model (with SR interaction). This suggests that the DE and 3D Heisenberg models [36,91] belong to the same universality class. Although a few perovskite manganite samples [162,167] are found to have critical indices near to the 3D Heisenberg model predictions, a vast majority of samples [142,68,92,117,220,185,233,52], as discussed above, exhibit a widely varying sets of critical indices including the tricritical mean-field exponents. Thus, although the DE is widely accepted as one of the key mechanisms for CMR in perovskite manganites, models involving the DE interaction can not capture their widely varying critical behavior near the PM-FM phase transition.

3.1.3 Theoretical Developments

As discussed earlier experiments indicate that chemical changes (via change in R, A, and x) in perovskite manganites lead to change in their critical indices. Since

such chemical changes are connected with the JT mechanism, It may be guessed that the critical properties are influenced by the corresponding spin-lattice coupling. In the early seventies [56,236,235,237,4,5,21], the investigation on the role of elastic degrees of freedom near the critical point brought out many interesting insight of compressible magnetic systems as discussed in Ch. 2. Fisher [56] considered a compressible Ising system where spin-lattice coupling occurs because the exchange interaction varies with the distance between the spins. Wagner [236,237] constructed an effective Hamiltonian for the compressible magnetic lattice under externally applied stress by introducing spin-lattice interactions where the exchange integral is assumed to depend on the lattice spacing. As a result, a long-range (nonlocal) four spin (quartic) interaction term is generated in the effective Hamiltonian. Aharony considered a continuum model [4] with a nonlocal quartic potential and showed that the system supports tricritical behavior. The effect of strain in perovskites was studied by Aharony and Bruce [5] showing that under different stress conditions, such crystals exhibit varying critical behavior, including bicritical and tricritical points, and crossover phenomena. In another theoretical work, Bergman and Halperin [21] considered a system of one-component Ising spin coupled with the elastic deformations of the cubic lattice. They also obtained a nonlocal quartic interaction term by integrating out the elastic variables (cf. Sec. 1.7). Recently, Tröster [228] considered a compressible ϕ^4 model that generates a quartic nonlocal ϕ^4 interaction term as a consequence of eliminating the elastic degrees of freedom.

3.1.4 A Phenomenological Model

As pointed out above, the quartic nonlocal term in the effective spin Hamiltonian emerges as a consequence of spin-lattice interaction. Although these theoretical studies showed the emergence of tricriticality in such systems, recent experiments,

as discussed above, indicate that perovskite manganites exhibit critical exponents both near and away from tricriticality. Since lattice distortions are shown to be important near the PM-FM phase transition of perovskite manganites, any model describing their critical properties should include the effect of spin-lattice coupling. The static critical behavior of a model Hamiltonian with a long-range algebraic interaction in the quartic term was presented in Ch. 2. Quite satisfactorily, this long-range model was found to represent critical exponents of some perovskite manganite samples that exhibit near triciritcal behavior. The model predicted that the spontaneous magnetization exponent β was restricted in the range $0.250 < \beta < 0.375$. However, experimental β values are found to lie in the range $0.23 \leqslant \beta \leqslant 0.515$, and thus the model is incapable of capturing those values lying in the range $0.375 \leqslant \beta \leqslant 0.515$. A suitable modification of the form of the nonlocal interaction is, therefore, required so that an extended range for β can be achieved. As we shall see, this is possible by replacing the infinite range interaction [Eq. (2.6)] with an interaction having a very small value of screening. Thus, we consider a nonlocal model Hamiltonian given by

$$H[\Phi] = \int d^d x \left[\frac{c_0}{2} |\nabla \Phi(\mathbf{x})|^2 + \frac{r_0}{2} \Phi^2(\mathbf{x}) + \int d^d x' \Phi^2(\mathbf{x}) u(\mathbf{x} - \mathbf{x}') \Phi^2(\mathbf{x}') \right], \tag{3.2}$$

where $\Phi^2 = \sum_{i=1}^{n} \phi_i^2$, $|\nabla \Phi|^2 = \sum_{i=1}^{n} \nabla \phi_i \cdot \nabla \phi_i$ with a screened long-range interaction represented by the coupling function

$$u(\mathbf{k}) = \frac{\lambda_0}{[\mathbf{k}^2 + m^2]^{\sigma}}, \tag{3.3}$$

in the Fourier space, where λ_0 is a coupling constant and m is a screening parameter. Since m is a parameter in the theory, we have the freedom to choose a very low value for m such that $m^{-1} \gg a$, where a is the lattice constant. This implies that the range of the interaction (m^{-1}) extents over many lattice points unlike the

short-ranged Φ^4 theory. With the above form of screened nonlocal coupling, we find that the allowed values for the critical exponents span over a wider range suitable for explaining the experimentally observed critical exponents (both near and away from tricriticality) in a wide variety of perovskite manganite samples.

Carrying out a Wilson type RG scheme at one-loop order we calculate the critical exponents in the leading order of $\epsilon = d_c - d$, where the upper critical dimension turns out to be $d_c = 4 + 2\sigma$. We find that the critical exponents for various values of σ for $n = 3$ in three dimensions with small screening are in good agreement with experimental estimates for a wide range of perovskite manganites as displayed in Table 3.2. Thus, it is evident that the model Hamiltonian with such nonlocal mode-coupling interactions [Eqs. (3.2) and (3.3)] contains a wide range of universality classes including the tricriticality in perovskite manganites.

3.2 Momentum Shell RG

Our starting point is the modified GL Hamiltonian given by Eq. (3.2), where we incorporated the effect of screened long-range interactions in the quartic term. To carry out the Wilson's momentum shell RG scheme[243,244,107], we Fourier transform the order parameter field $\Phi(\mathbf{x})$ in d dimensions as

$$\phi_i(\mathbf{x}) = \int \frac{d^d k}{(2\pi)^d}\, \phi_i(\mathbf{k})\, e^{i\mathbf{k}\cdot\mathbf{x}} \tag{3.4}$$

leading to the expression for the model Hamiltonian as

$$\begin{aligned} H[\Phi] \;=\; & \sum_{i=1}^{n} \int \frac{d^d k}{(2\pi)^d} \frac{c_0 \mathbf{k}^2 + r_0}{2} |\phi_i(\mathbf{k})|^2 + \sum_{i=1}^{n}\sum_{j=1}^{n} \int\int\int \frac{d^d k_1}{(2\pi)^d} \frac{d^d k_2}{(2\pi)^d} \frac{d^d k_3}{(2\pi)^d} \\ & u(-\mathbf{k}_1 - \mathbf{k}_2)\phi_i(\mathbf{k}_1)\phi_i(\mathbf{k}_2)\phi_j(\mathbf{k}_3)\phi_j(-\mathbf{k}_1 - \mathbf{k}_2 - \mathbf{k}_3), \end{aligned} \tag{3.5}$$

with the nonlocal coupling function $u(-\mathbf{k}_1-\mathbf{k}_2)$ given by Eq. (3.3). Nonzero lattice constant a imposes an ultraviolet cutoff $\Lambda(\sim a^{-1})$ to the momentum integrations.

Following momentum shell decimation scheme, we eliminate the "fast" modes $\phi_i^>(\mathbf{k})$ in the momentum shell $\Lambda/b \leqslant k \leqslant \Lambda$, where $b>1$ and Λ is an ultraviolet cut-off to the momentum integrations. This mode elimination process modifies the parameters of the original Hamiltonian and yields an effective Hamiltonian in terms of the "slow" degrees of freedom $\phi_i^<(\mathbf{k})$ in the reduced range $0<k<\Lambda/b$. A subsequent rescaling procedure restores the momenta to the full range $0 \leqslant k \leqslant \Lambda$.

In carrying out this shell elimination procedure we write the two-point correlation function of the order parameter as [139,71]

$$\langle \phi_i(\mathbf{q})\phi_j(\mathbf{q}')\rangle_0 = G_0(\mathbf{q})(2\pi)^d\delta^d(\mathbf{q}+\mathbf{q}')\delta_{ij}, \tag{3.6}$$

where

$$G_0(\mathbf{q}) = \frac{1}{c_0\mathbf{q}^2+r_0} \tag{3.7}$$

is the (bare) propagator.

3.2.1 Self-energy Corrections

Elimination of short wavelength fluctuations generates the Feynman diagrams shown in Fig. 3.1. The corresponding self-energy integrals, obtained from their amputated parts (excluding the external legs), are given by

$$\Sigma_a(\mathbf{0}) = 2n\int \frac{d^dq}{(2\pi)^d}\, u(\mathbf{0})\, G_0^>(\mathbf{q}), \tag{3.8}$$

and

$$\Sigma_b(\mathbf{k}) = 4\int \frac{d^dq}{(2\pi)^d}\, u(-\mathbf{k}-\mathbf{q})\, G_0^>(\mathbf{q}), \tag{3.9}$$

where the prefactors are combinatorial factors and the integrals are restricted to

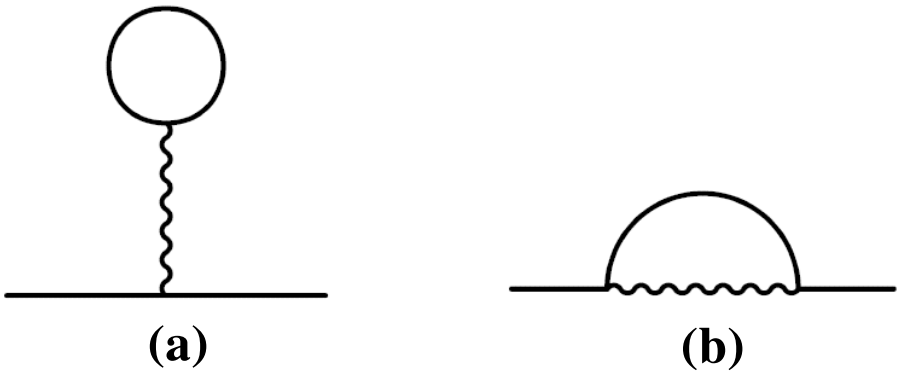

Figure 3.1: Feynman diagrams representing the self-energy corrections to r_0 and c_0. The wiggly lines represent $u(\mathbf{0})$ in (a) and $u(-\mathbf{k}-\mathbf{q})$ in (b); the internal solid lines represent correlation $G_0(\mathbf{q})$ between the fast modes.

the momentum shell $\Lambda/b \leqslant q \leqslant \Lambda$. These self energy integrals yield the relevant corrections Δr and Δc to the bare parameters r_0 and c_0, given by the expansion

$$\Sigma_a(\mathbf{0}) + \Sigma_b(\mathbf{k}) = \frac{1}{2}\Delta r + \frac{1}{2}\Delta c k^2 + \ldots \tag{3.10}$$

in the limit $q \gg k$. We note that in the self-energy integrals [Eqs. (3.8) and (3.9)] the internal momentum $q \sim \Lambda$. In addition, since $\Lambda \sim a^{-1}$, the choice of $m^{-1} \gg a$ implies $m \ll \Lambda$, consequently the internal momentum $q \gg m$ in the above integral for $\Sigma_b(\mathbf{k})$. Thus the vertex function $u(-\mathbf{k}-\mathbf{q})$ occurring inside the integral are expanded in a high momentum expansion in the limit $q \gg m$. Thus employing the expansion

$$u(-\mathbf{k}-\mathbf{q}) = \frac{\lambda_0}{[(\mathbf{k}+\mathbf{q})^2+m^2]^\sigma} = \frac{\lambda_0}{q^{2\sigma}}\left[1 - 2\sigma\frac{\mathbf{k}\cdot\mathbf{q}}{q^2} - \sigma\frac{k^2+m^2}{q^2} + 2\sigma(\sigma+1)\frac{(\mathbf{k}\cdot\mathbf{q})^2}{q^4} + \ldots\right], \tag{3.11}$$

we obtain from Eqs. (3.8), (3.9), and (3.10)

$$\Delta r = \frac{4n\lambda_0}{m^{2\sigma}}\frac{S_d}{(2\pi)^d}\left[\frac{(b^{2-d}-1)\Lambda^{d-2}}{c_0(2-d)} - \frac{r_0}{c_0^2}\frac{(b^{4-d}-1)\Lambda^{d-4}}{(4-d)}\right] +$$

$$+8\lambda_0\frac{S_d}{(2\pi)^d}\left[\frac{(b^{2\sigma+2-d}-1)\Lambda^{d-2\sigma-2}}{c_0(2\sigma+2-d)}-\left(\frac{r_0}{c_0^2}+\frac{\sigma m^2}{c_0}\right)\frac{(b^{2\sigma+4-d}-1)\Lambda^{d-2\sigma-4}}{(2\sigma+4-d)}\right], \quad (3.12)$$

and

$$\Delta c=\frac{8\lambda_0}{c_0}\frac{S_d}{(2\pi)^d}\frac{\sigma(2\sigma+2-d)}{d}\frac{(b^{2\sigma+4-d}-1)\Lambda^{d-4-2\sigma}}{(2\sigma+4-d)}. \quad (3.13)$$

It may be noted that the n-dependent correction to the bare parameter r_0 comes from Σ_a given by the first Feynman diagram [Fig. 3.1(a)].

3.2.2 Vertex Corrections

To calculate the vertex corrections we follow the same procedure of eliminating the fast modes $\phi_i^>(\mathbf{k})$ belonging to the high momentum shell $\Lambda/b\leqslant k\leqslant\Lambda$. The corresponding one-loop Feynman diagrams are shown in Fig. 3.2 and their amputated parts (excluding the four external legs) are represented by the integrals

$$\Pi_a(\mathbf{k}_1,\mathbf{k}_2)=-4nu^2(-\mathbf{k}_1-\mathbf{k}_2)\int\frac{d^dq}{(2\pi)^d}G_0^>(\mathbf{q})\,G_0^>(-\mathbf{k}_1-\mathbf{k}_2-\mathbf{q}), \quad (3.14)$$

$$\Pi_b(\mathbf{k}_1,\mathbf{k}_2,\mathbf{k}_3)=-16u(-\mathbf{k}_1-\mathbf{k}_2)\int\frac{d^dq}{(2\pi)^d}u(\mathbf{q}-\mathbf{k}_3)\,G_0^>(\mathbf{q})\,G_0^>(-\mathbf{k}_1-\mathbf{k}_2-\mathbf{q}), \quad (3.15)$$

and

$$\Pi_c(\mathbf{k}_1,\mathbf{k}_2,\mathbf{k}_3)=-16\int\frac{d^dq}{(2\pi)^d}u(-\mathbf{k}_1-\mathbf{q})\,u(\mathbf{q}-\mathbf{k}_2)\,G_0^>(\mathbf{q})\,G_0^>(-\mathbf{k}_1-\mathbf{k}_3-\mathbf{q}), \quad (3.16)$$

where $\mathbf{k}_1$, $\mathbf{k}_2$, $\mathbf{k}_3$, and $\mathbf{k}_4=-\mathbf{k}_1-\mathbf{k}_2-\mathbf{k}_3$ are the external momenta carried by the four external legs in Fig. 2.

From Eqs. (3.14), (3.15), and (3.16), we see that Π_a and Π_b share the form of the bare vertex $u(-\mathbf{k}_1-\mathbf{k}_2)$ in the original Hamiltonian given by Eq. (3.5). Consequently, they contribute as a correction $\Delta\lambda$ to the bare parameter λ_0. On the other hand, Π_c is irrelevant as it does not share the form of the bare vertex $u(-\mathbf{k}_1-\mathbf{k}_2)$.

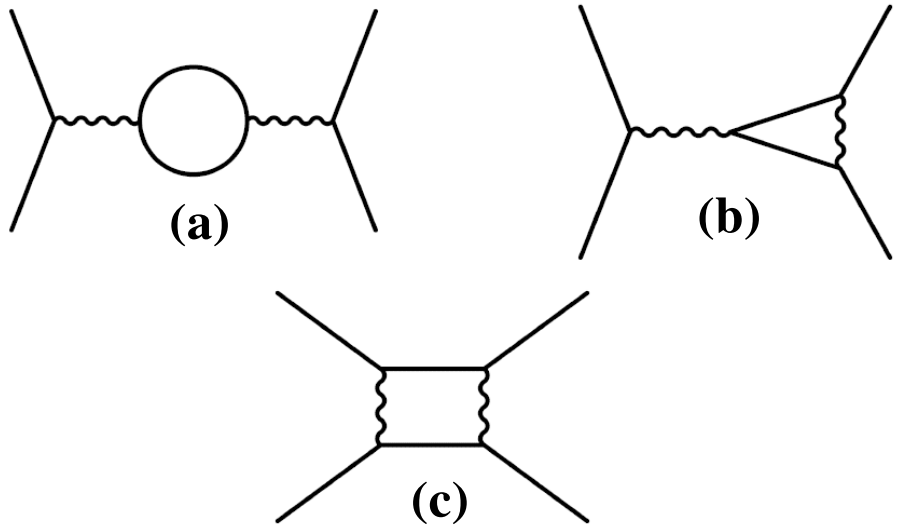

Figure 3.2: Feynamn diagrams representing corrections to the vertex $u(-\mathbf{k}_1-\mathbf{k}_2)$ at one-loop order.

Since in Wilson's renormalization procedure the effect of elimination of small scales (internal momentum q) on the large scales (external momenta k_i) is to be found out, the above corrections are expanded in the limit $q \gg k_i$ which is equivalent to an expansion about $\mathbf{k}_i = 0$. Since the integrals over q in the expressions for $\Pi_a(\mathbf{0},\mathbf{0})$ and $\Pi_b(\mathbf{0},\mathbf{0},\mathbf{0})$ are restricted in the high momentum shell $\Lambda/b \leqslant q \leqslant \Lambda$, this implies $q \sim \Lambda$, thus as described earlier, $q \gg m$. Thus the vertex function $(q^2+m^2)^{-\sigma}$ occurring inside the integral for Π_b is expanded in a high momentum expansion in the limit $q \gg m$, given by

$$(q^2+m^2)^{-\sigma} = q^{-2\sigma}\left[1-\frac{\sigma m^2}{q^2}+O\left(\frac{m^4}{q^4}\right)\right]. \tag{3.17}$$

Incorporating the contributions coming from the integrals Π_a and Π_b, yield the relevant corrections to λ_0 as

$$\Delta\lambda = \frac{-4n\lambda_0^2}{m^{2\sigma}}\frac{S_d}{(2\pi)^d}\left[\frac{(b^{4-d}-1)\Lambda^{d-4}}{c_0^2(4-d)} - \frac{2r_0}{c_0^3}\frac{(b^{6-d}-1)\Lambda^{d-6}}{(6-d)}\right]$$

$$-16\lambda_0^2\frac{S_d}{(2\pi)^d}\left[\frac{(b^{2\sigma+4-d}-1)\Lambda^{d-2\sigma-4}}{c_0^2(2\sigma+4-d)}-\left(\frac{\sigma m^2}{c_0^2}+\frac{2r_0}{c_0^3}\right)\frac{(b^{2\sigma+6-d}-1)\Lambda^{d-2\sigma-6}}{(2\sigma+6-d)}\right]. \tag{3.18}$$

3.3 RG Flow Equations and Stability

The above one-loop corrections to the model parameters enable us to derive their RG flow equations. From these flow equations, we obtain a nontrivial fixed point and perform its stability analysis. The detail calculations are given below.

3.3.1 Rescaling and Flow Equations

The mode elimination procedure carried out in previous section eliminates the modes lying in the range $\Lambda/b < q < \Lambda$ and thus lower the cut-off. To restore this change we rescale momenta and fields as

$$\mathbf{k}' = b\mathbf{k}, \qquad \Phi'(\mathbf{k}') = \zeta^{-1}\Phi(\mathbf{k}). \tag{3.19}$$

Assuming self-similarity and power-like fall off of the correlation function at the critical point [139,71] gives $\zeta = b^{(d+2-\eta)/2}$. Incorporating the one-loop corrections, given by Eqs. (3.12), (3.13), and (3.18), we obtain the RG recursion relations for the model parameters as

$$r' = b^{2-\eta}(r_0 + \Delta r), \tag{3.20}$$

$$c' = b^{-\eta}(c_0 + \Delta c), \tag{3.21}$$

$$\lambda' = b^{4-d-2\eta+2\sigma}(\lambda_0 + \Delta\lambda). \tag{3.22}$$

Taking $b = e^{\delta l}$, we construct the RG flow equations in the limit $\delta l \to 0$ from above recursion relations for the scale dependent parameters $r(l)$, $c(l)$ and $\lambda(l)$ and arrive

at

$$\frac{dr}{dl} = (2-\eta)r + \frac{4n\lambda S_d}{m^{2\sigma}(2\pi)^d}\left(\frac{\Lambda^{d-2}}{c} - \frac{r}{c^2}\Lambda^{d-4}\right) + \frac{8\lambda S_d}{(2\pi)^d}\left[\frac{\Lambda^{d-2-2\sigma}}{c} - \left(\frac{r}{c^2} + \frac{\sigma m^2}{c}\right)\Lambda^{d-4-2\sigma}\right], \tag{3.23}$$

$$\frac{dc}{dl} = -\eta c + \frac{8\sigma(2\sigma+2-d)\lambda S_d}{d(2\pi)^d}\frac{\Lambda^{d-4-2\sigma}}{c}, \tag{3.24}$$

and

$$\frac{d\lambda}{dl} = (4-d-2\eta+2\sigma)\lambda - \frac{4n\lambda^2 S_d}{m^{2\sigma}(2\pi)^d}\left(\frac{\Lambda^{d-4}}{c^2} - \frac{2r}{c^3}\Lambda^{d-6}\right) - \frac{16\lambda^2 S_d}{(2\pi)^d}\left[\frac{\Lambda^{d-4-2\sigma}}{c^2} - \left(\frac{2r}{c^3} + \frac{\sigma m^2}{c^2}\right)\Lambda^{d-6-2\sigma}\right]. \tag{3.25}$$

3.3.2 Fixed Point and Stability

Solving the above flow equations [Eqs. (3.23)–(3.25)] for the non-trivial fixed point $(r^*, \lambda^*, c^* = c)$, we obtain

$$\frac{r^*}{c} = -\frac{(4-d-2\eta+2\sigma)\left\{\frac{4n}{w^\sigma} + 8(1-\sigma w)\right\}\Lambda^2}{(2-\eta)\left\{\frac{4n}{w^\sigma} + 16(1-\sigma w)\right\} - (4-d-2\eta+2\sigma)(\frac{4n}{w^\sigma}+8)}, \tag{3.26}$$

and

$$\frac{\lambda^*}{c^2} = \frac{(4-d-2\eta+2\sigma)\Lambda^{4-d+2\sigma}}{\frac{S_d}{(2\pi)^d}\left\{\frac{4n}{w^\sigma} + 16(1-\sigma w)\right\}}, \tag{3.27}$$

where $w = m^2/\Lambda^2$ is a redefined dimensionless screening parameter. A linear stability analysis around this non-trivial fixed point by introducing small perturbations $\delta r = r - r^*$ and $\delta\lambda = \lambda - \lambda^*$ yields a matrix equation

$$\begin{bmatrix} d\delta r/dl \\ d\delta\lambda/dl \end{bmatrix} = \begin{bmatrix} y_1 & \frac{8S_d}{(2\pi)^d}\frac{\Lambda^{d-2\sigma-2}}{c}\left(1-\sigma w - \frac{r^*}{c\Lambda^2}\right) + \frac{4n}{w^\sigma}\frac{8S_d}{(2\pi)^d}\frac{\Lambda^{d-2\sigma-2}}{c} \\ 0 & y_2 \end{bmatrix}\begin{bmatrix} \delta r \\ \delta\lambda \end{bmatrix}, \tag{3.28}$$

with the eigenvalues y_1 and y_2 of the stability matrix as

$$y_1 = 2-\eta-(4-d-2\eta+2\sigma)\frac{(\frac{4n}{w^\sigma}+8)}{\left[\frac{4n}{w^\sigma}+16(1-\sigma w)\right]}, \tag{3.29}$$

and

$$y_2 = d-4+2\eta-2\sigma. \tag{3.30}$$

Here y_1 and y_2 correspond, respectively, to unstable and stable eigendirections in the RG flow. We identify the upper critical dimension d_c from the marginal stability of the stable eigenvalue y_2, giving

$$d_c = 4+2\sigma. \tag{3.31}$$

The stability analysis coupled with the conditions $y_1 \geqslant 0$ and $y_2 \leqslant 0$ impose restrictions on the allowed values of σ. For $d = n = 3$, we find that the value of σ is restricted in the range $-0.50 \leqslant \sigma \leqslant 0.51$ and, for $d = 2$ and $n = 3$, it is restricted in the range $-1.00 \leqslant \sigma \leqslant 0.16$ for small value of the screening parameter $w = 0.001$. These stability ranges are somewhat insensitive to the values of n and w as shown in Table. 3.1.

Table 3.1: Ranges of σ, $[\sigma_{\min}, \sigma_{\max}]$, for the non-trivial fixed point for $d, n = 1,2,3$ and for three different values of the screening parameter w.

w	d	$n=1$	$n=2$	$n=3$
0.0001	1	$[-1.50, 0.05]$	$[-1.50, 0.00]$	$[-1.50, -0.03]$
	2	$[-1.00, 0.21]$	$[-1.00, 0.17]$	$[-1.00, 0.14]$
	3	$[-0.50, 0.51]$	$[-0.50, 0.51]$	$[-0.50, 0.51]$
0.001	1	$[-1.50, 0.06]$	$[-1.50, 0.00]$	$[-1.50, -0.04]$
	2	$[-1.00, 0.25]$	$[-1.00, 0.19]$	$[-1.00, 0.16]$
	3	$[-0.50, 0.54]$	$[-0.50, 0.52]$	$[-0.50, 0.51]$
0.01	1	$[-1.50, 0.08]$	$[-1.50, 0.0]$	$[-1.50, -0.04]$
	2	$[-1.00, 0.30]$	$[-1.00, 0.23]$	$[-1.00, 0.20]$
	3	$[-0.50, 0.60]$	$[-0.50, 0.56]$	$[-0.50, 0.54]$

In the following section, we calculate the critical exponents in an ϵ-expansion scheme with the identification

$$\epsilon = d_c - d = 4 + 2\sigma - d. \tag{3.32}$$

3.4 Critical Exponents

We obtain the critical exponent ν, occurring in the correlation length $\xi \sim |T - T_c|^{-\nu}$, from the unstable eigenvalue y_1 [given by Eq. (3.29)] using the relation $\nu = 1/y_1$ (cf. Sec. 1.3), so that

$$\nu = \frac{1}{2} + \frac{\epsilon(\frac{n}{w^\sigma}+2)}{2\left(\frac{n}{w^\sigma}+4(1-\sigma w)\right)}\left\{\frac{1}{2} + \frac{2\sigma}{(\sigma+2)\left[\frac{n}{w^\sigma}+4(1-\sigma w)\right]-4\sigma}\right\} + \\ - \frac{\sigma\epsilon}{2(\sigma+2)\left[\frac{n}{w^\sigma}+4(1-\sigma w)\right]-8\sigma} + O(\epsilon^2). \tag{3.33}$$

The Fisher exponent η is obtained from Eq. (3.24) by setting $dc/dl = 0$, and we find

$$\eta = -\frac{2\sigma\epsilon}{(\sigma+2)\left[\frac{n}{w^\sigma}+4(1-\sigma w)\right]-4\sigma} + O(\epsilon^2). \tag{3.34}$$

It is interesting to note that we obtain a non-zero value for the exponent η in the first order of ϵ.

Using Eqs. (3.33) and (3.34) in the well known scaling laws (cf. Sec. 1.2), we calculate the other critical exponents, namely, specific heat exponent α, spontaneous magnetization exponent β, susceptibility exponent γ, and critical isotherm exponent δ, and obtain

$$\alpha = \frac{\epsilon+4}{2} - (\sigma+2)\left[1 + \frac{\epsilon(\frac{n}{w^\sigma}+2)}{\frac{n}{w^\sigma}+4(1-\sigma w)}\left\{\frac{1}{2} + \frac{2\sigma}{(\sigma+2)\left[\frac{n}{w^\sigma}+4(1-\sigma w)\right]-4\sigma}\right\} \right. \\ \left. - \frac{\sigma\epsilon}{(\sigma+2)\left[\frac{n}{w^\sigma}+4(1-\sigma w)\right]-4\sigma}\right] + O(\epsilon^2), \tag{3.35}$$

$$\beta = \frac{\sigma+1}{2} - \frac{\epsilon}{4}\left[1 + \frac{2\sigma(\sigma+2)}{(\sigma+2)\left[\frac{n}{w^\sigma}+4(1-\sigma w)\right]-4\sigma} - \frac{(\frac{n}{w^\sigma}+2)(2\sigma+2)}{\frac{n}{w^\sigma}+4(1-\sigma w)} \times \right.$$
$$\left. \times \left\{\frac{1}{2} + \frac{2\sigma}{(\sigma+2)\left[\frac{n}{w^\sigma}+4(1-\sigma w)\right]-4\sigma}\right\}\right] + O(\epsilon^2), \quad (3.36)$$

$$\gamma = 1 + \frac{\epsilon(\frac{n}{w^\sigma}+2)}{\frac{n}{w^\sigma}+4(1-\sigma w)}\left[\frac{1}{2} + \frac{2\sigma}{(\sigma+2)\left[\frac{n}{w^\sigma}+4(1-\sigma w)\right]-4\sigma}\right] + O(\epsilon^2), \quad (3.37)$$

$$\delta = \frac{\sigma+3}{\sigma+1} + \frac{\epsilon}{\sigma+1}\left[\frac{1}{\sigma+1} + \frac{2\sigma(\sigma+2)}{(\sigma+1)\left[(\sigma+2)\left\{\frac{n}{w^\sigma}+4(1-\sigma w)\right\}-4\sigma\right]}\right] + O(\epsilon^2). \quad (3.38)$$

We see that the analytical forms of the critical exponents, given by Eqs. (3.33)–(3.38), depend on the parameters n, d, σ, and w. In these expressions, the terms containing w and n do not vary strongly for different values of w and n. This is demonstrated in the graphical plots in Fig. 3.3 where the critical exponents show slow variation with respect to w for a range of σ relevant to the experimental samples given in Tables 3.2. In addition, we see that although the exponents ν, α, and β, γ undergo slight variation with respect to n (in the vicinity of $\sigma = 0$), these variations are quite smaller compare to short-range models.

3.5 Universality Classes in Perovskite Manganites

From the results of previous section, we see that the values of the critical exponents for the marginal case of $\epsilon = 0$ in $d = 3$ match exactly with those of tricritical mean field exponents [94], namely, $\alpha = \frac{1}{2}$, $\beta = \frac{1}{4}$, $\gamma = 1$, and $\delta = 5$. It may be noted that this result for the tricritical point is independent of the screening parameter w because

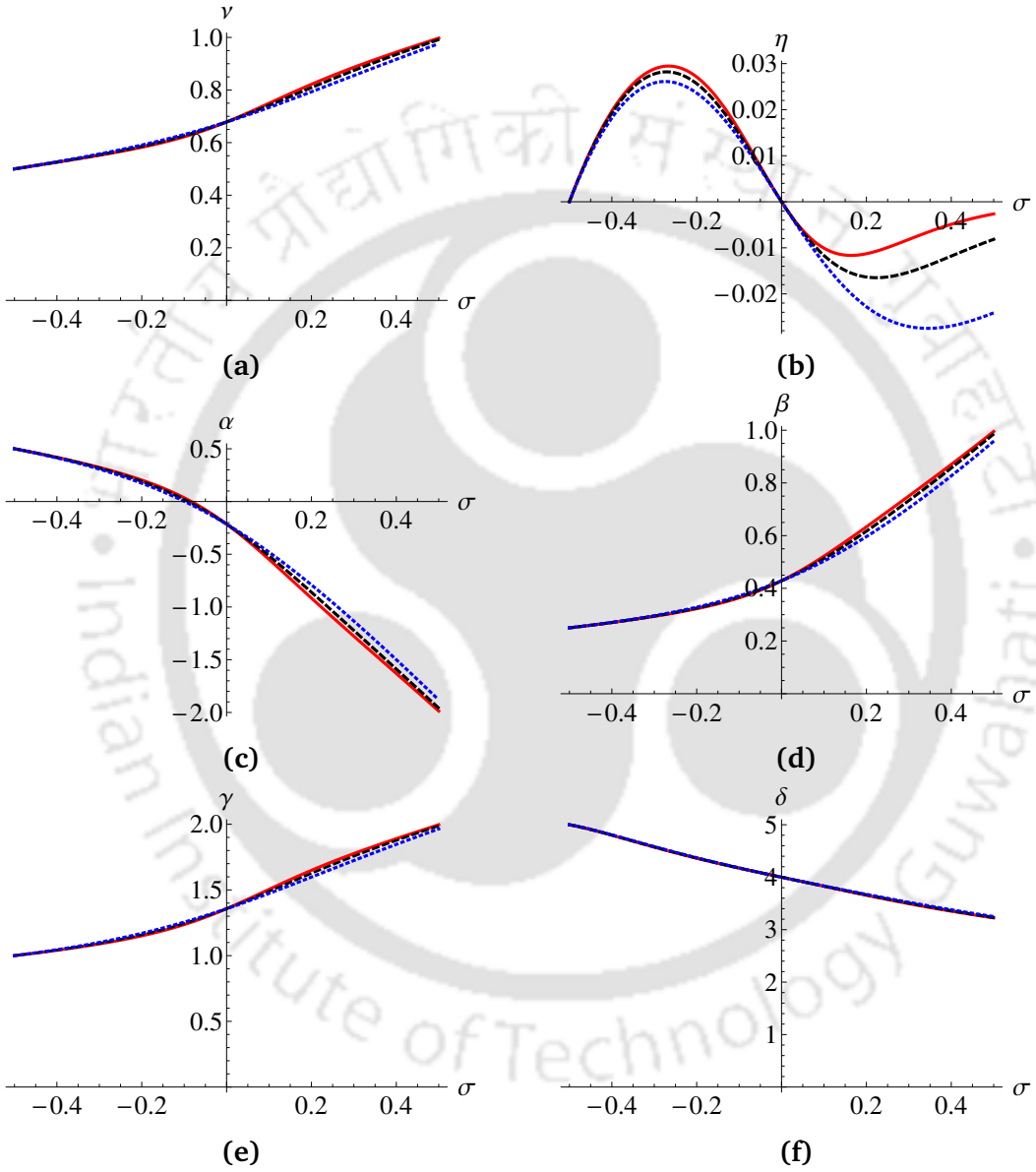

Figure 3.3: The critical exponents for $n = 3, d = 3$ for three different values of w. The solid, dashed, and dotted line in each figure corresponds to $w = 0.0001, 0.001, 0.01$ respectively.

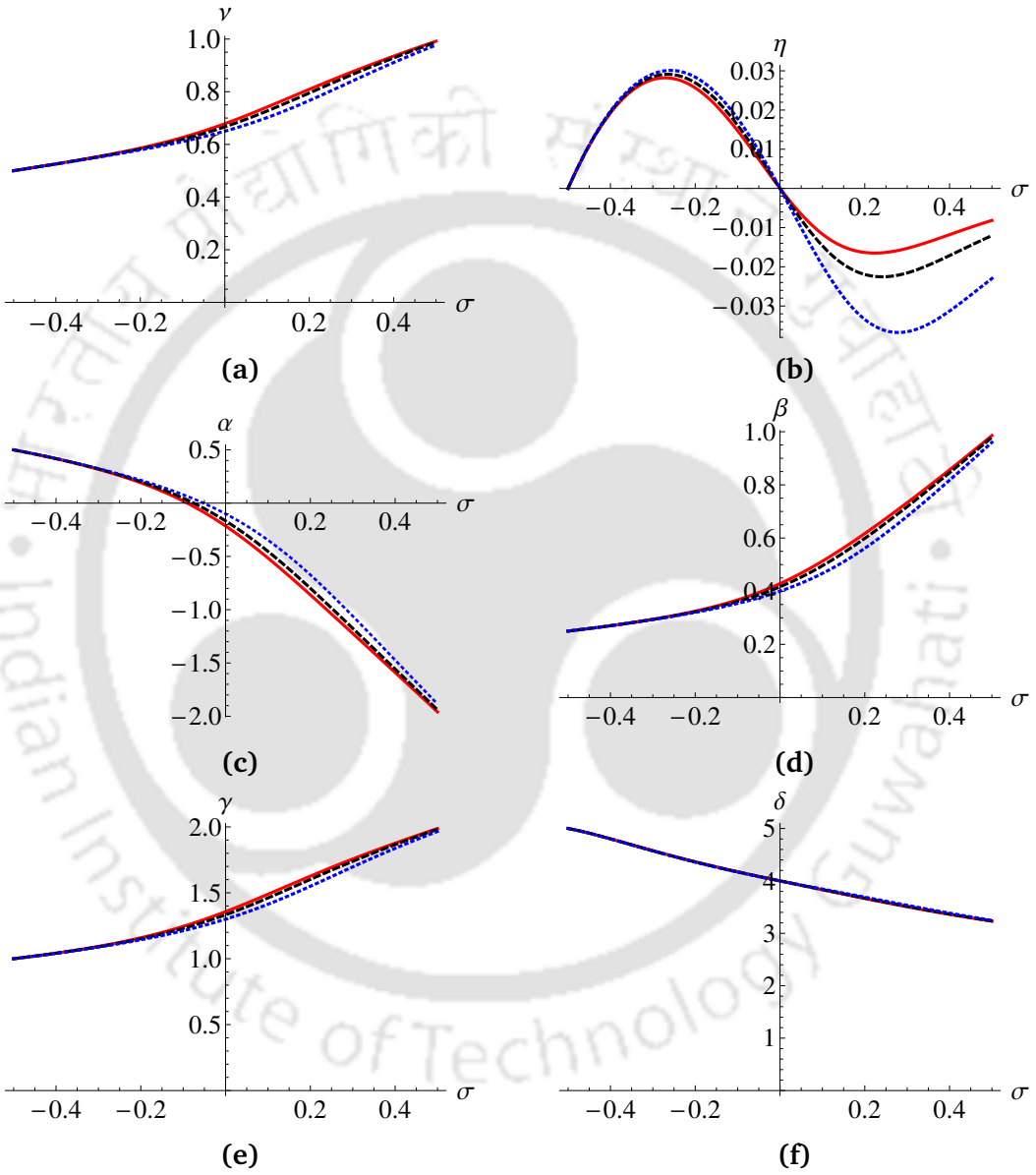

Figure 3.4: The critical exponents for $d = 3$ and $w = 0.001$, for three different values of n. The solid, dashed, and dotted line in each figure corresponds to $n = 3, 2, 1$ respectively.

it occurs in the $O(\epsilon)$ terms in the ϵ-expansion. For other values of ϵ, or σ the above analytical formulas yield a wide range of critical exponents both near and away from tricriticality in three dimensions. As shown in Table 3.2, the analytical results for the critical exponents following from Eqs. (3.36), (3.37), and (3.38), are compared with the available experimental estimates both near and away from tricriticality including β values higher than 0.375.

While comparing the experimental estimates with our theoretical results for the critical exponents β, γ, and δ, we first match the value of β. For a particular sample, we obtain from Eq. (3.36) the experimental β value (up to three significant figures) for a suitable value of σ. Using this value of σ, we calculated the values of γ and δ (for the same sample) from Eqs. (3.37) and (3.38), respectively. We find that for a range of experimental values of β, the corresponding values of γ and δ are in better agreement with those of experimental ones for $n = 3$ in three dimensions for $w = 0.001$ and, accordingly our present results are displayed in Table 3.2 for $n = 3$ and $w = 0.001$.

We see that our model Hamiltonian captures the experimental results for σ lying in the range $-0.499 \leqslant \sigma \leqslant 0.102$. Although in some of the experimental work, the estimated results are compared with those of short-range (Ising, 3D Heisenberg, mean-field) models and the LR model of Fisher *et al.*, our present estimates are in better agreement with experimental ones. For instance, in Ref.[68], for the sample $La_{0.7}Sr_{0.3}MnO_3$, the experimental results are compared with 3D Heisenberg, 3D Ising, and LR model of Fisher *et al*.

However, it was found that the estimated β, γ, and δ values do not completely agree with those of SR and LR models, suggesting a new universality class for this sample. The experimental values given in Ref.[68] are in good agreement with our present estimates for $\sigma = -0.094$ as displayed in Table. 3.2. In Ref.[185], for the

Table 3.2: Comparison of the critical exponents β, γ, and δ following from Eqs. (3.36), (3.37), and (3.38) for $n = d = 3$ and $w = 0.001$ with experimental estimates obtained for various perovskite manganite compounds. Abbreviations: PC; Polycrystalline, SC; Single-crystal

σ	Experimental sample	Ref.	β	γ	δ
-0.499			0.250	1.000	.999
	$La_{0.6}Ca_{0.4}MnO_3$ (PC)	[117]	0.25 ± 0.03	1.03 ± 0.05	5.0 ± 0.8
	$La_{0.6}Ca_{0.4}MnO_3$ (PC)	[163]	0.248	0.995	4.896
	$Nd_{0.67}Sr_{0.33}MnO_3$ (PC)	[233]	0.23 ± 0.02	1.05 ± 0.03	5.13 ± 0.04
	$La_{0.1}Nd_{0.6}Sr_{0.3}MnO_3$ (PC)	[52]	0.248 ± 0.006	1.066 ± 0.002	–
-0.463			0.257	1.015	4.936
	$La_{0.1}Nd_{0.6}Sr_{0.3}MnO_3$ (PC)	[52]	0.257 ± 0.005	1.12 ± 0.03	5.17 ± 0.02
-0.325			0.288	1.080	4.633
	$La_{0.5}Ca_{0.3}Ag_{0.2}MnO_3$ (PC)	[211]	0.288 ± 0.002	0.948 ± 0.008	4.90 ± 0.02
-0.300			0.295	1.094	4.577
	$La_{0.7}Sr_{0.3}MnO_3$ (SC)	[142]	0.295 ± 0.002	–	–
-0.243			0.311	1.129	4.454
	$La_{0.5}Ca_{0.4}Ag_{0.1}MnO_3$ (PC)	[211]	0.311 ± 0.003	1.146 ± 0.006	4.83 ± 0.01
-0.203			0.324	1.157	4.371
	$La_{0.67}Sr_{0.16}Ca_{0.17}MnO_3$ (PC)	[154]	0.324 ± 0.005	1.176 ± 0.03	4.415 ± 0.02
-0.193			0.328	1.164	4.351
	$La_{0.8}Ca_{0.2}MnO_3$	[114]	0.328	1.193	4.826
-0.150			0.344	1.199	4.268
	$Pr_{0.77}Pb_{0.23}MnO_3$ (SC)	[167]	0.344 ± 0.001	1.352 ± 0.006	4.69 ± 0.02
-0.115			0.360	1.231	4.203
	$La_{0.8}Ca_{0.2}MnO_3$ (SC)	[92]	0.36	1.45	5.03
-0.094			0.370	1.251	4.164
	$La_{0.7}Sr_{0.3}MnO_3$ (SC)	[68]	0.37 ± 0.04	1.22 ± 0.03	4.25 ± 0.2
-0.095			0.370	1.250	4.166
	$La_{0.875}Sr_{0.125}MnO_3$ (SC)	[162]	0.37 ± 0.02	1.38 ± 0.03	4.72 ± 0.04
-0.087			0.374	1.258	4.152
	$Nd_{0.6}Pb_{0.4}MnO_3$ (SC)	[193]	0.374 ± 0.006	1.329 ± 0.003	4.54 ± 0.10

σ	Experimental sample	Ref.	β	γ	δ
-0.039			0.400	1.311	4.067
	$La_{0.75}Sr_{0.25}MnO_3$ (SC)	[118]	0.40 ± 0.02	1.27 ± 0.06	4.12 ± 0.33
-0.036			0.404	1.314	4.062
	$Pr_{0.70}Pb_{0.30}MnO_3$ (SC)	[167]	0.404 ± 0.001	1.357 ± 0.006	4.73 ± 0.09
0.019			0.443	1.381	3.968
	$Pr_{0.50}Sr_{0.50}MnO_3$ (PC)	[185]	0.443 ± 0.002	1.339 ± 0.006	3.955 ± 0.001
	$Pr_{0.9}Pb_{0.1}MnO_3$ (PC)	[69]	0.443 ± 0.027	1.337 ± 0.042	3.99 ± 0.07
0.025			0.448	1.389	3.957
	$Pr_{0.50}Sr_{0.50}MnO_3$ (PC)	[185]	0.448 ± 0.009	1.334 ± 0.010	3.977 ± 0.006
0.029			0.451	1.394	3.950
	$La_{0.7}Sr_{0.3}MnO_3$ (SC)	[220]	0.45 ± 0.01	1.2	3.901
0.043			0.462	1.412	3.927
	$Pr_{0.52}Sr_{0.48}MnO_3$ (PC)	[192]	0.462 ± 0.002	1.210 ± 0.003	3.750 ± 0.02
	$Pr_{0.55}Sr_{0.44}MnO_3$ (PC)	[53]	0.462	1.033	3.24
0.045			0.464	1.415	3.923
	$La_{0.67}Ba_{0.33}MnO_3$ (PC)	[159]	0.464	1.29	–
0.050			0.468	1.421	3.915
	$Pr_{0.8}Pb_{0.2}MnO_3$ (PC)	[69]	0.468 ± 0.004	1.353 ± 0.083	3.78 ± 0.02
0.084			0.498	1.456	3.920
	$La_{0.9}Pb_{0.1}MnO_3$ (PC)	[176]	0.498	1.466	3.920
0.086			0.500	1.470	3.858
	$La_{0.8}Sr_{0.2}MnO_3$ (PC)	[155]	0.50 ± 0.02	1.08 ± 0.03	3.13 ± 0.20
0.102			0.515	1.492	3.827
	$Pr_{0.3}Nd_{0.2}Sr_{0.5}MnO_3$ (PC)	[256]	0.515	1.441	3.774

sample $Pr_{0.50}Sr_{0.50}MnO_3$, the estimated critical exponents are found to be inconsistent with SR models. The author's also discussed the possibility of LR interaction and made a comparison with LR model of Fisher *et al.*. However, it gives a counter intuitive results and led them to speculate that the critical phenomena in disordered magnetic systems could not be described by conventional models. Our present theoretical results for $\sigma = 0.019$ and $\sigma = 0.025$ are, in fact, very close to their experimental estimates obtained via MAP, KF, and CI analyses. As the critical exponents calculated in the leading order of ϵ are in good agreements with experimental predictions for a wide number of samples, it can be speculated that the present nonlocal model contains the universality classes of perovskite manganites.

3.6 Comparison with a Long-Range Model

In the previous chapter (Ch. 2), we discussed the RG results for a nonlocal model Hamiltonian with purely LR (without screening) quartic interactions. Thus, it would be interesting to compare the results of the present model with that of the former in the context of observed critical behavior in perovskite manganites.

The two models differ from one another due to their different forms of the coupling function, one with $u(\mathbf{k}) = \lambda_0|\mathbf{k}|^{2\rho}$ used in Ch. 2 and the other with $u(\mathbf{k}) = \lambda_0/(\mathbf{k}^2 + m^2)^\sigma$ used in the present Chapter. We have discussed in Ch. 2 that with $u(\mathbf{k}) = \lambda_0|\mathbf{k}|^{2\rho}$, the nonanalyticity of $u(\mathbf{k})$ at $k = 0$ appears which restricts the nonlocal exponent ρ to be strictly positive. Due to this nonanalyticity, we have shown in Ch. 2 that some Feynman diagrams corresponding to self-energy and four-point vertex do not contribute and, as a result, the critical exponents turns out to be n independent. Further, the corresponding RG calculation yields β values restricted in the range $0.250 < \beta < 0.375$. However, as we have elaborately discussed in this Chapter, the range of experimental β values is found to be $0.23 < \beta < 0.515$. Thus it

is transparent that a model Hamiltonian with a purely long-range quartic interaction is unable to capture the full experimental range for critical exponents observed in perovskite manganites.

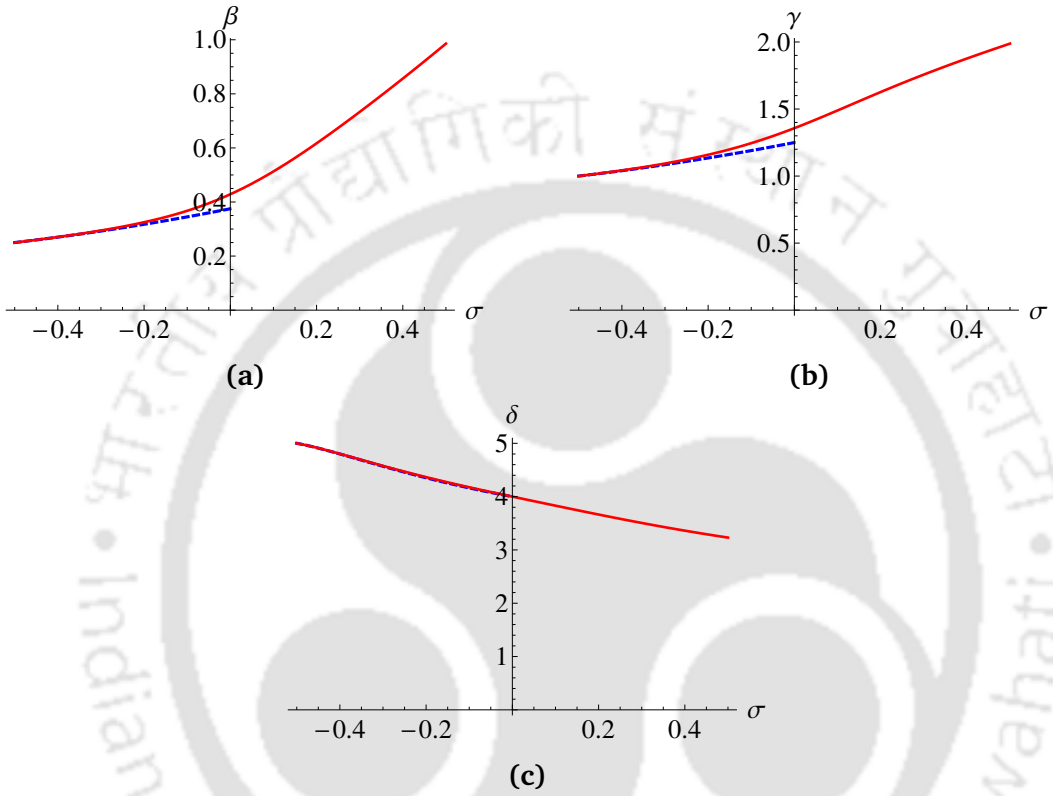

Figure 3.5: A comparison of the critical exponents in $d = 3$ obtained with (solid) and without (dotted) screening in the GL Hamiltonian. The results for the screening case are shown for $w = 0.001$ and $n = 3$.

To overcome this difficulty, in this Chapter we choose an alternative form, namely, $u(\mathbf{k}) = \lambda_0/(\mathbf{k}^2 + m^2)^\sigma$. The Feynman diagrams (Fig. 3.1(a) and Fig. 3.2(a)) which did not contribute in the previous case, now give relevant corrections and, as a result, the critical exponents turn out to be n dependant. As we have seen, Hamiltonian with this form of screened nonlocal coupling function possesses a stable non-trivial fixed point for $-0.5 < \sigma < 0.5$ in three dimensions. This extended range is solely attributed to the presence of screening in the model Hamiltonian.

In Fig. 3.5, we show a graphical comparison of the present result with our

previous results of Ch. 2. It is transparent from these plots that all the critical exponents have a wider range compared to those coming from without screening model. Thus the full experimental range, namely, $0.23 < \beta < 0.515$ is attainable only with screened nonlocal model Hamiltonian. Interestingly, we have seen [Table. 3.2] that the predictions of the screened nonlocal model Hamiltonian are in good agreement with experimental values of those samples having $\beta > 0.375$.

From the above comparison, one can conclude that the effect of screening in the nonlocal model Hamiltonian is to extend the range of stable non-trivial fixed point that, in turn, extends the range of critical exponents and, thus capability of capturing the widely varying universality classes in perovskite manganites.

3.7 Discussion and Conclusion

Employing Wilson's RG scheme, we investigated the critical behavior of a modified Ginzburg-Landau model [Eq. (3.2)] incorporating a nonlocal interaction in the quartic (Φ^4) term. We modelled the interaction term with a nonlocal character coupled with a screening parameter m and an exponent σ [Eq. (3.3)]. As a result, we obtained the renormalized corrections to the bare parameters r_0, c_0 and λ_0, in the model Hamiltonian. The ensuing RG flow equations led to the existence of a non-trivial fixed point and the marginal stability of the stable eigenvalue gave the upper critical dimension as $d_c = 4 + 2\sigma$. We calculated the critical exponents ν, η, α, β, γ, and δ at $O(\epsilon)$ via an ϵ-expansion in the parameter $\epsilon = d_c - d$ and found that the screening parameter $w = m^2/\Lambda^2$ plays some role in determining the critical exponents. However, the variations of the critical exponents with respect to w is slow as evident from the graphical plots of the exponents in Fig. 3.3. In addition, although the exponents ν, α, β, and γ undergo slight variations with n in the neighborhood of $\sigma = 0$ (as shown in Fig. 3.4), these variations are insignificant

compared to those of the short-range models, namely, 3D Ising and 3D Heisenberg.

We have compared our results with the experimentally available estimates for the critical exponents β, γ, and δ and found that our analytical estimates are in good agreement with those of the experiments for a wide variety of perovskite manganite samples including those showing tricritical mean field exponents. We can consider the agreements to be very good when we look at the nature of approximation involved in our RG calculations in that it is only at $O(\epsilon)$ and the higher order terms in ϵ are neglected. We have thus shown that the leading order in ϵ captures the correct trend of the critical exponents both near and away from tricriticality as observed experimentally in a wide range of perovskite manganite samples. We expect more exact agreements with the experimental numbers if we include the higher order terms in the ϵ-expansion. However, that would require a vast amount of calculations, probably up to four or five loop orders, so that a meaningful Borel summation [119] of the ϵ-expansion could be performed. We deem such detailed and exact calculation of critical exponents unnecessary at this stage as we are interested in identifying the correct form of the Hamiltonian capable of explaining the wide variety of universality classes of perovskite manganites. Since our RG results, at $O(\epsilon)$, have been able to capture a wide range of critical exponents comparable with experiments, it is fair to guess that the corresponding model Hamiltonian, given by Eqs. (3.2) and (3.3), contains a wide diversity of universality classes relevant to perovskite manganite samples.

It is interesting to note from the experiments that a change in doping level x as well as the elements (R and/or A) in the composition in perovskite manganites $R_{1-x}A_xMnO_3$ lead to different critical exponents. Different choices for R and A have different atomic sizes and therefore produce different internal stresses on the Mn-O-Mn bond [148,14,197]. This is characterized by the tolerance factor

$f = (\langle r_A \rangle + r_O)/[\sqrt{2}(r_{Mn} + r_O)]$ that compares the Mn–O separation with the separation of the oxygen atom and the A-site occupant. Thus, a change in either the doping level (x) or the tolerance factor (f) is found to lead to different universality classes (cf. Sec. 3.1.1). Our analytical calculations with the nonlocal model Hamiltonian are capable of reproducing the experimental results for different values of the nonlocal parameter σ, as shown in Table 3.2. It appears that the model parameter σ has a close connection with the experimental parameters x and f. However, finding this connection seems to pose further challenges because it requires the derivation of the nonlocal model Hamiltonian from a more microscopic Hamiltonian containing finer details that are to be eliminated as irrelevant degrees of freedom to arrive at the (less microscopic) nonlocal model Hamiltonian. This will be similar to the case of justifying the GL model for superconductivity from the microscopic BCS theory[73]. However, since our nonlocal model Hamiltonian captures a wide range of experimental observations, we shall not delve into such justification of the Hamiltonian from a more microscopic theory. This is in line with the notions and practices in condensed matter physics where detailed microscopic origins of model Hamiltonians are usually not deemed necessary.

We would also like to note that the experiments to study PM-FM phase transitions in perovskite manganites were based on four different techniques, namely, neutron scattering, dc magnetization, ac susceptibility, and specific heat measurements, followed by scaling analysis with Arrot plot, modified Arrot plot, Kouvel-Fisher formalism, and the study of critical isotherm. However, measurably different results were obtained from such experiments on $La_{0.7}Sr_{0.3}MnO_3$ [142,68,220,259] sample. Notably, four different sets of values for the critical exponents in the experiments were $\beta = 0.295 \pm 0.002$ in Ref. [142], $\beta = 0.37 \pm 0.04$, $\gamma = 1.22 \pm 0.03$, $\delta = 4.25 \pm 0.2$ in Ref. [68], $\beta = 0.45 \pm 0.01$, $\gamma = 1.2$, $\delta = 3.901$ in Ref. [220], and $\beta = 0.45 \pm 0.02$,

$\gamma = 1.08 \pm 0.04$ in Ref.[259], showing significant variations in the critical exponents for the same experimental sample. Similar disagreements between experimental results were also observed in the sample $La_{0.8}Ca_{0.2}MnO_3$ [92,114] for which $\beta = 0.36$, $\gamma = 1.45$, $\delta = 5.03$ in Ref.[92] and $\beta = 0.328$, $\gamma = 1.193$, $\delta = 4.826$ in Ref.[114]. Such disagreement was also observed for the case of $La_{0.7}Ca_{0.3}MnO_3$ [204,220] for which $\beta = 0.14$, $\gamma = 1.2$, $\delta = 1.22 \pm 0.02$ in Ref.[204] and $\beta = 0.36$, $\gamma = 1.2$ in Ref.[220] . This indicates that further experimental studies with high purity samples accompanied by more refined data analysis are required to rectify such experimental discrepancies.

In addition, we observe that the results $\beta = 0.5 \pm 0.02$, $\gamma = 1.08 \pm 0.03$, and $\delta = 3.13 \pm 0.20$ for $La_{0.8}Sr_{0.2}MnO_3$ [155] are close to mean-field results ($\beta = \frac{1}{2}$, $\gamma = 1$, and $\delta = 3$)[139]. We note that mean-field results cannot be reproduced by the present nonlocal theory. Since the present theory is an expansion about the tricritical point, it captures critical behavior near and around the tricritical point. Moreover, the results of Ref.[204] cannot be explained by the present theory as they deviate strongly from the Widom scaling law where the δ value is too low ($\delta = 1.22$), with $\beta = 0.14$ and $\gamma = 0.81$. Additionally, Ref.[103] presents the results for $La_{1-x}Ca_xMnO_3$ for $x = 0.21$ with unusual exponents $\beta = 0.09 \pm 0.01$, $\gamma = 1.71 \pm 0.1$, and $\delta = 20 \pm 1$. In contrast, it may be mentioned that for a slightly different value $x = 0.2$, this compound exhibits the usual behavior of perovskite manganites as observed in Refs.[92,114].

Finally, we would like to conclude by noting that the wide diversity in the critical behavior observed in perovskite manganites poses a challenging task for its description by means of a theoretical framework. As we have shown, within the context of GL model Hamiltonian with a nonlocal screened coupling in the quartic interaction term, it is possible to capture such diversity in the critical behavior

for a wide range of experimental samples. We hope that results of present Chapter would inspire further experimental work for further verification of the critical exponents.

Chapter 4

Critical Exponents for Mn-site Doped Perovskite Manganites

Summary

Various recent experiments indicate that the Mn-site doped perovskite manganites near the critical point of paramagnetic-to-ferromagnetic phase transition exhibit widely varying critical exponents which has no theoretical explanation. We show that the widely varying critical exponents of these compounds can be explained by employing the renormalization-group results of a nonlocal Ginzburg-Landau model where the quartic term involves a long-range screened interaction. It is shown for the first time that the predicted theoretical exponents agree well with the experimental estimates for a wide set of available measurements on Mn-site doped perovskite manganites.

4.1 Introduction

There has been a growing interest in perovskite manganites among the experimental researches and a lot of experimental data for their critical properties have already accumulated as discussed in the previous chapter (cf. Ch. 3). These com-

pounds belong to the group of highly correlated systems with a strong interrelation between charge, spin, and lattice degrees of freedom and they exhibit a wide variety of phases, namely, ferromagnetic, charge-ordered, antiferromagnetic, and orbital ordering. One of the important issues related to these materials is their critical behavior near their paramagnetic-to-ferromagnetic (PM-FM) phase transition points. Using molecular field theory, Kubo and Ohata[124] explained the dependence of the critical temperature (T_C) on charge carrier bandwidth and showed that the three-dimensional (3D) Heisenberg model is not adequate enough to represent the PM-FM phase transition in such systems. This inadequacy has also been confirmed from the existence of a wide diversity of critical exponents observed in an enormous number of experimental works on the critical behavior of perovskite manganites near the PM-FM phase transition (cf. Sec. 3.1.1).

Theoretical explanations for the transition from an insulating paramagnet to a metallic ferromagnet in manganese perovskites is usually based on the framework of spin-spin double exchange (DE) interaction[255] and electron-phonon Jahn-Teller (JT) coupling[102]. The itinerant spin-polarized electrons couple to the localized Mn^{4+} spin according to the Hund's rule such that, for ferromagnetic ordering the carrier can hop easily. This strong coupling between the charge carriers and the localized manganese moments although explain the origin of large magnetoresistance, it greatly overestimates the magnitude of both the conductivity and the critical temperature (T_c) and underestimates the magnetoresistance. To overcome these discrepancies, the polaronic effect due to a very strong electron-phonon JT coupling was incorporated[150,188] and the combined effect of DE and JT coupling was found to explain the metallic and insulating properties of colossal magnetoresistance (CMR) materials as well as the systematic variation of T_c with doping.

The strength of the DE interaction in manganese perovskites strongly depends

on the ratio Mn^{3+}/Mn^{4+} which can be altered by doping the direct Mn-site with $3d$ transition metals (e.g., Ti, V, Cr, Fe, Co, Ni, Zn, or Ga). In such systems, represented by $R_{1-x}A_xMn_{1-y}M_yO_3$ where M stands for transition metal elements, the interaction between Mn and M depends on whether M is magnetic or non-magnetic cation. For non-magnetic cations such as Ti, Zn, and Ga, there is no interaction between Mn and M whereas for magnetic cations such as Cr, Fe, Co, and Ni, Mn couples to neighbouring atoms by both antiferromagnetic super-exchange (SE) [72] and ferromagnetic DE mechanism. With increasing the doping concentration of magnetic cations, the DE bonds progressively break down, leading to a strong frustration and disorder into the spin system. As a result, there is a drastic change in the electronic and magnetic properties of such compounds. Recently, the critical behavior of such direct Mn-site doped perovskite manganites have been investigated in a number of experiments [248,86,250,165,67,20,45,46,191,178,153,177]. The experimental data indicate the existence of a wide range of critical exponents for varying doping level y as well as for varying doped metal element M, leading to a wide diversity of universality classes including tricriticality. So far, in most of the experimental works, the experimentally observed values of the critical exponents have been compared with the existing short-range models [139,107] as well as the LR model of Fisher *et al.* [57]. Experimental data suggested that the universality classes of direct Mn-site doped compounds differ from that of their parent compounds. For instance, in Ref. [165], it was observed from the MAP that with increasing doping concentration of non-magnetic Ga in $La_{0.75}(Sr,Ca)_{0.25}Mn_{1-y}Ga_yO_3$, the exponent β increases towards the mean field and the exponent γ decreases and approaches the 3D Ising value, while the parent undoped compounds exhibit a 3D Heisenberg like behavior. A similar trend was also observed in Ref. [46] where, increasing the doping level of Fe in $La_{0.7}Nd_{0.1}(CaSr)_{0.3}Mn_{1-y}Fe_yO_3$ samples led to a stronger

departure from the behavior observed in parent undoped compound.

The above situations indicate that a theoretical explanation for the wide diversity of critical exponents in Mn-site doped compounds is still missing and it is important to consider a theoretical model for this purpose. In Ch. 3, a nonlocal GL model was investigated from which a widely varying critical exponents were obtained for perovskite manganite samples for varying strengths of nonlocality. This model was found to captures satisfactorily the widely varying critical exponents measured in perovskite manganites for varying chemical compositions. This motivates us to explore here the critical properties of direct Mn-site doped perovskite manganite samples using the results of same nonlocal GL model employed in previous chapter. We find that the theoretically predicted critical exponents are in good agreement with the experimentally observed critical exponents. Thus this model offers a theoretical explanation for the critical exponents of Mn-site doped perovskite manganites.

4.2 Nonlocal Screened Model and Critical Exponents

In Ch. 3, we analytically treated a screened nonlocal model for an n-component order parameter $\Phi(\mathbf{x})$, expressed by the Hamiltonian in Fourier space

$$H = \sum_{i=1}^{n} \int \frac{d^d k}{(2\pi)^d} \frac{c_0 \mathbf{k}^2 + r_0}{2} |\phi_i(\mathbf{k})|^2 + \sum_{i=1}^{n} \sum_{j=1}^{n} \int\int\int \frac{d^d k_1}{(2\pi)^d} \frac{d^d k_2}{(2\pi)^d} \frac{d^d k_3}{(2\pi)^d} u(-\mathbf{k}_1 - \mathbf{k}_2)$$
$$\times \phi_i(\mathbf{k}_1)\phi_i(\mathbf{k}_2)\phi_j(\mathbf{k}_3)\phi_j(-\mathbf{k}_1 - \mathbf{k}_2 - \mathbf{k}_3), \tag{4.1}$$

with a screened nonlocal interaction represented by the coupling function

$$u(\mathbf{p}) = \frac{\lambda_0}{[\mathbf{p}^2 + m^2]^\sigma}, \tag{4.2}$$

where λ_0 is a coupling constant and m is a screening parameter.

We carried out the Wilson's momentum shell renormalization-group (RG) scheme at one-loop order on the above Fourier transformed model Hamiltonian [Eq. (4.1)] in the presence of the nonlocal coupling function [Eq. (4.2)]. The RG flow equations led us to the non-trivial fixed point $(r^*, \lambda^*, c^* = c)$. A linear stability analysis around that fixed point yields the eigenvalues y_1 and y_2 of the stability matrix. We identified the upper critical dimension d_c from the marginal stability of the stable eigenvalue y_2, giving $d_c = 4 - 2\sigma$. We thus calculated the critical exponents in an ϵ-expansion scheme with the identification $\epsilon = d_c - d$ and obtained

$$\beta = \frac{\sigma+1}{2} - \frac{\epsilon}{4}\left[1 + \frac{2\sigma(\sigma+2)}{(\sigma+2)\left[\frac{n}{w^\sigma}+4(1-\sigma w)\right]-4\sigma} - \frac{(\frac{n}{w^\sigma}+2)(2\sigma+2)}{\frac{n}{w^\sigma}+4(1-\sigma w)} \times \left\{\frac{1}{2} + \frac{2\sigma}{(\sigma+2)\left[\frac{n}{w^\sigma}+4(1-\sigma w)\right]-4\sigma}\right\}\right] + O(\epsilon^2), \tag{4.3}$$

$$\gamma = 1 + \frac{\epsilon(\frac{n}{w^\sigma}+2)}{\frac{n}{w^\sigma}+4(1-\sigma w)}\left[\frac{1}{2} + \frac{2\sigma}{(\sigma+2)\left[\frac{n}{w^\sigma}+4(1-\sigma w)\right]-4\sigma}\right] + O(\epsilon^2), \tag{4.4}$$

$$\delta = \frac{\sigma+3}{\sigma+1} + \frac{\epsilon}{\sigma+1}\left[\frac{1}{\sigma+1} + \frac{2\sigma(\sigma+2)}{(\sigma+1)\left[(\sigma+2)\left\{\frac{n}{w^\sigma}+4(1-\sigma w)\right\}-4\sigma\right]}\right] + O(\epsilon^2), \tag{4.5}$$

where $w = m^2/\Lambda^2$ is a dimensionless parameter.

4.3 Comparison with Experiments

In this section, we calculate the critical exponents predicted by Eqs. (4.3)–(4.5), and compare them with the experimental data for direct Mn-site doped perovskite manganites. While comparing, we first match the experimental value of β for a sample with our analytical results coming from Eq. (4.3) for a suitable value of σ. Using this value of σ, γ and δ values for the same sample are calculated from Eqs. (4.4) and (4.5) respectively. A detailed comparison of the theoretical predictions with the experimental data is given in Table 4.1. We see that, the predicted values

for the critical exponents β, γ, and δ agree well with the experimentally measured values and the available experimental critical exponents lie in the range $-0.499 < \sigma < 0.075$. Within this range of σ, the variation of the exponents are slow with respect to the model parameters w and n. We find that for the values of β, the corresponding values of γ and δ are close to those of experimental ones for $n = 3$ in three dimensions.

In Ref.[248] static magnetization measurements were performed on the ferromagnetic insulating system $LaMn_{1-y}Ti_yO_3$ for doping levels $y = 0.05, 0.1, 0.15, 0.2$. The values of the critical exponents, obtained via KF method and CI analysis, were $0.359 \leqslant \beta \leqslant 0.378$, $1.24 \leqslant \gamma \leqslant 1.29$, and $4.11 \leqslant \delta \leqslant 4.21$. However, it was suggested that the β values are Heisenberg-like and γ values are 3D Ising like. In fact, the 3D Heisenberg model[215], yields $\beta = 0.365 \pm 0.003$, $\gamma = 1.336 \pm 0.004$, $\delta = 4.80 \pm 0.04$ while the 3D Ising model[215] gives $\beta = 0.325 \pm 0.002$, $\gamma = 1.241 \pm 0.002$, and $\delta = 4.82 \pm 0.02$. Thus, one can see that the experimental values of δ, namely $4.11 \leqslant \delta \leqslant 4.21$, deviate much from that of both the 3D Heisenberg and 3D Ising models. In comparison, as displayed in Table 4.1, the present (nonlocal) model yields β, γ, and δ that are quite closer to the experimental predictions.

It is also important to note that, recently in Ref.[46], static magnetization measurements with MAP and CI analysis on the Fe-doped frustrated perovskite manganite samples $La_{0.6}Nd_{0.1}(Ca,Sr)_{0.3}Mn_{1-y}Fe_yO_3$ exhibited tricritical mean-field exponents for $y = 0.10$. A nearly tricritical behavior was also reported in Ref.[178] for the Ni-doped samples $La_{0.7}Ca_{0.3}Mn_{1-y}Ni_yO_3$ for $y = 0.09$ and $y = 0.12$. The present nonlocal model exhibits the interesting feature that it reproduces the tricritical mean-field behavior in three dimensions. The corresponding RG results are based on an $\epsilon = 4 - d + 2\sigma$ expansion about the tricritical mean-field and we obtain a wide range of critical exponents near and away from tricriticality by tuning the nonlo-

cal parameter σ. The critical exponents obtained for doping levels other than the above, namely $y = 0.05$ in Ref.[46] and $y = 0.15$ in Ref.[178] are away from tricritical mean-field and corresponding critical exponents are also in good agreement with our theoretical estimates, as displayed in Table 4.1.

In addition, the critical exponents for samples doped with iron[67], chromium [45,20], gallium[191,165], vanadium[153], and zinc[177] are also comparable with our analytical results as shown in Table 4.1. Corresponding to the experimental measurement in Ref.[67], the critical exponents for $La_{0.8}Ba_{0.2}Mn_{1-y}Fe_yO_3$ with $y = 0.15, 0.2$ obtained via KF method are in better agreement with our analytical estimates than that of 3D Heisenberg model. Further, the KF data of Ref.[165] for $La_{0.75}(Sr,Ca)_{0.25}Mn_{1-y}Ga_yO_3$, are also reproducible as shown in Table 4.1. In Ref.[20] it was suggested that for $y = 0.10$ the exponents are mean-field like while for $y = 0.15$ they are 3D Heisenberg-like. However, our models reproduces well these experimental values for different strength of nonlocality and they are comparatively closer than that of mean-field and 3D Heisenberg as displayed in Table 4.1. We see that, the experimental results of Ref.[20] for $y = 0.10$ are captured by our model for a positive value of σ, namely, $\sigma = 0.074$. Similarly, the results for Zn doped samples[177] are also reproducible for $\sigma = 0.057$.

It may be noted that, in most of the above mentioned experimental works, measurably different values for each of the critical exponents β and γ were obtained via MAP and KF methods. In our comparison table, we displayed only one set of values for each samples which matches well with our analytical estimates.

Table 4.1: Comparison of the theoretically predicted critical exponents β, γ, and δ with experimental estimates for various polycrystalline direct Mn-site doped perovskite manganite compounds. The experimental estimates for β and γ are obtained via Kouvel-Fisher (KF) method and modified Arrot plot (MAP) as indicated and the values of δ are obtained via critical isotherm (CI) analysis. The theoretical predictions follow from from Eqs. (4.3)–(4.5) for $n = d = 3$, and $w = 0.001$.

σ	Experimental sample	Ref.	β	γ	δ
-0.080			0.378	1.267	4.138
	$LaMn_{0.95}Ti_{0.05}O_3$ (KF)	[248]	0.378 ± 0.007	1.29 ± 0.02	4.19 ± 0.03
-0.085			0.375	1.260	4.148
	$LaMn_{0.90}Ti_{0.1}O_3$ (KF)	[248]	0.375 ± 0.005	1.25 ± 0.02	4.11 ± 0.04
-0.083			0.376	1.262	4.145
	$LaMn_{0.85}Ti_{0.15}O_3$ (KF)	[248]	0.376 ± 0.003	1.24 ± 0.01	4.16 ± 0.03
-0.117			0.359	1.229	4.206
	$LaMn_{0.80}Ti_{0.2}O_3$ (KF)	[248]	0.359 ± 0.004	1.28 ± 0.01	4.21 ± 0.05
-0.067			0.385	1.279	4.116
	$La_{0.75}Ca_{0.08}Sr_{0.17}Mn_{0.95}Ga_{0.05}O_3$ (KF)	[165]	0.385 ± 0.005	1.244 ± 0.004	4.12 ± 0.02
-0.001			0.428	1.356	4.002
	$La_{0.75}Ca_{0.08}Sr_{0.17}Mn_{0.90}Ga_{0.10}O_3$ (KF)	[165]	0.428 ± 0.005	1.286 ± 0.004	4.22 ± 0.04
-0.064			0.387	1.283	4.111
	$La_{0.67}Ca_{0.33}Mn_{0.90}Ga_{0.1}O_3$ (KF)	[191]	0.387 ± 0.006	1.362 ± 0.002	4.60 ± 0.03
-0.499			0.250	1.000	4.999
	$La_{0.7}Ca_{0.3}Mn_{0.01}Ni_{0.09}O_3$ (MAP)	[178]	0.171 ± 0.006	0.976 ± 0.012	6.7

σ	Experimental sample	Ref.	β	γ	δ
-0.440			0.262	1.024	4.889
	$La_{0.7}Ca_{0.3}Mn_{0.88}Ni_{0.12}O_3$ (MAP)	[178]	0.262 ± 0.005	0.979 ± 0.012	4.7
-0.214			0.320	1.149	4.394
	$La_{0.7}Ca_{0.3}Mn_{0.85}Ni_{0.15}O_3$ (MAP)	[178]	0.320 ± 0.009	0.990 ± 0.082	4.1
-0.206			0.323	1.154	4.377
	$La_{0.7}Ca_{0.2}Sr_{0.1}Mn_{0.85}Cr_{0.15}O_3$ (KF)	[45]	0.323 ± 0.04	1.22 ± 0.01	4.415 ± 0.02
-0.214			0.320	1.149	4.394
	$La_{0.7}Ca_{0.2}Sr_{0.1}Mn_{0.80}Cr_{0.20}O_3$ (KF)	[45]	0.320 ± 0.3	1.23 ± 0.2	5.05 ± 0.02
0.074			0.489	1.454	3.874
	$La_{0.65}Eu_{0.05}Sr_{0.3}Mn_{0.90}Cr_{0.10}O_3$ (MAP)	[20]	0.489 ± 0.04	1.17 ± 0.13	3.574
-0.064			0.387	1.283	4.111
	$La_{0.65}Eu_{0.05}Sr_{0.3}Mn_{0.85}Cr_{0.15}O_3$ (MAP)	[20]	0.387 ± 0.09	1.344 ± 0.03	4.459
-0.104			0.365	1.241	4.183
	$La_{0.6}Nd_{0.1}Ca_{0.15}Sr_{0.15}Mn_{0.95}Fe_{0.05}O_3$ (MAP)	[46]	0.365 ± 0.02	1.336 ± 0.0004	4.568 ± 0.054

σ	Experimental sample	Ref.	β	γ	δ
-0.499			0.250	1.000	4.999
	$La_{0.6}Nd_{0.1}Ca_{0.15}Sr_{0.15}Mn_{0.90}Fe_{0.10}O_3$ (MAP)	[46]	0.248 ± 0.001	0.998 ± 0.004	5.075 ± 0.040
-0.095			0.370	1.250	4.166
	$La_{0.8}Ba_{0.2}Mn_{0.85}Fe_{0.15}O_3$ (KF)	[67]	0.370 ± 0.002	1.359 ± 0.02	4.40 ± 0.03
-0.221			0.318	1.144	4.408
	$La_{0.8}Ba_{0.2}Mn_{0.80}Fe_{0.20}O_3$ (KF)	[67]	0.318 ± 0.02	1.159 ± 0.02	4.52 ± 0.03
-0.085			0.375	1.260	4.148
	$La_{0.67}Sr_{0.33}Mn_{0.85}V_{0.15}O_3$ (MAP)	[153]	0.375 ± 0.003	1.355 ± 0.006	4.347 ± 0.008
0.057			0.474	1.431	3.903
	$La_{0.7}Ca_{0.3}Mn_{0.9}Zn_{0.1}O_3$ (MAP)	[177]	0.474	1.152	3.425

4.4 A Discussion on Universality

We would like to note that, unlike in the standard (local) Φ^4 theory, the present critical exponents Eqs. (4.3), (4.4), (4.5) depend on the parameter σ and the dimensionless ratio $w = m^2/\Lambda^2$. This dependence emerges because the parameters σ, m and Λ occur in the model Hamiltonian [given by Eq. (4.1)]. Most simply, the dependence on m/Λ can be explained as follows. Unlike the Φ^4 model, the present model has three independent length scales, namely, the lattice constant (a), the range of interaction (m^{-1}), and the correlation length (ξ). Thus one can construct three independent dimensionless ratios, namely, a/ξ, m^{-1}/ξ and a/m^{-1}. Near the critical point, the first two ratios approach zero as $\xi \to \infty$. The third ratio $a/m^{-1} = m/\Lambda$ (because $\Lambda \sim a^{-1}$), being independent of temperature, remains finite near the critical point. Thus the critical properties of this new model depend on this dimensionless ratio m/Λ. As m/Λ remains finite at the critical point and σ is another parameter in the theory, the critical indices are found to depend on the values of σ and m/Λ. It is found that the critical indices vary slowly with respect to the parameter m/Λ whereas the variations with respect to σ are significant.

It is not surprising that the nonlocal model predicts critical exponents that vary with the parameters σ and $w = m^2/\Lambda^2$ as they occur in the model Hamiltonian. As a result, it produces a continuous set of universality classes different from that of the local Φ^4-theory. This situation is analogous to the case of Ashkin-Teller Potts model that yields critical exponents continuously varying with the parameter K_4 occurring in the Hamiltonian

$$H_{\mathrm{ATP}} = -J\sum_{nn} SS - K\sum_{nn} TT - K_4\sum_{nn} SSTT. \tag{4.6}$$

The line of critical points, does not need a revision of our basic ideas of renormalization-group, and universality[106,47], which is already a well accepted notion. We may

thus regard the cases with the same value of m/Λ to belong to a particular class wherein the variation of critical exponents with σ to different subclasses of universality.

Despite the fact that the present nonlocal model is capable of explaining satisfactorily the experimental exponents for perovskite manganites in addition to Mn-site doped manganese perovskites, the model has been attributed as falling in the same universality class as the local Φ^4 model[48]. This attribution is based on an ill-defined low momentum expansion in the interaction vertex. This low momentum expansion is invalid in the self-energy and vertex integrals that require a high momentum expansion (instead of a low momentum expansion) because the internal momenta in the loop-integrals are restricted in the high momentum band $\Lambda/b \leqslant q \leqslant \Lambda$. This has been explicitly proved in Ref.[209] where the self-energy and vertex integrals are shown to contain the vertex functions with high internal momentum q occurring inside the loop integrals so that they generate exactly the same self-energy and vertex corrections and hence the same critical exponents as in Ref.[205]. This shows that the nonlocal model does not belong to the universality class of the Φ^4 model and yields the same critical exponents as in Ref.[205] which have been employed in this Chapter to obtain critical exponents in agreement with the experimental ones for Mn-site doped manganese perovskites.

4.5 Conclusion

In this Chapter, we have shown that a nonlocal GL model Hamiltonian is capable of capturing the widely varying critical exponents for direct Mn-site doped perovskite manganite samples. The agreement of our present analytical estimates with experimental predictions indicates that the critical behavior near the PM-FM phase transition in such materials belong to the universality classes dictated by

the nonlocal GL model Hamiltonian [Eq. (4.1)]. Thus it signifies that the effective interactions among the modes of the order parameter in these systems have a nonlocal character near the critical point. This is expected because these systems posses a strong spin-lattice coupling that gives rise to a nonlocal character to the interaction as discussed earlier.

In addition to its success in explaining the varying critical exponents in perovskite manganites and Mn-site doped manganese perovskites it appears that our nonlocal model might provide an opportunity to study the partially understood physics of systems in which high density of electrons are strongly coupled to lattice and, in particular, to elucidate the critical behavior of systems where competing interactions of several electronic and lattice degrees of freedom lead to extremely rich and complex physics.

Chapter 5

Dynamic Critical Behavior of Perovskite Manganites

Summary

We investigate the nonconserved critical dynamics of a nonlocal model Hamiltonian incorporating screened long-range interactions in the quartic term. Employing dynamic renormalization-group analysis at one-loop order, we calculate the dynamic critical exponent $z = 2 + \epsilon f_1(\sigma, w, n) + O(\epsilon^2)$ and the linewidth exponent $\varpi = -\sigma + \epsilon f_2(\sigma, w, n) + O(\epsilon^2)$ in the leading order of ϵ, where $\epsilon = 4 - d + 2\sigma$, with d the space dimension, n the number of components in the order parameter, σ and w are parameters coming from the nonlocal interaction term. The resulting values of linewidth exponent ϖ for a wide range of σ is found to be in good agreement with the existing experimental estimates from spin relaxation measurements in perovskite manganite samples.

5.1 Introduction

The non-equilibrium dynamics of magnetic systems near the critical point received a continual attention for decades [77,78,80,79,81,89,146]. In a typical scenario, the system is quenched near the critical temperature T_c at time $t = 0$ from an equilibrium state away from T_c. A sudden quench near T_c causes the system to undergo a slow relaxation towards the new equilibrium state, refereed to as the critical slowing down. Theoretical models for the critical dynamics are usually based on a Langevin-type equation governed by the Ginzburg-Landau (GL) Hamiltonian for nonconserved or conserved order parameters [80,79,81,89,146]. These models elucidate the existence of various universality classes depending on the associated conservation laws and model parameters, namely, the number of components n of the order parameter and the space dimensionality d. In addition to the two independent static critical exponents [e.g., the correlation length exponent ν defined via $\xi \propto |T - T_c|^{-\nu}$ and the Fisher exponent η for the algebraic decay of the two point correlation function at criticality, $G(\mathbf{r} - \mathbf{r}') \propto |\mathbf{r} - \mathbf{r}'|^{-(d-2+\eta)}$], there exists a dynamic exponent z that governs the relaxation of the order parameter. The characteristic time scale diverges as $\tau \propto |T - T_c|^{-z\nu}$ upon approaching the transition point described as the the critical slowing down. Different values for z ensue depending on whether the order parameter is conserved and the existence of additional conserved quantities. The simplest cases among them are the purely relaxational models with either nonconserved (Model A) or conserved (Model B) order parameter Φ. The renormalization-group (RG) treatment for model A with short-range (SR) interactions gives $z = 2 + c\eta$ at two-loop order with $c = 6\ln(\frac{4}{3}) - 1$, yielding $z = 1.984$ in three dimensions [79,81,89].

While the above theoretical investigations were carried out for the model A with SR interactions, a long-range (LR) model was proposed by Fisher, Ma, and

Nickel[57] where the quadratic term in the model Hamiltonian was modified by incorporating LR interactions. Following this (LR) model, the corresponding non-conserved critical dynamics was investigated by Belim[19] in a field theoretic framework. Carrying out the calculations at two-loop order and employing the Padé-Borel resummation technique, it was found that the LR interaction affects the relaxation time of the system, indicated by the variation of z within the range $2.000072 \leqslant z \leqslant 2.006628$.

Recently, the perovskite manganites ($R_{1-x}A_xMnO_3$) have become the focus of scientific and technological interest as they exhibit colossal magnetoresistance (CMR)[148,68,14,197,42]. A number of experimental investigations on the critical slowing down of such compounds near the paramagnetic-to-ferromagnetic (PM-FM) phase transition were performed via a number of powerful techniques, namely, muon spin relaxation (μSR)[87,123] spectroscopy, inelastic-neutron-scattering[230], pump-probe method[133,132], and magnetic resonance methods[13,253]. In some of these experiments[133,132] the relaxation time exponent νz was measured for thin film samples while in some other experiments[123,13,253], the linewidth exponent $\varpi = \nu(z+2-d-\eta)$[79,90] was measured for bulk samples. In Ref.[123], μSR measurements were performed on a single crystal of $Nd_{0.5}Sr_{0.5}MnO_3$ exhibiting critical slowing down of Mn ion spin fluctuations in the critical paramagnetic regime. This facilitated the measurement of the linewidth exponent ϖ from the relaxation of the diffusive component, yielding $\varpi = 0.59 \pm 0.05$. Using the electron-paramagnetic resonance (EPR) technique, Atsarkin *et al.*[13] investigated the critical slowing down of longitudinal spin relaxation close to the PM-FM phase transition temperature T_c in $La_{1-x}Ca_xMnO_3$ for $x = 0.2$, 0.25, and 0.33. From the magnetic resonance linewidth measurements, they obtained the linewidth exponent $\varpi \approx 0.5$ for all samples. Using a similar experimental technique, Yassin *et al.*[253] measured ϖ

for $La_{0.67-2x}Nd_{2x}Ca_{0.33-x}Sr_xMnO_3$ with $x = 0$, 0.1, 0.15, 0.2, and 0.25 and found ϖ to be nearly a constant (≈ 0.5) for all samples. These spin relaxation experiments [123,13,253] indicate an interesting feature of perovskite manganite samples in the sense that the linewidth exponent ϖ near the critical point of PM-FM phase transition is close to $\varpi \approx 0.5$ independent of their chemical compositions (x, R, and A).

The theoretical explanations for the magnetic (and electrical) properties of perovskite manganites have so far been based on the framework of double exchange (DE) interaction [255,148,197] and electron-phonon Jahn-Teller (JT) coupling [102,148]. However, as discussed in Ref. [13], the above mentioned experimental results (namely, $w \approx 0.5$) contradict the predictions of the polaron hopping model based on JT lattice distortion, which was further confirmed in Ref. [253]. It was in fact suggested that the relaxation rate should increase near the critical temperature T_c due to the formation of conduction band [201,202]. Interestingly, Monte Carlo (MC) simulations have been performed [32,158,157,156,54] on a model Hamiltonian in the presence of DE interactions for the investigation of the static as well as dynamic critical behavior. These simulations yield $\nu = 0.6949 \pm 0.0038$, $\beta = 0.3535 \pm 0.0030$, $\gamma = 1.3909 \pm 0.0030$ in Ref. [32], $\beta \approx 0.365$ in Refs. [158,156], $\beta = 0.36 \pm 0.01$ in Ref. [157], and $\nu = 0.686 \pm 0.010$, $\beta = 0.356 \pm 0.006$, $z = 1.975 \pm 0.010$ in Ref. [54], which are close to 3D Heisenberg model with SR interactions. This suggests that the DE and 3D Heisenberg models [36,91] belong to the same universality class.

In addition to the above investigations, a considerable number of experimental studies have been conducted to find the static critical properties of doped perovskite manganite samples as elaborately discussed in Ch. 3. These studies indicate the existence of diverse universality classes in such materials in the sense that they exhibit widely varying values of the static critical indices near the critical point by

not only varying the doping level x but also by varying the sample composition R and/or A. In contrast, as discussed above, experiments on the dynamic critical behavior suggest an almost constant value for the linewidth exponent ϖ (≈ 0.5) although x, R, and A are varied in such samples. It can be guessed that such a strange critical behaviour cannot follow from the DE model because it belongs to the universality class of the SR Heisenberg model. Further, theoretical developments along the lines of the SR TDGL model [89] and its modified LR version [19] cannot be expected to reproduce their widely varying critical indices. This necessitates an alternative model capable of capturing the static as well as the dynamic critical exponents observed for experimental samples.

The static critical behavior of a nonlocal model Hamiltonian was studied by means of a Wilson type RG scheme in Ch. 3. The main distinguishing feature of the non-local model Hamiltonian was the incorporation of the LR interactions in the quartic term of the Ginzburg-Landau (GL) functional as $\int d^dx \int d^dx' \Phi^2(\mathbf{x}) u(\mathbf{x}-\mathbf{x}') \Phi^2(\mathbf{x}')$, where $u(\mathbf{x}-\mathbf{x}')$ is a nonlocal screened coupling function. Quite satisfactorily, this nonlocal model was found to represent a wide variety of universality classes corresponding to the static critical behavior of a wide range of perovskite manganite samples. This motivates us to investigate the dynamic critical behavior governed by this nonlocal model Hamiltonian in the spirit of Model A of Halperin and Hohenberg [80,89]. Through this nonlocal model Hamiltonian, we are particularly interested in capturing the dynamic critical behavior of perovskite manganites near the PM-FM phase transition.

In this Chapter, we write the nonconserved Langevin dynamics for the order parameter Φ governed by the above mentioned nonlocal model Hamiltonian. Employing dynamic RG calculations at one-loop order we obtain the dynamic exponent z and the linewidth exponent ϖ in the leading order of ϵ, where $\epsilon = 4-d+2\sigma$,

with d the space dimension and σ is a parameter occurring in the nonlocal interaction term. Interestingly, the linewidth exponent ϖ is found to be almost constant ($\varpi \approx 0.5$), although the static critical exponents vary with the nonlocal exponent σ in the range $-0.5 \leqslant \sigma \leqslant 0$. The critical exponents agree well with the available experimental estimates for different samples. This suggests that the nonlocal model Hamiltonian is a viable model for the critical behavior of PM-FM phase transition in perovskite manganites.

5.2 Nonlocal Unconserved Dynamics

The unconserved dynamics[80,89] of an n-component order parameter $\phi_i(\mathbf{x},t)$ is given by

$$\frac{\partial}{\partial t}\phi_i(\mathbf{x},t) = -\Gamma_0 \frac{\delta H}{\delta \phi_i(\mathbf{x},t)} + \eta_i(\mathbf{x},t), \tag{5.1}$$

where we incorporate nonlocal interactions in the quartic term of the GL free energy functional H as

$$H[\Phi] = \int d^d x dt \left[\frac{c_0}{2} |\nabla \Phi(\mathbf{x},t)|^2 + \frac{r_0}{2}\Phi^2(\mathbf{x},t) + \right.$$
$$\left. + \int d^d x' dt' \Phi^2(\mathbf{x},t) u(\mathbf{x}-\mathbf{x}') \delta(t-t') \Phi^2(\mathbf{x}',t') \right], \tag{5.2}$$

where d is the space dimension, $\Phi^2 = \sum_{i=1}^n \phi_i^2$, $|\nabla\Phi|^2 = \sum_{i=1}^n \nabla\phi_i \cdot \nabla\phi_i$ and $u(\mathbf{x}-\mathbf{x}')$ is the nonlocal coupling function. The term $\eta_i(\mathbf{x},t)$ represents a Gaussian white noise with zero mean and correlation

$$\langle \eta_i(\mathbf{x},t)\eta_j(\mathbf{x}',t')\rangle = 2\Gamma_0 \delta^d(\mathbf{x}-\mathbf{x}')\delta(t-t')\delta_{ij}. \tag{5.3}$$

Now using the $(d+1)$ dimensional Fourier transformation of the fields as

$$\psi_i(\mathbf{x},t) = \int \frac{d^d k}{(2\pi)^d} \frac{d\omega}{2\pi} \psi_i(\mathbf{k},\omega) e^{i(\mathbf{k}\cdot\mathbf{x}-\omega t)}, \tag{5.4}$$

where $\psi_i(\mathbf{x},t)$ is either $\phi_i(\mathbf{x},t)$, $\eta_i(\mathbf{x},t)$, or $u(\mathbf{x})$. With this definition, Eq. (5.1) can be portrayed in the Fourier space as

$$\phi_i(\mathbf{k},\omega) = \frac{G_0(\mathbf{k},\omega)\eta_i(\mathbf{k},\omega)}{\Gamma_0} - 4G_0(\mathbf{k},\omega)\sum_{j=1}^{n}\int\frac{d^dk_1}{(2\pi)^d}\frac{d\omega_1}{2\pi}\int\frac{d^dk_2}{(2\pi)^d}\frac{d\omega_2}{2\pi}u(\mathbf{k}_1-\mathbf{k})\phi_i(\mathbf{k}_1,\omega_1)$$

$$\times\,\phi_j(\mathbf{k}_2,\omega_2)\phi_j(\mathbf{k}-\mathbf{k}_1-\mathbf{k}_2,\omega-\omega_1-\omega_2), \tag{5.5}$$

where $G_0(\mathbf{k},\omega) = \left(\frac{-i\omega}{\Gamma_0} + r_0 + c_0k^2\right)^{-1}$ is the zeroth-order response function. We note that although the momentum integrations have a cut-off Λ, the frequency integrals run over all values from $-\infty$ to $+\infty$. Further, the noise-noise correlation in Fourier space is obtained as

$$\langle\eta_i(\mathbf{k},\omega)\eta_j(\mathbf{k}',\omega')\rangle = 2\Gamma_0(2\pi)^{d+1}\delta^d(\mathbf{k}+\mathbf{k}')\delta(\omega+\omega')\delta_{ij}. \tag{5.6}$$

5.3 Dynamic Renormalization-Group Calculation

In the static RG scheme, we began with the partition function and eliminated the fast modes $\phi_i^>(\mathbf{k})$ lying in the range $\Lambda/b \leqslant k \leqslant \Lambda$. We thus obtained a partition function in terms of the slow modes $\phi_i^<(\mathbf{k})$ lying in the range $0 < k < \Lambda/b$ with redefined model parameters. On the other hand, in the dynamic RG scheme, we perform the elimination of fast modes $\phi_i^>(\mathbf{k},\omega)$ directly from the Langevin-type equation. We solve the Langevin equation for the fast modes $\phi_i^>(\mathbf{k},\omega)$ and substitute this solution into the equation for slow modes $\phi_i^<(\mathbf{k},\omega)$. Subsequently we perform averaging over the fast modes of the noise $\eta_i^>(\mathbf{k},\omega)$, which is assumed to have a Gaussian statistics with the correlation given by Eq. (5.6). We further rescale the equation of motion for $\phi_i^<(\mathbf{k},\omega)$ so that it takes the same form as the original Langevin equation.

5.3.1 Self-energy Corrections

As mentioned above, we start with Eq. (5.5) and perform a dynamic RG analysis [139,89,146] at one-loop order. Decimation of scales from the momentum shell lying in the range $\frac{\Lambda}{b} \leqslant k \leqslant \Lambda$ (Λ being the ultraviolet cut-off) yields the equation of motion in the reduced range $0 < k < \frac{\Lambda}{b}$ as

$$\phi_i^<(\mathbf{k},\omega) = \frac{G_0^<(\mathbf{k},\omega)\eta_i^<(\mathbf{k},\omega)}{\Gamma_0} - 4G_0^<(\mathbf{k},\omega)\sum_{j=1}^{n}\int\frac{d^dk_1}{(2\pi)^d}\frac{d\omega_1}{2\pi}\int\frac{d^dk_2}{(2\pi)^d}\frac{d\omega_2}{2\pi}u(\mathbf{k}_1-\mathbf{k})$$
$$\times\,\phi_i^<(\mathbf{k}_1,\omega_1)\phi_j^<(\mathbf{k}_2,\omega_2)\phi_j^<(\mathbf{k}-\mathbf{k}_1-\mathbf{k}_2,\omega-\omega_1-\omega_2)$$
$$+\,G_0^<(\mathbf{k},\omega)R_i(\mathbf{k},\omega)+G_0^<(\mathbf{k},\omega)\Upsilon_i(\mathbf{k},\omega), \tag{5.7}$$

where

$$R_i(\mathbf{k},\omega) = -[\Sigma_a(\mathbf{0},0)+\Sigma_b(\mathbf{k},0)]\phi_i^<(\mathbf{k},\omega),$$

with the self-energy corrections (Fig. 5.1)

$$\Sigma_a(\mathbf{0},0) = \frac{8n}{\Gamma_0}\int\frac{d^dq}{(2\pi)^d}\frac{d\Omega}{2\pi}u(\mathbf{0})|G_0^>(\mathbf{q},\Omega)|^2, \tag{5.8}$$

$$\Sigma_b(\mathbf{k},0) = \frac{16}{\Gamma_0}\int\frac{d^dq}{(2\pi)^d}\frac{d\Omega}{2\pi}u(\mathbf{q}-\mathbf{k})|G_0^>(\mathbf{q},\Omega)|^2, \tag{5.9}$$

at one-loop order. We choose the form of the coupling function to be the same as that of the Ch. 3, given by

$$u(\mathbf{p}) = \frac{\lambda_0}{[\mathbf{p}^2+m^2]^\sigma} \tag{5.10}$$

where λ_0 is a coupling constant and m is a screening parameter.

In Eqs. (5.8) and (5.9) for the self-energy corrections, we first perform the Ω integrations. The integrands $\frac{1}{\left(\frac{-i\Omega}{\Gamma_0}+r_0+c_0q^2\right)\left(\frac{i\Omega}{\Gamma_0}+r_0+c_0q^2\right)}$ have one pole at the upper half plain and other at the lower half given by

$$\Omega = i\Gamma_0(c_0q^2+r_0), \tag{5.11}$$

and

$$\Omega = -i\Gamma_0(c_0 q^2 + r_0), \tag{5.12}$$

respectively. We choose the contour in the lower half plane to evaluate the residue

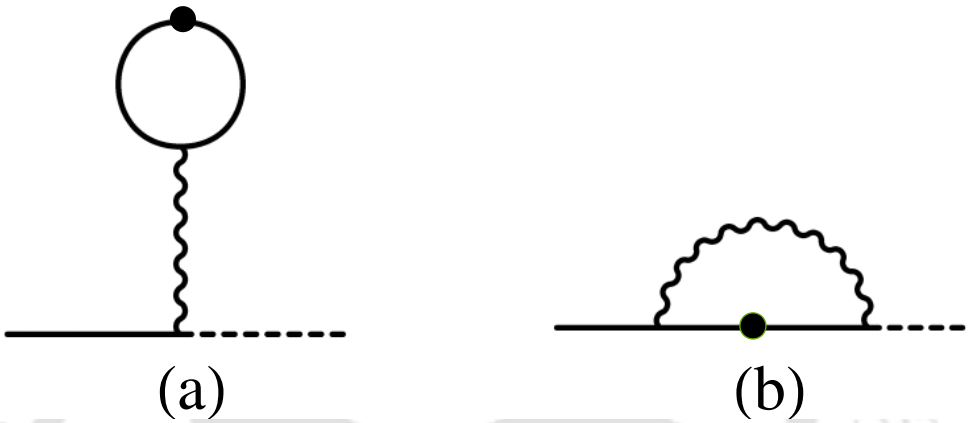

Figure 5.1: One-loop Feynman diagrams corresponding to the self energies (a) Σ_a and (b) Σ_b. Solid lines represent the propagator G_0, dashed lines the field ϕ_i, dots the noise correlation, and wiggly lines represent the nonlocal coupling $u(\mathbf{k})$.

at the pole. Residue at $\Omega = -i\Gamma_0(c_0 q^2 + r_0)$ is calculated as

$$\lim_{\Omega \to -i\Gamma_0(c_0 q^2 + r_0)} \Big(\Omega + i\Gamma_0(c_0 q^2 + r_0)\Big) \frac{1}{\left(\frac{-i\Omega}{\Gamma_0} + r_0 + c_0 q^2\right)\left(\frac{i\Omega}{\Gamma_0} + r_0 + c_0 q^2\right)}$$

$$= \frac{i\Gamma_0}{2(c_0 q^2 + r_0)}, \tag{5.13}$$

which yields

$$\int_{-\infty}^{+\infty} \frac{d\Omega}{2\pi} |G_0^{>}(\mathbf{q}, \Omega)|^2 = \frac{\Gamma_0}{2(c_0 q^2 + r_0)}. \tag{5.14}$$

Plugging this expression into the Eqs. (5.8) and (5.9) and performing the momentum integrations, we obtain

$$\Sigma_a(\mathbf{0}, 0) = \frac{4nS_d\lambda_0}{c_0 m^{2\sigma}[2\pi]^d}\left[\left(\frac{b^{2-d}-1}{2-d}\right)\Lambda^{d-2} - \frac{r_0}{c_0}\left(\frac{b^{4-d}-1}{4-d}\right)\Lambda^{d-4}\right], \tag{5.15}$$

$$\Sigma_b(\mathbf{k}, 0) = \frac{8S_d\lambda_0}{c_0[2\pi]^d}\left[\left(\frac{b^{2-d+2\sigma}-1}{2-d+2\sigma}\right)\Lambda^{d-2-2\sigma} - (\frac{r_0}{c_0} + \sigma m^2)\left(\frac{b^{4-d+2\sigma}-1}{4-d+2\sigma}\right)\Lambda^{d-4-2\sigma}\right]$$

$$+\frac{8S_d\lambda_0}{c_0[2\pi]^d}k^2\left[\frac{\sigma(2\sigma+2-d)}{d}\left(\frac{b^{4-d+2\sigma}-1}{4-d+2\sigma}\right)\Lambda^{d-4-2\sigma}\right], \tag{5.16}$$

in the large-scale and long-time limits ($k\to 0,\omega\to 0$), where $S_d = 2\pi^{d/2}/\Gamma(d/2)$ is the surface area of a unit sphere embedded in a d-dimensional space. These expressions for self-energy give rise to corrections Δr and Δc to the bare coefficients r_0 and c_0. To identify Δr and Δc, we see that the zeroth-order response function has modified as

$$(G^{(1)})^{-1}(\mathbf{k},\omega) = G_0^{-1}(\mathbf{k},\omega)+\Sigma_a(\mathbf{0},0)+\Sigma_b(\mathbf{k},0). \tag{5.17}$$

Using the explicit form of $G(\mathbf{k},\omega)$, we can write

$$\frac{-i\omega}{\Gamma^{(1)}}+r^{(1)}+c^{(1)}k^2 = \frac{-i\omega}{\Gamma_0}+r_0+c_0k^2+\Sigma_a(\mathbf{0},0)+\Sigma_b(\mathbf{k},0), \tag{5.18}$$

thus we obtain

$$r^{(1)} = r_0+\Delta r, \tag{5.19}$$

$$c^{(1)} = c_0+\Delta c, \tag{5.20}$$

and

$$\Gamma^{(1)} = \Gamma_0+\Delta\Gamma, \tag{5.21}$$

where

$$\Delta r = \frac{4nS_d\lambda_0}{c_0m^{2\sigma}[2\pi]^d}\left[\left(\frac{b^{2-d}-1}{2-d}\right)\Lambda^{d-2}-\frac{r_0}{c_0}\left(\frac{b^{4-d}-1}{4-d}\right)\Lambda^{d-4}\right]$$
$$+\frac{8S_d\lambda_0}{c_0[2\pi]^d}\left[\left(\frac{b^{2-d+2\sigma}-1}{2-d+2\sigma}\right)\Lambda^{d-2-2\sigma}-(\frac{r_0}{c_0}+\sigma m^2)\left(\frac{b^{4-d+2\sigma}-1}{4-d+2\sigma}\right)\Lambda^{d-4-2\sigma}\right], \tag{5.22}$$

$$\Delta c = \frac{8\sigma(2\sigma+2-d)S_d\lambda_0}{c_0d[2\pi]^d}\left(\frac{b^{4-d+2\sigma}-1}{4-d+2\sigma}\right)\Lambda^{d-4-2\sigma}, \tag{5.23}$$

and

$$\Delta\Gamma = 0. \tag{5.24}$$

We find that the noise amplitude Γ_0 does not acquire any correction at this order of calculation because $\frac{\partial\Sigma}{\partial(-i\omega)}\Big|_{\mathbf{k}=0,\omega=0} = 0$.

5.3.2 Vertex Corrections

Within the same calculational framework, we also obtain the relevant corrections to the bare nonlocal vertex λ_0 (Fig. 5.2) at one-loop order and obtain

$$\Upsilon_a = \frac{64n}{\Gamma_0}\sum_{j=1}^{n}\int\frac{d^dk_1d\omega_1}{[2\pi]^{d+1}}\int\frac{d^dk_2d\omega_2}{[2\pi]^{d+1}}u(\mathbf{k}_1-\mathbf{k})\phi_i^<(\mathbf{k}_1,\omega_1)\phi_j^<(\mathbf{k}_2,\omega_2)$$

$$\phi_j^<(\mathbf{k}-\mathbf{k}_1-\mathbf{k}_2,\omega-\omega_1-\omega_2)\int\frac{d^dqd\Omega}{[2\pi]^{d+1}}u(\mathbf{k}_1-\mathbf{k})|G_0^>(\mathbf{q},\Omega)|^2G_0^>(\mathbf{k}-\mathbf{k}_1-\mathbf{q},\omega-\omega_1-\Omega), \tag{5.25}$$

$$\Upsilon_b = \frac{256}{\Gamma_0}\sum_{j=1}^{n}\int\frac{d^dk_1d\omega_1}{[2\pi]^{d+1}}\int\frac{d^dk_2d\omega_2}{[2\pi]^{d+1}}u(\mathbf{k}_1-\mathbf{k})\phi_i^<(\mathbf{k}_1,\omega_1)\phi_j^<(\mathbf{k}_2,\omega_2)$$

$$\times\phi_j^<(\mathbf{k}-\mathbf{k}_1-\mathbf{k}_2,\omega-\omega_1-\omega_2)\int\frac{d^dqd\Omega}{[2\pi]^{d+1}}u(\mathbf{q}-\mathbf{k}+\mathbf{k}_1+\mathbf{k}_2)|G_0^>(\mathbf{q},\Omega)|^2$$

$$\times G_0^>(\mathbf{k}-\mathbf{k}_1-\mathbf{q},\omega-\omega_1-\Omega), \tag{5.26}$$

$$\Upsilon_c = \frac{256}{\Gamma_0}\sum_{j=1}^{n}\int\frac{d^dk_1d\omega_1}{[2\pi]^{d+1}}\int\frac{d^dk_2d\omega_2}{[2\pi]^{d+1}}\phi_i^<(\mathbf{k}_1,\omega_1)\phi_j^<(\mathbf{k}_2,\omega_2)$$

$$\times\phi_j^<(\mathbf{k}-\mathbf{k}_1-\mathbf{k}_2,\omega-\omega_1-\omega_2)\int\frac{d^dqd\Omega}{[2\pi]^{d+1}}u(\mathbf{q}-\mathbf{k})u(\mathbf{q}-\mathbf{k}_1)|G_0^>(\mathbf{q},\Omega)|^2$$

$$\times G_0^>(\mathbf{k}_1+\mathbf{k}_2-\mathbf{q},\omega_1+\omega_2-\Omega). \tag{5.27}$$

Plugging the form of $G_0(\mathbf{q},\Omega) = \left(\frac{-i\Omega}{\Gamma_0}+r_0+c_0q^2\right)^{-1}$ in the above expressions for Υ_a and Υ_b, we see that the integrands $\frac{1}{\left(\frac{-i\Omega}{\Gamma_0}+r_0+c_0q^2\right)\left(\frac{i\Omega}{\Gamma_0}+r_0+c_0q^2\right)^2}$ have double poles in the upper half plain and simple poles in the lower half plane given by

$$\Omega = i\Gamma_0(c_0q^2+r_0), \tag{5.28}$$

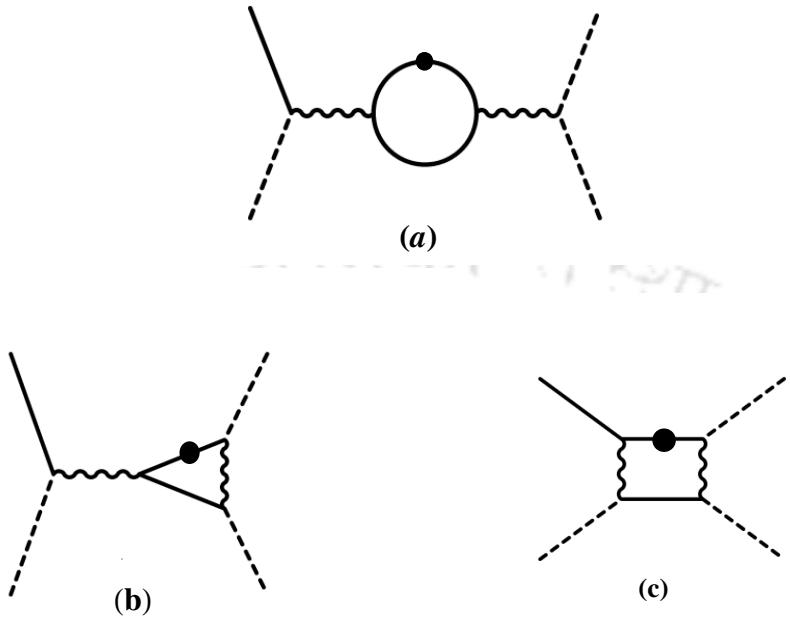

Figure 5.2: One-loop Feynman diagrams for the vertex $u(\mathbf{k}_1 - \mathbf{k})$. Figs. (a), (b), and (c) correspond to Υ_a, Υ_b, and Υ_c given in Eqs. (5.25)–(5.27). The various lines and the dots have the same meanings as in Fig. 5.1.

and

$$\Omega = -i\Gamma_0(c_0 q^2 + r_0), \tag{5.29}$$

respectively. We choose the contour in the lower half plane to evaluate the residue at the simple pole. Residue at $\Omega = -i\Gamma_0(cq^2 + r_0)$ is calculated as

$$\lim_{\Omega \to -i\Gamma_0(c_0 q^2 + r_0)} \Big(\Omega + i\Gamma_0(c_0 q^2 + r_0)\Big) \frac{1}{\Big(\frac{-i\Omega}{\Gamma_0} + r_0 + c_0 q^2\Big)\Big(\frac{i\Omega}{\Gamma_0} + r_0 + c_0 q^2\Big)^2}$$

$$= \frac{i\Gamma_0}{4(c_0 q^2 + r_0)^2}. \tag{5.30}$$

We thus have by the residue theorem

$$\int_{-\infty}^{+\infty} \frac{d\Omega}{2\pi} |G_0^>(\mathbf{q}, \Omega)|^2 G_0^>(-\mathbf{q}, -\Omega) = \frac{\Gamma_0}{4(c_0 q^2 + r_0)^2}. \tag{5.31}$$

Using this expression in Eqs. (5.25) and (5.26) and performing the momentum integrations, we calculate the correction to the nonlocal four-point vertex as

$$\lambda^{(1)} = \lambda_0 + \Delta\lambda, \tag{5.32}$$

where

$$\Delta\lambda = -\frac{4nS_d\lambda_0^2}{c_0^2 m^{2\sigma}[2\pi]^d}\left[\left(\frac{b^{4-d}-1}{4-d}\right)\Lambda^{d-4} - \frac{2r_0}{c_0}\left(\frac{b^{6-d}-1}{6-d}\right)\Lambda^{d-6}\right]$$
$$-\frac{16S_d\lambda_0^2}{c_0^2[2\pi]^d}\left[\left(\frac{b^{4-d+2\sigma}-1}{4-d+2\sigma}\right)\Lambda^{d-4-2\sigma} - \left(\frac{2r_0}{c_0}+\sigma m^2\right)\left(\frac{b^{6-d+2\sigma}-1}{6-d+2\sigma}\right)\Lambda^{d-6-2\sigma}\right], \tag{5.33}$$

in the large scale long time limit ($\mathbf{k}\to 0$, $\omega\to 0$). We note that Υ_c does not share the same momentum dependence as in Eq. (5.5) for the nonlocal vertex and hence it does not contribute to $\Delta\lambda$.

5.3.3 Rescaling

The next step is to carry out a rescaling on the coarse-grained dynamical equation [Eq. (5.7)]. We thus relabel

$$\begin{aligned}\mathbf{k}' &= b\mathbf{k},\\ \omega' &= b^z\omega,\\ \Phi'(\mathbf{k}',\omega') &= \zeta^{-1}\Phi^<(\mathbf{k},\omega).\end{aligned} \tag{5.34}$$

With these transformations the response function is rescaled as

$$G(\mathbf{k},\omega) = \left(\frac{-i\omega'}{b^z\Gamma_0} + r^{(1)} + c^{(1)}b^{-2}k'^2\right)^{-1}. \tag{5.35}$$

Assuming $\Gamma' = b^y\Gamma_0$, the explicit form of y is derived below. We can write

$$G(\mathbf{k},\omega) = G'(\mathbf{k}',\omega')b^{z-y}, \tag{5.36}$$

with

$$r' = b^{z-y} r^{(1)}, \tag{5.37}$$

and

$$c' = b^{z-2-y} c^{(1)}. \tag{5.38}$$

Using Eqs. (5.34) and (5.36), we write the coarse-grained dynamical equation as

$$\phi_i'(\mathbf{k}',\omega') = \frac{G^{'}(\mathbf{k}',\omega')\zeta^{-1}\eta_i(\mathbf{k},\omega)b^{z-y}}{\Gamma' b^{-y}} - 4\frac{G^{'}(\mathbf{k}',\omega')\zeta^2 b^{z-y+2\sigma}}{b^{2d+2z}} \int \frac{d^d k_1'}{(2\pi)^d}\frac{d\omega_1'}{2\pi}\int \frac{d^d k_2'}{(2\pi)^d}\frac{d\omega_2'}{2\pi}$$

$$\frac{\lambda^{(1)}}{((\mathbf{k}_1'-\mathbf{k}')^2+m'^2)^\sigma}\phi_i'(\mathbf{k}_1',\omega_1')\phi_j'(\mathbf{k}_2',\omega_2')\phi_j'(\mathbf{k}'-\mathbf{k}_1'-\mathbf{k}_2',\omega'-\omega_1'-\omega_2'). \tag{5.39}$$

With the rescale noise and coupling constants the above equation becomes

$$\phi_i'(\mathbf{k}',\omega') = \frac{\eta_i'(\mathbf{k}',\omega')G_0'(\mathbf{k}',\omega')}{\Gamma'} - 4\int \frac{d^d k_1'}{(2\pi)^d}\frac{d\omega_1'}{2\pi}\int \frac{d^d k_2'}{(2\pi)^d}\frac{d\omega_2{}'}{2\pi}$$

$$\frac{\lambda'}{((\mathbf{k}_1'-\mathbf{k}')^2+m'^2)^\sigma}\phi_i'(\mathbf{k}_1',\omega_1')\phi_j'(\mathbf{k}_2',\omega_2')\phi_j'(\mathbf{k}'-\mathbf{k}_1'-\mathbf{k}_2',\omega'-\omega_1'-\omega_2'), \tag{5.40}$$

where

$$\eta_i'(\mathbf{k}',\omega') = \zeta^{-1}b^z\eta_i(\mathbf{k},\omega), \tag{5.41}$$

$$\lambda' = \frac{\zeta^2 b^{z-y+2\sigma}}{b^{2d+2z}}\lambda^{(1)}. \tag{5.42}$$

The scale factor ζ can be calculated by looking at the rescaled field-field correlation

$$\langle\phi_i'(\mathbf{k}_1',\omega_1')\phi_j'(\mathbf{k}_2',\omega_2')\rangle = C'(\mathbf{k}_1',\omega_1')(2\pi)^{d+1}\delta^d(\mathbf{k}_1'+\mathbf{k}_2')\delta(\omega_1'+\omega_2')\delta_{ij}, \tag{5.43}$$

where $C'(\mathbf{k}_1',\omega_1')$ is coarse grained time-correlation function. Using the dynamic scaling[139,146] $C(\mathbf{q},\omega;X(T_c)) = \left(\frac{\Lambda}{q}\right)^{2-\eta+z} C(\Lambda,\omega\left(\frac{q}{\Lambda}\right)^{-z};X^*)$ for the correlation function, we obtain the field rescaling factor as

$$\zeta = b^{1+\frac{d}{2}+z-\frac{\eta}{2}}. \tag{5.44}$$

Further, in order to calculate the explicit form of y, we consider the noise-noise correlation for coarse grained η as

$$\langle \eta_i'(\mathbf{k}_1',\omega_1')\eta_j'(\mathbf{k}_2',\omega_2')\rangle = 2\Gamma'(2\pi)^{d+1}\delta^d(\mathbf{k}_1'+\mathbf{k}_2')\delta(\omega_1'+\omega_2')\delta_{ij}. \tag{5.45}$$

This together with Eqs. (5.41) and (5.44) yields

$$y = z-2+\eta. \tag{5.46}$$

5.4 Flow Equations and Fixed Point

Using Eqs. (5.44) and (5.46) in Eqs. (5.37), (5.38), and (5.42) we obtain

$$\Gamma' = b^{z-2+\eta}(\Gamma_0+\Delta\Gamma), \tag{5.47}$$

$$r' = b^{2-\eta}(r_0+\Delta r), \tag{5.48}$$

$$c' = b^{-\eta}(c_0+\Delta c), \tag{5.49}$$

$$\lambda' = b^{4-d+2\sigma-2\eta}(\lambda_0+\Delta\lambda). \tag{5.50}$$

Thus, incorporating the corrections to r_0, c_0, and λ_0 given by Eqs. (5.22), (5.23), and (5.33), we obtain the final form for the RG recursion relations as

$$\Gamma' = b^{z-2+\eta}\Gamma_0. \tag{5.51}$$

$$\begin{aligned} r' = b^{2-\eta}\Bigg[r_0 + \frac{4n\lambda_0 S_d}{m^{2\sigma}[2\pi]^d}\left\{\frac{(b^{2-d}-1)\Lambda^{d-2}}{c_0(2-d)} - \frac{r_0}{c_0^2}\frac{(b^{4-d}-1)\Lambda^{d-4}}{(4-d)}\right\} \\ + \frac{8\lambda_0 S_d}{[2\pi]^d}\left\{\frac{(b^{2\sigma+2-d}-1)\Lambda^{d-2\sigma-2}}{c_0(2\sigma+2-d)} - \left(\frac{r_0}{c_0^2}+\frac{\sigma m^2}{c_0}\right)\frac{(b^{2\sigma+4-d}-1)\Lambda^{d-2\sigma-4}}{(2\sigma+4-d)}\right\}\Bigg], \end{aligned} \tag{5.52}$$

$$c' = b^{-\eta}\left[c_0 + \frac{8\sigma(2-d+2\sigma)\lambda_0 S_d}{d[2\pi]^d}\left\{\frac{(b^{4-d+2\sigma}-1)\Lambda^{d-4-2\sigma}}{c(4-d+2\sigma)}\right\}\right], \tag{5.53}$$

$$\lambda' = b^{4-d-2\eta+2\sigma}\left[\lambda_0 - \frac{4n\lambda_0^2}{m^{2\sigma}}\frac{S_d}{[2\pi]^d}\left\{\frac{(b^{4-d}-1)\Lambda^{d-4}}{c_0^2(4-d)} - \frac{2r_0}{c_0^3}\frac{(b^{6-d}-1)\Lambda^{d-6}}{(6-d)}\right\}\right.$$
$$\left. - \frac{16\lambda_0^2 S_d}{[2\pi]^d}\left\{\frac{(b^{4-d+2\sigma}-1)\Lambda^{d-4-2\sigma}}{c_0^2(4-d+2\sigma)} - \left(\frac{\sigma m^2}{c_0^2}+\frac{2r_0}{c_0^3}\right)\frac{(b^{6-d+2\sigma}-1)\Lambda^{d-6-2\sigma}}{(6-d+2\sigma)}\right\}\right]. \tag{5.54}$$

Assuming $b = e^{\delta l}$ in the above recursion relations in the limit of $\delta l \to 0$, we construct the continuous RG flow equations as

$$\frac{d\Gamma}{dl} = (z-2+\eta)\Gamma, \tag{5.55}$$

$$\begin{aligned}\frac{dr}{dl} &= (2-\eta)r + \frac{4n\lambda S_d}{m^{2\sigma}(2\pi)^d}\left(\frac{\Lambda^{d-2}}{c} - \frac{r}{c^2}\Lambda^{d-4}\right)\\ &\quad + \frac{8\lambda S_d}{(2\pi)^d}\left[\frac{\Lambda^{d-2-2\sigma}}{c} - \left(\frac{r}{c^2}+\frac{\sigma m^2}{c}\right)\Lambda^{d-4-2\sigma}\right],\end{aligned} \tag{5.56}$$

$$\frac{dc}{dl} = -\eta c + \frac{8\sigma(2\sigma+2-d)\lambda S_d}{d(2\pi)^d}\frac{\Lambda^{d-4-2\sigma}}{c}, \tag{5.57}$$

and

$$\begin{aligned}\frac{d\lambda}{dl} &= (4-d-2\eta+2\sigma)\lambda - \frac{4n\lambda^2 S_d}{m^{2\sigma}(2\pi)^d}\left(\frac{\Lambda^{d-4}}{c^2} - \frac{2r}{c^3}\Lambda^{d-6}\right)\\ &\quad - \frac{16\lambda^2 S_d}{(2\pi)^d}\left[\frac{\Lambda^{d-4-2\sigma}}{c^2} - \left(\frac{2r}{c^3}+\frac{\sigma m^2}{c^2}\right)\Lambda^{d-6-2\sigma}\right].\end{aligned} \tag{5.58}$$

These RG flow equations suggest the existence of a non-trivial fixed point $r \to r^*$, $\lambda \to \lambda^*$, $c \to c^* = c$, and $\Gamma_0 \to \Gamma_0^* = \Gamma_0$, corresponding to

$$\frac{r^*}{c} = -\frac{(4-d-2\eta+2\sigma)\left\{\frac{n}{w^\sigma}+2(1-\sigma w)\right\}\Lambda^2}{(2-\eta)\left\{\frac{n}{w^\sigma}+4(1-\sigma w)\right\} - (4-d-2\eta+2\sigma)(\frac{n}{w^\sigma}+2)}, \tag{5.59}$$

and

$$\frac{\lambda^*}{c^2} = \frac{(4-d-2\eta+2\sigma)\Lambda^{4-d+2\sigma}}{\frac{S_d}{(2\pi)^d}\left\{\frac{4n}{w^\sigma}+16(1-\sigma w)\right\}}, \tag{5.60}$$

where $w = m^2/\Lambda^2$ is a redefined screening parameter. Linearizing Eqs. (5.56) and (5.58) about this fixed point yields the eigenvalues y_1 and y_2 of the stability matrix as

$$y_1 = 2 - \eta - (4 - d - 2\eta + 2\sigma)\frac{(\frac{4n}{w^\sigma} + 8)}{\left[\frac{4n}{w^\sigma} + 16(1 - \sigma w)\right]}, \tag{5.61}$$

and

$$y_2 = d - 4 + 2\eta - 2\sigma. \tag{5.62}$$

This Indicates that the above fixed point is stable for values of σ lying in the range $-0.5 \leqslant \sigma \leqslant 0.5$ in three dimensions. Further, the upper critical dimension d_c turns out to be

$$d_c = 4 + 2\sigma. \tag{5.63}$$

It may be noted that these results are consistent with our static RG analysis presented in Ch. 3.

5.5 Critical Exponents

From Eq. (5.57), the Fisher exponent η can be calculated in the leading order of $\epsilon = d_c - d$ as

$$\eta = -\frac{2\sigma\epsilon}{(\sigma + 2)\left[\frac{n}{w^\sigma} + 4(1 - \sigma w)\right] - 4\sigma} + O(\epsilon^2). \tag{5.64}$$

Eq. (5.55) yields the dynamic critical exponent z as $z = 2 - \eta$, giving

$$z = 2 + \frac{2\sigma\epsilon}{(\sigma + 2)\left[\frac{n}{w^\sigma} + 4(1 - \sigma w)\right] - 4\sigma} + O(\epsilon^2). \tag{5.65}$$

Thus, we find $z = 2 + \epsilon f_1(\sigma, w, n) + O(\epsilon^2)$. In Fig. 5.3, we display the variations of z with (a) order parameter components n and (b) screening parameter w in the physically allowed range of σ in three dimensions. In Fig. 5.3a, we show the variations of z with n for $w = 0.001$ while in Fig. 5.3b we show the variation of z

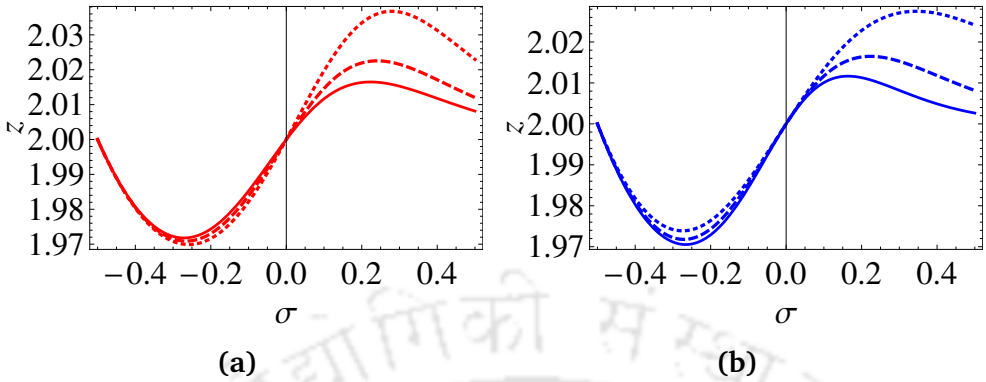

Figure 5.3: Plots for $z = 2 + \epsilon f_1(\sigma, w, n) + O(\epsilon^2)$. Fig. (a) shows the variation of z with n for $w = 0.001$ and Fig. (b) shows the variation of z with w for $n = 3$ in $d = 3$. The dotted, dashed, and solid curves correspond to $n = 1, 2, 3$ in Fig. (a), and $w = 0.0001, 0.001, 0.01$ in Fig. (b).

with w for $n = 3$. These plots clearly show that the dynamic exponent z undergoes negligible variation with respect to n and w in the negative regime of σ including the region near $\sigma \approx 0$.

It may be noted that, similar to the original model A dynamics with SR Φ^4 potential, the present LR model does not give any relevant RG corrections to the noise amplitude Γ_0 at one-loop order. However, due to the incorporation of nonlocal coupling function $u(\mathbf{k})$, we obtain a non-zero correction to η at one-loop order in the leading order of ϵ. Thus, it is the renormalization of η that leads to strikingly different long-range dependent results for the dynamic exponent z. We find that the value of z lies in the range $1.972 \leqslant z \leqslant 2.016$ for $n = d = 3$.

In order to calculate the linewidth exponent ϖ, given by the scaling relation $\varpi = \nu(z + 2 - d - \eta) = \nu(4 - d - 2\eta)$, we calculate the correlation length exponent ν from y_1 as $\nu = 1/y_1$, and obtain

$$\nu = \frac{1}{2} + \frac{\epsilon(\frac{n}{w^\sigma} + 2)}{2\left(\frac{n}{w^\sigma} + 4(1 - \sigma w)\right)} \left\{ \frac{1}{2} + \frac{2\sigma}{(\sigma + 2)\left[\frac{n}{w^\sigma} + 4(1 - \sigma w)\right] - 4\sigma} \right\}$$
$$- \frac{\sigma\epsilon}{2(\sigma + 2)\left[\frac{n}{w^\sigma} + 4(1 - \sigma w)\right] - 8\sigma} + O(\epsilon^2). \tag{5.66}$$

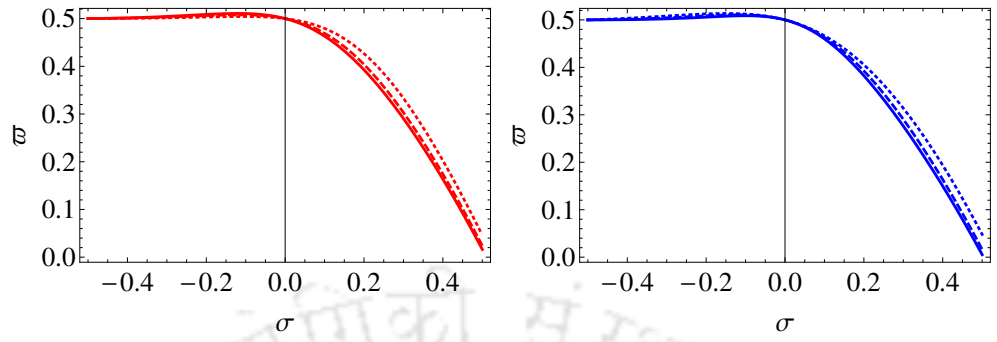

Figure 5.4: Plots for $\varpi = -\sigma + \epsilon f_2(\sigma,\kappa,n) + O(\epsilon^2)$. Fig. (a) shows the variation of ϖ with n for $w = 0.001$ and Fig. (b) shows the variation of ϖ with w for $n = 3$ in $d = 3$. The dotted, dashed, and solid curves correspond to $n = 1,2,3$ in Fig. (a), and $w = 0.0001, 0.001, 0.01$ in Fig. (b).

This together with Eq. (5.64) yield

$$\varpi = -\sigma + \epsilon\left[\frac{1}{2} + \frac{\sigma}{(\sigma+2)\left\{\frac{n}{w^\sigma}+4(1-\sigma w)\right\}-4\sigma}\left\{(2+\sigma) - \frac{2\sigma(\frac{n}{w^\sigma}+2)}{\left\{\frac{n}{w^\sigma}+4(1-\sigma w)\right\}}\right\}\right]$$
$$-\epsilon\left[\frac{\sigma(\frac{n}{w^\sigma}+2)}{2\left\{\frac{n}{w^\sigma}+4(1-\sigma w)\right\}}\right] + O(\epsilon^2). \tag{5.67}$$

In Fig. 5.4, we display the variations of ϖ with (a) n and (b) w in three dimensions. In Fig. 5.4a, we show the variations of ϖ with n for $w = 0.001$ while in Fig. 5.4b we show the variation of ϖ with w for $n = 3$. These plots clearly show that the dependence on n and w of the linewidth exponent ϖ is insignificant and, interestingly, $\varpi \approx 0.5$ in the range $-0.5 < \sigma < 0$. Further, the exponent νz, related to the characteristic time scale as $\tau \propto |T - T_c|^{-z\nu}$, is obtain as

$$\nu z = 1 + \frac{\epsilon(\frac{n}{w^\sigma}+2)}{\left\{\frac{n}{w^\sigma}+4(1-\sigma w)\right\}}\left\{\frac{1}{2} + \frac{2\sigma}{(\sigma+2)\left[\frac{n}{w^\sigma}+4(1-\sigma w)\right]-4\sigma}\right\} + O(\epsilon^2), \tag{5.68}$$

The other static critical exponents, namely, the spontaneous magnetization exponent β, susceptibility exponent γ, and critical isotherm exponent δ, can be obtained by using the expressions for η and ν from Eqs. (5.64) and (5.66) in the well-known

scaling relations. This yields

$$\beta = \frac{\sigma+1}{2} - \frac{\epsilon}{4}\left[1 + \frac{2\sigma(\sigma+2)}{(\sigma+2)\left[\frac{n}{w^\sigma}+4(1-\sigma w)\right]-4\sigma} - \frac{(\frac{n}{w^\sigma}+2)(2\sigma+2)}{\frac{n}{w^\sigma}+4(1-\sigma w)} \times \right.$$
$$\left. \times \left\{\frac{1}{2} + \frac{2\sigma}{(\sigma+2)\left[\frac{n}{w^\sigma}+4(1-\sigma w)\right]-4\sigma}\right\}\right] + O(\epsilon^2), \quad (5.69)$$

$$\gamma = 1 + \frac{\epsilon(\frac{n}{w^\sigma}+2)}{\frac{n}{w^\sigma}+4(1-\sigma w)}\left[\frac{1}{2} + \frac{2\sigma}{(\sigma+2)\left[\frac{n}{w^\sigma}+4(1-\sigma w)\right]-4\sigma}\right] + O(\epsilon^2), \quad (5.70)$$

and

$$\delta = \frac{\sigma+3}{\sigma+1} + \frac{\epsilon}{\sigma+1}\left[\frac{1}{\sigma+1} + \frac{2\sigma(\sigma+2)}{(\sigma+1)\left[(\sigma+2)\left\{\frac{n}{w^\sigma}+4(1-\sigma w)\right\}-4\sigma\right]}\right] + O(\epsilon^2). \quad (5.71)$$

We note that the expressions for η and ν obtained from the dynamic RG analysis presented in this chapter are consistent with those obtained from the static RG analysis presented in Ch. 3. Consequently, the expressions for β, γ, and δ turn out to be in agreement with the previous calculations.

5.6 Comparison with Experiments

As noted earlier, in recent experimental studies on the critical behavior of perovskite manganites [123,13,253,133,132], the relaxation rate of the system near the critical point has been measured by various techniques. In Table 5.1 and 5.2, we display the experimental results and compare them with our calculated results. To compare the results, we first match the experimental value of β with our theoretical estimate from Eq. (5.69) by tuning the long-range exponent σ. For the same value of σ, we then calculate the other exponents, namely γ, δ, z, w, and νz from

Eqs. (5.70), (5.71), (5.65), (5.67), and (5.68), respectively.

Atsarkin *et al.* [13] investigated the critical slowing down of longitudinal spin relaxation close to the PM-FM critical point T_c in $La_{1-x}Ca_xMnO_3$ for $x = 0.2$, 0.25, 0.33. It is interesting to note that they measured the exponent $\varpi \approx 0.5$ for all those samples from EPR linewidth measurements. Using a similar experimental technique, Yassin *et al.* [253] also obtained the same value ($\varpi \approx 0.5$) for a wide range of doping levels x in $La_{0.67-2x}Nd_{2x}Ca_{0.33-x}Sr_xMnO_3$, namely, $x = 0$, 0.1, 0.15, 0.2, and 0.25. These experimental estimates for ϖ are in excellent agreement with our calculated results for ϖ in the range $-0.5 < \sigma < 0$ as shown in Fig. 5.4. Thus the nonlocal model Hamiltonian governing the critical dynamics correctly captures the trend of a constant value of ϖ for a wide range of σ akin to the wide range of x in the experimental samples. This trend appears to be true for different constituent R and A in perovskite manganites. In addition, we see from Table 5.1 that the values of β, γ, and δ for $\sigma = -0.193$ are in close agreement for the sample $La_{1-x}Ca_xMnO_3$ with $x = 0.2$ [114]. For $x = 0.33$, the β value is available in Ref. [87] and we display it in Table 5.1. For the other doping level, namely, $x = 0.25$, the experimental estimates for static critical exponents are not available at present. Similarly, the static critical exponents for the samples $La_{0.67-2x}Nd_{2x}Ca_{0.33-x}Sr_xMnO_3$ studied in Ref. [253], are not available except for $x = 0$ [87].

Krishnamurthy *et al.* [123] performed μSR experiment and studied the critical slowing down of Mn ion spin fluctuations in the critical paramagnetic regime in single crystal $Nd_{0.5}Sr_{0.5}MnO_3$ and obtained $\varpi = 0.59 \pm 0.05$. From this value of ϖ, they estimated the value $z = 2.00 \pm 0.12$ from the scaling law $\varpi = \nu(z + 2 - d - \eta)$, where the value $\nu = 0.61 \pm 0.02$ was taken from another experiment [190] and $\eta = 0.031 \pm 0.004$ from the RG calculation of model C [90]. In addition to the linewidth exponent ϖ, they [123] also measured the static critical exponents β, γ, and δ. Here

we compare them with our results and find that although there is a slight departure in the ϖ value, the values for z, β, γ, and δ are in good agreement.

In a few other experiments on perovskite manganites [133,132], direct observational values for z and ϖ are not available. For example, Liu *et al.* [133,132] measured the relaxation time exponent $\nu z = 1.39$ for the thin film samples $La_{0.7}Sr_{0.3}MnO_3$ and $La_{0.7}Ca_{0.3}MnO_3$. Based on the closeness of this experimental value with the prediction of the 3D Heisenberg model, they concluded that the critical behavior of both the samples should be governed by the 3D Heisenberg model. However, in a different set of experiments on $La_{0.7}Sr_{0.3}MnO_3$ [68] and $La_{0.7}Ca_{0.3}MnO_3$ [220], it was concluded from the results of static critical exponents that the 3D Heisenberg model is not adequate enough to describe their critical behavior. This casts some doubt on the applicability of the 3D Heisenberg model on these samples. It is important to note that this disagreement in the experimental results, despite the same chemical composition of the two samples, is most likely due to the difference in their physical forms in these two experiments. In Refs. [133,132], the samples were thin films of thicknesses ~ 200 nm, whereas in Refs. [68,220] the experiments were performed on bulk samples. Consequently, it is expected that the finite size effects will play some role in determining the critical behavior in the thin films case. It is apparent that the experimental measurements on the thin films did not take this finite size effect into consideration and, as a result, the corresponding critical exponents cannot be expected to agree with those coming from the bulk samples. As we see from Table 5.2, although our theoretical values for the critical exponents β, γ, and δ agree well with the experimental ones, the value of νz does not agree too well with the thin film measurements. We cannot expect a good agreement with the thin film samples because our results are applicable for bulk samples without any finite size effects.

Table 5.1: Comparison of the critical exponents z, ϖ, β, γ, and δ following from Eqs. (5.65), (5.67), (5.69), (5.70), and (5.71) for $n = d = 3$ and $w = 0.001$ with experimental estimates obtained for perovskite manganite compounds. Unavailable experimental data are indicated by dashes, PC stands for polycrystalline and SC for single-crystal samples.

σ	Experimental sample	Ref.	z	ϖ	β	γ	δ
-0.148			1.979	0.510	0.345	1.201	4.264
	$La_{0.67}Ca_{0.33}MnO_3$ (PC)	[13,253,87]	$--$	0.50	0.345 ± 0.015	$--$	$--$
-0.193			1.975	0.509	0.328	1.164	4.351
	$La_{0.8}Ca_{0.2}MnO_3$ (SC)	[13,114]	$--$	0.50	0.328	1.193	4.826
-0.186			1.975	0.509	0.330	1.170	4.338
	$Nd_{0.5}Sr_{0.5}MnO_3$ (SC)	[123]	2.00 ± 0.12	0.59 ± 0.05	0.33 ± 0.02	1.24 ± 0.03	$--$
	$La_{0.75}Ca_{0.25}MnO_3$ (SC)	[13]	$--$	0.50	$--$	$--$	$--$
	$La_{0.47}Nd_{0.2}Ca_{0.23}Sr_{0.1}MnO_3$ (PC)	[253]	$--$	0.49	$--$	$--$	$--$
	$La_{0.37}Nd_{0.30}Ca_{0.18}Sr_{0.15}MnO_3$ (PC)	[253]	$--$	0.49	$--$	$--$	$--$
	$La_{0.27}Nd_{0.4}Ca_{0.13}Sr_{0.2}MnO_3$ (PC)	[253]	$--$	0.49	$--$	$--$	$--$
	$La_{0.17}Nd_{0.5}Ca_{0.08}Sr_{0.25}MnO_3$ (PC)	[253]	$--$	0.50	$--$	$--$	$--$

Table 5.2: Comparison of the critical exponents νz, β, γ, and δ following from Eqs. (5.68), (5.69), (5.70), and (5.71) for $n = d = 3$ and $w = 0.001$ with experimental estimates obtained for perovskite manganite compounds.

σ	Experimental sample	Ref.	νz	β	γ	δ
-0.094			1.251	0.370	1.251	4.164
	$La_{0.7}Sr_{0.3}MnO_3$ (SC)	[133]	1.39	$--$	$--$	$--$
	$La_{0.7}Sr_{0.3}MnO_3$ (SC)	[68]	–	0.37 ± 0.04	1.22 ± 0.03	4.25 ± 0.2
-0.114			1.232	0.360	1.232	4.201
	$La_{0.7}Ca_{0.3}MnO_3$ (SC)	[132]	1.39 ± 0.06	$--$	$--$	$--$
	$La_{0.7}Ca_{0.3}MnO_3$ (SC)	[220]	–	0.36 ± 0.01	1.2	4.263

5.7 Discussions and Conclusions

In this Chapter, we have explored the nonconserved critical dynamics of a modified GL model Hamiltonian with nonlocal screened interaction in the quartic term. The motivation for exploring such a nonlocal dynamics model is due to the following facts. Experimental observations indicate that the static critical behavior of perovskite manganites near the PM-FM phase transition exhibit a wide diversity of universality classes. In an attempt to capture the static critical behavior of such samples, it was demonstrated in Ch. 3 that the incorporation of screened nonlocal quartic interactions in the GL free energy functional leads to a wide range of universality classes that captures satisfactorily the static critical exponents for widely varying compositions of such samples. At the same time, a few experimental investigations [13,253] suggested that the linewidth exponent ϖ for perovskite manganite samples has an almost constant value $\varpi \approx 0.5$. The experimental agreements in the cases of static critical exponents inspire us to investigate the corresponding dynamic critical behavior.

We have performed a dynamic RG analysis on the nonconserved dynamics [Eq. (5.5)] govern by the screened nonlocal model Hamiltonian [Eq. (5.2)]. Carrying out the calculations at one-loop order in the leading order of $\epsilon = 4 - d + 2\sigma$, we have seen that the non-trivial fixed point is stable in the range $-0.5 \leqslant \sigma \leqslant 0.5$ in three dimensions. Within this range of σ, our present model Hamiltonian yields non-zero values of the Fisher exponent η, giving $z = 2 + \epsilon f_1(\sigma, w, n) + O(\epsilon^2)$. Plots for z are given in Fig. 5.3 which indicate their dependences on the model parameters n and w are insignificant in the negative range of σ. It may be noted that the dynamic exponent z lies in the range $1.972 \leqslant z \leqslant 2.016$ for $n = 3$ in three dimensions. We have derived an expression [Eq. 5.67] for the linewidth exponent ϖ in the leading order of ϵ yielding $\varpi = -\sigma + \epsilon f_2(\sigma, w, n) + O(\epsilon^2)$. This leads to $\varpi \approx 0.5$ in three dimensions in the range $-0.5 \leqslant \sigma \leqslant 0$ irrespective of the values of the model parameters n and w, as shown in Fig. 5.4. This is consistent with the experimental investigations [13,253] suggesting that the linewidth exponent ϖ for perovskite manganite samples has an almost constant value $\varpi \approx 0.5$ irrespective of their chemical compositions.

A few experiments studying the dynamic critical behavior of perovskite manganites measured the value of the relaxation time exponent νz. Consequently, we calculated its value leading to $\nu z = 1 + \epsilon f_3(\sigma, w, n) + O(\epsilon^2)$, at one-loop order. The currently available experimental estimates for the exponents ϖ and νz lie well within the range $-0.5 \leqslant \sigma \leqslant 0$, as shown in Table 5.1 and Table 5.2. In addition, as displayed in Table 5.1, within the same stable range of the nontrivial fixed point, the present nonlocal model Hamiltonian reproduces satisfactorily the static critical exponents for the samples for which experimental values of the linewidth exponent are also available from various spin relaxation experiments [123,13,253] . It is worth noting that in Refs. [13,253] the value of $\varpi = 0.5$ was obtained from the EPR

linewidth for various doping levels x. The measured static critical exponents β, γ, and δ in the available experiments[114,87] are also presented in Table 5.1 and they agree well with the present theoretical estimates. However, the estimates coming from μSR experiment[123] yields $\varpi \approx 0.59$. This value although slightly deviates from our model predictions ($\varpi \approx 0.5$), the other critical exponents z, β, and γ obtained in the same experiment[123] are in good agreements.

Further, while comparing the relaxation exponent νz in Table 5.2, with the available experimental estimates[133,132], we observed a slight mismatch which appears to be a consequence of finite size effects for which one expects finite size corrections in the thin film samples, as discussed earlier in Sec. 5.6. However, the static critical exponents for the same (bulk) samples, as available in Refs.[68,220], match well with our model predictions as displayed in Table 5.2.

In summary, it is worthwhile to mention that the screened nonlocal interaction yields both static and dynamic critical exponents for perovskite manganite samples up to a good level of satisfaction. It is indeed satisfying to note that such interaction is capable of predicting a constant value for the linewidth exponent vis-a-vis varying static critical exponents as observed in experimental samples for perovskite manganites. Thus it is no exaggeration to mention that such type of interaction governs the critical behavior near the PM-FM phase transition in perovskite manganites.

We would like to conclude by noting that the critical behavior near the second-order phase transition in CMR materials has been extensively explored in the recent past due to their high technological demands. Since there has been a great deal of experimental data on the critical behavior of these systems, it is an interesting adventure to explore them on theoretical grounds. The nonlocal model in this work is only an initial theoretical attempt to describe their dynamic critical behavior. It

is, however, worth remarking that a very few experimental works on the dynamic critical behavior of perovskite manganites have been reported in comparison to the enormous number of static critical measurements. Additional experimental investigations on the dynamic critical behavior will be required to verify the model predictions. Particularly, the dynamic exponents need to be measured for varying compositions of perovskite manganite samples. We hope that the present work will inspire to carry out further experimental research along this line.

Chapter 6

Critical Properties of Uranium Ferromagnetic Superconductors

Summary

A recent theoretical study[38] has revealed that systems such as uranium ferromagnetic superconductors obey conserved dynamics. In order to capture the critical behavior near the paramagnetic to ferromagnetic phase transition of these compounds, we study the conserved critical dynamics of a nonlocal Ginzburg-Landau model. A dynamic renormalization-group calculation at one-loop order yields the critical indices in the leading order of $\epsilon = d_c - d$, where $d_c = 4 - 2\rho$ is the upper critical dimension with ρ an exponent in the nonlocal interaction. The predicted static critical exponents are found to be comparable with the available experimentally observed critical exponents for strongly uniaxial uranium ferromagnetic superconductors. The corresponding dynamic exponent z and linewidth exponent ϖ are found to be $z = 4 - \rho\epsilon/4 + O(\epsilon^2)$ and $\varpi = 1 + \rho + 3\epsilon/4 + O(\epsilon^2)$.

6.1 Introduction

In this Chapter, we make an attempt to capture the critical behavior of strongly uniaxial uranium ferromagnetic superconductors. These compounds have attained a great deal of interest in recent years due to the coexistence of superconductivity and ferromagnetism. In these systems the critical temperature is found to be sensitive with a change in pressure indicating the presence of a strong magnetoelastic coupling. The total spin in these systems, being local and itinerant in character, was shown to be a conserved quantity. These motivates us to propose here a model to capture their observed critical properties. Before staring the calculation, we describe below the existing theoretical and experimental findings with a special emphasise on the nature of interaction in these compounds.

6.1.1 Magnetoelastic Coupling

The recent discovery of superconductivity below 1 K within a limited pressure range in the intermetallic uranium compounds UGe_2, URhGe, UIr, and UCoGe triggered many experimental and theoretical investigations on the coexistence of superconductivity and strong ferromagnetism in uranium ferromagnetic superconductors [198,12,203,140,252,97,129,98,173,216]. The possibility of the coexistence of superconductivity and ferromagnetism, proposed sixty years ago by Ginzburg [70], led to a new line of thinking about the underlying low temperature physics of such systems where superconductivity is mediated by magnetic fluctuations [143,129] instead of phonons (in conventional superconductors). In these systems, the $5f$ electrons possess itinerant as well as localized characters [252,65,246,63,64]. Magnetic measurements in UGe_2, URhGe, and UIr [65,196,221] indicate that they exhibit strong uniaxial anisotropy. In single crystal URhGe [12], the ferromagnetic phase appears bellow $T_c = 9.5$ K and it becomes superconducting with transition temperature 0.27 K

at ambient pressure. Paramagnetic to ferromagnetic (PM-FM) phase transition in single-crystal UGe_2 occurs at the Curie temperature $T_c \approx 52.5$ K while the superconductivity appears in the high-pressure ferromagnetic phase [198]. Similarly, UIr orders ferromagnetically bellow $T_c \approx 45$ K and superconductivity appears at high pressure in the ferromagnetic phase [7,121]. On the other hand, UCoGe has $T_c = 3$ K and superconductivity, appears bellow 0.6 K [98], survives not only in the FM state but also in the PM state [84,210,83].

In addition to the above features, experiments also indicate that T_c in these systems [84,210,83,96,174,222,82] is strongly dependent on pressure. In UGe_2 [96,174,222], it is shown that under the application of sufficient pressure (≈ 1.42 Kbar), the nature of phase transition changes from second-order to first-order at the tricritical point (≈ 24 K). In URhGe, the FM transition is second order at $p = 0$ and moves away from tricriticality with increasing pressure as $\partial T_c/\partial p > 0$ [82]. In UCoGe, T_c decreases with increasing pressure and vanishes at critical pressure $p_c \approx 10$ Kbar [84,210,83]. A first-order PM-FM phase transition for UCoGe was suggested in Ref. [85]. Similarly, T_c in UIr was found to decrease under the application of pressure ($\partial T_c/\partial p < 0$) [7,120,195,121].

The observed dependence of T_c on pressure necessarily means that the magnetic energy is coupled to the lattice, as suggested in Ref. [16]. A strong influence of magnetoelastic coupling on the phase transition in UGe_2 was inferred from neutron scattering experiments [212]. Within the Ginzburg-Landau (GL) phenomenological model for an Ising-type ferromagnet, Mineev [152] showed that the magnetoelastic mechanism leads to a first-order transition when the transition temperature strongly depends on pressure. From Landau theory without including fluctuations, Gehring [66] demonstrated that the transition temperature T_c is a very strong function of strain near the quantum critical point and $\partial T_c/\partial p$ diverges as the quantum

critical point is approached, indicating a first-order transition. A recent microscopic study of a simple symmetry-allowed model Hamiltonian describing magnetoelastic interaction [170] indicates that the magnetoelastic coupling is an important microscopic ingredient for describing the induced quantum fluctuations and phase transitions in ferromagnetic superconductors.

6.1.2 Theoretical Investigations

The effect of pressure on phase transition and the change in critical properties due to magnetoelastic interactions in a compressible lattice have been investigated over many years in a number of theoretical works [16,144,236,4,101,100]. Bean and Rodbell [16] showed, within the molecular field approximation, that for a compressible lattice if the exchange interaction is a strong function of interatomic spacing, application of sufficient external pressure reduces T_c and the transition changes from second-order to first-order. Mattis *et al.* [144] developed a magneto-thermomechanical theory where the magnetic Hamiltonian is assumed to depend linearly on strain and showed that the results for a compressible lattice at temperature T and pressure p may be mapped onto an incompressible lattice at temperature T^*. It is shown that a first-order transition is inevitable if the magnetic specific heat diverges on an incompressible lattice or if $\partial T_c/\partial p$ is large enough. Wagner [236] considered a model Hamiltonian for a compressible Ising lattice in the presence of lattice degrees of freedom. By integrating exactly over the harmonic lattice degrees of freedom for zero external forces, he obtained an effective Hamiltonian with long-range four spin interactions. Treating Wagner Hamiltonian within the RG framework, Aharony [4] showed, by neglecting irrelevant variables, that the Hamiltonian amounts to a replacement of the four-spin amplitude u_0 by $a(T - T_1)$ with T_1 proportional to the lattice compressibility and the system ex-

hibits first-order transition for $T_c < T_1$. Introducing pressure effects into compressible magnetic systems, Imry [100] showed, after integrating out the elastic modes, that the magnetoelastic coupling term gives rise to an effective Hamiltonian with a modified quartic (ϕ^4) interaction term. Bergman and Halperin [21] considered a one-component GL model with the lattice degrees of freedom and suggested a non-local quartic interaction term by integrating out the elastic variables. Tröster [228] considered this compressible ϕ^4 model and obtained evidence for a tricritical point.

6.1.3 Static Critical Behavior

Recently, the static critical properties of single crystals uranium ferromagnetic superconductors, namely, UGe_2, URhGe, and UIr in the vicinity of the ferromagnetic transition temperatures have been explored in Refs. [120,195,221] and found that their critical behavior do not belong to any known universality classes of critical phenomena. Although a three-dimensional (3D) Ising universality class was expected due to their strong uniaxial anisotropy, the susceptibility exponent γ and critical isotherm exponent δ are found to be measurably smaller than those of 3D Ising model. Further, the estimation of the specific heat exponent $\alpha \approx 0.3$ for UGe_2 and URhGe [221] from the scaling law indicates departure from the mean-field theory. As discussed clearly in Ref. [221], the predicted critical exponents for these samples are not reproducible following from model involving spatial anisotropic exchange interaction [254] or the anisotropic next nearest neighbour 3D Ising model [161]. Further, they are not reproducible from the LR model of Fisher *et al.* [57] and the models involving either isotropic or anisotropic dipole-dipole interaction [60,61]. In Table 6.1, we display the critical exponents obtained from various theoretical models along with experimentally observed critical indices for UGe_2, URhGe and UIr. We see that the theoretically predicted exponents do not agree with the experimen-

Table 6.1: Available experimental critical exponents β, γ, and δ for strongly uniaxial uranium superconductors and theoretical predictions from the existing models of critical phenomena (ID: isotropic dipolar, TMF: tricritical mean-field, MF: mean-field, FMN: Fisher, Ma, Nickel). The ranges for the critical exponents shown for the 'FMN' model correspond to the model parameter range $1.5 \leqslant \sigma \leqslant 1.981$ with single component order-parameter in three dimensions.

	URhGe	UGe_2	UIr	3D Heisenberg	3D Ising	2D Ising	ID	TMF	MF	FMN
β	0.303(2)	0.331(2)	0.355(5)	0.367	0.326	0.125	0.381	0.25	0.5	[0.5, 0.338]
γ	1.01(2)	1.03(2)	1.07(10)	1.388	1.238	1.75	1.372	1.00	1	[1.0, 1.240]
δ	4.41(2)	4.16(2)	4.01(5)	4.78	4.80	15	4.454	5.00	3	[3.0, 4.076]
Ref.	[221]	[221]	[120,195]	[107]	[107]	[94]	[29]	[94]	[125]	[57]

tal ones. This suggests the existence of a new universality class for ferromagnetic transition in the uranium ferromagnetic superconductors.

6.1.4 Dynamic Critical Behavior

In addition to the above mentioned experiments on the static critical behavior, muon spin relaxation (μSR) measurements on UGe_2 was performed in Ref.[252]. This allowed for the measurement of the spin-lattice relaxation rate λ_z at the muon site which is found to fit well with the prediction of conventional dipolar Heisenberg model[251]. However, in contrast to the observation that UGe_2 possesses strong uniaxial anisotropy[198,221], the μSR measurements indicate weak anisotropy as it cannot detect the fluctuations of the localized $5f$ electrons. Thus the μSR data are incomplete in the sense that it records only the fluctuations due to band like electrons without detecting the fluctuation due to localized $5f$ electrons. Although the λ_z values fit well with that of conventional dipolar Heisenberg model, the static critical exponents of the same model are not consistent with that of UGe_2 samples as measured in Ref.[221]. In addition, inelastic neutron scattering experiments[97,187] suggested that the total spin of single crystal UGe_2 sample is

not conserved and the value of its dynamic critical exponent is $z = 2$. On the other hand, recent theoretical studies [39,38] on ferromagnetic superconductors, indicate that although the total spin of the localized fermions is not a conserved quantity, in the presence of itinerant electrons total spin conservation is obeyed. It is also suggested that the inelastic neutron scattering experiments [97,187] picked up the contribution only from the localized electrons leaving out the contribution from the itinerant electrons.

6.1.5 Present Motivation

The above mentioned experimental and theoretical findings on the static and dynamic critical behavior of uranium ferromagnetic superconductors motivate us to investigate a different theoretical model respecting spin-conservation for capturing their universality classes near the PM-FM phase transition. As discussed above, the earlier theoretical works [16,144,236,4,101,100] suggested that the quartic nonlocality in the GL model Hamiltonian arises as a result of magnetoelastic interaction in a compressible lattice. The static critical behavior of a quartic nonlocal model Hamiltonian was studied in Ch. 2, where the original quartic interaction (Φ^4) term in the GL model Hamiltonian was modified to a nonlocal interaction term as $\int d^dx \int d^dx' \, \Phi^2(\mathbf{x})\, u(\mathbf{x}-\mathbf{x}')\, \Phi^2(\mathbf{x}')$ with the algebraic form of the coupling as $u(\mathbf{k}) = \lambda_0 |\mathbf{k}|^{2\rho}$ in the Fourier space, where λ_0 is the coupling constant and ρ is referred to as the nonlocal exponent. An RG calculation at one-loop order revealed that the model is capable of yielding the critical exponents near tricriticality. This motivates us to explore the conserved critical dynamics (akin to model B of Halperin and Hohenberg [89]) of this model Hamiltonian to identify the universality classes of uranium ferromagnetic superconductors. Carrying out a dynamic RG calculation at one-loop order, we calculate the static and dynamic critical expo-

nents. We find that the static critical exponents are comparable with the available experimentally observed critical exponents for strongly uniaxial uranium ferromagnetic superconductors. Further, the dynamic exponent $z = 4 - \rho\epsilon/4 + o(\epsilon^2)$ and the linewidth exponent $\varpi = 1 + \rho + 3\epsilon/4 + O(\epsilon^2)$ are found to lie in the ranges $3.970 \leqslant z \leqslant 4.000$ and $1.50 \leqslant \varpi \leqslant 1.75$, in three dimensions.

6.2 Conserved Nonlocal Dynamics

Conserved critical dynamics of a single component order parameter $\phi(\mathbf{x},t)$ is expressed as [89]

$$\frac{\partial}{\partial t}\phi(\mathbf{x},t) = \Gamma_0 \nabla^2 \frac{\delta H}{\delta \phi(\mathbf{x},t)} + \eta(\mathbf{x},t), \tag{6.1}$$

where $\eta(\mathbf{x},t)$ is a Gaussian white noise with zero mean and correlation

$$\langle \eta(\mathbf{x},t)\eta(\mathbf{x}',t')\rangle = -2\Gamma_0 \nabla^2 \delta^d(\mathbf{x}-\mathbf{x}')\delta(t-t'). \tag{6.2}$$

We incorporate nonlocal interactions in the quartic term of the GL free energy functional H as

$$H[\phi] = \int d^d x\ dt \left[\frac{c_0}{2}|\nabla\phi(\mathbf{x},t)|^2 + \frac{r_0}{2}\phi^2(\mathbf{x},t) + \int d^d x'\ dt' \phi^2(\mathbf{x},t) u(\mathbf{x}-\mathbf{x}')\delta(t-t')\phi^2(\mathbf{x}',t')\right], \tag{6.3}$$

with d the space dimension and $u(\mathbf{x}-\mathbf{x}')$ is the nonlocal coupling function. Using this Hamiltonian, Eq. (6.1) can be portrayed in the Fourier space as

$$\left[\frac{-i\omega}{\Gamma_0 k^2} + r_0 + c_0 k^2\right]\phi(\mathbf{k},\omega) = \frac{\eta(\mathbf{k},\omega)}{\Gamma_0 k^2} - 4\int \frac{d^d k_1 d\omega_1}{(2\pi)^{d+1}} \int \frac{d^d k_2 d\omega_2}{(2\pi)^{d+1}} u(\mathbf{k}_1 - \mathbf{k})\phi(\mathbf{k}_1,\omega_1) \times \phi(\mathbf{k}_2,\omega_2)\phi(\mathbf{k}-\mathbf{k}_1-\mathbf{k}_2, \omega-\omega_1-\omega_2), \tag{6.4}$$

where an ultraviolet cut-off Λ is assumed in the momentum integrations because of finite lattice constant a related as $\Lambda \sim a^{-1}$. Using the zeroth-order response function

$$G_0(\mathbf{k},\omega) = \left(\frac{-i\omega}{\Gamma_0 k^2} + r_0 + c_0 k^2\right)^{-1}, \tag{6.5}$$

we rewrite Eq. (6.4) as

$$\phi(\mathbf{k},\omega) = \frac{G_0(\mathbf{k},\omega)\eta(\mathbf{k},\omega)}{\Gamma_0 k^2} - 4G_0(\mathbf{k},\omega)\int \frac{d^d k_1}{(2\pi)^d}\frac{d\omega_1}{2\pi}\int \frac{d^d k_2}{(2\pi)^d}\frac{d\omega_2}{2\pi} u(\mathbf{k}_1-\mathbf{k})\phi(\mathbf{k}_1,\omega_1)$$

$$\times \phi(\mathbf{k}_2,\omega_2)\phi(\mathbf{k}-\mathbf{k}_1-\mathbf{k}_2,\omega-\omega_1-\omega_2), \tag{6.6}$$

where the coupling function $u(\mathbf{p})$ is assumed to have the algebraic form

$$u(\mathbf{p}) = \lambda_0 |\mathbf{p}|^{2\rho}, \tag{6.7}$$

with λ_0 is the coupling constant and the exponent ρ is referred to as the nonlocal exponent. We use the Fourier transformed expression for the noise correlation given by

$$\langle \eta(\mathbf{k},\omega)\eta(\mathbf{k}',\omega')\rangle = 2\Gamma_0 k^2 (2\pi)^{d+1}\delta^d(\mathbf{k}+\mathbf{k}')\delta(\omega+\omega'). \tag{6.8}$$

6.3 Momentum Shell Decimation

We begin with Eq. (6.6) and perform dynamic RG calculations [139,89,166,146] at one-loop order. Elimination of modes $\phi^{>}(\mathbf{k},\omega)$ lying in the momentum range $\frac{\Lambda}{b} \leqslant k \leqslant \Lambda$ yields the equation of motion in terms of the remaining modes $\phi^{<}(\mathbf{k},\omega)$ in the reduced range $0 \leqslant k \leqslant \frac{\Lambda}{b}$, leading to

$$\left[\frac{-i\omega}{\Gamma_0 k^2} + r_0 + c_0 k^2\right]\phi^{<}(\mathbf{k},\omega) = \frac{\eta^{<}(\mathbf{k},\omega)}{\Gamma_0 k^2} - 4\int \frac{d^d k_1 d\omega_1}{(2\pi)^{d+1}}\int \frac{d^d k_2 d\omega_2}{(2\pi)^{d+1}} u(\mathbf{k}_1-\mathbf{k})\phi^{<}(\mathbf{k}_1,\omega_1)$$

$$\times \phi^{<}(\mathbf{k}_2,\omega_2)\phi^{<}(\mathbf{k}-\mathbf{k}_1-\mathbf{k}_2,\omega-\omega_1-\omega_2) + R(\mathbf{k},\omega) + \Upsilon(\mathbf{k},\omega), \tag{6.9}$$

where $R(\mathbf{k},\omega)$ and $\Upsilon(\mathbf{k},\omega)$ are the contributions coming from the self-energy diagrams [Fig. 6.1] and vertex diagrams [Fig. 6.2] respectively. We obtain

$$R(\mathbf{k},\omega) = -[\Sigma_a + \Sigma_b(\mathbf{k},\omega)]\phi^{<}(\mathbf{k},\omega)$$

with the self-energy corrections at one-loop order

$$\Sigma_a = 8\int \frac{d^d q d\Omega}{(2\pi)^{d+1}} \frac{u(\mathbf{0})}{\Gamma_0 q^2} |G_0^{>}(\mathbf{q},\Omega)|^2, \tag{6.10}$$

$$\Sigma_b(\mathbf{k},\omega) = 16\int \frac{d^d q d\Omega}{(2\pi)^{d+1}} \frac{u(\mathbf{q}-\mathbf{k})}{\Gamma_0 q^2} |G_0^{>}(\mathbf{q},\Omega)|^2. \tag{6.11}$$

Performing frequency convolutions in above self-energy corrections, one can readily obtain poles from the integrands $\frac{1}{\left(\frac{-i\Omega}{\Gamma_0 q^2}+r_0+c_0q^2\right)\left(\frac{i\Omega}{\Gamma_0 q^2}+r_0+c_0q^2\right)}$ as

$$\Omega = i\Gamma_0 q^2(c_0 q^2 + r_0), \tag{6.12}$$

and

$$\Omega = -i\Gamma_0 q^2(c_0 q^2 + r_0). \tag{6.13}$$

Using residue calculus, contour in the lower half plane gives the residue at $\Omega = -i\Gamma_0 q^2(c_0 q^2 + r_0)$, we thus obtain

$$\lim_{\Omega\to -i\Gamma_0 q^2(c_0q^2+r_0)} \left(\Omega + i\Gamma_0 q^2(c_0 q^2 + r_0)\right) \frac{1}{\left(\frac{-i\Omega}{\Gamma_0 q^2}+r_0+c_0q^2\right)\left(\frac{i\Omega}{\Gamma_0 q^2}+r_0+c_0q^2\right)}$$

$$= \frac{i\Gamma_0 q^2}{2(r_0 + cq^2)}, \tag{6.14}$$

which yields

$$\int_{-\infty}^{+\infty} \frac{d\Omega}{2\pi} |G_0^{>}(\mathbf{q},\Omega)|^2 = \frac{\Gamma_0 q^2}{2(c_0 q^2 + r_0)}. \tag{6.15}$$

Using this result in Eqs. (6.10) and (6.11), we see that the integrand of the self-energy correction Σ_a given by Eq. (6.10) diverges for negative values of ρ. Thus,

finiteness of the free energy restricts ρ to positive values. However, for any positive value of ρ it does not contribute. We perform momentum integration over the internal momentum q in Eq. (6.11). Since the integration over q is restricted in the high momentum shell $\Lambda/b \leqslant q \leqslant \Lambda$, the integrand in $\Sigma_b(\mathbf{k},\omega)$ is expanded in the limit $q \gg k$. The resulting large-scale long-time expansion turns out to be

$$\Sigma_b(\mathbf{k},0) = \frac{8S_d\lambda_0}{c_0[2\pi]^d}\left[\left(\frac{b^{2-d-2\rho}-1}{2-d-2\rho}\right)\Lambda^{d-2+2\rho} - \frac{r_0}{c_0}\left(\frac{b^{4-d-2\rho}-1}{4-d-2\rho}\right)\Lambda^{d-4+2\rho}\right]$$
$$+\frac{8S_d\lambda_0}{c_0[2\pi]^d}k^2\left[\frac{\rho(d+2\rho-2)}{d}\left(\frac{b^{4-d-2\rho}-1}{4-d-2\rho}\right)\Lambda^{d-4+2\rho}\right], \tag{6.16}$$

where $S_d = 2\pi^{d/2}/\Gamma(d/2)$ is the surface area of a unit sphere embedded in the d-dimensional space. This expression for $\Sigma_b(\mathbf{k},0)$ gives rise to corrections Δr and Δc to the bare parameters r_0 and c_0, given by

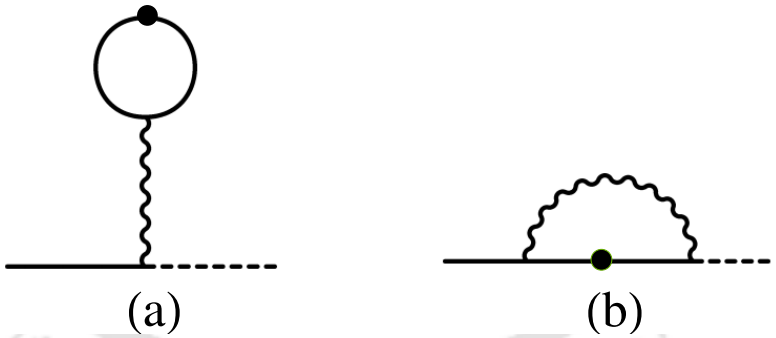

Figure 6.1: Feynman diagrams corresponding to the self energies (a) Σ_a and (b) $\Sigma_b(\mathbf{k},\omega)$. Solid lines represent the propagator $G_0(\mathbf{k},\omega)$, dashed lines the field $\phi(\mathbf{k},\omega)$, the dots noise correlation, and the wiggly lines represent the nonlocal coupling $u(\mathbf{k})$.

$$r_0 + \Delta r = r_0 + \frac{8S_d\lambda_0}{c_0[2\pi]^d}\left[\left(\frac{b^{2-d-2\rho}-1}{2-d-2\rho}\right)\Lambda^{d-2+2\rho} - \frac{r_0}{c_0}\left(\frac{b^{4-d-2\rho}-1}{4-d-2\rho}\right)\Lambda^{d-4+2\rho}\right], \tag{6.17}$$

and

$$(c_0+\Delta c)k^2 = c_0k^2 + \frac{8\rho(2\rho-2+d)S_d\lambda_0}{c_0d[2\pi]^d}k^2\left[\left(\frac{b^{4-d-2\rho}-1}{4-d-2\rho}\right)\Lambda^{d-4+2\rho}\right]. \tag{6.18}$$

We see that $\lim_{\mathbf{k}\to 0,\omega\to 0}\left(\frac{\partial\Sigma}{\partial(-i\omega/k^2)}\right)=0$, so that the correction $\Delta\Gamma=0$ at this order of calculation.

The above momentum shell decimation scheme gives rise to vertex corrections at one-loop order as shown in Fig. 6.2. These Feynman diagrams in Figs. 6.2(a), 6.2(b), 6.2(c) takes the mathematical forms

$$\Upsilon_a = 64\int\frac{d^dk_1d\omega_1}{[2\pi]^{d+1}}\int\frac{d^dk_2d\omega_2}{[2\pi]^{d+1}}u(\mathbf{k}_1-\mathbf{k})\phi^<(\mathbf{k}_1,\omega_1)\phi^<(\mathbf{k}_2,\omega_2)$$
$$\phi^<(\mathbf{k}-\mathbf{k}_1-\mathbf{k}_2,\omega-\omega_1-\omega_2)\int\frac{d^dqd\Omega}{[2\pi]^{d+1}}\frac{u(\mathbf{k}_1-\mathbf{k})}{\Gamma_0q^2}|G_0^>(\mathbf{q},\Omega)|^2G_0^>(\mathbf{k}-\mathbf{k}_1-\mathbf{q},\omega-\omega_1-\Omega), \tag{6.19}$$

$$\Upsilon_b = 256\int\frac{d^dk_1d\omega_1}{[2\pi]^{d+1}}\int\frac{d^dk_2d\omega_2}{[2\pi]^{d+1}}u(\mathbf{k}_1-\mathbf{k})\phi^<(\mathbf{k}_1,\omega_1)\phi^<(\mathbf{k}_2,\omega_2)$$
$$\phi^<(\mathbf{k}-\mathbf{k}_1-\mathbf{k}_2,\omega-\omega_1-\omega_2)\int\frac{d^dqd\Omega}{[2\pi]^{d+1}}\frac{u(\mathbf{k}_1+\mathbf{k}_2+\mathbf{q}-\mathbf{k})}{\Gamma_0q^2}|G_0^>(\mathbf{q},\Omega)|^2$$
$$G_0^>(\mathbf{k}-\mathbf{k}_1-\mathbf{q},\omega-\omega_1-\Omega), \tag{6.20}$$

and

$$\Upsilon_c = 256\int\frac{d^dk_1d\omega_1}{[2\pi]^{d+1}}\int\frac{d^dk_2d\omega_2}{[2\pi]^{d+1}}\phi^<(\mathbf{k}_1,\omega_1)\phi^<(\mathbf{k}_2,\omega_2)$$
$$\phi^<(\mathbf{k}-\mathbf{k}_1-\mathbf{k}_2,\omega-\omega_1-\omega_2)\int\frac{d^dqd\Omega}{[2\pi]^{d+1}}\frac{u(\mathbf{q}-\mathbf{k})u(\mathbf{q}-\mathbf{k}_1)}{\Gamma_0q^2}|G_0^>(\mathbf{q},\Omega)|^2$$
$$G_0^>(\mathbf{k}_1+\mathbf{k}_2-\mathbf{q},\omega_1+\omega_2-\Omega), \tag{6.21}$$

respectively.

In the above expressions for Υ_a and Υ_b, Ω integrals can be evaluated by using residue calculus. Using $G_0(\mathbf{q},\Omega)=\left(\frac{-i\Omega}{\Gamma_0q^2}+r_0+c_0q^2\right)^{-1}$ in the above expressions for Υ_a and Υ_b in the large scale long time limit (vanishing $\mathbf{k}\to 0$, $\omega\to 0$), we see that integrands $\frac{1}{\left(\frac{-i\Omega}{\Gamma_0}+r_0+c_0q^2\right)\left(\frac{i\Omega}{\Gamma_0q^2}+r_0+c_0q^2\right)^2}$ have double poles at

$$\Omega = i\Gamma_0q^2(c_0q^2+r_0), \tag{6.22}$$

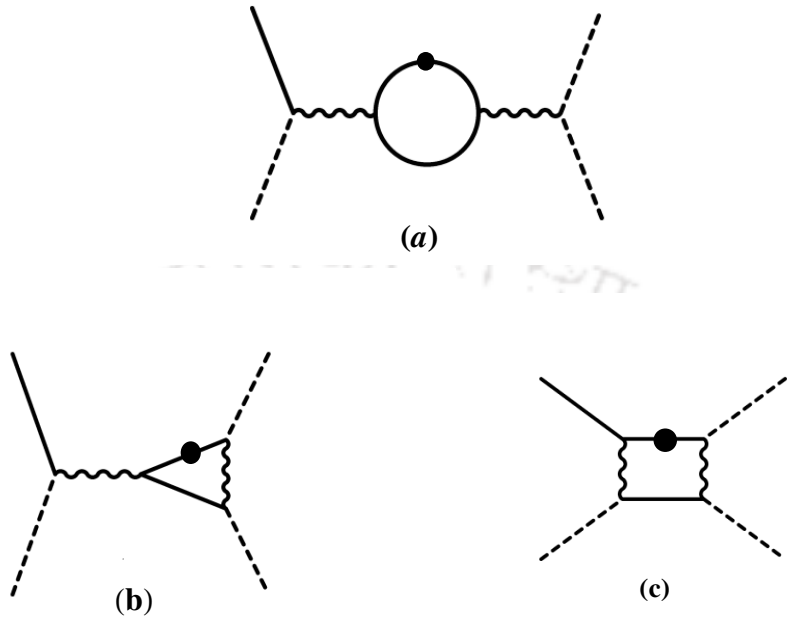

Figure 6.2: Feynman diagrams corresponding to the vertex corrections coming from (a) Υ_a, (b) Υ_b, and (c) Υ_c. The lines and the dots have the same meanings as in Fig. 6.1.

and simple poles at

$$\Omega = -i\Gamma_0 q^2(c_0 q^2 + r_0). \tag{6.23}$$

We thus choose the contour in the lower half plane to evaluate these simple poles. Residue at $\Omega = -i\Gamma_0 q^2(c_0 q^2 + r_0)$ is calculated as

$$\lim_{\Omega \to -i\Gamma_0 q^2(c_0 q^2 + r_0)} \Big(\Omega + i\Gamma_0 q^2(c_0 q^2 + r_0)\Big) \frac{1}{\Big(\frac{-i\Omega}{\Gamma_0 q^2} + r_0 + c_0 q^2\Big)\Big(\frac{i\Omega}{\Gamma_0 q^2} + r_0 + c_0 q^2\Big)^2}$$

$$= \frac{i\Gamma_0 q^2}{4(c_0 q^2 + r_0)} \tag{6.24}$$

which yields

$$\int_{-\infty}^{+\infty} \frac{d\Omega}{2\pi} |G_0^>(\mathbf{q}, \Omega)|^2 G_0^>(-\mathbf{q}, -\Omega) = \frac{\Gamma_0 q^2}{4(c_0 q^2 + r_0)^2}. \tag{6.25}$$

Due to the same reason as for Σ_a, Υ_a does not contribute in the large-scale long-

time limit. Performing the loop integration appearing in Υ_b, we obtain the correction to the bare coupling constant λ_0 as

$$\lambda_0+\Delta\lambda=\lambda_0-\frac{16S_d\lambda_0^2}{c_0^2[2\pi]^d}\left[\left(\frac{b^{4-d-2\rho}-1}{4-d-2\rho}\right)\Lambda^{d-4+2\rho}-\frac{2r_0}{c_0}\left(\frac{b^{6-d-2\rho}-1}{6-d-2\rho}\right)\Lambda^{d-6+2\rho}\right]. \tag{6.26}$$

Further, Υ_c is irrelevant because it does not yield a correction similar to the original vertex factor (which is proportional to $k^{2\rho}$).

6.4 Renormalization-Group Transformation

The RG transformation requires that the form of the original dynamical equation, namely, Eq. (6.4), is maintained with respect to scale elimination. The reduced range $0\leqslant k\leqslant\frac{\Lambda}{b}$ is thus projected into the full (original) range ($0\leqslant k\leqslant\Lambda$) by rescaling the variables and the field as $\mathbf{k}'=b\mathbf{k}$, $\omega'=b^z\omega$, and $\phi'(\mathbf{k}',\omega')=\zeta^{-1}\phi(\mathbf{k},\omega)$. These transformations changes the response function as

$$G(\mathbf{k},\omega)=\left(\frac{-i\omega'}{b^{z-2}\Gamma_0 k'^2}+(r_0+\Delta r)+(c_0+\Delta c)b^{-2}k'^2\right)^{-1}. \tag{6.27}$$

We thus have

$$G(\mathbf{k},\omega)=G'(\mathbf{k}',\omega')b^{z-y-2}, \tag{6.28}$$

with

$$\Gamma'=b^y\Gamma_0, \tag{6.29}$$

$$r'=b^{z-y-2}(r_0+\Delta r), \tag{6.30}$$

and

$$c'=b^{z-y-4}(c_0+\Delta c). \tag{6.31}$$

With these rescaled parameters, we see that the coarse-grained dynamical equation becomes

$$\phi'(\mathbf{k}',\omega') = \frac{G'(\mathbf{k}',\omega')\zeta^{-1}\eta^{<}(\mathbf{k},\omega)b^{z-y-2}}{\Gamma' k'^2 b^{-(y+2)}} - 4\frac{G'(\mathbf{k}',\omega')\zeta^2 b^{z-y-2-\rho}}{b^{2d+2z}}\int \frac{d^d k_1'}{(2\pi)^d}\frac{d\omega_1'}{2\pi}$$

$$\int \frac{d^d k_2'}{(2\pi)^d}\frac{d\omega_2'}{2\pi}(\lambda_0+\Delta\lambda)|\mathbf{k}_1'-\mathbf{k}'|^{2\rho}\phi'(\mathbf{k}_1',\omega_1')\phi'(\mathbf{k}_2',\omega_2')\phi'(\mathbf{k}'-\mathbf{k}_1'-\mathbf{k}_2',\omega'-\omega_1'-\omega_2'). \tag{6.32}$$

We rewrite the above equation as

$$\phi(\mathbf{k}',\omega') = \frac{\eta'(\mathbf{k}',\omega')G'(\mathbf{k}',\omega')}{\Gamma' k'^2} - 4G'(\mathbf{k}',\omega')\int \frac{d^d k_1'}{(2\pi)^d}\frac{d\omega_1'}{2\pi}\int \frac{d^d k_2'}{(2\pi)^d}\frac{d\omega_2{}'}{2\pi}$$

$$\lambda^{'}|\mathbf{k}_1'-\mathbf{k}'|^{2\rho}\phi'(\mathbf{k}_1',\omega_1')\phi'(\mathbf{k}_2',\omega_2')\phi'(\mathbf{k}'-\mathbf{k}_1'-\mathbf{k}_2',\omega'-\omega_1'-\omega_2'), \tag{6.33}$$

with

$$\eta'(\mathbf{k}',\omega') = \zeta^{-1}b^z\eta^{<}(\mathbf{k},\omega), \tag{6.34}$$

$$\lambda' = \frac{\zeta^2 b^{z-y-2-\rho}}{b^{2d+2z}}(\lambda_0+\Delta\lambda). \tag{6.35}$$

Field rescaling factor ζ is calculated conventionally and obtained as

$$\zeta = b^{1+\frac{d}{2}+z-\frac{\eta}{2}}. \tag{6.36}$$

To calculate the rescaling factor for noise amplitude Γ, we consider scaled noise-noise correlation

$$\langle\eta'(\mathbf{k}_1',\omega_1')\eta'(\mathbf{k}_2',\omega_2')\rangle = 2\Gamma' k'^2(2\pi)^{d+1}\delta^d(\mathbf{k}_1'+\mathbf{k}_2')\delta(\omega_1'+\omega_2'), \tag{6.37}$$

this together with Eqs. (6.34) and (6.36) yields

$$y = z-4+\eta. \tag{6.38}$$

Using the above equation in Eqs. (6.30), (6.31), and (6.35), we obtain the RG recursion relations

$$\Gamma' = b^{z-4+\eta}\Gamma_0, \tag{6.39}$$

$$r' = b^{2-\eta}(r_0 + \Delta r), \tag{6.40}$$

$$c' = b^{-\eta}(c_0 + \Delta c), \tag{6.41}$$

$$\lambda' = b^{4-d-2\rho-2\eta}(\lambda_0 + \Delta\lambda) \tag{6.42}$$

Using $b = e^{\delta l}$, and incorporating Eqs. (6.17), (6.18), and (6.26), for Δr, Δc, and $\Delta\lambda$ respectively, we obtain the RG flow equations as

$$\frac{d\Gamma}{dl} = (z-4+\eta)\Gamma, \tag{6.43}$$

$$\frac{dr}{dl} = (2-\eta)r + \frac{8\lambda S_d}{(2\pi)^d}\left(\frac{\Lambda^{d-2+2\rho}}{c} - \frac{r}{c^2}\Lambda^{d-4+2\rho}\right), \tag{6.44}$$

$$\frac{dc}{dl} = -\eta c - \frac{8\rho(2-2\rho-d)\lambda S_d}{d(2\pi)^d}\frac{\Lambda^{d-4+2\rho}}{c}, \tag{6.45}$$

$$\frac{d\lambda}{dl} = (4-d-2\eta-2\rho)\lambda - \frac{16\lambda^2 S_d}{(2\pi)^d}\left(\frac{\Lambda^{d-4+2\rho}}{c^2} - \frac{2r}{c^3}\Lambda^{d-6+2\rho}\right). \tag{6.46}$$

These RG flow equations can be analyzed in a convenient way if we cast them in terms of non-dimensional quantities. Thus, for convenience we redefine the dimensionless parameters as

$$R = \frac{r}{\Lambda^2}, \qquad U = \frac{\lambda S_d}{(2\pi)^d \Lambda^{4-d-2\rho}}, \tag{6.47}$$

and obtain the RG flow equations as

$$\frac{dR}{dl} = (2-\eta)\,R + \frac{8U}{c}\left(1 - \frac{R}{c}\right), \tag{6.48}$$

$$\frac{dU}{dl} = (4-d-2\eta-2\rho)U - \frac{16U^2}{c^2}\left(1 - \frac{2R}{c}\right). \tag{6.49}$$

In the next section, we shall analyzed the non-trivial fixed point coming from the above flow equations and obtain the corresponding critical exponents.

6.5 Fixed Point and Critical Exponents

The perturbation expansion and the consequent RG transformation can be performed systematically in powers of a small parameter $\epsilon = 4 - d - 2\rho$. Since, the present RG analysis is at one-loop order, we shall carry out the expansion in the leading order of ϵ. Using Eqs. (6.48) and (6.49), the resulting flow equations can be expressed as

$$\frac{dR}{dl} = \left(2 - \frac{\rho\epsilon}{4}\right) R + \frac{8U}{c}\left(1 - \frac{R}{c}\right), \tag{6.50}$$

$$\frac{dU}{dl} = U\left[\left(\epsilon - \frac{\rho\epsilon}{2}\right) - \frac{16U}{c^2}\right]. \tag{6.51}$$

From the above flow equations we find that their exists a non-trivial fixed point given by

$$\frac{R^*}{c} = -\frac{\epsilon}{4}\left(1 - \frac{\rho}{2}\right) + O(\epsilon^2), \tag{6.52}$$

$$\frac{U^*}{c^2} = \frac{\epsilon}{16}\left(1 - \frac{\rho}{2}\right) + O(\epsilon^2). \tag{6.53}$$

Equations (6.50) and (6.51) are linearised around this fixed point to obtain a matrix equation $\frac{d}{dl}\delta X = M\delta X$ where $\delta X = X - X^*$ is the coloumn matrix formed by δR, and δU, and M is a 2×2 matrix whose eigen-values are $y_1 = 2 - \frac{\epsilon}{2}$, $y_2 = -\epsilon(1 - \frac{\rho}{2})$ corresponding to R and U respectively. The condition $y_1 > 0$, $y_2 < 0$ gives the “stability" ranges $0 < \rho < \frac{1}{2}$ in three dimensions and $0 < \rho < 1$ in two dimensions.

The correlation-length exponent ν is related to the unstable eigenvalue y_1, as $\nu = 1/y_1$ (cf. Sec. 1.3), so that

$$\nu = \frac{1}{2} + \frac{\epsilon}{8} + O(\epsilon^2). \tag{6.54}$$

From Eq. (6.45), the Fisher exponent η is calculated in the leading order of ϵ as

$$\eta = \frac{\rho\epsilon}{4} + O(\epsilon^2). \tag{6.55}$$

Substituting Eqs. (6.54) and (6.55) in the Joshephson's scaling law (cf. Sec. 1.2), we obtain

$$\beta = \frac{1-\rho}{2} - \frac{\epsilon(2+\rho)}{16} + O(\epsilon^2). \tag{6.56}$$

Further, Fisher's scaling gives

$$\gamma = 1 + \frac{\epsilon}{4}\left[1 - \frac{\rho}{2}\right] + O(\epsilon^2). \tag{6.57}$$

Using Eqs. (6.56) and (6.57) in Rushbrooke's scaling, we obtain

$$\alpha = \rho\left[1 + \frac{\epsilon}{4}\right] + O(\epsilon^2). \tag{6.58}$$

Finally, using Widom scaling, we obtain the critical isotherm exponent as

$$\delta = \frac{3-\rho}{1-\rho} + \frac{\epsilon}{(1-\rho)^2}\left[1 + \frac{\rho(\rho-2)}{4}\right] + O(\epsilon^2). \tag{6.59}$$

For the noise amplitude Γ to reach Γ^*, Eq. (6.43) yields the dynamic critical exponent z as $z = 4 - \eta$. Thus using Eq. (6.55) we obtain

$$z = 4 - \frac{\rho\epsilon}{4} + O(\epsilon^2). \tag{6.60}$$

In order to calculate the linewidth exponent ϖ (cf. 1.5), we use Eqs. (6.55), (6.54), and (6.60) giving

$$\varpi = 1 + \rho + \frac{3\epsilon}{4} + O(\epsilon^2). \tag{6.61}$$

We see that the dynamic exponent z and the linewidth exponent ϖ lie in the ranges

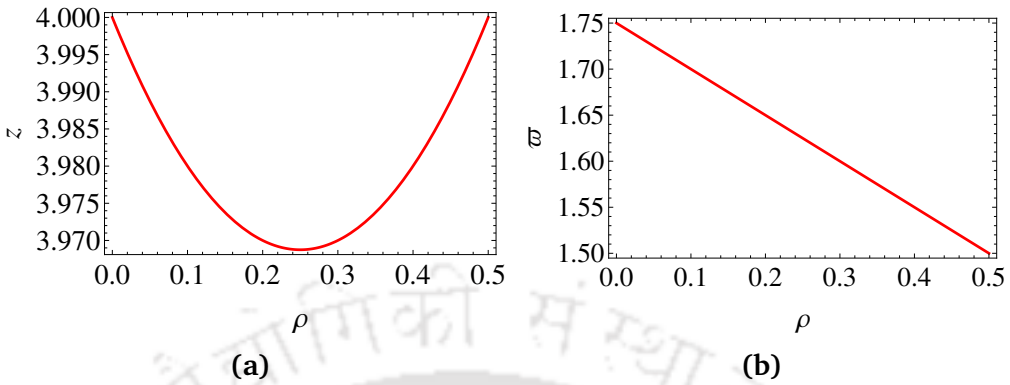

Figure 6.3: Variation of the dynamic critical exponent (a) z and (b) ϖ in three dimensions for the allowed range $0 < \rho < 0.5$.

$3.970 \leqslant z \leqslant 4.000$ and $1.50 \leqslant \varpi \leqslant 1.75$ respectively, in three dimensions. Graphical plots for z and ϖ as a function of ρ for $d = 3$ are shown in Fig. 6.3a and Fig. 6.3b respectively.

6.6 Experimental Data and Model Predictions

As we have already pointed out in Sec. 6.1.3, experiments have been performed recently to determine the critical behavior near the second-order phase transition in uranium ferromagnetic superconductors, namely, UGe_2 [221], URhGe [221], and UIr [120,195]. For UGe_2, the Kouvel-Fisher (KF) method yields $\beta = 0.331 \pm 0.002$ and $\gamma = 1.03 \pm 0.02$ while the critical isotherm gives $\delta = 4.16 \pm 0.02$. Although the β value is close to 3D Ising ($\beta = 0.326$) and γ value is close to mean-field ($\gamma = 1.00$), the δ value does not belong to any known universality class. In Table 6.2, we compare these experimental results with the critical exponents predicted by the present theory. We find that for $\rho = 0.150$, Eq. (6.56) yields $\beta = 0.331$. For the same value of ρ, Eqs. (6.57) and (6.59) yield $\gamma = 1.162$ and $\delta = 4.255$. Thus our model predictions are close to the experimental values.

Using the same procedure, we determine the critical exponents for URhGe and

find that for $\rho = 0.258$, $\beta = 0.303$, $\gamma = 1.105$, $\delta = 4.476$, and $\alpha = 0.289$. These values are comparable to the experimental critical exponents for URhGe namely, $\beta = 0.303 \pm 0.002$, $\gamma = 1.01 \pm 0.02$, $\delta = 4.41 \pm 0.02$, and $\alpha = 0.3$. We see that the static critical exponents, calculated in the leading order of ϵ, are in very good agreement with the experimental estimates.

In the single crystal UIr sample, the experimental critical exponents $\beta = 0.355 \pm 0.05$, $\gamma = 1.07 \pm 0.10$, and $\delta = 4.01 \pm 0.05$, have been estimated in Refs. [120,195]. From the present theory, we obtain $\beta = 0.355$ for $\rho = 0.065$ and for the same value of ρ, the values for γ and δ turn out to be $\gamma = 1.210$ and $\delta = 4.103$. These values are in satisfactory agreement with the experimental ones.

It is worthwhile to note that an elaborate discussion on the universality class of the above mentioned experimental samples has been given in Ref. [221]. It was pointed out that the model involving spatial anisotropic exchange interaction [254], the anisotropic next nearest neighbour 3D Ising model [161], the LR model of Fisher *et al.* [57], and the models involving either isotropic or anisotropic dipole-dipole interaction [60,61] could not capture the above experimental critical exponents. From the agreement of the present theoretical predictions with the experimental exponents, it may be stated that the quartic nonlocality in the model Hamiltonian [Eqs. (6.3) and (6.7)] describes the effective interaction in the above experimental samples for uranium ferromagnetic superconductors.

It may further be noted that for UCoGe the critical region is estimated to be much narrower ($\Delta T_G \sim 1$ mK) [216,11] than the above samples. Consequently, the experimental critical exponents for this sample are expected to be same as those of the mean-field theory. Therefore, we do not expect the strong coupling fixed point of the present theory to yield these critical exponents.

In Table 6.2, we also display the present theoretical estimates for the dynamic

Table 6.2: Present theoretical predictions for the critical exponents β, γ, δ, α, z, and ϖ in the leading order of ϵ in three dimensions and the corresponding experimental estimates for strongly uniaxial uranium ferromagnetic superconductors.

ρ	Experimental sample	Ref.	β	γ	δ	α	z	ϖ
0.150			0.331	1.162	4.255	0.176	3.974	1.675
	UGe_2	[221]	0.331 ± 0.002	1.03 ± 0.02	4.16 ± 0.02	$--$	$--$	$--$
0.258			0.303	1.105	4.476	0.289	3.969	1.621
	URhGe	[221]	0.303 ± 0.002	1.01 ± 0.02	4.41 ± 0.02	0.3	$--$	$--$
0.065			0.355	1.210	4.103	0.079	3.986	1.718
	UIr	[120,195]	0.355 ± 0.05	1.07 ± 0.10	4.01 ± 0.05	$--$	$--$	$--$

critical exponent z and the linewidth exponent ϖ calculated for the values of ρ corresponding to which the static critical exponents are determined. It may be noted that, several studies on heavy fermion systems indicate dual (localized and itinerant) nature of the $5f$ electrons [252,246,63,38,64] which is regarded as the key point for the coexistence of ferromagnetism and superconductivity. It has been pointed out in Refs. [221,38] that the μSR experiment [252] and inelastic neutron scattering experiment [97,187] are not able to capture the total fluctuations due to both the localized and itinerant $5f$ electrons. Consequently, these experiments inferred that the total spin of single crystal UGe_2 sample is not conserved. However, recent theoretical studies [39,38] on ferromagnetic superconductors indicate that although the total spin of the localized fermions is not a conserved quantity, in the presence of itinerant fermions total spin conservation is respected. Thus, to determine the complete dynamic critical behavior of uranium ferromagnetic superconductors, it is important for the experiments to pick up contributions from both localized as well as itinerant $5f$ electrons. We hope, such experimental attempts will be made in the future to provide reliable estimates for the dynamic critical exponents z and ϖ so that our model predictions could be verified more concretely.

6.7 Discussion and Conclusion

In this Chapter, we have explored the conserved critical dynamics of a model Hamiltonian where the quartic interaction is assumed to be nonlocal. We consider a conserved dynamics because recent theoretical studies [39,38] on systems involving localized and itinerant electrons (for example, uranium superconductors) indicate conservation of total (localized and itinerant) spin. A number of earlier theoretical works [16,144,56,236,4,101,100] suggested that quartic nonlocality arises as a result of magnetoelastic interactions in a compressible lattice. Recently, a simple model Hamiltonian with displacement dependent exchange interaction describing magnetoelastic interaction [170] is found to be useful in understanding the induced quantum fluctuations and phase transition in ferromagnetic superconductors. Moreover, as observed in experiments, suppression of T_c under the application of sufficient pressure on itinerant ferromagnetic superconductors [96,174,222,229] indicates a direct coupling of magnetic energy to the lattice. Influence of magnetoelastic coupling on the phase transition in UGe_2 was also revealed by neutron scattering experiments [212]. Theoretical investigation within the GL phenomenological model showed [152] that the magnetoelastic mechanism leads to a first-order transition and that the transition temperature strongly depends on pressure. These theoretical and experimental investigations suggesting strong magnetoelastic coupling along with the earlier theoretical attempts suggesting nonlocal quartic interactions motivated us to consider the nonlocal model Hamiltonian given by Eqs. (6.3) and (6.7) in this work. Our motivation is further strengthened by the fact that the universality class of uranium ferromagnetic superconductors near the PM-FM phase transition does not belong to any known universality classes corresponding to the existing models of critical phenomena. This is shown in Table 6.1 by comparing critical exponents predicted by the existing models with the experimental

critical exponents for ferromagnetic superconductors.

We have carried out dynamic RG calculation at one-loop order in the momentum shell decimation scheme and derived the expressions for the critical exponents in the leading order of $\epsilon = 4 - d - 2\rho$. In Table 6.2, we have displayed our results for different values of the nonlocal exponent ρ and compared them with the available experimental estimates for uranium ferromagnetic superconductors. We have seen that the experimentally measured static critical exponents for uranium ferromagnetic superconductors, namely, UGe_2, URhGe, and UIr, are obtained satisfactorily from the present nonlocal model Hamiltonian at one-loop order. In Table 6.2, we have also displayed the corresponding values of dynamic critical exponent z and linewidth exponent ϖ (obtained for the same values of ρ). We are unable to compare these theoretical predictions with experimental estimates because, to our knowledge, their exist no experimental data for the dynamic exponents z and ϖ for these samples. It may be noted that, an inelastic neutron scattering experiment on UGe_2 measured the dynamic exponent z and obtained $z = 2$ [187]. However, as pointed out in Ref. [38], inelastic neutron scattering picks up contribution only from the localized electrons giving the impression that the dynamics is non-conserved ($z = 2$) in distinction with the fact that the total spin (localised and itinerant) dynamics is to be conserved. On the other hand, μSR experiments measure fluctuations only due to bandlike electrons and not due to localized $5f$ electrons, thus predicting a relatively weak unaixal anisotropy in comparison to that of Refs. [198,221]. This necessitates further experimental attempts for the dynamic critical properties of uranium superconductors.

We conclude by noting that understanding the nature of magnetic phase transition near the critical point represents one of the central themes in modern condensed matter physics. The critical behavior of uranium ferromagnetic supercon-

ductors is particularly important due to the observed magnetically mediated superconductivity as well as the change in the nature of phase transition with applied pressure. It is interesting that the static critical exponents of uranium ferromagnetic superconductors can be captured by means of a nonlocal GL model Hamiltonian, as we have shown here. However, our model predictions for the dynamic critical exponents for uranium ferromagnetic superconductors need further experiments to investigate the spin dynamics of such systems near their critical points of the PM-FM phase transition. We hope, our work will inspire such experiments for the dynamic critical behavior.

Chapter 7

Anomalous Critical Behavior of Some Uniaxial Ferromagnets

Summary

We investigate the conserved critical dynamics govern by a model Hamiltonian involving screened nonlocal interaction in the quartic term. Employing Wilson's momentum shell decimation scheme, we carry out a dynamic renormalization-group analysis at one-loop order. This yields, the dynamic critical exponent z and the linewidth exponent ϖ as $z = 4 + \epsilon f_1(\sigma, w, n) + O(\epsilon^2)$, and $\varpi = 1 - \sigma + \epsilon f_2(\sigma, w, n) + O(\epsilon^2)$, where σ, w, and n are dimensionless quantities coming from the model parameters. The static critical exponents are found to agree well with the experimental measurements for uniaxial ferromagnets that behave anomalously and deviate from the expected logarithmic behavior. The corresponding dynamic exponents z and ϖ are also estimated by the present theory.

7.1 Introduction

Critical properties of non-equilibrium systems has attracted a lot of attention for many years owing to their appearance in many substances [89,166]. Systems that are

in the same static universality class can fall into different dynamic universality subclasses determined by conservation laws constraining how fluctuations dissipate. Theoretical investigations of dynamic critical phenomena for conserved order parameter begins from the pioneering work due to Kawasaki [113] who considers the transition mechanism of spins as nearest neighbour spin-pair exchange and studied the critical phenomena of the kinetic Ising model. Following Kawasaki's work, a considerable number of numerical works, mostly Monte-Carlo (MC) simulations, have been performed to investigate the critical behaviour of conserved systems.

A MC renormalization-group on the two dimensional Kawasaki model yields dynamic critical exponent $z = 3.80$ [245] which is close to the exact result $z = 3.75$ [112] in two dimensions. Further, Zheng [258] carried out a MC simulation on the two dimensional kinetic Ising model with conserved order parameter and found $z = 3.95$ which is higher than the usual 2D model B value $z = 4 - \eta = 3.75$.

Theoretical understanding of critical dynamics in uniaxial ferromagnets has been mainly based on the realization that an additional interaction, such as the dipole-dipole interaction, can lead to a qualitatively new behavior of the frequency and wave-vector dependences of the spin-spin correlation functions [59]. The Landau-Ginzburg (LG) free energy functional for an n-component uniaxial spin system with isotropic exchange coupling and dipolar interaction was investigated by means of renormalization-group (RG) analyses in Refs. [126,3,29,58,60] where a dipolar interaction term was introduced in the Gaussian term that suppresses the fluctuations in the z direction.

Larkin and Khmel'nitskii [126] considered the case of anisotropic dipolar interaction in uniaxial ferroelectric substances and obtained logarithmic corrections in three dimensions by means of a renormalized perturbation scheme. They obtained the specific heat $C \sim \ln^{1/3} |T - T_c|$ and susceptibility $\chi \sim (T_c - T)^{-1} \ln^{1/3} |T - T_c|$.

This result for susceptibility was fitted with the parallel susceptibility data in an experiment on $LiHoF_4$ [17] suggesting uniaxial nature of this ferromagnet. However the experiment could not discriminate between this logarithmic law and a power law with the susceptibility exponent $\gamma = 1.05$. Further experimental study [74] on $LiHoF_4$ exhibited a simple power law behavior for the spontaneous magnetization with $\beta = 0.355 \pm 0.005$. Bruce and Aharony [29] considered the dipolar interaction to be isotropic. Incorporating it in the quadratic term of the Hamiltonian, they carried out an RG analysis at two-loop order to obtain the critical exponents up to $O(\varepsilon^2)$ where $\varepsilon = 4 - d$. The corresponding results for $d = 3$ are shown in Table. 7.1 that are close to the the corresponding standard ϕ^4 results. However, assuming dipolar interaction to be anisotropic [3], RG calculations predicted a crossover from the Ising regime in $d < 3$ to dipolar regime $d > 3$ that reproduced Larkin and Khmel'nitskii's results for $d = 3$. Folk *et al.* [58] considered a generalized anisotropic problem and carried out an RG analyses for the corresponding unconserved and conserved dynamics. This yielded, for the uniaxial case, $z = 2 + c\eta$, and $z = 4 - \eta$, respectively, with $c = 0.92$ and $\eta = \frac{4(n+2)\varepsilon'^2}{9(n+8)^2} + O(\varepsilon'^3)$, where $\varepsilon' = 3 - d$. This indicates that the upper critical dimension is three so that the critical exponents acquire logarithmic corrections in three dimensions. This in fact gives back and Khmel'nitskii's result for χ.

The uniaxial ferromagnetic sample of TbF_3 was studied [28] for its static critical properties. Although simple power laws were not ruled out it was observed that the experimental data agreed well with the mean field behavior with logarthmic corrections as predicted by the above theories. Frey and Schwabl [60] considered the above problem with uniaxial anisotropy in the Gaussian term involving a parameter g and carried out a field-theoretic RG scheme at one loop order. They obtained a crossover form Ising regime to uniaxial dipolar regime with classical exponents

coupled with logarithmic corrections. Experimental data from measurements on specific heat and susceptibity for $LiTbF_4$ were found to be in good agreement with this theoretical prediction for an appropriate choice of the the parameter g.

While the pure (undoped) uniaxial ferromagnetic samples (for example, TbF_3 $LiTbF_4$ and presumably other pure uniaxial ferromagnets) [28,62] exhibit consistency with the theoretically predicted logarithmic behavior coupled with mean field exponents, there exists impure (doped) uniaxial ferromagnetic compounds, that do not exhibit logarithmic behavior. For example, for the doped samples $LiTb_{1-x}Y_xF_4$, experiments exhibit power laws (instead of logarithmic behavior) for the susceptibility (and presumably other quantities). The exponents vary with doping concentration x as shown in Table. 7.1. Other doped uniaxial ferromagnets that have attracted considerable interest in recent past due to their importance as efficient laser host materials are $LiY_{1-x}R_xF_4$ series, where R is a rare earth element [18,141]. In these samples the measured susceptibility exponent γ are found to depends on the impurity concentration x. It was also suggested that increasing doping concentration may lead to a stronger departure [18] from the log laws giving unusual susceptibility exponent.

Critical phenomena in uniaxial ferromagnetic systems have been explored over the decades via a number of experiments in widely different systems [217,231,232]. One such example that exhibits uniaxial ferromagnetic behavior is copper ammonium bromide, $Cu(NH_4)_2Br_4.2H_2O$ [231,232]. It was also shown that $CuRb_2Br_4.2H_2O$ and $CuK_2Cl_4.2H_2O$ exhibit similar magnetic behavior. The experimental values for the static critical exponents, (namely, β, γ, δ and α), although have been compared with the 3D Heisenberg model, the γ and δ values for these three isomorphous salts undergo measurable deviation from those of the 3D Heisenberg values as shown in Table 7.1. Table also shows departure of these experimental critical exponents

Table 7.1: Available experimental estimates for critical exponents β, γ, and δ for doped and undoped uniaxial ferromagnets, including some isomorphous salts. For comparison, existing theoretical predictions are also displayed.

Sample or Theory	Ref.	β	γ	δ
$LiTb_{1-x}Y_xF_4$ $[0.127 \leqslant x \leqslant 0.7]$	[17,122]	–	$[1.088, 1.80]$	–
$Gd_xNd_{1-x}Cl_3$ $[0.028 \leqslant x \leqslant 0.122]$	[122]	–	$[1.043, 1.057]$	–
$Gd_{0.963}La_{0.037}Cl_3$	[122]	–	1.043	–
$Cu(NH_4)_2Br_4.2H_2O$	[231]	$0.38(1)$	$1.26(1)$	$4.3(2)$
$Cu(NH_4)_2Br_4.2H_2O$	[232]	$0.375(8)$	$1.275(17)$	$4.21(5)$
$CuK_2Cl_4.2H_2O$	[232]	$0.354(10)$	$1.28(1)$	$4.4(15)$
$CuRb_2Br_4.2H_2O$	[232]	$0.373(7)$	$1.29(1)$	$4.20(7)$
CrO_2 film	[247]	0.370	1.40	–
$LiHoF_4$	[17,74]	$0.355(5)$	$1.05(1)$	–
3D Heisenberg	[107]	0.367	1.388	4.78
3D Ising	[107]	0.326	1.238	4.80
2D ising	[94]	0.125	1.75	15
Isotropic dipolar (RG)	[29]	0.381	1.372	4.454

from the values predicted by the isotropic dipolar model [29].

In addition to the above examples, phase transition in a thin magnetic film (thickness~ 5000Å) [247] has been studied due to their high technological demands, for example, as magnetic storage devices. From the theoretical point of view, in strictly 2D isotropic systems with continuous symmetry and SR interaction, the conventional LR order is excluded due to the Mermin-Wagner theorem [147]. However, a satisfactory theoretical explanation for the phase transition in such systems is still lacking as they exhibit a variety of new and interesting phases due to the combination of various anisotropies, dipole-dipole interaction, and enhanced importance of thermal fluctuations [168,9,8].

The above situations point to the fact that a suitable theoretical explanation is needed for doped uniaxial ferromagnets and isomorphous salts that do not exhibit logarithmic behavior. Since the predictions for the critical exponents given by the

existing theories do not agree with those of the experimental estimates (as shown in Table 7.1), it is worthwhile to look for a different theory in the hope of reasonable theoretical predictions. As a candidate for such a theory, we take the nonlocal model Hamiltonian of Ch. 5 and explore in detail how the ensuing static critical exponents fare in terms of predictability. The order parameter in uniaxial ferromagnets is expected to be conserve as argued in Ref.[79]. Consequently, we explore the conserved dynamics govern by this model Hamiltonian and calculate the dynamic critical exponents z and ϖ. For the purpose of comparison we also present the corresponding unconserved dynamic critical exponents z' and ϖ' so that any future experiments on the dynamic properties would validate (or invalidate) these dynamic exponents.

In this Chapter, we investigate the conserved critical dynamics govern by a model Hamiltonian incorporating a screened nonlocal interaction in the quartic term. Carrying out a dynamic RG calculation via momentum shell decimation scheme at one-loop order, we find that the dynamic critical exponents z and ϖ lie in the range $3.871 < z < 4.027$ and $1.5 < \varpi < 2.046$ respectively in three dimensions. We also find satisfactory agreements with the experimentally observed static critical exponents for the above-mentioned samples.

7.2 Conserved Screened Nonlocal Dynamics

Conserved critical dynamics of an n-component order parameter $\phi_i(\mathbf{x},t)$ is governed by the equation of motion[89]

$$\frac{\partial}{\partial t}\phi_i(\mathbf{x},t) = \Gamma_0\nabla^2\frac{\delta H}{\delta\phi_i(\mathbf{x},t)} + \eta_i(\mathbf{x},t), \tag{7.1}$$

where $\eta_i(\mathbf{x},t)$ is a Gaussian white noise with correlations

$$\langle \eta_i(\mathbf{x},t)\rangle = 0, \tag{7.2}$$

$$\langle \eta_i(\mathbf{x},t)\eta_j(\mathbf{x}',t')\rangle = -2\Gamma_0\nabla^2\delta^d(\mathbf{x}-\mathbf{x}')\delta(t-t')\delta_{ij}. \tag{7.3}$$

We bring nonlocality in space through the quartic term of the GL free energy functional H expressed by the equation

$$H = \sum_{i=1}^{n}\int d^dx\ dt\left[\frac{c_0}{2}|\nabla\phi_i(\mathbf{x},t)|^2 + \frac{r_0}{2}\phi_i^2(\mathbf{x},t) + \sum_{j=1}^{n}\int d^dx'\ dt'\phi_i^2(\mathbf{x},t)u(\mathbf{x}-\mathbf{x}')\delta(t-t')\phi_j^2(\mathbf{x}',t')\right], \tag{7.4}$$

with d the space dimension and $u(\mathbf{x}-\mathbf{x}')$ is the nonlocal coupling function. In order to perform the momentum shell decimation scheme, we use the $(d+1)$ dimensional Fourier transform for the fields

$$\psi_i(\mathbf{x},t) = \int \frac{d^dk}{(2\pi)^d}\frac{d\omega}{2\pi}\psi_i(\mathbf{k},\omega)e^{i(\mathbf{k}\cdot\mathbf{x}-\omega t)}, \tag{7.5}$$

where $\psi_i(\mathbf{x},t)$ is either $\phi_i(\mathbf{x},t)$, $\eta_i(\mathbf{x},t)$, or $u(\mathbf{x})$. Using this definition, together with Eq. (7.4), we write the governing dynamics [Eq. (7.1)] in the Fourier-space as

$$\left[\frac{-i\omega}{\Gamma_0k^2} + r_0 + c_0k^2\right]\phi_i(\mathbf{k},\omega) = \frac{\eta_i(\mathbf{k},\omega)}{\Gamma_0k^2} - 4\sum_{j=1}^{n}\int\frac{d^dk_1d\omega_1}{(2\pi)^{d+1}}\int\frac{d^dk_2d\omega_2}{(2\pi)^{d+1}}u(\mathbf{k}_1-\mathbf{k})\phi_i(\mathbf{k}_1,\omega_1) \times \phi_j(\mathbf{k}_2,\omega_2)\phi_j(\mathbf{k}-\mathbf{k}_1-\mathbf{k}_2,\omega-\omega_1-\omega_2), \tag{7.6}$$

where momentum integrations have an ultraviolet cut-off Λ because of finite lattice constant a related as $\Lambda \sim a^{-1}$. Thus the order parameter $\phi_i(\mathbf{x},t)$ contains the variations smaller than Λ. We choose the coupling function $u(\mathbf{p})$ to have the form

$$u(\mathbf{p}) = \frac{\lambda_0}{[\mathbf{p}^2+m^2]^\sigma}, \tag{7.7}$$

where λ_0 is the coupling constant and m is the screening parameter. To carry out momentum shell decimation in the next section, we write the Fourier transformed expression for the noise-noise correlation as

$$\langle \eta_i(\mathbf{k},\omega)\eta_j(\mathbf{k}',\omega')\rangle = 2\Gamma_0 k^2 (2\pi)^{d+1}\delta^d(\mathbf{k}+\mathbf{k}')\delta(\omega+\omega')\delta_{ij}. \tag{7.8}$$

7.3 Momentum Shell Decimation

From Eq. (7.6), we eliminate small scale modes $\phi_i^>(\mathbf{k},\omega)$ lying in the momentum range $\frac{\Lambda}{b} \leqslant k \leqslant \Lambda$ [139,79,81,89]. This mode elimination yields the dynamical equation in terms of the large scale modes $\phi_i^<(\mathbf{k},\omega)$ in the reduced range $0 \leqslant k \leqslant \frac{\Lambda}{b}$ as

$$\left[\frac{-i\omega}{\Gamma_0 k^2} + r_0 + c_0 k^2\right]\phi_i^<(\mathbf{k},\omega) = \frac{\eta_i^<(\mathbf{k},\omega)}{\Gamma_0 k^2} - 4\sum_{j=1}^{n}\int \frac{d^dk_1}{(2\pi)^d}\frac{d\omega_1}{2\pi}\int \frac{d^dk_2}{(2\pi)^d}\frac{d\omega_2}{2\pi}u(\mathbf{k}_1-\mathbf{k})$$

$$\phi_i^<(\mathbf{k}_1,\omega_1)\phi_j^<(\mathbf{k}_2,\omega_2)\phi_j^<(\mathbf{k}-\mathbf{k}_1-\mathbf{k}_2,\omega-\omega_1-\omega_2) + R_i(\mathbf{k},\omega) + \Upsilon_i(\mathbf{k},\omega), \tag{7.9}$$

where

$$R_i(\mathbf{k},\omega) = -(\Sigma_a+\Sigma_b)\phi_i^<(\mathbf{k},\omega)$$

with the self-energy corrections at one-loop order

$$\Sigma_a = 8n\int \frac{d^dq}{(2\pi)^d}\frac{d\Omega}{2\pi}\frac{u(\mathbf{0})}{\Gamma_0 q^2}|G_0^>(\mathbf{q},\Omega|^2, \tag{7.10}$$

$$\Sigma_b(\mathbf{k},\omega) = 16\int \frac{d^dq}{(2\pi)^d}\frac{d\Omega}{2\pi}\frac{u(\mathbf{k}_1-\mathbf{k})}{\Gamma_0 q^2}|G_0^>(\mathbf{q},\Omega)|^2. \tag{7.11}$$

where $G_0(\mathbf{k},\omega) = \left(\frac{-i\omega}{\Gamma_0 k^2} + r_0 + c_0 k^2\right)^{-1}$ is the bare propagator. The Feynman diagrams for these self-energy corrections are same as those of Ch. 6 (cf. Fig. 6.1). Frequency integrations in the above self-energy Eqs. (7.10) and (7.11) runs from $-\infty$ to $+\infty$ whereas the momentum integrations are restricted in the shell $\Lambda/b < q < \Lambda$. To evaluate these integrals, we first perform the frequency convolutions and sub-

sequently the momentum integrations. This yields

$$\Sigma_a(\mathbf{0},0) = \frac{4nS_d\lambda_0}{c_0 m^{2\sigma}[2\pi]^d}\left[\left(\frac{b^{2-d}-1}{2-d}\right)\Lambda^{d-2} - \frac{r_0}{c_0}\left(\frac{b^{4-d}-1}{4-d}\right)\Lambda^{d-4}\right], \tag{7.12}$$

in the large-scale long-time limit ($k \to 0, \omega \to 0$). The integrand in $\Sigma_b(\mathbf{k},\omega)$ is expanded in the limit $q >> k$ to yield

$$\Sigma_b(\mathbf{k},0) = \frac{8S_d\lambda_0}{c_0[2\pi]^d}\left[\left(\frac{b^{2-d+2\sigma}-1}{2-d+2\sigma}\right)\Lambda^{d-2-2\sigma} - \left(\frac{r_0}{c_0}+\sigma m^2\right)\left(\frac{b^{4-d+2\sigma}-1}{4-d+2\sigma}\right)\Lambda^{d-4-2\sigma}\right]$$
$$+ \frac{8S_d\lambda_0}{c_0[2\pi]^d}k^2\left[\frac{\sigma(2\sigma+2-d)}{d}\left(\frac{b^{4-d+2\sigma}-1}{4-d+2\sigma}\right)\Lambda^{d-4-2\sigma}\right], \tag{7.13}$$

in the large scale long-time, where $S_d = 2\pi^{d/2}/\Gamma(d/2)$ is the surface area of a unit sphere in the d-dimensional space. Due to the above momentum shell decimation process, the bare parameters r_0, and c_0 acquire corrections. Corrections to the bare parameters r_0 and c_0 are obtained as

$$\Delta r = \frac{4nS_d\lambda_0}{c_0 m^{2\sigma}[2\pi]^d}\left[\left(\frac{b^{2-d}-1}{2-d}\right)\Lambda^{d-2} - \frac{r_0}{c_0}\left(\frac{b^{4-d}-1}{4-d}\right)\Lambda^{d-4}\right]$$
$$+ \frac{8S_d\lambda_0}{c_0[2\pi]^d}\left[\left(\frac{b^{2-d+2\sigma}-1}{2-d+2\sigma}\right)\Lambda^{d-2-2\sigma} - (\frac{r_0}{c_0}+\sigma m^2)\left(\frac{b^{4-d+2\sigma}-1}{4-d+2\sigma}\right)\Lambda^{d-4-2\sigma}\right], \tag{7.14}$$

and

$$\Delta c = \frac{8\sigma(2\sigma+2-d)S_d\lambda_0}{c_0 d[2\pi]^d}\left[\left(\frac{b^{4-d+2\sigma}-1}{4-d+2\sigma}\right)\Lambda^{d-4-2\sigma}\right], \tag{7.15}$$

respectively. It may be noted that the correction $\Delta\Gamma = 0$ at this order of calculation because no term proportional to $-i\omega/k^2$ is generated in the large scale long-time limit.

We also obtain corrections to the bare coupling λ_0 from the following integrals. The Feynman diagrams for which are same as those of Ch. 6 (cf. Fig. 6.2)

$$\Upsilon_a = 64n\sum_{j=1}^{n}\int\frac{d^dk_1d\omega_1}{[2\pi]^{d+1}}\int\frac{d^dk_2d\omega_2}{[2\pi]^{d+1}}u(\mathbf{k}_1-\mathbf{k})\phi_i^<(\mathbf{k}_1,\omega_1)\phi_j^<(\mathbf{k}_2,\omega_2)$$

$$\phi_j^<(\mathbf{k}-\mathbf{k}_1-\mathbf{k}_2,\omega-\omega_1-\omega_2)\int\frac{d^dqd\Omega}{[2\pi]^{d+1}}\frac{u(\mathbf{k}_1-\mathbf{k})}{\Gamma_0q^2}|G_0^>(\mathbf{q},\Omega)|^2G_0^>(\mathbf{k}-\mathbf{k}_1-\mathbf{q},\omega-\omega_1-\Omega), \tag{7.16}$$

$$\Upsilon_b = 256\sum_{j=1}^{n}\int\frac{d^dk_1d\omega_1}{[2\pi]^{d+1}}\int\frac{d^dk_2d\omega_2}{[2\pi]^{d+1}}u(\mathbf{k}_1-\mathbf{k})\phi_i^<(\mathbf{k}_1,\omega_1)\phi_j^<(\mathbf{k}_2,\omega_2)$$

$$\times\phi_j^<(\mathbf{k}-\mathbf{k}_1-\mathbf{k}_2,\omega-\omega_1-\omega_2)\int\frac{d^dqd\Omega}{[2\pi]^{d+1}}\frac{u(\mathbf{q}-\mathbf{k}+\mathbf{k}_1+\mathbf{k}_2)}{\Gamma_0q^2}|G_0^>(\mathbf{q},\Omega)|^2$$

$$\times G_0^>(\mathbf{k}-\mathbf{k}_1-\mathbf{q},\omega-\omega_1-\Omega), \tag{7.17}$$

$$\Upsilon_c = 256\sum_{j=1}^{n}\int\frac{d^dk_1d\omega_1}{[2\pi]^{d+1}}\int\frac{d^dk_2d\omega_2}{[2\pi]^{d+1}}\phi_i(\mathbf{k}_1,\omega_1)\phi_j(\mathbf{k}_2,\omega_2)\phi_j(\mathbf{k}-\mathbf{k}_1-\mathbf{k}_2,\omega-\omega_1-\omega_2)$$

$$\times\int\frac{d^dqd\Omega}{[2\pi]^{d+1}}\frac{u(\mathbf{q}-\mathbf{k})u(\mathbf{q}-\mathbf{k}_1)}{\Gamma_0q^2}|G_0(\mathbf{p},\Omega)|^2G_0(\mathbf{k}_1+\mathbf{k}_2-\mathbf{q},\omega_1+\omega_2-\Omega). \tag{7.18}$$

Performing the frequency and momentum integrations appearing in the above expressions for Υ_a and Υ_b, we obtain the correction $\Delta\lambda$ to λ_0 as

$$\Delta\lambda = -\frac{4nS_d\lambda_0^2}{c_0^2m^{2\sigma}[2\pi]^d}\left[\left(\frac{b^{4-d}-1}{4-d}\right)\Lambda^{d-4}-\frac{2r_0}{c_0}\left(\frac{b^{6-d}-1}{6-d}\right)\Lambda^{d-6}\right]$$

$$-\frac{16S_d\lambda_0^2}{c_0^2[2\pi]^d}\left[\left(\frac{b^{4-d+2\sigma}-1}{4-d+2\sigma}\right)\Lambda^{d-4-2\sigma}-\left(\frac{2r_0}{c_0}+\sigma m^2\right)\left(\frac{b^{6-d+2\sigma}-1}{6-d+2\sigma}\right)\Lambda^{d-6-2\sigma}\right] \tag{7.19}$$

in the $k\to0,\omega\to0$ limit.

We note that Υ_c is irrelevant and it does not contribute to $\Delta\lambda$ because it does not generate a correction in a form proportional to the original vertex factor.

7.4 Renormalization-Group Transformation

The momentum shell decimation process carried out in the previous section reduces the momentum range to $0\leqslant k\leqslant\frac{\Lambda}{b}$. To get the full momentum range we rescale $\mathbf{k}'=b\mathbf{k}$, $\omega'=b^z\omega$, and $\Phi'(\mathbf{k}',\omega')=\zeta^{-1}\Phi(\mathbf{k},\omega)$. The field rescaling factor ζ is

found to follow the relation

$$\zeta = b^{1+d/2+z-\eta/2}, \tag{7.20}$$

as obtained from the two-point dynamic spin-spin correlation at the critical point, where η is the Fisher's exponent. Thus incorporating the corrections to r_0, c_0, and λ_0 given by Eqs. (7.14), (7.15), and (7.19), we obtain the RG recursion relations as

$$\Gamma' = b^{z-4+\eta}\Gamma_0, \tag{7.21}$$

$$r' = b^{2-\eta}\left[r_0 + \frac{4n\lambda_0 S_d}{m^{2\sigma}[2\pi]^d}\left\{\frac{(b^{2-d}-1)\Lambda^{d-2}}{c_0(2-d)} - \frac{r_0}{c_0^2}\frac{(b^{4-d}-1)\Lambda^{d-4}}{(4-d)}\right\}\right.$$
$$\left. + \frac{8\lambda_0 S_d}{[2\pi]^d}\left\{\frac{(b^{2\sigma+2-d}-1)\Lambda^{d-2\sigma-2}}{c_0(2\sigma+2-d)} - \left(\frac{r_0}{c_0^2}+\frac{\sigma m^2}{c_0}\right)\frac{(b^{2\sigma+4-d}-1)\Lambda^{d-2\sigma-4}}{(2\sigma+4-d)}\right\}\right], \tag{7.22}$$

$$c' = b^{-\eta}\left[c_0 + \frac{8\sigma(2-d+2\sigma)\lambda_0 S_d}{d[2\pi]^d}\frac{(b^{4-d+2\sigma}-1)\Lambda^{d-4-2\sigma}}{c(4-d+2\sigma)}\right], \tag{7.23}$$

$$\lambda' = b^{4-d-2\eta+2\sigma}\left[\lambda_0 - \frac{4n\lambda_0^2}{m^{2\sigma}}\frac{S_d}{[2\pi]^d}\left\{\frac{(b^{4-d}-1)\Lambda^{d-4}}{c_0^2(4-d)} - \frac{2r_0}{c_0^3}\frac{(b^{6-d}-1)\Lambda^{d-6}}{(6-d)}\right\}\right.$$
$$\left. -16\lambda_0^2\frac{S_d}{[2\pi]^d}\left\{\frac{(b^{4-d+2\sigma}-1)\Lambda^{d-4-2\sigma}}{c_0^2(4-d+2\sigma)} - \left(\frac{\sigma m^2}{c_0^2}+2\frac{r_0}{c_0^3}\right)\frac{(b^{6-d+2\sigma}-1)\Lambda^{d-6-2\sigma}}{(6-d+2\sigma)}\right\}\right], \tag{7.24}$$

Assuming $b = e^{\delta l}$, the above recursion relations can be transformed into continuous flow equations as

$$\frac{d\Gamma}{dl} = (z-4+\eta)\Gamma, \tag{7.25}$$

$$\frac{dr}{dl} = (2-\eta)r + \frac{4n\lambda S_d}{m^{2\sigma}(2\pi)^d}\left(\frac{\Lambda^{d-2}}{c} - \frac{r}{c^2}\Lambda^{d-4}\right)$$
$$+\frac{8\lambda S_d}{(2\pi)^d}\left[\frac{\Lambda^{d-2-2\sigma}}{c} - \left(\frac{r}{c^2}+\frac{\sigma m^2}{c}\right)\Lambda^{d-4-2\sigma}\right], \tag{7.26}$$

$$\frac{dc}{dl} = -\eta c + \frac{8\sigma(2\sigma+2-d)\lambda S_d}{d(2\pi)^d}\frac{\Lambda^{d-4-2\sigma}}{c}, \tag{7.27}$$

$$\frac{d\lambda}{dl} = (4-d-2\eta+2\sigma)\lambda - \frac{4n\lambda^2 S_d}{m^{2\sigma}(2\pi)^d}\left(\frac{\Lambda^{d-4}}{c^2} - \frac{2r}{c^3}\Lambda^{d-6}\right) - \frac{16\lambda^2 S_d}{(2\pi)^d}\left[\frac{\Lambda^{d-4-2\sigma}}{c^2} - \left(\frac{2r}{c^3} + \frac{\sigma m^2}{c^2}\right)\Lambda^{d-6-2\sigma}\right]. \tag{7.28}$$

7.5 Fixed Point and Critical Exponents

The RG flow equations, given by Eqs. (7.26), (7.28), (7.27), and (7.25) suggest the existence of a non-trivial fixed point $r \to r^*$, $\lambda \to \lambda^*$, $c \to c^* = c$, and $\Gamma_0 \to \Gamma_0^* = \Gamma_0$, corresponding to

$$\frac{r^*}{c} = -\frac{(4-d-2\eta+2\sigma)\left\{\frac{4n}{w^\sigma}+8(1-\sigma w)\right\}\Lambda^2}{(2-\eta)\left\{\frac{4n}{w^\sigma}+16(1-\sigma w)\right\} - (4-d-2\eta+2\sigma)(\frac{4n}{w^\sigma}+8)}, \tag{7.29}$$

and

$$\frac{\lambda^*}{c^2} = \frac{(4-d-2\eta+2\sigma)\Lambda^{4-d+2\sigma}}{\frac{S_d}{(2\pi)^d}\left\{\frac{4n}{w^\sigma}+16(1-\sigma w)\right\}}, \tag{7.30}$$

where $w = m^2/\Lambda^2$. A linear stability analysis indicates that the above fixed point is stable for values of σ lying in the range $-0.5 \leqslant \sigma \leqslant 0.5$ in three dimensions.

We calculate the critical exponents in an ϵ expansion scheme with the identification

$$\epsilon = d_c - d = 4 + 2\sigma - d. \tag{7.31}$$

The Fisher exponent η is calculated in the leading order of ϵ as

$$\eta = -\frac{2\sigma\epsilon}{(\sigma+2)\left[\frac{n}{w^\sigma}+4(1-\sigma w)\right]-4\sigma} + O(\epsilon^2). \tag{7.32}$$

Further, the correlation length exponent exponent ν is calculated as

$$\nu = \frac{1}{2} + \frac{\epsilon(\frac{n}{w^\sigma}+2)}{2\left(\frac{n}{w^\sigma}+4(1-\sigma w)\right)}\left\{\frac{1}{2} + \frac{2\sigma}{(\sigma+2)\left[\frac{n}{w^\sigma}+4(1-\sigma w)\right]-4\sigma}\right\}$$

$$-\frac{\sigma\epsilon}{2(\sigma+2)\left[\frac{n}{w^\sigma}+4(1-\sigma w)\right]-8\sigma}+O(\epsilon^2). \tag{7.33}$$

The other static critical exponents, namely, the spontaneous magnetization exponent β, susceptibility exponent γ, critical isotherm exponent δ, and specific heat exponent α, are also calculated from the standard scaling laws (cf. Sec. 1.2), and they are obtained as

$$\beta=\frac{\sigma+1}{2}-\frac{\epsilon}{4}\left[1+\frac{2\sigma(\sigma+2)}{(\sigma+2)\left[\frac{n}{w^\sigma}+4(1-\sigma w)\right]-4\sigma}-\frac{(\frac{n}{w^\sigma}+2)(2\sigma+2)}{\frac{n}{w^\sigma}+4(1-\sigma w)}\times\right.$$
$$\left.\times\left\{\frac{1}{2}+\frac{2\sigma}{(\sigma+2)\left[\frac{n}{w^\sigma}+4(1-\sigma w)\right]-4\sigma}\right\}\right]+O(\epsilon^2), \tag{7.34}$$

$$\gamma=1+\frac{\epsilon(\frac{n}{w^\sigma}+2)}{\frac{n}{w^\sigma}+4(1-\sigma w)}\left[\frac{1}{2}+\frac{2\sigma}{(\sigma+2)\left[\frac{n}{w^\sigma}+4(1-\sigma w)\right]-4\sigma}\right]+O(\epsilon^2), \tag{7.35}$$

$$\delta=\frac{\sigma+3}{\sigma+1}+\frac{\epsilon}{\sigma+1}\left[\frac{1}{\sigma+1}+\frac{2\sigma(\sigma+2)}{(\sigma+1)\left[(\sigma+2)\left\{\frac{n}{w^\sigma}+4(1-\sigma w)\right\}-4\sigma\right]}\right]+O(\epsilon^2). \tag{7.36}$$

$$\alpha=\frac{\epsilon+4}{2}-(\sigma+2)\left[1+\frac{\epsilon(\frac{n}{w^\sigma}+2)}{\frac{n}{w^\sigma}+4(1-\sigma w)}\left\{\frac{1}{2}+\frac{2\sigma}{(\sigma+2)\left[\frac{n}{w^\sigma}+4(1-\sigma w)\right]-4\sigma}\right\}\right.$$
$$\left.-\frac{\sigma\epsilon}{(\sigma+2)\left[\frac{n}{w^\sigma}+4(1-\sigma w)\right]-4\sigma}\right]+O(\epsilon^2) \tag{7.37}$$

We see that these results are same as those of Ch. 5, wherein we studied the analysis of a nonconserved dynamics. To see something different, we shall calculate the dynamic exponents z and ϖ which is the focus of this Chapter. We thus calculate from Eq. (7.25) the dynamic critical exponent z as

$$z=4+\frac{2\sigma\epsilon}{(\sigma+2)\left[\frac{n}{w^\sigma}+4(1-\sigma w)\right]-4\sigma}+O(\epsilon^2). \tag{7.38}$$

The graphical plots for the dynamic critical exponent z are shown in Fig. 7.1. We see that z show slow variations with respect to the model parameters, namely, the

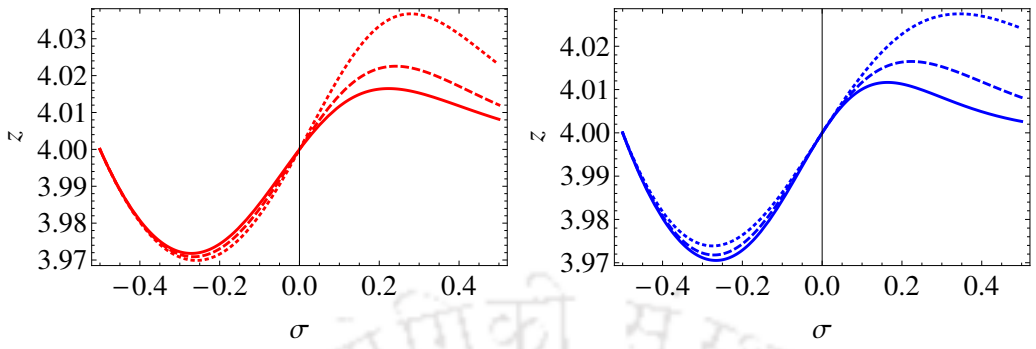

Figure 7.1: Critical exponent z for (a) varying n where the dotted, dashed, and solid curves correspond to $n = 1, 2$, and 3. (b) varying w where the dotted, dashed, and solid curves correspond to $w = 0.0001, 0.001$, and 0.01, respectively.

number of component n and the screening parameter w in the negative regime of σ where we find most of the experimental estimates for uniaxial ferromagnetic compounds. In order to calculate the linewidth exponent ϖ, we use Eqs. (7.32), (7.33), and (7.38) to obtain

$$\varpi = (1-\sigma+\epsilon/2)+(1-\sigma)\epsilon\frac{(\frac{n}{w^\sigma}+2)}{(\frac{n}{w^\sigma}+4(1-\sigma w))}\left\{\frac{1}{2}+\frac{2\sigma}{(\sigma+2)\left[\frac{n}{w^\sigma}+4(1-\sigma w)\right]-4\sigma}\right\}+$$
$$+\frac{\sigma\epsilon(1+\sigma)}{(\sigma+2)\left[\frac{n}{w^\sigma}+4(1-\sigma w)\right]-4\sigma}+O(\epsilon^2). \tag{7.39}$$

Graphical plots for ϖ are shown in Fig. 7.2, indicating slow variations with respect to n and w. Further, the exponent νz, related to the characteristic time scale as $\tau \propto |T-T_c|^{-z\nu}$, is obtain as

$$\nu z = 2-\frac{\sigma\epsilon}{(\sigma+2)\left[\frac{n}{w^\sigma}+4(1-\sigma w)\right]-4\sigma}+\frac{2\epsilon(\frac{n}{w^\sigma}+2)}{\left(\frac{n}{w^\sigma}+4(1-\sigma w)\right)}\times$$
$$\times\left\{\frac{1}{2}+\frac{2\sigma}{(\sigma+2)\left[\frac{n}{w^\sigma}+4(1-\sigma w)\right]-4\sigma}\right\}+O(\epsilon^2), \tag{7.40}$$

For the purpose of comparison, we also present the dynamic critical exponent z' and the linewidth exponent ϖ' for the case of nonconserved order parameter as

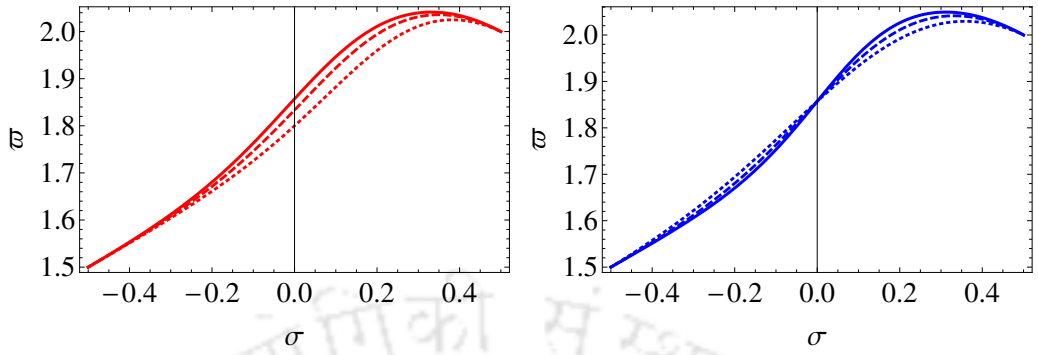

Figure 7.2: Plots for ϖ. Fig. (a) shows the variation of ϖ with n for $w = 0.001$, dotted, dashed, and solid curves correspond to $n = 1, 2$, and 3 and Fig. (b) shows the variation of ϖ with w for $n = 1$ in $d = 3$, dotted, dashed, and solid curves correspond to $w = 0.0001, 0.001$, and 0.01.

calculated in Ch. 5, given by

$$z' = 2 + \frac{2\sigma\epsilon}{(\sigma+2)\left[\frac{n}{w^\sigma} + 4(1-\sigma w)\right] - 4\sigma} + O(\epsilon^2), \tag{7.41}$$

$$\varpi' = -\sigma + \epsilon\left[\frac{1}{2} + \frac{\sigma}{(\sigma+2)\left\{\frac{n}{w^\sigma} + 4(1-\sigma w)\right\} - 4\sigma}\left\{(2+\sigma) - \frac{2\sigma(\frac{n}{w^\sigma}+2)}{\left\{\frac{n}{w^\sigma} + 4(1-\sigma w)\right\}}\right\}\right] - \epsilon\left[\frac{\sigma(\frac{n}{w^\sigma}+2)}{2\left\{\frac{n}{w^\sigma} + 4(1-\sigma w)\right\}}\right] + O(\epsilon^2), \tag{7.42}$$

and

$$(\nu z)' = 1 + \frac{\epsilon(\frac{n}{w^\sigma}+2)}{\left(\frac{n}{w^\sigma} + 4(1-\sigma w)\right)}\left\{\frac{1}{2} + \frac{2\sigma}{(\sigma+2)\left[\frac{n}{w^\sigma} + 4(1-\sigma w)\right] - 4\sigma}\right\} + O(\epsilon^2). \tag{7.43}$$

Tables 7.2 and 7.3 show the values of z' and ϖ' in addition to z and w and the static critical exponents for uniaxial ferromagnets. All these values are calculated from the above expressions taking $n = 1$, and $d = 3$.

Table 7.2: Experimental estimates for available critical exponents for doped uniaxial ferromagnetic samples and their comparison with the predictions following from the present theory. The exponents β, γ, δ, α, z, ϖ, z' ϖ', νz, and $(\nu z)'$ are calculated from Eqs. (7.34)–(7.43) for $n = 1$ and $d = 3$.

σ	Experimental sample	Ref.	β	γ	δ	α	z	ϖ	z'	ϖ'	νz	$(\nu z)'$
-0.386			0.273	1.047	4.769	0.407	3.978	1.558	1.978	0.5001	2.105	1.047
	$Gd_{0.972}Nd_{0.028}Cl_3$	[122]	$--$	1.047 ± 0.005	$--$	$--$						
-0.374			0.276	1.052	4.742	0.396	3.977	1.565	1.977	0.5007	2.116	1.052
	$Gd_{0.931}Nd_{0.069}Cl_3$	[122]	$--$	1.052 ± 0.006	$--$	$--$						
-0.363			0.279	1.057	4.716	0.386	3.978	1.570	1.976	0.501	2.127	1.057
	$Gd_{0.878}Nd_{0.122}Cl_3$	[122]	$--$	1.057 ± 0.003	$--$	$--$						
-0.394			0.271	1.043	4.788	0.414	3.979	1.554	1.979	0.5005	2.097	1.043
	$Gd_{0.963}La_{0.037}Cl_3$	[122]	$--$	1.043 ± 0.010	$--$	$--$						
-0.300			0.293	1.088	4.572	0.326	3.971	1.604	1.971	0.502	2.191	1.088
	$LiTb_{0.873}Y_{0.127}F_4$	[122]	$--$	1.088 ± 0.003	$--$	$--$						
-0.096			0.356	1.215	4.161	0.073	3.983	1.728	1.982	0.504	2.439	1.215
	$LiTb_{0.5}Y_{0.5}F_4$	[18]	$--$	1.215 ± 0.01	$--$	$--$						
0.373			0.780	1.800	3.424	-1.360	4.033	2.025	2.033	0.241	3.583	1.801
	$LiTb_{0.3}Y_{0.7}F_4$	[18]	$--$	1.80 ± 0.04	$--$	$--$						

Table 7.3: Experimental estimates for available critical exponents for undoped uniaxial ferromagnets and their comparison with the predictions following from the present theory. The exponents β, γ, δ, α, z, ϖ, z' ϖ', νz, and $(\nu z)'$ are calculated from Eqs. (7.37)–(7.43) for $n = 1$ and $d = 3$.

σ	Experimental sample	Ref.	β	γ	δ	α	z	ϖ	z'	ϖ'	νz	$(\nu z)'$
-0.04			0.380	1.262	4.065	-0.021	3.992	1.768	1.992	0.503	2.528	1.296
	$Cu(NH_4)_2Br_4 . 2H_2O$	[231]	0.38(1)	1.26(1)	4.3(2)	0	$--$	$--$				
-0.050			0.375	1.253	4.082	-0.003	3.990	1.761	1.990	0.503	2.511	1.253
	$Cu(NH_4)_2Br_4 . 2H_2O$	[232]	0.375(8)	1.275(17)	4.21(5)	$--$	$--$	$--$				
-0.054			0.373	1.250	4.088	0.004	3.990	1.758	1.998	0.503	2.505	1.250
	$CuRb_2Br_4 . 2H_2O$	[232]	0.373(7)	1.29(1)	4.20(7)	$-0.041(14)$	$--$	$--$				
-0.10			0.354	1.212	4.178	0.080	3.992	1.726	1.990	0.503	2.434	1.212
	$CuK_2Cl_4 . 2H_2O$	[232]	0.354(10)	1.28(1)	4.4(15)	$--$	$--$	$--$				
-0.097			0.355	1.214	4.162	0.075	3.983	1.727	1.983	0.504	2.438	1.215
	$LiHoF_4$	[17,74]	0.355(5)	1.05(1)	$--$	$--$	$--$	$--$				
-0.006			0.371	1.245	4.099	0.014	3.989	1.754	1.989	0.504	2.589	1.294
	CrO_2	[247]	0.371 ± 0.005	1.43 ± 0.01	$--$	$--$						

7.6 Discussion and Conclusion

In this Chapter, we have explored the critical behavior of a dynamic model with a conserved order parameter where the dynamics is governed by a model Hamiltonian with a nonlocal screened interaction in the quartic term. The main motivation for taking up a model Hamiltonian different from the existing ones comes from the fact that there has so far been no satisfactory agreement of the critical exponents predicted by the existing theories to those estimated by experiments on doped uniaxial ferromagnets and isomorphous salts as shown in Table 7.1. We find that the static critical exponents for most of the doped uniaxial ferromagnets measured so far, are satisfactorily predictable in three dimensions, from the present nonlocal screened model Hamiltonian within a one-loop RG calculation, as displayed in Table 7.2. We also see from Table 7.3 that the static critical exponents for undoped uniaxial systems, namely, isomorphous salts, $LiHoF_4$, and a magnetic thin film (thickness $\sim 5000\text{Å}$) are also comparable with the present estimates and found to match satisfactorily with the experimental predictions. The thin film sample, having a thickness of $\sim 5000\text{Å}$, will roughly have about 500 lattice points spanning the thickness of the sample so that it may be considered to be a three dimensional sample.

Further from Table 7.1, we see that the experimentally measured γ values for a class of impure uniaxial ferromagnets, namely, $Gd_xNd_{1-x}Cl_3$ lie in the range $1.047 \leqslant \gamma \leqslant 1.057$ for $0.028 \leqslant x \leqslant 0.122$. This range of low values of γ is not reproducible by the existing theories as shown in Table 7.1. From Table 7.2, we see that these low values for γ are reproducible from the present nonlocal model Hamiltonian. The corresponding theoretical predictions for β and δ values are also shown in Table 7.2.

We however note that for the doped uniaxial ferromagnets $LiTb_{1-x}Y_xF_4$ [17],

the experimentally measured γ values turn out as $\gamma = 1.088 \pm 0.003$ for $x = 0.127$, $\gamma = 1.215 \pm 0.01$, for $x = 0.5$ and $\gamma = 1.80 \pm 0.04$ for $x = 0.7$. Although the second γ value is predictable form the 3D Ising model, the first and third γ values are not predictable by any existing theory as shown in Table 7.1. In fact, the third γ value was interpreted as a dramatic departure [18] in critical behavior for this class of samples giving evidence for a departure from the marginal dimensionality (that is $d_c = 3$) due to the the doping of non-magnetic impurities in place of magnetic ions. We show in Table 7.2 that all these three γ values are reproducible from the present model Hamiltonian. In addition, we display the corresponding β and δ values for these samples. We note that experimental values only for one critical exponent, namely, γ are currently available for the above impure uniaxial ferromagnets. The corresponding theoretically predicted β and δ values need further experiments to be conducted in the future for experimental verification.

In addition to displaying the experimental and theoretical static exponents in Tables 7.2 and 7.3 for various uniaxial ferromagnets, we also display the corresponding dynamic exponents z and ϖ (for the case of conserved dynamics) and z' and ϖ' (for the case of unconserved dynamics). As per arguments given in Ref. [79] the spin dynamics of a uniaxial ferromagnet is expected to obey a conserved dynamics in the sense of model B that we have primarily explored in this paper with the screened nonlocal Hamiltonian given by Eq. (7.4). Although there is no disagreement to this argument at the present time, we have displayed the dynamic exponents z' and ϖ' coming from the unconserved dynamics in the sense of model A govern by the screened nonlocal Hamiltonian given by Eq. (7.4). At the present time, there seems to be no experimental measurements for the dynamic exponents for these samples. The main motivation for displaying both types (conserved and unconserved) of dynamic exponents is due to the fact that there seems to be no

experimental research so far for the verification whether the spin dynamics is conserved or unconserved. Apart from the theoretical apprehension, it is of course very much important to verify the nature of dynamics by experimental measurements of the dynamic exponents z and ϖ (or z' and ϖ').

With advances in the experimental techniques, it seems possible to investigate the spin dynamics near the critical point of the PM-FM phase transition, particularly the linewidth exponent of the spin-spin correlation function for uniaxial ferromagnets. Such experimental progress will be helpful for a thorough understanding of the spin dynamics and to test the predictions from the available theory. We hope, our work will inspire such experiments to verify the validity of the model predictions.

Chapter 8

Critical Properties of Hexagonal Antiferromagnetic Manganites

Summary

We investigate the critical properties of a model Hamiltonian involving a four-spin long-range interaction together with energy-energy and energy-spin couplings. Employing Wilson's momentum shell decimation scheme at one loop order, we perform a renormalization-group analysis and obtain the critical exponents corresponding to the non-trivial fixed point invoking a double-expansion. We find that the specific heat exponent α lies in the *negative* range $-0.20 < \alpha < 0$ in the physically allowed range of the nonlocal parameter ρ in three dimensions. This is consistent with the range $-0.19 \leqslant \alpha \leqslant -0.09$ obtained in recent thermal measurements [164] in the vicinity of the Néel temperature for various experimental samples of hexagonal antiferromagnetic manganites.

8.1 Introduction

In this Chapter, we devote ourself to calculate the critical properties associated with the paramagnetic-to-antiferromagnetic (PM-AFM) phase transition in multiferroic

hexagonal manganites. Keeping in mind that spin-lattice interaction plays a dominant role in these systems, we aim at formulating a suitable model Hamiltonian in the presence of spin-lattice interaction and see how this model fares in predicting the experimental estimates. Before making an analytical attempt, we make an overview of the experimental and theoretical developments in these systems.

8.1.1 Spin-Lattice Coupling

In the present world of information storage and processing, substances such as colossal magnetoresistive compounds and multiferroic materials posses a great deal of technological applications [214,50,88]. In particular, most of the pervoskite manganites $R_{1-x}A_xMnO_3$ (where R and A represent rare earth and alkaline earth elements, respectively) exhibit colossal magnetoresistive behavior whereas the hexagonal manganites $RMnO_3$ belonging to the heavier lanthanides with smaller atomic radii (R =Ho, Er, Tm, Yb, Lu, Y, Sc, In), exhibit multiferroic behavior. Importance of coupling between spin and lattice degrees of freedom in these substances has been elucidated by various theoretical [148,184,224] and experimental [257,14,145,49,171,51] studies. Different samples of perovskite manganites undergo lattice distortion due to imposed strain for various species of R and A with varying values of concentration x as evident from a number of investigations [200,148,149,26]. In these systems, the spin degrees of freedom are coupled with the atomic displacements. Such a coupling is generated because the strength of exchange interaction depends on the separation between the spins [237,30,31]. The role of spin-lattice coupling in multiferroic hexagonal rare earth manganites ($RMnO_3$) has been explored recently in a series of experiments comprising imaging with second harmonic generation [55], neutron diffraction [160,169,127,128,51,35], inelastic neutron scattering [171,51], X-ray diffraction [95,128], thermal expansion measurements [41], ultrasound [184] and

resonant ultrasound spectroscopy[224]. Hexagonal manganites RMnO$_3$ undergo ferro-electric transition at high temperatures ($T_c \sim 900$ K) and antiferromagnetic transition at low temperatures ($T_N \sim 100$ k)[95,50,37]. A coupling between the magnetic and ferroelectric order parameters is likely to generate a strong spin-lattice coupling[171,199]. An evidence for the coupling between the ferroelectric and antiferromagnetic degrees of freedom in these systems has been obtained in the spatial map of both ferroelectric and antiferromagnetic domains via optical second harmonic generation[55]. In YMnO$_3$, an abrupt change of all structural parameters at the Néel temperature T_N has been observed through high resolution neutron diffraction[127], indicating a strong and direct evidence for spin-lattice coupling. A striking evidence for strong magnetoelastic coupling was inferred in similar studies[128] near T_N from exceptionally large atomic displacements for every atom within the unit cell in YMnO$_3$ and LuMnO$_3$. Inelastic neutron scattering measurements on single crystals of YMnO$_3$[171], HoMnO$_3$, YbMnO$_3$, and ScMnO$_3$[51] also provide evidence for a strong coupling between spin and lattice degrees of freedom in these multiferroic systems. Distinct anomalies in the dielectric constant and thermal expansion coefficients at the magnetic transition temperature (T_N) of HoMnO$_3$ revealed strong spin-lattice coupling[41]. A neutron diffraction experiment[35], studying the magnetoelastic effect in multiferroic YMnO$_3$, indicated that the lattice strain couples with the square of the order parameter. An ultrasonic investigation of the elastic constants of a single crystal YMnO$_3$ in the temperature range 2–150 K (both above and below T_N)[184] revealed stiffening anomalies in four out of the five elastic constants on passing through $T_N = 72.4$ K. To account for the anomalies, a coupling between the strain and the magnetic order parameter was assumed in the Landau free energy functional.

8.1.2 Critical Properties

Critical properties of the PM-AFM transition in hexagonal antiferromagnets have been investigated in various experiments [108,219,189,184,34,164]. In a recent high resolution measurement of specific heat in the vicinity of the Néel temperature [164], the exponent α was measured for single crystal RMnO$_3$ samples. This exponent was found to be *negative* and it varied from one sample to another. The measurements yielded, $\alpha = -0.09 \pm 0.01$ for ErMnO$_3$, $\alpha = -0.12 \pm 0.01$ for YMnO$_3$, $\alpha = -0.12 \pm 0.01$ for LuMnO$_3$, $\alpha = -0.14 \pm 0.01$ for HoMnO$_3$, $\alpha = -0.18 \pm 0.01$ for YbMnO$_3$, and $\alpha = -0.19 \pm 0.01$ for TmMnO$_3$. In addition, an ultrasonic investigation [184] on a single crystal YMnO$_3$ yielded the magnetization exponent $\beta = 0.42 \pm 0.03$. These values for α and β indicate that RMnO$_3$ belong to universality classes different from those of short-range 3D Heisenberg, 3D Ising, and XY models.

8.1.3 Previous Theoretical Developments

In the recent past, theoretical analysis of a generalized Ginzburg-Landau (GL) model Hamiltonian was performed via renormalization-group (RG) [111,110] technique to explain the observed critical behavior near the PM-AFM phase transition in triangular antiferromagnets. These analyses suggested the existence of new universality classes for such systems: chiral XY and chiral Heisenberg. Numerical simulations [109] yielded $\alpha = +0.34$ and $\beta = 0.25$ for the chiral XY and $\alpha = +0.24$ and $\beta = 0.30$ for the chiral Heisenberg models. However, the above mentioned experimental estimates for hexagonal RMnO$_3$ do not belong to any one of these chiral classes.

Over the past couple of decades, the magnetic and elastic properties of a number of triangular antiferromagnets of AMX$_3$ type (where A=Rb, Cs; M=Ni, Mn, Cu and X=Cl, F, Br) have been investigated within Landau-type phenomenol-

ogy[183,181,182,180,186]. In order to study the magnetoelastic coupling induced anomalous strain effects in hexagonal $CsNiF_3$, Plumer and Caillé[183,181] proposed a nonlocal free-energy functional that explained the three-domain antiferromagnetic structure of $CsNiF_3$. Recently, this nonlocal free energy model has been shown to explain the types of anomalies observed at the different phase boundaries in triangular antiferromagnet $CsNiCl_3$[186].

8.1.4 Formulation of a Model

As discussed in Sec. 8.1.1, experimental investigations on hexgonal manganites ($R\mathrm{MnO_3}$) give strong indications of dominant role of spin-lattice coupling[127,171,35] in these systems. In this context, it may be mentioned that theoretical investigations of model Hamiltonians with nonlocal interactions in the quartic term have a long history in elucidating the role of spin-lattice interaction near the critical point[56,236,235,237,4,21]. These studies showed that a long-range four spin (quartic) interaction term is generated from the spin-lattice interaction present in magnetic systems. Moreover, it has been shown in Ch. 2[208] that a long-range interaction in the quartic term generates the observed tricritical behavior in some perovskite manganites ($\mathrm{R_{1-}}_x\mathrm{A}_x\mathrm{MnO_3}$), which are also spin-lattice coupled systems. Consequently, it would be interesting to see whether such a long-range quartic interaction would be capable of explaining the critical properties of $R\mathrm{MnO_3}$ near the Néel temperature.

In this Chapter, we make this attempt by considering a model Hamiltonian involving long-range interaction in the quartic term. The long-range four-spin coupling is assumed to have the algebraic form $u(\mathbf{k}) \sim |\mathbf{k}|^{2\rho}$. In addition, we consider a coupling between the spin modes and energy fluctuations in the spirit of model C of Halperin, Hohenberg, and Ma[79,81] so that it accounts for local temperature

variations in the system. With this choice, we carry out a momentum shell decimation scheme at one-loop order and perform an RG analysis. Invoking a double expansion, we obtain the critical exponents corresponding to the nontrivial fixed point. We find that the specific heat exponent $-0.20 < \alpha < 0$ for the theoretically allowed range of model parameter ρ in three dimensions. This theoretical range for α is consistent with the above mentioned experimental range $-0.19 \leqslant \alpha \leqslant -0.09$ [164] observed in various antiferromagnetic hexagonal manganites.

8.2 Long-Range Model Hamiltonian with Energy-Spin Coupling

We consider a modified GL type model Hamiltonian $H[\Phi, \varepsilon]$ for an n-component order parameter $\Phi(\mathbf{x})$ that couples with the energy field $\varepsilon(\mathbf{x})$. The effective long-range Hamiltonian is given by

$$H[\Phi,\varepsilon] = \int d^d\mathbf{x} \left[\frac{c_0}{2}|\nabla\Phi(\mathbf{x})|^2 + \frac{r_0}{2}\Phi^2(\mathbf{x}) + \right. \\ \left. + \int d^d\mathbf{x}'\Phi^2(\mathbf{x})u(\mathbf{x}-\mathbf{x}')\Phi^2(\mathbf{x}') + \frac{C_0^{-1}}{2}\varepsilon^2(\mathbf{x}) + g_0\Phi^2(\mathbf{x})\varepsilon(\mathbf{x}) \right], \tag{8.1}$$

where $\Phi^2 = \sum_{i=1}^{n} \phi_i^2$, $|\nabla\Phi|^2 = \sum_{i=1}^{n} \nabla\phi_i \cdot \nabla\phi_i$, $u(\mathbf{x}-\mathbf{x}')$ is the long-range coupling function, and the term involving g_0 takes into account of energy-spin coupling in the system.

Using d-dimensional Fourier transform for $\psi(\mathbf{x})$ as

$$\psi(\mathbf{x}) = \int \frac{d^dk}{(2\pi)^d}\psi(\mathbf{k})e^{i\mathbf{k}.\mathbf{x}}, \tag{8.2}$$

where $\psi(\mathbf{x})$ is either $\phi_i(\mathbf{x})$, $\varepsilon(\mathbf{x})$, or $u(\mathbf{x})$, the Hamiltonian H can be expressed in

the Fourier space as

$$H[\Phi,\varepsilon]=\sum_{i=1}^{n}\int\frac{d^dk}{(2\pi)^d}\frac{c_0\mathbf{k}^2+r_0}{2}|\phi_i(\mathbf{k})|^2+\sum_{i=1}^{n}\sum_{j=1}^{n}\int\int\int\frac{d^dk_1}{(2\pi)^d}\frac{d^dk_2}{(2\pi)^d}\frac{d^dk_3}{(2\pi)^d}$$

$$u(-\mathbf{k}_1-\mathbf{k}_2)\phi_i(\mathbf{k}_1)\phi_i(\mathbf{k}_2)\phi_j(\mathbf{k}_3)\phi_j(-\mathbf{k}_1-\mathbf{k}_2-\mathbf{k}_3)$$

$$+\sum_{i=1}^{n}\int\int\frac{d^dk_1}{(2\pi)^d}\frac{d^dk_2}{(2\pi)^d}g_0\varepsilon(\mathbf{k}_1)\phi_i(\mathbf{k}_2)\phi_i(-\mathbf{k}_1-\mathbf{k}_2)+\int\frac{d^dk}{(2\pi)^d}\frac{C_0^{-1}}{2}|\varepsilon(\mathbf{k})|^2. \tag{8.3}$$

We choose the form of the coupling function $u(\mathbf{p})$ to have the algebraic form

$$u(\mathbf{p})=\lambda_0|\mathbf{p}|^{2\rho}, \tag{8.4}$$

where λ_0 is the coupling constant and the exponent ρ is a parameter in the theory.

We write the two-point bare correlation function of the order parameter ϕ_i as [139]

$$\langle\phi_i(\mathbf{q})\phi_j(\mathbf{q}')\rangle_0=G_0(\mathbf{q})(2\pi)^d\delta^d(\mathbf{q}+\mathbf{q}')\delta_{ij}, \tag{8.5}$$

and similarly, for the energy field ε as

$$\langle\varepsilon(\mathbf{q})\varepsilon(\mathbf{q}')\rangle_0=C_0(2\pi)^d\delta^d(\mathbf{q}+\mathbf{q}'), \tag{8.6}$$

where $G_0(\mathbf{q})=(c_0\mathbf{q}^2+r_0)^{-1}$ and C_0 are the bare propagators for order parameter Φ and energy density ε respectively.

8.3 Momentum Shell Decimation Scheme

We begin with the Hamiltonian given by Eq. (8.3) and perform Wilson's momentum shell decimation scheme [139,79,81,89] at one-loop order. Elimination of modes $\phi_i^{>}(\mathbf{q})$ and $\varepsilon^{>}(\mathbf{q})$ lying in the momentum range $\frac{\Lambda}{b}\leqslant q\leqslant\Lambda$ yields the Hamiltonian in terms of the remaining modes $\phi_i^{<}(\mathbf{k})$, $\varepsilon^{<}(\mathbf{k})$ in the reduced range $0\leqslant k\leqslant\frac{\Lambda}{b}$. In this process, the bare parameters r_0, c_0, C_0^{-1}, λ_0, and g_0 acquire corrections that

can be obtained by considering the relevant Feynman diagrams.

8.3.1 Self-energy Corrections

Corrections to bare parameters r_0 and c_0, obtained from the Feynman diagrams given in Fig. 8.1, are represented by the self-energy integrals

$$\Sigma_a = 2n \int \frac{d^d q}{(2\pi)^d} u(\mathbf{0}) G_0^>(\mathbf{q}), \tag{8.7}$$

$$\Sigma_b(\mathbf{k}) = 4 \int \frac{d^d q}{(2\pi)^d} u(-\mathbf{q}-\mathbf{k}) G_0^>(\mathbf{q}), \tag{8.8}$$

$$\Sigma_c = -n g_0^2 C_0 \int \frac{d^d q}{(2\pi)^d} G_0^>(\mathbf{q}), \tag{8.9}$$

$$\Sigma_d = -2 g_0^2 C_0 \int \frac{d^d q}{(2\pi)^d} G_0^>(\mathbf{q}). \tag{8.10}$$

We note that the self-energy correction Σ_a involves $u(\mathbf{0})$ that diverges for negative values of ρ. Consequently, finiteness of the free energy demands that $\rho > 0$. However, for any positive values of ρ, $u(\mathbf{0}) = 0$ so that Σ_a gives vanishing contribution. Thus only Σ_b, Σ_c, and Σ_d contribute in the theory.

Incorporating the form of the coupling function [Eq. (8.4)] into the integral in Eq. (8.8), and integrating over the internal momentum q in Eqs. (8.8), (8.9), and (8.10) in the range $\Lambda/b \leqslant q \leqslant \Lambda$, we obtain the total corrections to the bare parameters r_0 and c_0 as

$$\Delta r = \frac{8\lambda_0 S_d}{(2\pi)^d} \left[\frac{(b^{2-2\rho-d}-1)\Lambda^{d+2\rho-2}}{c_0(2-2\rho-d)} - \frac{r_0}{c_0^2} \frac{(b^{4-2\rho-d}-1)\Lambda^{d+2\rho-4}}{(4-2\rho-d)} \right],$$
$$- \frac{(2n+4) g_0^2 C_0 S_d}{(2\pi)^d} \left[\frac{(b^{2-d}-1)\Lambda^{d-2}}{c_0(2-d)} - \frac{r_0}{c_0^2} \frac{(b^{4-d}-1)\Lambda^{d-4}}{(4-d)} \right], \tag{8.11}$$

and

$$\Delta c = -\frac{8\rho(2-2\rho-d)\lambda_0 S_d}{d(2\pi)^d} \left[\frac{(b^{4-2\rho-d}-1)\Lambda^{d+2\rho-4}}{c_0(4-2\rho-d)} \right], \tag{8.12}$$

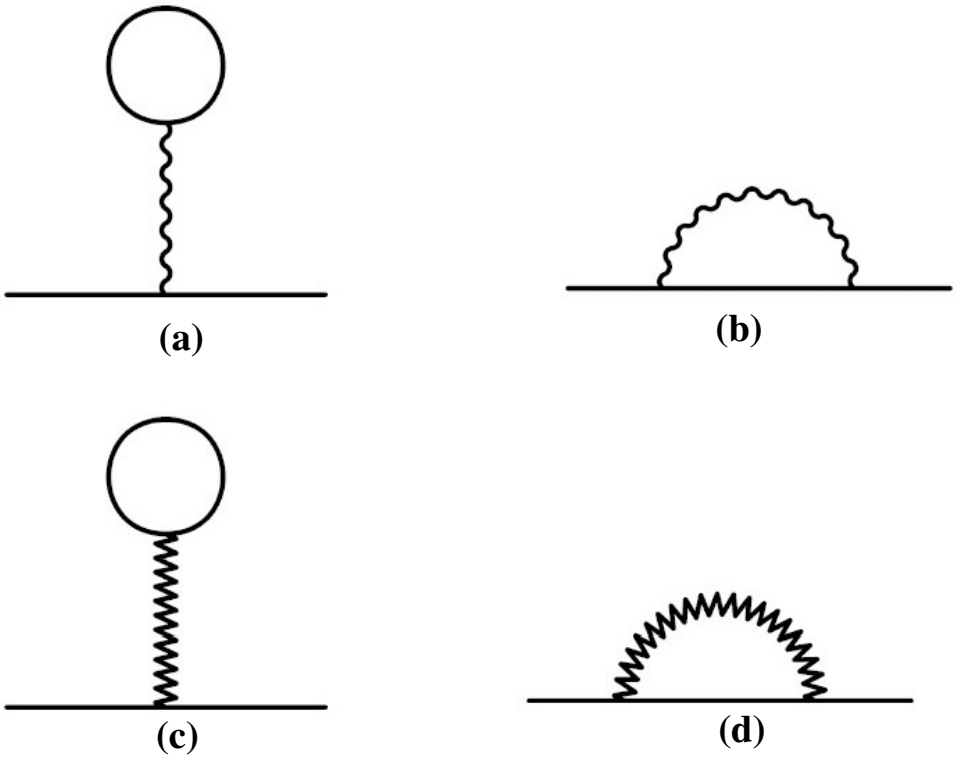

Figure 8.1: Feynman diagrams giving self-energy corrections to r_0, and c_0. The wiggly lines represent $u(\mathbf{0})$ in (a) and $u(-\mathbf{q}-\mathbf{k})$ in (b); the internal solid lines represent correlation between the fast modes of Φ fields. Zigzag lines in Figs. (c), and (d) represent correlation between the fast modes of ε fields.

in the long-wavelength limit, where S_d is the surface area of a unit sphere in d-space dimensions. Further, the self-energy diagram given in Fig. 8.2 yields the expression

$$\Sigma_\varepsilon = -ng_0^2 \int \frac{d^d q}{(2\pi)^d} G_0(\mathbf{q}) G_0(-\mathbf{q}-\mathbf{k}_1). \tag{8.13}$$

Following the same procedure as before, this yields a correction to C_0^{-1} as

$$\Delta C^{-1} = -\frac{2ng_0^2 S_d}{(2\pi)^d}\left[\frac{(b^{4-d}-1)\Lambda^{d-4}}{c_0^2(4-d)} - \frac{2r_0}{c_0^3}\frac{(b^{6-d}-1)\Lambda^{d-6}}{(6-d)}\right], \tag{8.14}$$

in the long-wavelength limit.

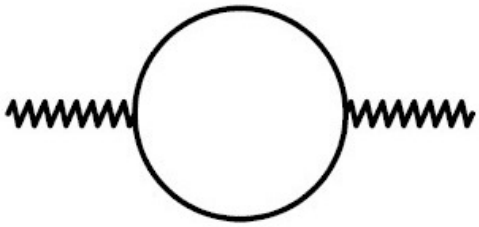

Figure 8.2: Feynman diagram giving the self-energy correction to C_0^{-1}. The two solid lines in the loop represent correlations between the fast modes of the Φ fields.

8.3.2 Vertex Corrections

Corrections to the bare four-point coupling constant λ_0 are obtained from Feynman diagrams given in Fig. 8.3 expressed by the following integrals (excluding external legs)

$$\Pi_a(\mathbf{k}_1,\mathbf{k}_2) = -4n\,u^2(-\mathbf{k}_1-\mathbf{k}_2)\int \frac{d^dq}{(2\pi)^d}\,G_0^>(\mathbf{q})\,G_0^>(-\mathbf{k}_1-\mathbf{k}_2-\mathbf{q}), \tag{8.15}$$

$$\Pi_b(\mathbf{k}_1,\mathbf{k}_2,\mathbf{k}_3) = -16u(-\mathbf{k}_1-\mathbf{k}_2)\int \frac{d^dq}{(2\pi)^d}\,u(\mathbf{q}-\mathbf{k}_3)\,G_0^>(\mathbf{q})\,G_0^>(-\mathbf{k}_1-\mathbf{k}_2-\mathbf{q}), \tag{8.16}$$

$$\Pi_c(\mathbf{k}_1,\mathbf{k}_2,\mathbf{k}_3) = -16\int \frac{d^dq}{(2\pi)^d}\,u(-\mathbf{k}_1-\mathbf{q})\,u(\mathbf{q}-\mathbf{k}_2)\,G_0^>(\mathbf{q})\,G_0^>(-\mathbf{k}_1-\mathbf{k}_3-\mathbf{q}), \tag{8.17}$$

$$\Pi_d(\mathbf{k}_1,\mathbf{k}_2) = 8\,u(-\mathbf{k}_1-\mathbf{k}_2)g_0^2C_0\int \frac{d^dq}{(2\pi)^d}\,G_0^>(\mathbf{q})\,G_0^>(-\mathbf{k}_1-\mathbf{k}_2-\mathbf{q}), \tag{8.18}$$

$$\Pi_e(\mathbf{k}_1,\mathbf{k}_3) = 16g_0^2C_0\int \frac{d^dq}{(2\pi)^d}u(-\mathbf{k}_1-\mathbf{q})\,G_0^>(\mathbf{q})\,G_0^>(-\mathbf{k}_1-\mathbf{k}_3-\mathbf{q}), \tag{8.19}$$

and

$$\Pi_f(\mathbf{k}_1,\mathbf{k}_3) = -4g_0^4 C_0^2 \int \frac{d^d q}{(2\pi)^d}\, G_0^{>}(\mathbf{q})\, G_0^{>}(-\mathbf{k}_1-\mathbf{k}_3-\mathbf{q}), \tag{8.20}$$

where $\mathbf{k}_1$, $\mathbf{k}_2$, $\mathbf{k}_3$, and $\mathbf{k}_4 = -\mathbf{k}_1 - \mathbf{k}_2 - \mathbf{k}_3$ are the external momenta carried by the four external legs in Fig. 8.3[(a)–(f)]. We see that the expressions for Π_a, Π_b,

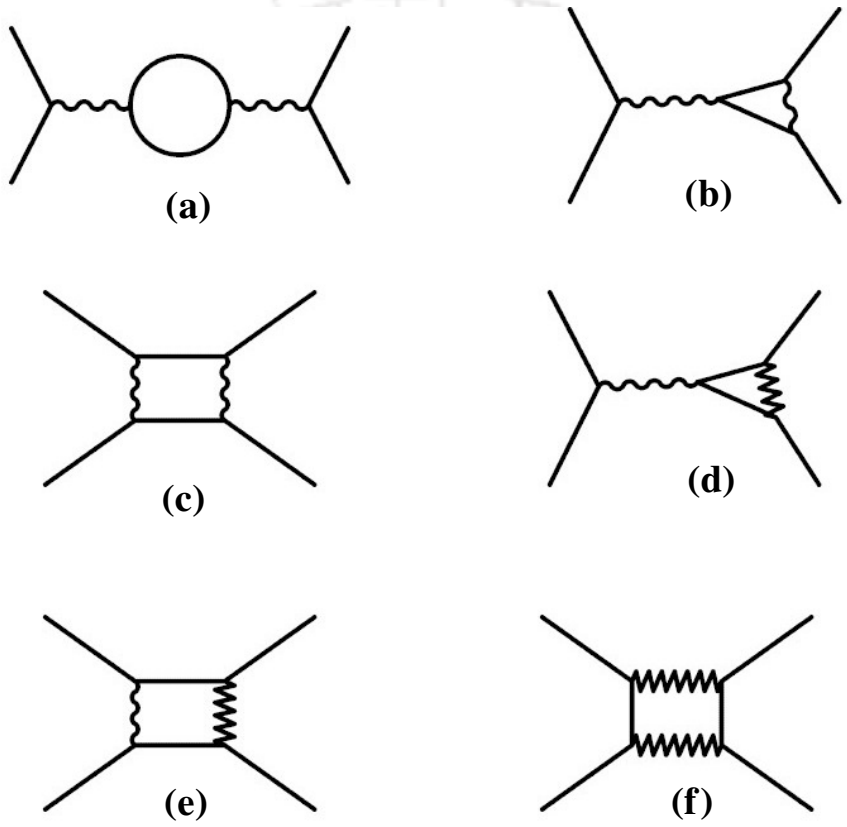

Figure 8.3: Feynman diagrams for corrections to the bare vertex λ_0. The internal solid, wiggly, and zigzag lines have the same meaning as in Fig. 8.1

and Π_d are in the form of the bare vertex $u(-\mathbf{k}_1-\mathbf{k}_2)$ appearing in the original Hamiltonian. Consequently, they yield correction $\Delta\lambda$ to the bare parameter λ_0. However, the expression for Π_c, Π_e, and Π_f cannot be accommodated as a term similar to the bare vertex $[u(-\mathbf{k}_1-\mathbf{k}_2)]$ in Eq. (8.3), and therefore Π_c, Π_e, and Π_f are irrelevant. Further, in the limit of vanishing external momenta, the expression

for Π_a does not contribute as it gives a factor of $u(\mathbf{0})$ which is zero in the physical range $\rho > 0$. Thus, only the integrals Π_b and Π_d contribute corrections to the bare coupling constant λ_0.

The internal momenta q in the vertex integrals Π_b and Π_d are restricted in the high momentum shell $\Lambda/b \leqslant q \leqslant \Lambda$ whereas the external moments k_i are in the band $0 < k_i < \Lambda/b$. For long wavelength limit, we thus take $q \gg k_i$ in the above integrals and obtain their values in the leading order. This yields the correction to the bare coupling constant λ_0 as

$$\Delta\lambda = -\frac{16\lambda_0^2 S_d}{(2\pi)^d}\left[\frac{(b^{4-2\rho-d}-1)\Lambda^{d+2\rho-4}}{c_0^2(4-2\rho-d)} - \frac{2r_0}{c_0^3}\frac{(b^{6-2\rho-d}-1)\Lambda^{d+2\rho-6}}{(6-2\rho-d)}\right] + \frac{8\lambda_0 g_0^2 C_0 S_d}{(2\pi)^d}\left[\frac{(b^{4-d}-1)\Lambda^{d-4}}{c_0^2(4-d)} - \frac{2r_0}{c_0^3}\frac{(b^{6-d}-1)\Lambda^{d-6}}{(6-d)}\right]. \tag{8.21}$$

We also obtain corrections to the three-point bare vertex g_0, representing the strength of energy-spin coupling, given by Feynman diagrams in Fig. 8.4 as

$$\Upsilon_a(\mathbf{k}_1) = -4ng_0 u(-\mathbf{k}_1)\int \frac{d^d q}{(2\pi)^d} G_0^>(\mathbf{q}) G_0^>(-\mathbf{k}_1-\mathbf{q}), \tag{8.22}$$

$$\Upsilon_b(\mathbf{k}_1,\mathbf{k}_2) = -8g_0 \int \frac{d^d q}{(2\pi)^d} u(\mathbf{q}-\mathbf{k}_2) G_0^>(\mathbf{q}) G_0^>(-\mathbf{k}_1-\mathbf{q}), \tag{8.23}$$

and

$$\Upsilon_c(\mathbf{k}_1) = 4g_0^3 C_0 \int \frac{d^d q}{(2\pi)^d} G_0^>(\mathbf{q}) G_0^>(-\mathbf{k}_1-\mathbf{q}). \tag{8.24}$$

In the limit of vanishing external momenta, the expression for Υ_a does not contribute as it gives a factor of $u(\mathbf{0})$ which is 0 in the physical range $\rho > 0$, as explained above. Thus, only the integrals Υ_b and Υ_c contribute corrections to the bare coupling constant g_0. Solving these integrals in the limit $q \gg k_i$, Eqs. (8.23) and (8.24) yield total correction to g_0 as

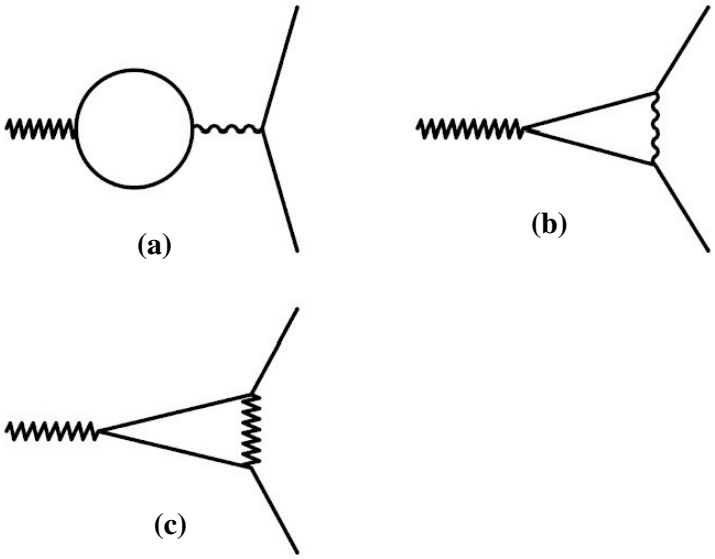

Figure 8.4: Feynman diagrams for corrections to the bare vertex g_0. The internal solid, wiggly, and zigzag lines have the same meaning as in Fig. 8.1

$$\Delta g = -\frac{8\lambda_0 g_0 S_d}{(2\pi)^d}\left[\frac{(b^{4-2\rho-d}-1)\Lambda^{d+2\rho-4}}{c_0^2(4-2\rho-d)} - \frac{2r_0}{c_0^3}\frac{(b^{6-2\rho-d}-1)\Lambda^{d+2\rho-6}}{(6-2\rho-d)}\right]$$
$$+\frac{4g_0^3 C_0 S_d}{(2\pi)^d}\left[\frac{(b^{4-d}-1)\Lambda^{d-4}}{c_0^2(4-d)} - \frac{2r_0}{c_0^3}\frac{(b^{6-d}-1)\Lambda^{d-6}}{(6-d)}\right]. \tag{8.25}$$

8.4 Rescaling

The momentum shell decimation scheme carried out in the previous section, eliminates modes lying in the range $\Lambda/b \leqslant k \leqslant \Lambda$. The resulting Hamiltonian is thus expressed in terms of the redefined parameters and in terms of the remaining modes $\phi^<(\mathbf{k})$ and $\epsilon^<(\mathbf{k})$ lying in the reduced range $0 < k < \Lambda/b$. To recover the Hamiltonian in its original form in the full momentum range, we rescale momentum and fields as $\mathbf{k}' = b\mathbf{k}$, $\Phi'(\mathbf{k}') = b^{-x}\Phi^<(\mathbf{k})$, and $\varepsilon'(\mathbf{k}) = b^y\varepsilon^<(k)$. The exponents x and y

are found to follow the relations

$$x = (d+2-\eta)/2, \tag{8.26}$$

$$y = -\frac{1}{2}(d+\frac{\alpha}{\nu}), \tag{8.27}$$

as obtained from the two-point spin-spin correlation [$\sim r^{-(d-2+\eta)}$] and energy-energy correlation [$\sim r^{-(d-\alpha/\nu)}$] at the transition temperature[79,81,139], where η is the Fisher exponent, α is the specific heat exponent, and ν is the correlation-length exponent.

The above rescaling leads to recursion relations for the model parameters r_0, c_0, C_0^{-1}, λ_0 and g_0 as

$$r' = b^{2-\eta}(r_0 + \Delta r), \tag{8.28}$$

$$c' = b^{-\eta}(c_0 + \Delta c), \tag{8.29}$$

$$(C^{-1})' = b^{\alpha/\nu}(C_0^{-1} + \Delta C^{-1}), \tag{8.30}$$

$$\lambda' = b^{4-d-2\eta-2\rho}(\lambda_0 + \Delta\lambda), \tag{8.31}$$

$$g' = b^{\frac{4-d-2\eta+\alpha/\nu}{2}}(g_0 + \Delta g) \tag{8.32}$$

.

8.5 Renormalization-Group Flow Equations

Using the expressions for Δr, Δc, ΔC^{-1}, $\Delta\lambda$, and Δg given by Eqs. (8.11), (8.12), (8.14), (8.21), and (8.25), the above recursion relations Eqs. (8.28)–(8.32) lead to the following RG flow eqations.

$$\frac{dr}{dl} = (2-\eta)r + \frac{8\lambda S_d}{(2\pi)^d}\left(\frac{\Lambda^{d-2+2\rho}}{c} - \frac{r}{c^2}\Lambda^{d-4+2\rho}\right) - \frac{(2n+4)g^2 C S_d}{(2\pi)^d}\left(\frac{\Lambda^{d-2}}{c} - \frac{r}{c^2}\Lambda^{d-4}\right), \tag{8.33}$$

$$\frac{dc}{dl} = -\eta c - \frac{8\rho(2-2\rho-d)\lambda S_d}{d(2\pi)^d}\left(\frac{\Lambda^{d-4+2\rho}}{c}\right), \tag{8.34}$$

$$\frac{dC^{-1}}{dl} = (\alpha/\nu)C^{-1} - \frac{2ng^2 S_d}{(2\pi)^d}\left(\frac{\Lambda^{d-4}}{c^2} - \frac{2r}{c^3}\Lambda^{d-6}\right), \tag{8.35}$$

$$\frac{d\lambda}{dl} = (4-d-2\eta-2\rho)\lambda - \frac{16\lambda^2 S_d}{(2\pi)^d}\left(\frac{\Lambda^{d+2\rho-4}}{c^2} - \frac{2r}{c^3}\Lambda^{d+2\rho-6}\right) + \frac{8\lambda g^2 C S_d}{(2\pi)^d} \times \left(\frac{\Lambda^{d-4}}{c^2} - \frac{2r}{c^3}\Lambda^{d-6}\right), \tag{8.36}$$

and

$$\frac{dg}{dl} = \left(\frac{4-d-2\eta+\alpha/\nu}{2}\right)g - \frac{8\lambda g S_d}{(2\pi)^d}\left(\frac{\Lambda^{d+2\rho-4}}{c^2} - \frac{2r}{c^3}\Lambda^{d+2\rho-6}\right) + \frac{4g^3 C S_d}{(2\pi)^d} \times \left(\frac{\Lambda^{d-4}}{c^2} - \frac{2r}{c^3}\Lambda^{d-6}\right), \tag{8.37}$$

where $b = e^{\delta l}$. We now redefine the dimensionless parameters as

$$R = \frac{r}{\Lambda^2}, \tag{8.38}$$

$$U = \frac{\lambda S_d}{(2\pi)^d \Lambda^{4-d-2\rho}}, \tag{8.39}$$

$$F = \frac{g^2 C S_d}{(2\pi)^d \Lambda^{4-d}}, \tag{8.40}$$

and obtained their flow equations as

$$\frac{dR}{dl} = (2-\eta)R + \frac{8U}{c}\left(1-\frac{R}{c}\right) - \frac{(2n+4)F}{c}\left(1-\frac{R}{c}\right), \tag{8.41}$$

$$\frac{dU}{dl} = (4-d-2\eta-2\rho)U - \frac{16U^2}{c^2}\left(1-\frac{2R}{c}\right) + \frac{8UF}{c^2}\left(1-\frac{2R}{c}\right), \tag{8.42}$$

$$\frac{dF}{dl} = (4-d-2\eta)F + \frac{(2n+8)F^2}{c^2}\left(1-\frac{2R}{c}\right) - \frac{16FU}{c^2}\left(1-\frac{2R}{c}\right). \tag{8.43}$$

8.6 Fixed Point and Stability

The perturbation expansion and the consequent RG transformation can be performed systematically in powers of two small parameters $\epsilon = 4-d-2\rho$ and $\epsilon' = 4-d$. Since, the present RG analysis is at one-loop order, we shall carry out the expansions in the leading order of ϵ and ϵ' invoking a double expansion [238]. These small parameters ϵ and ϵ' ensure consistency of the approximation scheme because the fixed point values R^*, U^*, and F^* turn out to be of order $O(\epsilon, \epsilon')$. The above flow equations can be expressed in terms of these small parameters as

$$\frac{dR}{dl} = 2R + \frac{8U}{c}\left(1-\frac{R}{c}\right) - \frac{(2n+4)F}{c}\left(1-\frac{R}{c}\right), \tag{8.44}$$

$$\frac{dU}{dl} = \epsilon U - \frac{16U^2}{c^2} + \frac{8UF}{c^2}, \tag{8.45}$$

$$\frac{dF}{dl} = \epsilon' F + \frac{(2n+8)F^2}{c^2} - \frac{16FU}{c^2}, \tag{8.46}$$

in the leading order of ϵ and ϵ'. From the above flow equations we find that their exists a non-trivial fixed point given by

$$\frac{R^*}{c} = -\frac{(2\epsilon'-\epsilon)}{4}, \tag{8.47}$$

$$\frac{U^*}{c^2} = \frac{\epsilon(n+4)-4\epsilon'}{16n}, \tag{8.48}$$

$$\frac{F^*}{c^2} = \frac{\epsilon-\epsilon'}{2n}. \tag{8.49}$$

Eqs. (8.44)–(8.46) are linearized around this fixed point to obtain a matrix equation $\frac{d}{dl}\delta X = M\delta X$ where $\delta X = X - X^*$ is the column matrix formed by δR, δU and δF and M is a 3×3 matrix. The matrix M has eigenvalues

$$y_1 = 2 + \frac{\epsilon}{2} - \epsilon', \tag{8.50}$$

$$y_2 = \epsilon - \frac{2}{n}\left[\epsilon(n+4) - 4\epsilon'\right] - \frac{4}{n}(\epsilon' - \epsilon), \tag{8.51}$$

and

$$y_3 = \epsilon' - \frac{(2n+8)}{n}(\epsilon' - \epsilon) - \frac{1}{n}\left[\epsilon(n+4) - 4\epsilon'\right]. \tag{8.52}$$

For critical properties, the conditions $y_1 > 0$, $y_2 < 0$, and $y_3 < 0$, imply a stable fixed point. These conditions give different stability ranges for different values of n in three dimensions, namely, $0 < \rho < 0.10$ for $n = 1$, $0 < \rho < 0.17$ for $n = 2$ and $0 < \rho < 0.21$ for $n = 3$.

8.7 Critical Exponents

The correlation-length exponent ν is related to the unstable eigenvalue y_1, as $\nu = 1/y_1$ (cf. Sec. 1.3), so that

$$\nu = \frac{1}{2} + \frac{\epsilon'}{4} - \frac{\epsilon}{8} + O(\epsilon^2, \epsilon\epsilon', \epsilon'^2). \tag{8.53}$$

As obtained from Eq. (8.34), the Fisher exponent η turns out to be zero at this order of calculation so that

$$\eta = 0 + O(\epsilon^2, \epsilon\epsilon', \epsilon'^2). \tag{8.54}$$

Putting Eq. (8.49) in Eq. (8.35) the ratio α/ν in the leading order of ϵ and ϵ' turns out to be

$$\frac{\alpha}{\nu} = \epsilon - \epsilon' + O(\epsilon^2, \epsilon\epsilon', \epsilon'^2). \tag{8.55}$$

Using Eq. (8.53) in above equation for α/ν, we obtain

$$\alpha = \frac{\epsilon - \epsilon'}{2} + O(\epsilon^2, \epsilon\epsilon', \epsilon'^2). \tag{8.56}$$

Further, using the Fisher's scaling (cf. Sec. 1.2) , we obtain

$$\gamma = 1 + \frac{\epsilon'}{2} - \frac{\epsilon}{4} + O(\epsilon^2, \epsilon\epsilon', \epsilon'^2). \tag{8.57}$$

Using this expression in Rushbrooke's scaling (cf. Sec. 1.2), together with Eq. (8.56), we obtain

$$\beta = \frac{1}{2} - \frac{\epsilon}{8} + O(\epsilon^2, \epsilon\epsilon', \epsilon'^2). \tag{8.58}$$

Finally, using Widom scaling law (cf. Sec. 1.2), we obtain

$$\delta = 3 + \epsilon' + O(\epsilon^2, \epsilon\epsilon', \epsilon'^2). \tag{8.59}$$

It may be noted that the critical exponents are independent of the number of com-

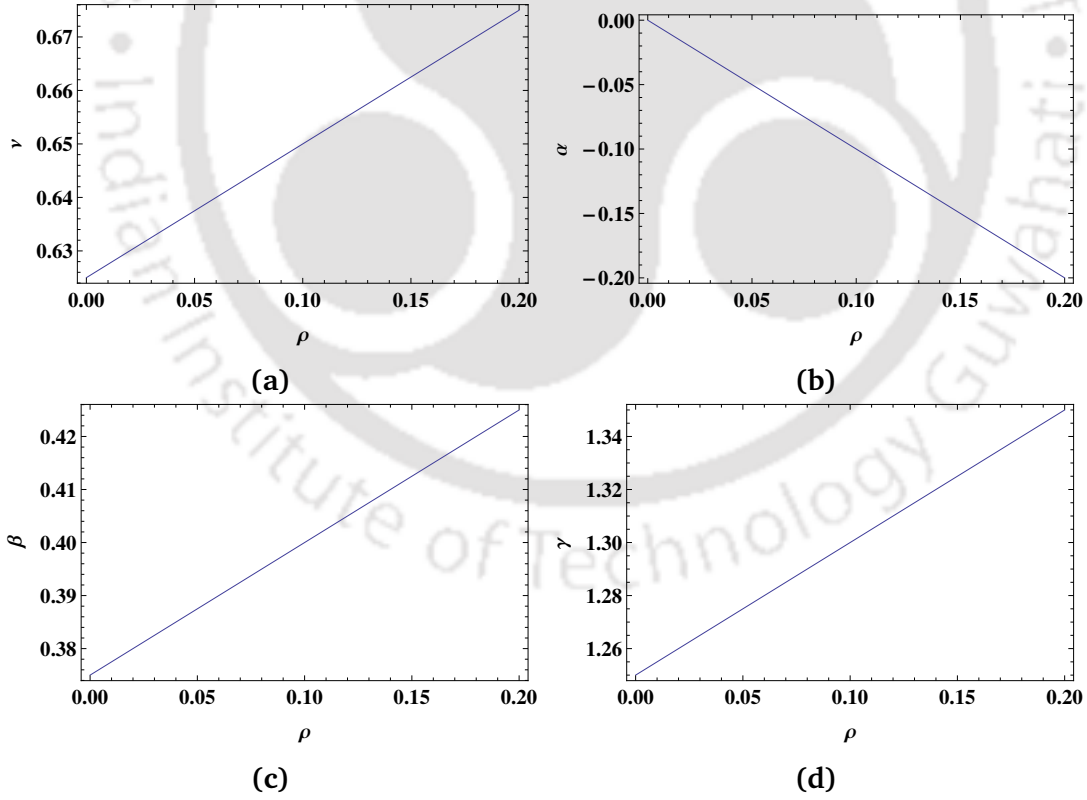

Figure 8.5: Variation of critical exponents (a) ν (b) α (c) β and (d) γ with ρ for $n = 3$ in three dimensions.

ponents n of the order parameter whereas the stability ranges (in terms of ρ) do

Table 8.1: Experimental estimates for available critical exponents for single-crystal hexagonal $R\mathrm{MnO_3}$ samples and their comparison with the predictions following from the present theory. The exponents α, β, γ, ν, are calculated from Eqs. (8.56), (8.58), (8.57), and (8.53) for $n = 3$ in three dimensions. Unavailable data are indicated by dashes.

ρ	Experimental sample	Ref.	α	β	γ	ν
0.09			-0.090	0.398	1.295	0.648
	$ErMnO_3$	[164]	-0.09 ± 0.01	$--$	$--$	$--$
0.12			-0.120	0.405	1.310	0.655
	$YMnO_3$	[164,184]	-0.12 ± 0.01	0.42 ± 0.03	$--$	$--$
	$LuMnO_3$	[164]	-0.12 ± 0.01	$--$	$--$	$--$
0.14			-0.140	0.410	1.320	0.660
	$HoMnO_3$	[164]	-0.14 ± 0.01	$--$	$--$	$--$
0.18			-0.180	0.420	1.340	0.670
	$YbMnO_3$	[164]	-0.18 ± 0.01	$--$	$--$	$--$
0.19			-0.190	0.423	1.345	0.673
	$TmMnO_3$	[164]	-0.19 ± 0.01	$--$	$--$	$--$

depend on n. Plots for the critical exponents ν, α, β, γ with respect to the parameter ρ in three dimensions are shown in Fig. 8.5. We evaluate the above sets of critical exponents for fixed values of ρ within the stability range and compare them with experimental critical exponents for hexagonal antiferromagnetic manganites in Table 8.1. A detailed discussion regarding the comparison with the experiments appears in the next section.

8.8 Discussion and Conclusion

In this Chapter, our goal was to investigate a theory capable of explaining the negative values of the specific heat exponent α experimentally observed in vari-

ous hexagonal $R\mathrm{MnO}_3$ in the vicinity of the Néel temperature. It is remarkable that the measured values of the critical exponent α turn out to be negative and it varies from one sample to another for these systems. It appears that there have so far been no theoretical attempts to explain this set of varying negative exponents. To achieve our goal, we first observed that these systems are dominated by a strong spin-lattice coupling as evidenced by several previous experimental studies [127,171,128,51,35]. It is important to mention that there have been a few theoretical attempts [237,4] to describe spin-lattice coupled systems, wherein the coupling is generated because the exchange interaction varies with the separation between the spins in a compressible lattice. Such studies indicated that the effective interaction between the spins can be represented by a long-range potential in the four-spin term when the lattice degrees of freedom are eliminated. It was also shown that such a modelling could generate tricritical behavior in the system [4]. When such a long-range model (cf. Ch. 2) was analysed in detail via an RG analysis, it was found that the resulting critical exponents near tricriticality were comparable to those observed in some perovskite manganites that are also known to be spin-lattice coupled systems. It is thus natural to extend this model to describe the critical properties of other spin-lattice coupled systems such as hexagonal $R\mathrm{MnO}_3$, which is the main focus in this Chapter. We performed this task by augmenting the Hamiltonian to include energy-energy and energy-spin couplings as suggested by Halperin, Hohenberg, and Ma [79]. Starting with this augmented Hamiltonian, we carried out a momentum shell decimation scheme at one-loop order and analysed the ensuing RG flow equations. We found that there exists a non-trivial fixed point for a restricted range in the model parameter ρ, the range being determined by the number of components n of the order parameter and the space dimension d. The critical exponents are calculated in a double expansion in the leading order of

$\epsilon = 4-d-2\rho$ and $\epsilon' = 4-d$. These small parameters ϵ and ϵ' ensure consistency of the approximation scheme because the fixed point values turn out to be of order $O(\epsilon, \epsilon')$. It is interesting to note that the specific heat exponent α so calculated falls in the range $-0.21 < \alpha < 0$ [Fig. 8.5b] for $n = d = 3$ in the theoretically allowed range $0 < \rho < 0.21$. This negative range of α is consistent with the experimental range $-0.19 \leqslant \alpha \leqslant -0.09$ as observed by Olega *et al.*[164] in various samples of hexagonal antiferromagnetic manganites (RMnO$_3$) near their Néel temperatures. For the sample YMnO$_3$, experimental values for *two* critical exponents (namely, α, β) are available as $\alpha = -0.12 \pm 0.01$[164] and $\beta = 0.42 \pm 0.03$[184]. It is important to note that *both* these critical exponents are reproducible by the present theory as $\alpha = -0.12$ and $\beta = 0.41$ by tuning only *one* parameter ρ in the theory. This gives some confidence in the predictability for the critical properties of hexagonal antiferromagnetic manganites by the present theory. Reliable estimates for the experimental β values in the case of other hexagonal mangnaites are currently not available. However, since the theoretical range of α is consistent with the experimental range for the other hexagonal manganites, it appears that the corresponding theoretical range $0.375 < \beta < 0.421$ could also be confirmed via future experiments (by measuring the β values for the other hexagonal manganites).

Since the present theory is capable of predicting all critical exponents by tuning a single parameter (namely, ρ), we display in Table 8.1 the predicted values for the other critical exponents (β, γ, and ν) for suitable values of ρ that match the experimental α values. For example, for the sample YMnO$_3$, we have first tuned ρ in Eq. (8.56) so that experimental mean value -0.12 in $\alpha = -0.12 \pm 0.01$[164] is matched. Employing the same value of ρ we calculated the other critical exponents (β, γ, and ν) from Eqs. (8.58), (8.57), and (8.53) as theoretically predicted values for YMnO$_3$. As stated earlier, the predicted β value turns out to be $\beta = 0.41$ which

falls within the error bar of the experimental estimate $\beta = 0.42 \pm 0.03$ by Poirier *et al.* [184]. For the same value of ρ, the other theoretical predictions for $YMnO_3$ are $\gamma = 1.31$ and $\nu = 0.66$.

It may be mentioned that in an experimental report by Chatterji *et. al.* [34] the estimates $\beta = 0.295 \pm 0.008$, $\gamma = 0.97 \pm 0.05$, and $\nu = 0.45 \pm 0.08$ were obtained for single-crystal $YMnO_3$. The experimental mean value $\beta = 0.295$ does not agree with the present theoretical prediction $\beta = 0.41$ as well as the experimental estimate $\beta = 0.42 \pm 0.03$ by Poirier *et al.*. Moreover, using the mean values $\gamma = 0.97$ and $\nu = 0.45$ in the standard scaling relations, one obtains $\alpha = 0.65$, and $\beta = 0.19$. This value $\beta = 0.19$ does not agree with the same [34] experimental estimate $\beta = 0.295$. In addition, as stated in the same work [34], this value ($\beta = 0.295 \pm 0.008$) cannot really be identified with the critical exponent because, the value of T_N was refined from the temperature dependence of the intensity of magnetic Bragg peak instead of determining independently from the divergence of the diffusive intensity at the ordering temperature [40]. Furthermore, the value $\alpha = 0.65$ following from γ and ν values of Ref. [34], is positive and does not agree with the recent experimental estimate $\alpha = -0.12 \pm 0.01$ [164]. Consequently, these experimental values [34] are doubtful and they cannot be matched with the present theoretical predictions. We further note that in polycrystalline $YMnO_3$, inelastic neutron scattering above the Néel temperature [189] yielded $\beta = 0.187 \pm 0.002$. This value of β cannot also be identified with the critical exponent because this value was obtained by fitting the intensity data belonging to the noncritical range of temperature as pointed by Bahoosh *et. al.* [15].

In addition to the above mentioned experimental results, different values of α were obtained in other measurements for $RMnO_3$ [108,219], the correctness of which remains doubtful [15]. Regarding the specific heat exponent α for $YMnO_3$,

Tachibana *et al.*[219] obtained $\alpha = -0.16$ whereas Katsufuji *et al.*[108] obtained $\alpha \sim 0.25$. In both cases, the reduced temperature range was too narrow to obtain conclusive results as pointed out in Ref.[164]. For $LuMnO_3$, Katsufuji *et al.*[108] obtained two different values: $\alpha = 0.22$ for $T > T_N$ and $\alpha = 0.10$ for $T < T_N$. These values are doubtful as one expects the same value of critical exponent above and below the transition temperature.

It may be noted that, a recent microscopic model[239,15] proposed for capturing the critical exponents of RMnO$_3$, yields $\beta = 0.421 \pm 0.006$ and $\gamma = 1.280 \pm 0.012$ via the Green's function technique. Using these values on the scaling relation, the other exponents are obtained as $\alpha = -0.122$, $\delta = 3.945$, and $\nu = 0.707$. The β value is in very good agreement with the experimental data of Poirier *et al.*[184] for $YMnO_3$. The α value is comparable with $\alpha = -0.12$ for $YMnO_3$ and $LuMnO_3$[164]. In comparison, the present theoretical model involves a tuning parameter ρ that yields varying critical exponents within the allowed range of ρ and thus capable of capturing the experimentally observed exponents for varying chemical compositions of RMnO$_3$ samples.

In conclusion we note that the present model Hamiltonian differs from the original Φ^4 model in two respects. First, It involves a long-range potential of the form $|\mathbf{k}|^{2\rho}$ in the quartic term unlike the short-range Φ^4 theory. Second, the present model has additional terms accounting for energy-energy and energy spin couplings as in the model C Hamiltonian of Halperin, Hohenberg and Ma[79]. However, because of the inclusion of the long-range Φ^4 term, the present model Hamiltonian yields critical behavior different from that of the model C Hamiltonian. The model C Hamiltonian yields an α value that is positive in the strong coupling ($g \neq 0$) regime. In comparison, the present model Hamiltonian yields α values restricted in the negative range $-0.21 < \alpha < 0$ for varying strengths of nonlocal-

ity in the strong coupling regime. In addition, the present model Hamiltonian is capable of capturing the experimental critical exponents for $R\mathrm{MNO}_3$ satisfactorily. However further experimental work in verifying the rest of the critical exponents would be needed to fully confirm the predictions of the theory.

Chapter 9

Epilogue

Experimental investigations on the critical behavior of perovskite manganites show a wide diversity of critical exponents near and away from tricriticality. Standard theories do not explain this kind of diversity in critical exponents. In addition, there are uranium superconductors, and hexagonal antiferromagnetic manganites that exhibit critical exponents not explainable by the existing theories. There exist evidences that spin systems in these compounds are coupled to the underlying lattice suggesting that the spin-lattice coupling plays an important role in determining their critical properties near the second order phase transition point. In this thesis, we considered the task to formulate models in order to explain the wide diversity of critical indices in these compounds. In addition, we demonstrated that a suitable model has the potential to explain the critical indices in the cases of doped uniaxial ferromagnets and isomorphous salts which show anomalous behavior and varying critical exponents.

The lesson we learned from early theoretical attempts is that spin-lattice interaction can generate tricritical behavior through an effective long-range interaction in the quartic term of Ginzburg-Landau (GL) Hamiltonian. However, perovskite manganites exhibit a range of critical exponents both near and away from tricriticality and thus a huge set of experimental data still remained unexplained.

In the case of perovskite manganites, experimental and theoretical investigations indicate that the lattice distortions (due to strong electron-phonon coupling) play a significant role in addition to the double exchange (DE) mechanism in determining the colossal magnetoresistance as well as the systematic variation of transition temperature with doping. In fact, lattice distortions or strain, which can be imposed via changing the chemical composition, have been shown to provide a natural framework to describe the observed features of perovskite manganites. However, DE interaction has been proved to fall in the same universality class as that of the 3D Heisenberg model.

In this light, we considered the effective form of the nonlocal interaction to be long-range in nature. Carrying out a Wilson-type renormalization-group (RG) calculation at one-loop order, the critical exponents were derived in the leading order of ϵ. The ϵ-expansion turned out to be an expansion about the tricritical mean field. It was found that the model captured satisfactorily the critical exponents of those perovskite manganite samples that show nearly tricritical behavior. Samples exhibiting critical exponents away from tricriticality were not represented properly by these analytical estimates. Thus a modification in the model Hamiltonian was needed so that all critical exponents, both near and away from tricriticality, could be captured.

We made this attempt to predict the complete set of critical exponents for perovskite manganite samples. This was achieved by modelling the interaction term by means of bringing up screening into the nonlocal character of the potential. We invoked a very low value for screening so that the interaction extends over many lattice points unlike the conventional models with nearest neighbour interactions. An RG calculation at one-loop order revealed that the screening plays an important role in extending the stability range and in determining the critical exponents.

However, the critical exponents have a weak dependence on the screening. It is gratifying to mention that the analytical estimates for the critical exponents were found to be in good agreement with those of the experiments for a wide variety of perovskite manganite samples both near and away from tricriticality.

We further verified the applicability of the above screened nonlocal model in predicting the critical exponents for Mn-site doped perovskite manganites. In the context of such an extensive predictability, it is worthwhile to mention about the known fact that critical exponents can vary with the strength of coupling for models with energy-energy coupling. In the Ashkin-Teller Potts model, there are two sets of Ising spins given by the Hamiltonian $-J\sum_{nn}SS - K\sum_{nn}TT - K_4\sum_{nn}SSTT$ that yields critical exponents which vary continuously with the coupling constant K_4 [106]. The line of critical points, instead of separated critical points, does not need a revision of our basic ideas of renormalization-group, and universality [106,47].

As it has been seen by experiments, perovskite manganites exhibit an almost constant value for the linewidth exponent vis-a-vis varying static critical exponents. This surprising feature appears to delude any theoretical explanation at the first sight. However, when we applied the same nonlocal screened model in the the nonconserved dynamic model A it reproduced this behavior quite satisfactorily. This remarkable agreement indeed provides a great amount of confidence in the screened nonlocal model.

Having thus gained confidence in the nonlocal model Hamiltonian, we next addressed the critical exponents for uranium ferromagnetic superconductors that are also spin-lattice coupled systems. Since most of these samples exhibit critical exponents near tricriticality, we took up the unscreened nonlocal model explored in the beginning. Knowing that the order parameter in these systems obey a conserved

dynamics, we investigated the model B dynamics governed by the the long-range Hamiltonian. Carrying out a dynamic RG calculation, we calculated the static and dynamic critical exponents in the leading order of ϵ. It is satisfying to note that the theoretically predicted static critical exponents compared well with those of the experimentally observed exponents in uranium ferromagnetic superconductors. However, more reliable experimental estimates for the dynamic exponents are still required for a concrete validation of the theory.

Apart from the above, there exist other types of samples such as doped uniaxial ferromagnets and isomorphous salts that exhibit anomalous critical behavior. We saw that these anomalous critical exponents are explained satisfactorily by the screened nonlocal model. This was achieved by considering a conserved dynamics and by invoking a dynamic RG analysis at one-loop order. Although there exist no experimental evidence for spin-lattice coupling in these systems, the agreement of the critical exponents via the screened nonlocal model suggests the presence of such coupling in these systems. Suitable experiments to find the signature of spin-lattice coupling in these systems would further validate (or invalidate) this proposition.

A Recent study on the paramagnetic-to-antiferromagnetic (PM-AFM) transition in multiferroic hexagonal rare earth manganites yielded specific heat exponent falling in a negative range. In an attempt to explain this behavior, we investigated the critical properties of a quartic long-range model Hamiltonian incorporating energy-energy and energy-spin couplings. Carrying out an RG analysis at one loop order, the stable fixed point yielded negative values for the specific heat exponent in the allowed range in consistency with the experiments. This indicates that the nonlocal quartic interaction is a relevant ingredient for understanding the critical behavior of hexagonal manganites near their Néel temperatures.

It is worth noting that the above theoretical predictions in a variety of systems were made at the level of one-loop approximation. Although the agreements indicated this approximation to be well justified, it is always desirable to go further beyond this approximation. This can be achieved by going to the next higher order, that is, a two-loop approximation. To obtain a still better accuracy, it requires to carry out the calculations up to four or five loop orders followed by a Borel summation of the resulting ϵ-expansion. Such calculations are analytically demanding tasks and one would employ algebraic computation to attain this goal. These explorations may be left for the future.

The research work carried out in this thesis consisted of analytical investigations of critical behavior in various strongly correlated magnetic systems. Although this work is related to only the PM-FM and PM-AFM transitions, there is a tremendous possibility to push beyond these boundaries via exploring the occurrences of multiple phases including structural phase transitions in these technologically demanding materials. Below we provide a few immediate possibilities of further research along this line.

By taking into account of the magnetoelastic coupling, we have explored the PM-FM phase transition in uranium ferromagnetic superconductors. As our analytical RG results are in close agreement with experimental predictions, it motivates to extend our work to explore the quantum phase transition (QPT) occurring in such systems under the application of pressure, magnetic field, or disorder. In fact, magnetoelastic interaction was shown to be an important ingredient for describing the induced quantum fluctuations and phase transitions in iron ferromagnetic superconductors [170]. Indeed, a recent theoretical work [1], suggested that the effective bosonic theory becomes nonlocal upon integrating out the fermionic degrees-of-freedom. Thus, it would be quite interesting and highly relevant to investigate the

role of magnetoelastic interaction in the vicinity of QPT in such itinerant systems.

Since there are a number of experimental evidences suggesting that the spin-lattice interaction plays a dominant role in multiferroic manganites, our analytical studies can suitably be turned towards exploring the multiferroic behavior of such systems. The idea is to construct a suitable model Hamiltonian in the presence of the spin-lattice interaction. As we have shown, the RG calculations along this line gave us some profound motivating results related to PM-AFM phase transition in multiferroic manganites. This, indeed, further motivates us to explore within the GL phenomenology the effect of spin-lattice coupling on the ferroelectrically induced magnetization, and vice versa in such multiferroic systems. Within the GL approach, by incorporating the spin-lattice interaction, it would be possible to see how the commensurability of magnetic vector[22] changes as a function of lattice strain and how it affects the nature of multiferroicity.

Thus it appears that the nonlocal models adopted in this thesis might provide an unprecedented opportunity to study various above mentioned condensed systems. We leave such works for future explorations.

Bibliography

[1] Ar. Abanov and A. Chubukov. *Phys. Rev. E* **93**, 255702 (2004).

[2] A. Aharony. *Phys. Rev. B* **9**, 2416 (1974).

[3] A. Aharony. *Phys. Rev. B* **8**, 3363 (1973).

[4] A. Aharony. *Phys. Rev. B* **8**, 4314 (1973).

[5] A. Aharony and A. D. Bruce. *Phys. Rev. Lett.* **33**, 427 (1974).

[6] K. H. Ahn, T. Lookman, and A. R. Bishop. *Nature* **428**, 401 (2004).

[7] T. Akazawa, H. Hidaka, H. Kotegawa, T. C. Kobayashi, T. Fujiwara, E. Yamamoto, Y. Haga, R. Settai, and Y. Ōnuki. *J. Phys. Soc. Jpn.* **73**, 3129 (2004).

[8] R. Allenspach. *J. Magn. Magn. Mater.* **129**, 160 (1994).

[9] R. Allenspach and A. Bischof. *Phys. Rev. Lett.* **69**, 3385 (1992).

[10] D. J. Amit and V. Martin-Mayor. *Field Theory, the Renormalization Group, and Critical Phenomena*. 3rd ed., World Scientific, Singapore (2005).

[11] D. Aoki and J. Flouquet. *J. Phys. Soc. Jpn.* **81**, 011003 (2012).

[12] D. Aoki, A. Huxley, E. Ressouche, D. Braithwaite, J. Flouquet, J. P Brison, E. Lhotel, and C. Paulsen. *Nature (London)* **413**, 613 (2001).

[13] V. A. Atsarkin, V. V. Demidov, G. A. Vasneva, and K. Conder. *Phys. Rev. B* **63**, 092405 (2001).

[14] N. A. Babushkina, L. M. Belova, O. Yu. Gorbenko, A. R. Kaul, A. A. Bosak, V. I. Ozhogin, and K. I. Kugel. *Nature (London)* **391**, 159 (1998).

[15] S. G. Bahoosh and J. M. Wesselinowa. *Phys. Status Solidi B* **249**, 2227 (2012).

[16] C. P. Bean and D. S. Rodbell. *Phys. Rev.* **126**, 104 (1962).

[17] P. Beauvillain, J.-P. Renard, I. Laursen, and P. J. Walker. *Phys. Rev. B* **18**, 3360 (1978).

[18] P. Beauvillain, J. Seiden, and I. Laursen. *Phys. Rev. Lett.* **45**, 1362 (1980).

[19] S. V. Belim. *JETP Lett.* **98**, 745 (2004).

[20] R. Bellouz, M. Oumezzine, E. K. Hlil, and E. Dhahri. *Physica B* **456**, 93 (2015).

[21] D. J. Bergman and B. I. Halperin. *Phys. Rev. B* **13**, 2145 (1976).

[22] J. J. Betouras, G. Giovannetti, and J. van den Brink. *Phys. Rev. Lett.* **98**, 257602 (2007).

[23] J. K. Bhattacharjee, J. L. Cardy, and D. J. Scalapino. *Phys. Rev. B* **25**, 1681 (1982).

[24] S. J. L. Billinge, R. G. DiFrancesco, G. H. Kwei, J. J. Neumeier, and J. D. Thompson. *Phys. Rev. Lett.* **77**, 715 (1996).

[25] T. Blanchard, M. Picco, and M. A. Rajabpour. *Europhys. Lett.* **101**, 56003 (2013).

[26] C. H. Booth, F. Bridges, G. H. Kwei, J. M. Lawrence, A. L. Cornelius, and J. J. Neumeier. *Phys. Rev. Lett.* **80**, 853 (1998).

[27] E. S. Bozin, M. Schmidt, A. J. DeConinck, G. Paglia, J. F. Mitchell, T. Chatterji, P. G. Radaelli, Th. Proffen, , and S. J. L. Billinge. *Phys. Rev. Lett.* **98**, 137203 (2007).

[28] J. Brinkmann, R. Courths, and H. J. Guggenheim. *Phys. Rev. Lett.* **40**, 1286 (1978).

[29] A. D. Bruce and A. Aharony. *Phys. Rev. B* **10**, 2078 (1974).

[30] E. R. Callen and H. B. Callen. *Phys. Rev. B* **129**, 578 (1963).

[31] E. R. Callen and H. B. Callen. *Phys. Rev. B* **139**, A455 (1965).

[32] A. A. Caparica, A. Bunker, and D. P. Landau. *Phys. Rev. B* **62**, 9458 (2000).

[33] P. M. Chaikin and T. C. Lubensky. *Principles of Condensed Matter Physics*. Cambridge University Press, Cambridge (1998).

[34] T. Chatterji, S. Ghosh, A. Singh, L. P. Regnault, and M. Rheinstädter. *Phys. Rev. B* **76**, 144406 (2007).

[35] T. Chatterji, B. Ouladdiaf, P. F. Henry, and D. Bhattacharya. *J. Phys.: Condens. Matt.* **24**, 336003 (2012).

[36] K. Chen, A. M. Ferrenberg, and D. P. Landau. *Phys. Rev. B* **48**, 3249 (1993).

[37] S. W. Cheong and M. Mostovoy. *Nature Mater.* **6**, 13 (2007).

[38] A. V. Chubukov, J. J. Betouras, and D. V. Efremov. *Phys. Rev. Lett.* **112**, 037202 (2014).

[39] A. V. Chubukov and D. L. Maslov. *Phys. Rev. Lett.* **103**, 216401 (2009).

[40] M. F. Collins. *Magnetic critical scattering*. Oxford University Press, Oxford (1989).

[41] C. d.-Cruz, F. Yen, B. Lorenz, Y. Q. Wang, Y. Y. Sun, M. M. Gospodinov, and C. W. Chu. *Phys. Rev. B* **71**, 060407(R) (2005).

[42] E. Dagotto. *Nanoscale Phase Separation and Colossal Magnetoresistance*. Springer, Berlin (2002).

[43] P. Dai, J. Zhang, H. A. Mook, S.-H. Liou, P. A. Dowbwn, and E. W. Plummer. *Phys. Rev. B* **54**, R3694 (1996).

[44] P.-G. DeGennes. *Phys. Rev.* **118**, 141 (1960).

[45] Ah. Dhahri, M. Jemmali, M. Hussein, E. Dhahri, A. Koumina, and E. K. Hlil. *J. Alloys Compd.* **618**, 788 (2015).

[46] Ja. Dhahri, A. Dhahri, M. Oummezzine, and E. K. Hlil. *Physica B* **458**, 132 (2015).

[47] D. Dhar. *Private communication*, (2016).

[48] H. W. Diehl. arXiv/1602.02087 (2016).

[49] M. Doerr, M. Rotter, and A. Lindbaum. *Adv. Phys.* **54**, 1 (2005).

[50] W. Eerenstein, N. D. Mathur, and J. F. Scott. *Nature (London)* **442**, 759 (2006).

[51] X. Fabréges, S. Petit, I. Mirebeau, S. Pailhés, L. Pinsard, A. Forget, M. T. Fernandez-Diaz, and F. Porcher. *Phys. Rev. Lett.* **103**, 067204 (2009).

[52] J. Fan, L. Ling, B. Hong, L. Zhang, L. Pi, and Y. Zhang. *Phys. Rev. B* **81**, 144426 (2010).

[53] J. Fan, L. Pi, L. Zhang, W. Tong, L. Ling, B. Hong, Y. Shi, W. Zhang, D. Lu, and Y. Zhang. *Appl. Phys. Lett.* **98**, 072508 (2011).

[54] H. A. Fernandes, J. R. Drugowich de Felício, and A. A. Caparica. *Phys. Rev. B* **72**, 054434 (2005).

[55] M. Fiebig, Th. Lottermoser, D. Fröhlich, A. V. Goltsev, and R. V. Pisarev. *Nature* **419**, 818 (2002).

[56] M. E. Fisher. *Phys. Rev.* **176**, 257 (1968).

[57] M. E. Fisher, S.-k. Ma, and B. G. Nickel. *Phys. Rev. Lett.* **29**, 917 (1972).

[58] R. Folk, H. Iro, and F. Schwabl. *Z. Phys. B* **27**, 169 (1977).

[59] E. Frey and F. Schwabl. *Phys. Lett. A* **123**, 49 (1987).

[60] E. Frey and S. Schwabl. *Phys. Rev. B* **42**, 8261 (1990).

[61] E. Frey and S. Schwabl. *Phys. Rev. B* **43**, 833 (1991).

[62] R. Frowein, J. Kötzler, B. Schaub, and H. G. Schuster. *Phys. Rev. B* **25**, 4905 (1982).

[63] S. Fujimori, I. Kawasaki, A. Yasui, Y. Takeda, T. Okane, Y. Saitoh, A. Fujimori, H. Yamagami, Y. Haga, E. Yamamoto, and Y. Ōnuki. *Phys. Rev. B* **89**, 104518 (2014).

[64] S. Fujimori, T. Ohkochi, I. Kawasaki, A. Yasui, Y. Takeda, T. Okane, Y. Saitoh, A. Fujimori, H. Yamagami, Y. Haga, E. Yamamoto, and Y. Ōnuki. *Phys. Rev. B* **91**, 174503 (2015).

[65] A. Galatanu, Y. Haga, T. D. Matsuda, S. Ikeda, E. Yamamoto, D. Aoki, T. Takeuchi, and Y. Ōnuki. *J. Phys. Soc. Jpn.* **74**, 1582 (2005).

[66] G. A. Gehring. *Europhys. Lett.* **82**, 60004 (2008).

[67] S. Ghodhbane, A. Dhahri, N. Dhahri, E. K. Hlil, J. Dhahri, M. Alhabradi, and M. Zaidi. *J. Alloys. Comp.* **580**, 558 (2013).

[68] K. Ghosh, C. J. Lobb, R. L. Greene, S. G. Karabashev, D. A. Shulyatev, A. A. Arsenov, and Y. Mukovskii. *Phys. Rev. Lett.* **81**, 4740 (1998).

[69] D. Ginting, S. C. Yu D. Nanto, Y. D. Zhang, and T.-L. Phan. *J. Appl. Phys.* **113**, 17E110 (2013).

[70] V. L. Ginzburg. *Sov. Phys. JETP* **4**, 153 (1957).

[71] N. Goldenfeld. *Lectures on Phase Transitions and the Renormalization Group*. Addison-Wesley, Reading, MA (1992).

[72] J. B. Goodenough, A. Wold, R. J. Arnott, and N. Menyuk. *Phys. Rev.* **124**, 373 (1961).

[73] L. P. Gor'kov. *Sov. Phys. JETP* **9**, 1364 (1959).

[74] J. A. Griffin, M. Huster, and R. J. Folweiler. *Phys. Rev. B* **22**, 4370 (1980).

[75] J. C. Le Guillou and J. Zinn-Justin. *Phys. Rev. B* **21**, 3976 (1980).

[76] M. A. Gusmão and W. K. Theumann. *Phys. Rev. B* **28**, 6545 (1983).

[77] B. I. Halperin and P. C. Hohenberg. *Phys. Rev. Lett.* **19**, 700 (1967).

[78] B. I. Halperin and P. C. Hohenberg. *Phys. Rev.* **177**, 952 (1969).

[79] B. I. Halperin, P. C. Hohenberg, and S.-k. Ma. *Phys. Rev. B* **10**, 139 (1974).

[80] B. I. Halperin, P. C. Hohenberg, and S.-k. Ma. *Phys. Rev. Lett.* **29**, 1548 (1972).

[81] B. I. Halperin, P. C. Hohenberg, and S.-k. Ma. *Phys. Rev. B* **13**, 4119 (1976).

[82] F. Hardy, A. Huxley, J. Flouquet, B. Salce, G. Knebel, D. Braithwaite, D. Aoki, M. Uhlarz, and C. Pfleiderer. *Physica B* **359-361**, 1111 (2005).

[83] E. Hassinger, D. Aoki, G. Knebel, and J. Flouquet. *J. Phys.: Conf. Ser.* **200**, 012055 (2010).

[84] E. Hassinger, D. Aoki, G. Knebel, and J. Flouquet. *J. Phys. Soc. Jpn.* **77**, 073703 (2008).

[85] T. Hattori, K. Ishida, Y. Nakai, T. Ohta, K. Deguchi, N. K. Sato, and I. Satoh. *Physica C* **470**, S561 (2009).

[86] S. Hébert, C. Martin, A. Maignan, R. Retoux, M. Hervieu, N. Nguyen, and B. Raveau. *Phys. Rev. B* **65**, 104420 (2002).

[87] R. H. Heffner, L. P. Le, M. F. Hundley, J. J. Neumeier, G. M. Luke, K. Kojima, B. Nachumi, Y. J. Uemura, D. E. MacLaughlin, and S-W. Cheong. *Phys. Rev. Lett.* **77**, 1869 (1996).

[88] J. T. Heron, M. Trassin, K. Ashraf, M. Gajek, Q. He, S. Y. Yang, D. E. Nikonov, Y.-H. Chu, S. Salahuddin, and R. Ramesh. *Phys. Rev. Lett.* **107**, 217202 (2011).

[89] P. C. Hohenberg and B. I. Halperin. *Rev. Mod. Phys.* **49**, 435 (1977).

[90] C. Hohenemser, N. Rosov, and A. Kleinhammes. *Hyperfine Interact.* **49**, 267 (1989).

[91] C. Holm and W. Janke. *Phys. Rev. B* **48**, 936 (1993).

[92] C. S. Hong, W. S. Kim, and N. H. Hur. *Phys. Rev. B* **63**, 092504 (2001).

[93] J. Honkonen. *J. Phys. A: Math. Gen.* **23**, 825 (1990).

[94] K. Huang. *Statistical Mechanics*. 2nd ed., Wiley, New York (1987).

[95] Z. J. Huang, Y. Cao, Y. Y. Sun, Y. Y. Xue, and C. W. Chu. *Phys. Rev. B* **56**, 2623 (1997).

[96] A. Huxley, I. Sheikin, and D. Braithwaite. *Physica B* **284-288**, 1277 (2000).

[97] A. D. Huxley, S. Raymond, and E. Ressouche. *Phys. Rev. Lett.* **91**, 207201 (2003).

[98] N. T. Huy, A. Gasparini, D. E. de Nijs, Y. Huang, J. C. P. Klaasse, T. Gortenmulder, A. de Visser, A. Hamann, Görlach, and H. v. Löhneysen. *Phys. Rev. Lett.* **99**, 067006 (2007).

[99] H. Y. Hwang, S.-W. Cheong, P. G. Radaelli, M. Marezio, and B. Batlogg. *Phys. Rev. Lett.* **75**, 994 (1995).

[100] Y. Imry. *Phys. Rev. Lett.* **33**, 1304 (1974).

[101] Y. Imry, O. E.-Wohlman, and D. J. Bergman. *J. Phys. C* **6**, 2846 (1973).

[102] H. A. Jahn and E. Teller. *Proc. R. Soc. London A* **161**, 220 (1937).

[103] W. Jiang, X. Zhou, G. Williams, Y. Mukovskii, and K. Glazyrin. *Phys. Rev. Lett.* **99**, 177203 (2007).

[104] S. Jin, T. Tiefel, M. McCormack, R. Fastnacht, R. Ramesh, and L. H. Chen. *Science* **264**, 413 (1994).

[105] J. H. Jung, K. H. Kim, T. W. Noh, E. J. Choi, and J. Yu. *Phys. Rev. B* **57**, R10043 (1998).

[106] L. P. Kadanoff. *Annals of Physics* **120**, 39 (1979).

[107] M. Kardar. *Statistical Physics of Fields*. Cambridge University Press, Cambridge (2007).

[108] T. Katsufuji, S. Mori, M. Masaki, Y. Moritomo, N. Yamamoto, and H. Takagi. *Phys. Rev. B* **64**, 104419 (2001).

[109] H. Kawamura. *J. Phys. Soc. Jpn.* **61**, 1299 (1992).

[110] H. Kawamura. *J. Phys.: Condens. Matter* **10**, 4707 (1998).

[111] H. Kawamura. *Phys. Rev. B* **38**, 4916 (1988).

[112] K. Kawasaki. *Phys. Rev.* **165**, 224 (1964).

[113] K. Kawasaki. *Phys. Rev.* **145**, 224 (1966).

[114] M. Khlifi, A. Tozri, M. Bejar, E. Dhahri, and E. K. Hlil. *J. Magn. Magn. Mater.* **324**, 2142 (2012).

[115] D. I. Khomskii and K. I. Kugel. *Phys. Rev. B* **67**, 134401 (2003).

[116] D. I. Khomskii and K. I. Kugel. *Europhys. Lett.* **55**, 208 (2001).

[117] D. Kim, B. Revaz, B. L. Zink, F. Hellman, J. J. Rhyne, and J. F. Mitchell. *Phys. Rev. Lett.* **89**, 227202 (2002).

[118] D. Kim, B. L. Zink, F. Hellman, and J. M. D. Coey. *Phys. Rev. B.* **65**, 214424 (2002).

[119] H. Kleinert and V. S.-Frohlinde. *Critical Properties of ϕ^4-Theories*. World Scientific, Singapore, (2001).

[120] W. Knafo, C. Meingast, S. Sakarya, N. H. van Dijk, Y. Huang, H. Rakoto, J-M. Broto, and H. v. Löhneysen. *J. Phys. Soc. Jpn.* **78**, 043707 (2009).

[121] H. Kotegawa, S. Araki, T. Akazawa, A. Hori, Y. Irie, S. Fukushima, H. Hidaka, T. C. Kobayashi, K. Takeda, Y. Ohishi, K. Murata, E. Yamamoto, S. Ikeda, Y. Haga, R. Settai, and Y. Onuki. *Phys. Rev. B* **84**, 054524 (2011).

[122] J. Kötzler, H. Reinhardt, R. Liebmann, and H. G. Schuster. *Phys. Rev. B* **23**, 1476 (1981).

[123] V. V. Krishnamurthy, I. Watanabe, K. Nagamine, H. Kuwahara, and Y. Tokura. *Phys. Rev. B* **61**, 4060 (2000).

[124] K. Kubo and N. Ohata. *J. Phys. Soc. Japan* **33**, 21 (1972).

[125] L. D. Landau and E. M. Lifshitz. *Statistical Physics*. Part1, 3rd. ed., Pergamon Press, England (1980).

[126] A. I. Larkin and D. E. Khmel'nitskii. *Sov. Phys. JETP* **29**, 1123 (1969).

[127] S. Lee, A. Pirogov, J. H. Han, J.-G. Park, A. Hoshikawa, and T. Kamiyama. *Phys. Rev. B* **71**, 180413(R) (2005).

[128] S. Lee, A. Pirogov, M. Kang, K.-H Jang, M. Yonemura, T. Kamiyama, S.-W. Cheong, F. Gozzo, N. Shin, H. Kimura, Y. Noda, and J.-G. Park. *Nature* **451**, 805 (2008).

[129] F. Lévy, I. Sheikin, B. Grenier, and A. D. Huxley. *Science* **309**, 1343 (2005).

[130] H. J. Lewtas, A. T. Boothroyd, M. Rotter, D. Prabhakaran, H. Müller, M. D. Le, B. Roessli, J. Gavilano, and P. Bourges. *Phys. Rev. B* **82**, 184420 (2010).

[131] R. Li, C. Zhang, L. Pi, and Y. Zhang. *Euro. Phys. Lett.* **107**, 47006 (2014).

[132] X. J. Liu, Y. Moritomo, A. Nakamura, H. Tanaka, and T. Kawai. *Phys. Rev. B* **64**, 100401(R) (2001).

[133] X. J. Liu, Y. Moritomo, A. Nakamura, H. Tanaka, and T. Kawai. *J. Phys. Soc. Jpn.* **70**, 3466 (2001).

[134] E. Luijten and H. W. J. Blöte. *Phys. Rev. Lett.* **89**, 025703 (2002).

[135] E. Luijten and H. W. J. Blöte. *Phys. Rev. Lett.* **76**, 1557 (1996).

[136] E. Luijten and H. W. J. Blöte. *Phys. Rev. B* **56**, 8945 (1997).

[137] E. Luijten, H. W. J. Blöte, and K. Binder. *Phys. Rev. E* **54**, 4626 (1996).

[138] S.-k. Ma. *Rev. Mod. Phys.* **45**, 589 (1973).

[139] S.-k. Ma. *Modern Theory of Critical Phenomena*. Benjamin, Reading, MA (1976).

[140] K. Machida and T. Ohmi. *Phys. Rev. Lett.* **86**, 850 (2001).

[141] J. Magariño, J. Tuchendler, P. Beauvillain, and I. Laursen. *Phys. Rev. B* **21**, 18 (1980).

[142] M. C. Martin, G. Shirane, Y. Endoh, K. Hirota, Y. Moritomo, and Y. Tokura. *Phys. Rev. B* **53**, 14285 (1996).

[143] N. D. Mathur, F. M. Grosche, S. R. Julian, I. R. Walker, D. M. Freye, R. K. W. Haselwimmer, and G. G. Lonzarich. *Nature (London)* **394**, 39 (1998).

[144] D. C. Mattis and T. D. Schultz. *Phys. Rev.* **129**, 175 (1963).

[145] I. D. Mayergoyz. *Handbook of Giant Magnetoresistive Materials*. Academic Press, San Diego, CA (2000).

[146] G. F. Mazenko. *Nonequilibrium Statistical Mechanics*. Wiley-Vch, Weinheim (2006).

[147] N. D. Mermin and H. Wagner. *Phys. Rev. Lett.* **17**, 1133 (1966).

[148] A. J. Millis. *Nature (London)* **392**, 147 (1998).

[149] A. J. Millis, T. Darling, and A. Migliori. *J. Appl. Phys.* **83**, 1588 (1998).

[150] A. J. Millis, P. B. Littlewood, and B. I. Shraiman. *Phys. Rev. Lett.* **74**, 5144 (1995).

[151] A. J. Millis, B. I. Shraiman, and R. Mueller. *Phys. Rev. Lett.* **77**, 175 (1996).

[152] V. P. Mineev. *J. Phys. Conf. Ser.* **400**, 032053 (2012).

[153] S. Mnefgui, N. Zaidi, A. Dhahri, E. K. Hlil, and J. Dhahri. *J. Solid State Chem.* **215**, 193 (2014).

[154] Za. Mohamed, E. Tka, J. Dhahri, and E. K. Hlil. *J. Alloys. Comp.* **619**, 520 (2014).

[155] Ch. V. Mohan, M. Seeger, H. Kronmüller, P. Murugaraj, and J. Maier. *J. Magn. Magn. Mater.* **183**, 348 (1998).

[156] Y. Motome and N. Furukawa. *Phys. Rev. B* **68**, 144432 (2003).

[157] Y. Motome and N. Furukawa. *J. Phys. Soc. Jpn.* **72**, 2126 (2003).

[158] Y. Motome and N. Furukawa. *J. Phys. Soc. Jpn.* **69**, 3785 (2000).

[159] N. Moutis, I. Panagiotopoulos, M. Pissas, and D. Niarchos. *Phys. Rev. B* **59**, 1129 (1999).

[160] A. Muñoz, J. A. Alonso, M. J. Martínez-Lope, M. T. Casáis, J. L. Martínez, and M. T. Fernández-Diaz. *Phys. Rev. B* **62**, 9498 (2000).

[161] A. K. Murtazev and Zh. G. Ibaev. *J. Exp. Theor. Phys.* **113**, 106 (2011).

[162] S. Nair, A. Banerjee, A. V. Narlikar, D. Prabhakaran, and A. T. Boothroyd. *Phys. Rev. B* **68**, 132404 (2003).

[163] M. Nasri, M. Triki, E. Dhahri, and E. K. Hlil. *J. Alloys Compd.* **546**, 84 (2013).

[164] A. Oleaga, A. Salazar, D. Prabhakaran, J.-G. Cheng, and J.-S. Zhou. *Phys. Rev. B* **85**, 184425 (2012).

[165] A. Omri, A. Tozri, M. Bejar, E. Dhahri, and E.K. Hlil. *J. Magn. Magn. Mater.* **324**, 3122 (2012).

[166] A. Onuki. *Phase Transition Dynamics*. Cambridge Univ. Press, Cambridge, UK (2002).

[167] B. Padmanabhan, H. L. Bhat, S. Elizabeth, S. Rößler, U. K. Rößler, K. Dörr, and K. H. Müller. *Phys. Rev. B* **75**, 024419 (2007).

[168] D. P. Pappas, K.-P. Kämper, and H. Hopster. *Phys. Rev. Lett.* **64**, 3179 (1990).

[169] J. Park, U. Kong, A. Pirogov, S. I. Choi, J.-G. Park, Y. N. Choi, C. Lee, and W. Jo. *Appl. Phys. A* **74**, 796 (2002).

[170] I. Paul. *Phys. Rev. Lett.* **107**, 047004 (2011).

[171] S. Petit, F. Moussa, M. Hennion, S. Pailhés, L. P.-Gaudart, and A. Ivanov. *Phys. Rev. Lett.* **99**, 266604 (2007).

[172] P. Pfeuty and G. Toulouse. *Introduction to the Renormalization Group, and to Critical Phenomena*. John Villey and Sons, Singapore (1977).

[173] C. Pfleiderer. *Rev. Mod. Phys.* **81**, 1551 (2009).

[174] C. Pfleiderer and A. D. Huxley. *Phys. Rev. Lett.* **89**, 147005 (2002).

[175] M. H. Phan, V. Franco, N. S. Bingham, H. Srikanth, N. H. Hur, and S. C. Yu. *J. Alloys. Compd.* **508**, 238 (2010).

[176] T.-L. Phan, S. G. Min, S. C. Yu, and S. K. Oh. *J. Magn. Magn. Mater.* **304**, e778 (2006).

[177] T.-L. Phan, P. Q. Thanh, N. H. Sinh, K. W. Lee, and S. C. Yu. *Cur. Appl. Phys.* **11**, 830 (2011).

[178] T.-L. Phan, Q. T. Tran, P. Q. Thanh, P. D. H. Yen, T. D. Thanh, and S. C. Yu. *Solid State Commun.* **184**, 40 (2014).

[179] M. Picco. arXiv/1207.1018 (2012).

[180] M. L. Plumer and A. Caillé. *Phys. Rev. B* **41**, 2543 (1990).

[181] M. L. Plumer and A. Caillé. *Phys. Rev. B* **37**, 7712 (1988).

[182] M. L. Plumer, A. Caillé, and K. Hood. *Phys. Rev. B* **39**, 4489 (1989).

[183] M. L. Plumer, K. Hood, and A. Caillé. *Phys. Rev. Lett.* **60**, 45 (1988).

[184] M. Poirier, F. Laliberté, L. P.-Gaudart, and A. Revcolevschi. *Phys. Rev. B* **76**, 174426 (2007).

[185] A. K. Pramanik and A. Banerjee. *Phys. Rev. B* **79**, 214426 (2009).

[186] G. Quirion, X. Han, and M. L. Plumer. *Phys. Rev. B* **84**, 014408 (2011).

[187] S. Raymond and A. Huxley. *Physica B* **350**, 33 (2004).

[188] H. Röder, J. Zang, and A. R. Bishop. *Phys. Rev. Lett.* **76**, 1356 (1996).

[189] B. Roessli, S. N. Gvasaliya, E. Pomjakushina, and K. Conder. *JETP Lett.* **81**, 287 (2005).

[190] S. Rosenkranz, R. Osborn, J. F. Mitchell, U. Geiser, J. Ku, A. J. Schultz, and D. M. Young. *Physica B* **241-243**, 448 (1998).

[191] S. Rößler, U. K. Rößler, K. Nenkov, D. Eckert, S. M. Yusuf, K. Dörr, and K.-H. Müller. *Phys. Rev. B* **70**, 104417 (2004).

[192] Sk. Sabyasachi, A. Bhattacharyya, S. Majumdar, S. Giri, and T. Chatterji. *J. Appl. Phys.* **577**, 165 (2013).

[193] M. Sahana, U. K. Rössler, N. Ghosh, S. Elizabeth, H. L. Bhat, K. Dörr, D. Eckert, M. Wolf, and K.-H. Müller. *Phys. Rev. B* **68**, 144408 (2003).

[194] J. Sak. *Phys. Rev. B* **8**, 281 (1973).

[195] S. Sakarya, W. Knafo, N. H. van Dijk, Y. Huang, C. Meingast, and H. v. Löhneysen. *J. Phys. Soc. Jpn.* **79**, 014702 (2010).

[196] S. Sakarya, N. H. van Dijk, A. d Visser, E. Bruck, Y. Huang, J. A. A. J. Perenboom, H. Rakoto, and J.-M. Broto. *J. Magn. Magn. Mater* **310**, 1564 (2007).

[197] M. B. Salamon and M. Jaime. *Rev. Mod. Phys.* **73**, 583 (2001).

[198] S. S. Saxena, P. Agarwal, K. Ahilan, F. M. Grosche, R. K. W. Haselwimmer, M. J. Steiner, E. Pugh, I. R. Walker, S. R. Julian, P. Monthoux, G. G. Lonzarich, A. Huxley, I. Sheikin, D. Braithwaite, and J. Flouquet. *Nature (London)* **406**, 587 (2000).

[199] P. A. Sharma, J. S. Ahn, N. Hur, S. Park, S. B. Kim, S. Lee, J.-G. Park, S. Guha, and S-W. Cheong. *Phys. Rev. Lett.* **93**, 177202 (2004).

[200] R. P. Sharma, G. C. Xiong, C. Kwon, R. Ramesh, R. L. Greene, and T. Venkatesan. *Phys. Rev. B* **54**, 10014 (1996).

[201] A. Shengelaya, G.-M Zhao, H. Keller, and K. A. Müller. *Phys. Rev. Lett.* **77**, 5296 (1996).

[202] A. Shengelaya, G.-M Zhao, H. Keller, K. A. Müller, and B. I. Kochelaev. *Phys. Rev. B* **61**, 5888 (2000).

[203] A. B. Shick and W. E. Pickett. *Phys. Rev. Lett.* **86**, 300 (2001).

[204] H. S. Shin, J. E. Lee, Y. S. Nam, H. L. Ju, and C. W. Park. *Solid State Commun.* **118**, 377 (2001).

[205] R. Singh, K. Dutta, and M. K. Nandy. *Phys. Rev. E* **92**, 012123 (2015).

[206] R. Singh, K. Dutta, and M. K. Nandy. *Phys. Rev. E* **95**, 012133 (2017).

[207] R. Singh, K. Dutta, and M. K. Nandy. *Phys. Rev. E* **93**, 052132 (2016).

[208] R. Singh, K. Dutta, and M. K. Nandy. *Euro. Phys. Lett.* **110**, 16003 (2015).

[209] R. Singh, K. Dutta, and M. K. Nandy. arXiv/1608.07404 (2016).

[210] E. Slooten, T. Naka, A. Gasparini, Y. K. Huang, and A. de Visser. *Phys. Rev. Lett.* **103**, 097003 (2009).

[211] M. Smari, I. Walha, A. Omri, J. J. Rousseau, E. Dhahri, and E. K. Hlil. *Cermaic. Int.* **40**, 8945 (2014).

[212] D. A. Sokolov, R. Ritz, C. Pfleiderer, T. Keller, and A. D. Huxley. *J. Phys.: Conf. Ser.* **273**, 012085 (2011).

[213] A. B. Souchkov, J. R. Simpson, M. Quijada, H. Ishibashi, N. Hur, J. S. Ahn, S.W. Cheong, A. J. Millis, and H. D. Drew. *Phys. Rev. Lett.* **91**, 027203 (2003).

[214] N. A. Spaldin and M. Fiebig. *Nature (London)* **309**, 391 (2005).

[215] H. E. Stanley. *Introduction to Phase Transitions and Critical Phenomena*. Oxford University Press, New York (1971).

[216] C. Stock, D. A. Sokolov, P. Bourges, P. H. Tobash, K. Gofryk, F. Ronning, E. D. Bauer, K. C. Rule, and A. D. Huxley. *Phys. Rev. Lett.* **107**, 187202 (2011).

[217] H. Suzuki and T. Watanabe. *J. Phys. Soc. Jpn.* **30**, 367 (1971).

[218] M. Suzuki, Y. Yamazaki, and G. Igarashi. *Phys. Lett.* **42A**, 313 (1972).

[219] M. Tachibana, J. Yamazaki, H. Kawaji, and T. Atake. *Phys. Rev. B* **72**, 064434 (2005).

[220] S. Taran, B. K. Chaudhuri, S. Chatterjee, H. D. Yang, S. Neeleshwar, and Y. Y. Chen. *J. Appl. Phys.* **98**, 103903 (2005).

[221] N. Tateiwa, Y. Haga, T. D. Matsuda, E. Yamamoto, and Z. Fisk. *Phys. Rev. B* **89**, 064420 (2014).

[222] V. Taufour, D. Aoki, G. Knebel, and J. Flouquet. *Phys. Rev. Lett.* **105**, 217201 (2010).

[223] A. Theumann. *J. Phys. A: Math. Gen.* **14**, 2759 (1981).

[224] R. I. Thomson, T. Chatterji, C. J. Howard, T. T. M. Palstra, and M. A. Carpenter. *J. Phys.: Condens. Matt.* **26**, 045901 (2014).

[225] A. Tröster. *Phys. Rev. B* **76**, 012402 (2007).

[226] A. Tröster. *Phys. Rev. E* **79**, 036707 (2009).

[227] A. Tröster. *Phys. Rev. B* **81**, 125135 (2010).

[228] A. Tröster. *Phys. Rev. Lett.* **100**, 140602 (2008).

[229] M. Uhlarz, C. Pfleiderer, and S. M. Hayden. *Phys. Rev. Lett.* **93**, 256404 (2004).

[230] L. V.-Doloc, J. W. Lynn, Y. M. Mukovskii, A. A. Arsenov, and D. A. Shulyatev. *J. Appl. Phys.* **83**, 7342 (1998).

[231] E. Velu, D. Cadoul, B. Lécuyer, and J.-P. Renard. *Phys. Lett.* **36A**, 443 (1971).

[232] E. Velu, J.-P. Renard, and B. Lécuyer. *Phys. Rev. B* **14**, 5088 (1976).

[233] R. Venkatesh, M. Pattabiraman, K. Sethupathi, G. Rangaragan, S. Angappane, and J.-G. Park. *J. Appl. Phys.* **103**, 07B319 (2008).

[234] R. von Helmolt, J. Wecker, B. Holzapfel, L. Schultz, and K. Samwer. *Phys. Rev. Lett.* **71**, 2331 (1993).

[235] H. Wagner. *Phys. Rev. Lett.* **25**, 261 (1970).

[236] H. Wagner. *Phys. Rev. Lett.* **25**, 31 (1970).

[237] H. Wagner and J. Swift. *Z. Phys.* **239**, 182 (1970).

[238] A. Weinrib and B. I. Halperin. *Phys. Rev. B.* **27**, 413 (1983).

[239] J. M. Wesselinowa, A. T. Apostolov, I. N. Apostolova, and S. G. Bahoosh. *Bulg. J. Phys.* **38**, 420 (2011).

[240] B. Widom. *J. Chem. Phys.* **43**, 3898 (1963).

[241] K. G. Wilson. *Phys. Rev. Lett.* **28**, 548 (1972).

[242] K. G. Wilson. *Rev. Mod. Phys.* **55**, 583 (1983).

[243] K. G. Wilson and M. E. Fisher. *Phys. Rev. Lett.* **28**, 240 (1972).

[244] K. G. Wilson and J. Kogut. *Phys. Rep.* **12**, 75 (1974).

[245] M. C. Yalabik and J. D. Gunton. *Phys. Rev. B* **25**, 534 (1982).

[246] H. Yamagami, T. Ohkochi, S. Fujimori, T. Toshimitsu, A. Yasui, T. Okane, Y. Saitoh, A. Fujimori, Y. Haga, E. Yamamoto, S. Ikeda, and Y. Ōnuki. *J. Phys.: Conf. Ser.* **200**, 012229 (2010).

[247] F. Y. Yang, C. L. Chien, X. W. Li, G. Xiao, and A. Gupta. *Phys. Rev. B* **63**, 092403 (2001).

[248] J. Yang and Y. P. Lee. *Appl. Phys. Lett.* **91**, 142512 (2007).

[249] J. Yang, Y. P. Lee, and Y. Li. *Phys. Rev. B* **76**, 054442 (2007).

[250] J. Yang, Y. Q. Ma, R. L. Zhang, B. C. Zhao, R. Ang, W. H. Song, and Y. P. Sun. *Solid State Commun.* **136**, 268 (2005).

[251] A. Yaouanc, P. Dalmas de Réotier, and E. Frey. *Phys. Rev. B* **47**, 796 (1993).

[252] A. Yaouanc, P. Dalmas de Réotier, P. C. M. Gubbens, C. T. Kaiser, A. A. Menovsky, M. Mihalik, and S. P. Cottrell. *Phys. Rev. Lett.* **89**, 147001 (2002).

[253] O. A. Yassin, M. I. Mohamed, and S. N. Bhatia. *Phys. Stat. Sol. (b)* **245**, 745 (2008).

[254] M. A. Yurishchev. *Phys. Rev. B* **50**, 13533 (1994).

[255] C. Zener. *Phys. Rev.* **82**, 403 (1951).

[256] P. Zhang, T. D. Thanh, T.-L. Phan, and S. C. Yu. *J. Appl. Phys.* **113**, 17E144 (2013).

[257] G.-M. Zhao, K. Konder, H. Keller, and K. A. Müller. *Nature (London)* **381**, 676 (1996).

[258] B. Zheng. *Phys. Lett. A* **282**, 132 (2001).

[259] M. Ziese. *J. Phys.: Condens. Matter* **13**, 2919 (2001).

[260] J. Zinn-Justin. *Quantum Field Theory and Critical Phenomena*. Oxford Univ. Press, Oxford (2002).

List of Publications

1. Rohit Singh, Kishore Dutta, and Malay K. Nandy.
   Nonlocal mode-coupling interactions and phase transition near tricriticality.
   Europhys. Lett. **110**, 16003 (2015).

2. Rohit Singh, Kishore Dutta, and Malay K. Nandy.
   Nonlocal quartic interactions and universality classes in perovskite manganites.
   Phys. Rev. E **92**, 012123 (2015).

3. Rohit Singh, Kishore Dutta, and Malay K. Nandy.
   Critical dynamics of a nonlocal model and critical behavior of perovskite manganites.
   Phys. Rev. E **93**, 052132 (2016).

4. Rohit Singh, Kishore Dutta, and Malay K. Nandy.
   Conserved nonlocal dynamics and critical behavior of uranium ferromagnetic superconductors.
   Phys. Rev. E **95**, 012133 (2017).